Department of Chemistry

Aerosol-Assisted Chemical Vapour Deposition of Doped Titania films; Characterisation and Functional Properties

A thesis is submitted in partial fulfilment of the requirements for the degree of Doctor of Material Science (chemistry)

By

Abdullah Mohmmed Alotaibi

Supervisors: Professor Ivan P. Parkin and Dr. Sean Nair

UCL

2019

Declaration

I, Abdullah Mohmmed Alotaibi, confirm that the work presented in this thesis is my own. Where information has been derived from other sources, I confirm that this has been indicated in the thesis.

Abdullah Mohmmed Alotaibi

January 2019

Abstract

Titanium dioxide (TiO_2) is the leading material for self-cleaning applications due to its unique properties¸ including the fact that it exhibits high photocatalysis, mechanical robustness, chemical inertness, low cost, environmentally friendliness and abundance. The bandgap of TiO_2 is relatively large, and this limits its outdoor applications. Another obstacle for its use as a photocatalyst is the high level of electron–hole recombination and low rate of photoreaction with reactants. There have been great efforts to improve the photocatalytic properties of TiO_2. These have involved searching for ways of decreasing the bandgap structure and recombination rate, as well as improving the electronic structure to enhance its functional properties under visible light. One useful approach for achieving a suitable bandgap and improving electron–hole separation is combining or doping TiO_2 with anionic and/or cationic species.

In this study, Cu-doped TiO_2 films were deposited via aerosol-assisted chemical vapour deposition (AACVD). The Cu-doped TiO_2 films system in both phases (anatase and rutile) were specifically investigated for improved photocatalytic and antimicrobial properties of TiO_2 under UVA compared with pure TiO_2 thin films. Interactions between substitutional (replacing oxygen sites) and interstitial (sitting in the TiO_2 lattice) Cu in the anatase lattice may also explain the enhancement in exciton lifetimes. A range of copper concentrations (2, 5, 10 and 20%) was investigated so that the photocatalytic and antibacterial abilities (vs. *S. aureus* and *E. coli*) could be determined. Effective dopant selection and concentration control is key to providing the maximum efficiency in terms of carrier lifetimes for migration to the surface for the necessary reactions to take place in photocatalysis and antibacterial activity.

Interestingly, the AACVD system could be used to deposit TiO_2 in rutile form on a thin layer of ZrO_2 at 500°C. Cu-doped rutile–TiO_2 films using a range of copper concentrations (2, 5, 10 and 20%) were investigated as well. The films showed surface plasmon resonance (SPR).

In addition, these films exhibited enhanced photocatalytic activity under visible light irradiation, which could have been due to SPR.

To the best of our knowledge, this is the first time that the brookite thin film form has been deposited by AACVD; in using AACVD to deposit the brookite TiO_2 thin films, the band structure and photocatalytic properties were investigated. The brookite films grown by AACVD showed a direct bandgap of 3.4 eV. It was found that the photocatalytic properties of the brookite form, in comparison with degradation of stearic acid, were greater than the activity of anatase TiO_2 thin films, as well as active glass. In addition, transient absorption spectroscopy (TAS) measurements showed that the hole–electron recombination dynamics are similar in both phases. The high surface area of the brookite form compared with the surface area of the anatase thin film could be the primary reason for the super-photocatalytic properties. Surprisingly, the brookite film exhibited superhydrophilic properties prior to any irradiation.

The addition of Zn and nitrogen into the matrix of TiO_2 films by AACVD was studied most extensively to improve the functional properties of TiO_2 and achieve its activity under visible light. The oxygen atom in TiO_2 lattice can be replaced by a nitrogen atom, which is called Ns (substitutional doping) in this case; alternatively, nitrogen atoms can be set in the TiO_2 lattice, and this is called Ni (interstitial doping). These approaches create NH_X and NO_X surface species, which were observed using the X-ray photoelectron spectroscopy (XPS) results in this research. Transient absorption spectroscopy (TAS) was used to investigate the addition of (N + Zn) on the charge carrier dynamics of TiO_2.

Heterojunction systems of semiconductor materials are employed in different applications, such as water splitting, catalysis and electronic devices. These systems strengthen the synergistic effect, electron tunnelling and electron transfer, thereby leading to improved performance compared with the individual components. By using AACVD and APCVD

processes with heterojunction systems, TiO_2/Fe_2O_3 films were deposited, and different thicknesses of TiO_2 were used on the Fe_2O_3 films. The resulting TiO_2/Fe_2O_3 films exhibited enhanced performance in terms of the photocatalytic properties for the degradation of stearic acid under white light, as well as better photocurrent density and stability of the TiO_2/α-Fe_2O_3 heterojunction. The TAS measurements showed the extent of its lifetime photogenerated charges.

Impact Statement

In this thesis, we explored titanium dioxide and doped titanium dioxide systems for photocatalysis and antimicrobial purposes and that we are looking to understand the mechanism of action through theory and TAS measurements.

The discovery and development of a method of increasing photocatalytic performance of TiO_2 coatings can be used in many countries for water purification. In addition, antimicrobial surfaces are developed by doping TiO_2 with certain metals; the resulting materials can be used in the hospital touch surface applications as an approach to reducing incidents caused by hospital-acquired infections (HAIs). In this thesis, for the first time, we develop a new method of depositing brookite TiO_2 thin films, and their photocatalytic properties were investigated. This could open the door for further studies on brookite thin films and their applications. Moreover, the kinetics of electron–hole recombination for these films are investigated using TAS, and the hole–electron wavelengths of TiO_2 thin films are identified, while the rate of recombination is quantified by finding the time when half the initial absorption is lost ($t_{50\%}$). This could open the door for further studies on the charge carrier dynamics of TiO_2 thin films. In this thesis also, heterojunction system, TiO_2/α-Fe_2O_3 was grown by CVD methods. The

resulting TiO_2/α-Fe_2O_3 heterojunction films revealed charge transfer phenomena. TAS was employed to demonstrate electron-hole recombination. It was found that TiO_2/α-Fe_2O_3 heterojunction films extend lifetime and reduce electron-hole recombination. This reduction in the electron-hole recombination has a dramatic impact on the photocatalytic efficiency of TiO_2/α-Fe_2O_3 heterojunction system.

List of publications

- Abdullah M. Alotaibi, Sanjayan Sathasivam, Benjamin A. D. Williamson, Andreas Kafizas, Carlos Sotelo-Vazquez, Alaric Taylor, David O. Scanlon, and Ivan P. Parkin "Chemical Vapor Deposition of Photocatalytically Active Pure Brookite TiO_2 Thin Films" Chemistry of Materials 2018, 30, 1353−1361.

- Abdullah M. Alotaibi, Sanjayan Sathasivam and Ivan P. Parkin, "Aerosol assisted chemical vapour deposition of a ZrO_2–TiO_2 composite thin film with enhanced photocatalytic activity" RSC Adv., 2015, 5, 67944–67950.

- Abdullah M. Alotaibi, Sanjayan Sathasivam, Sean P. Nair and Ivan P. Parkin, "Antibacterial properties of Cu–ZrO_2 thin films prepared via aerosol assisted chemical vapour deposition" J. Mater. Chem. B, 2016, 4, 666—671.

- Arreerat Jiamprasertboon, Michael J. Powell, Sebastian C. Dixon, Raul Quesada-Cabrera, Abdullah M. Alotaibi, Yao Lu, Aoyun Zhuang, Sanjayan Sathasivam, Theeranun Siritanon, Ivan P. Parkin and Claire J. Carmalt "Photocatalytic and electrically conductive transparent Cl-doped ZnO thin films via aerosol-assisted chemical vapour deposition" J. Mater. Chem. A, 2018, 6, 12682-12692.

- Abdullah M. Alotaibi, Benjamin A. D. Williamson, Sanjayan Sathasivam, Andreas Kafizas, Carlos Sotelo-Vazquez, John Buckeridge, Jiang Wu, Sean P. Nair, James R. Durrant, David O. Scanlon and Ivan P. Parkin"Uncovering the Origin of the Enhanced Photocatalytic and Antibacterial Ability of Cu-doped Anatase TiO_2 Thin Films through Theory and Experiment" In submission, 2018.

- Abdullah M. Alotaibi, Sanjayan Sathasivam, Carlos Sotelo-Vasquez, Ivan P. Parkin"Low temperature chemical vapour deposition of pristine and doped rutile TiO_2 plasmonic thin films" In submission, 2018.

- Abdullah M Alotaibi, Gi Byoung Hwang, Sean Near, Andreas Kafizas and Ivan P Parkin"Aerosol-assisted chemical vapour deposition of (N, Zn)-doped TiO_2 thin films: photocatalytic and antimicrobial studies" In submission 2018.

- Abdullah M. Alotaibi, Yajun Gao, Permrudee Promdet, Fan Cui, Andreas Kafizasb, Jiang Wu, Frédéric Laqua and Ivan P. Parkina"Stable and highly efficient

photoelectrochemical water splitting of the TiO_2/α-Fe_2O_3 heterojunction films by chemical vapour deposition" In submission, 2018.

- Arreerat Jiamprasertboon, Andreas Kafizas, Michael Sachs, Min Ling, Abdullah M. Alotaibi, Yao Lu, Theeranun Sirithanon, Ivan P. Parkin and Claire J. Carmalt, "Heterojunction α-Fe_2O_3/ZnO films with enhanced photocatalytic properties grown by aerosol-assisted chemical vapour deposition (AACVD) " In submission, 2019.

Acknowledgements

First, I would like to thank my primary supervisor, Professor Ivan P. Parkin, for his encouragement, advice, inspiration and support throughout my PhD. It has been a wonderful and helpful experience to work with him. I would also like to thank my secondary supervisor, Dr Sean Nair, for all the discussions, support and help with my microbiology research.

I am very grateful to Dr Sanjayan Sathasivam for his help, guidance and useful discussion during my PhD. I would like to say thank you for the friendship and for being there whenever I needed help during these years. In addition, I would like to take this opportunity to thank Dr Andreas Kafizas for his help, discussions about the TAS measurements and data analysis, support and advice, as well as for treating me like a brother. Furthermore, I would like to express my appreciation to Dr David O. Scanlon for his help with the theoretical studies presented in chapters 2 and 4 of this thesis.

I would like to thank all the staff at the Department of Chemistry who have encouraged me and helped me during my PhD study. Especially, I would like to thank Mr. Martin Vickers for helping me with the XRD analysis, Dr Steve Firth for helping me with SEM and Raman analysis, Dr Carlos Sotelo-Vazquez for assistance with FT-IR and photocatalytic analysis and Mr. Tom Bridges for his help with fixing the AACVD technique.

Table of Contents

List of Figures

List of symbols and acronyms

θ	theta
%	percent
°	degree
°C	degree Celsius
K	kelvin
Å	angstroms
eV	Electron volt
E_f	Fermi energy
nm	nanometer
E_g	Band gap
V_o	Oxygen vacancy
mol.%	mole percent
at.%	atomic percent
a.u.	Arbitrary units
TiO_2	Titanium dioxide
ZrO_2	Zirconium dioxide
DOS	density of States
N,Zn(0.2%)	(N, Zn(0.2%) doped TiO_2
N,Zn(0.5%)	(N, Zn(0.5%) doped TiO_2
N,Zn(1.0%)	(N, Zn(1.0%) doped TiO_2
N,Zn(1.5%)	(N, Zn(1.5%) doped TiO_2
WHO	World Health Organisation
AACVD	Aerosol Assisted Chemical Vapour Deposition
APCVD	Atmospheric Pressure Chemical Vapor Deposition
CVD	Chemical Vapor Deposition
FQE	Formal Quantum Efficiency
TAS	Transient Absorption Spectroscopy
XPS	X-ray Photoelectron Spectroscopy
XRD	X-ray Diffraction
UV/Vis	Ultraviolet-visible
FTIR	Fourier transform infrared spectroscopy
VB	Valence band
CB	Conduction band
EDX	Energy Dispersive X-ray spectroscopy
FTO	flurine co-doped tin(IV) oxide
FWHM	Full width half maximum
EXPGUI	Experiment graphical user interface
ROS	Reactive Oxygen Species
ALD	Atomic Layer Deposition
CFU	Colony Forming Units
PBS	Phosphate Buffered Saline
RHE	Reversible hydrogen electrode
AFM	atomic force microscope
PEC	photoelectrochemical
IPCE	Incident-photon-to-current efficiency
PL	Photoluminescence Spectra

Chapter 1

Introduction

"This chapter presents the aim and a brief introduction of important photocatalytic applications in the degradation of organic pollutants and for antimicrobial activity. The following chapter introduces a historical review and efforts to enhance photocatalytic activity of TiO_2. The principles and basics of chemical vapour deposition system is presented in this chapter. In this chapter, a brief introduction of transient absorption spectroscopy is also given."

1.1 Introduction

Today, the ever-growing size of the world's population demands a new strategy for the reduction environmental pollutants, including waterborne or airborne pollutants such as bacteria and other organic materials. Ensuring that water is free of pollutants is particularly important, as it is considered to be the main transmission medium for disease, and therefore has an extremely significant effect both on the environment and human health.[1] The problem is exacerbated by the fact that many of these pollutants – both water and airborne - have a long lifecycle, and, over time, accumulate to the extent that they have not only a direct impact on human health, but an indirect one, as they affect both the food chain and wildlife.[2] Furthermore, the issue is a deeply ingrained one, dating back to the years after WW II, when there was a large and fast growth in the production of chemical compounds for commercial use. This put great pressure on nations to develop domestic systems to deal with domestic sewage as well as agricultural and industrial waste from sources such as plastic producers, pharmaceutical plants and refineries. Despite this, however, the World Health Organisation (WHO), reports that some 2.5 billion people (39% of the World's population) do not have adequate sanitation systems, and that 884 million people lack clean drinking water. Within this total lies the startling statistic that some 16% of people in Sub-Saharan Africa lack access to safe drinking water.[3, 4]

This raises the obvious question of how the problem can be effectively dealt with. One approach which is thought to hold real promise is through photocatalysis, the utilisation of "ambient energy" (mainly from the sun). This process is currently thought to offer an effective and encouraging way of reducing the risks from airborne and waterborne pollutants to mankind.[5] This is because photocatalytic materials have shown significant potential in their ability to remove organic pollutants from the environment. Furthermore, one photocatalyst - TiO_2 - is abundant, non-toxic and low-cost, so it has the potential to be developed into an effective and relatively inexpensive way of dealing with the environmental pollution problem

being discussed here. In contrast, the use of conventional water treatment methods, such as treatment by ozone, chlorine, electrocatalytic oxidation processes and membrane systems, requires intensive energy usage and is highly expensive. As a result, the development of photocatalytic techniques, particularly those based on TiO_2 has become a principal focus of many research projects.

The aim of this thesis is to present ways of improving the functional properties of titanium dioxide (TiO_2) films, with a view to their effective use in the degradation of organic pollutants and reduction of antimicrobial activity.

In order to improve the functional properties of titania, it is necessary to investigate the incorporation of titania with metals and/or non-metals, because incorporation is observed to enhance photocatalytic and antimicrobial performance. This, in turn, is because incorporation leads to improved electronic structure, reduced bandgap in the visible region, and enhanced charge carrier recombination. In this thesis, we will investigate the activity of copper doped TiO_2 films in the anatase and rutile phases, (Zn + N) doped TiO_2, brookite TiO_2 thin films and TiO_2/Fe_2O_3 layer films. In addition, charge carrier recombination and lifetime will be investigated by transient absorption spectroscopy (TAS) and photoluminescence (PL).

1.2 Photocatalysis

Photocatalysis is a well-known process that uses the energy from light radiation to accelerate (catalyse) a chemical reaction, without forming part of the final product. It is used in a wide range of applications, including self-cleaning, water splitting, hydrogen production and photovoltaics.[6] Photocatalytic reactions may be homogenous or heterogeneous, depending on whether the reactants and the photocatalyst are in the same phase (homogenous) or not (heterogenous). One example of homogenous photocatalytic activity is the ozone and photo-

Fenton process, while examples of heterogeneous photocatalysis are found in semiconductors and transition metal oxides.[7-9]

1.2.1 Mechanism of photocatalysis

In the case of semiconductors (such as TiO_2) there are several steps in the photocatalytic mechanism: [10-16]

(1) Photoexcitation

Here, energy is absorbed by the semiconductor from the visible or UV spectrum. If the energy of the absorbed photons is greater than, or equal to, the band gap of semiconductor (Figure 1.1), electrons are promoted from the valence band (VB) to the conduction band (CB). This result is an electron-hole pairs, with the hole (h^+) on the VB and the electron (e^-) on the CB.[9] This is described by the equation:

$$TiO_2 + hv \rightarrow h_{VB}^{+} + e_{CB}^{-} \qquad (1\text{-}1)$$

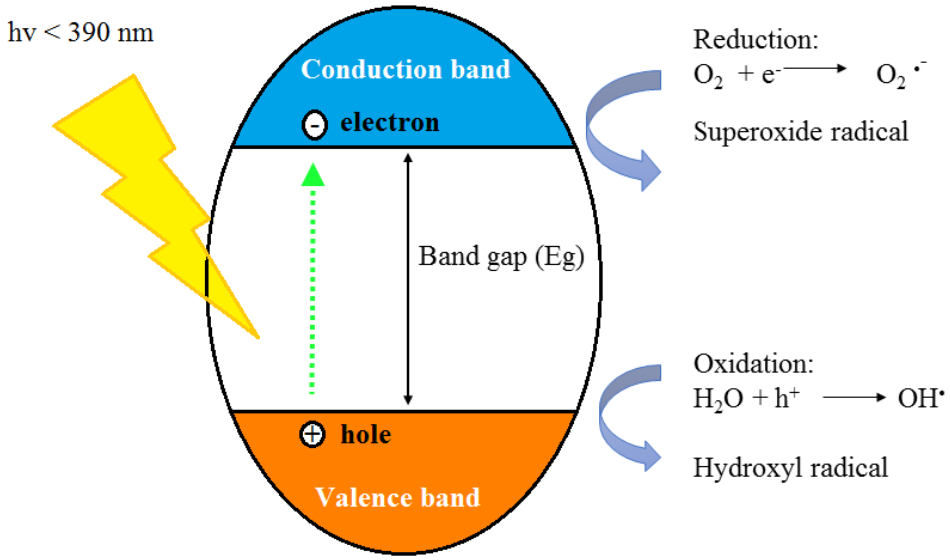

Figure 1.1. The general photocatalytic process of TiO_2

(2) Diffusion

This step is summarised in the following reactions:

$Ti^{IV} + H_2O \rightarrow Ti^{IV}\text{-}\ H_2O$

Ti^{IV} + organic pollutants (OR) $\rightarrow Ti^{IV}\text{-}\ (OR)_{ads}$ (1-2)

Here, organic pollutants (OR) and molecules of water (H_2O) are diffused on the surface of TiO_2 , generating a bond between (OR) and H_2O on the TiO_2 surface.

(3) Trapping

This occurs on the surface of TiO_2, when H_2O and OH^- react with a positive hole (h^+) to generate the hydroxyl radical ($OH^\bullet$) due to H_2O and OH^- can react as an electron donor (equation 1-3). Reduction of O_2 also occurs, when it is adsorbed on the surface of TiO_2 and reacts with a photogenerated electron (e^-) to form the superoxide radical ($O_2^{\bullet -}$) due to (O_2) is available as electron accepters as described by equation (1-4).

$Ti^{IV}\text{-}\ H_2O/OH^- + h^+ \rightarrow OH^\bullet + H^+$ (1-3)

$O_2 + e^- \rightarrow O_2^{\bullet -}$ (1-4)

(4) Oxidation

Here, hydroxyl radicals ($OH^\bullet$) can oxidise organic pollutants (OR) to mineral salts such as CO_2 and H_2O as described by equation (1-5). The superoxide radical ($O_2^{\bullet -}$) (equation 1-4) may react with H^+ (equation 1-3) to produce $^\bullet OOH$ (equation 1-6), and the hydroperoxyl radical ($^\bullet OOH$) may generate hydrogen peroxide (H_2O_2) and oxygen (O_2), according to equation 1-7. Further reactions include the oxidisation of organic

pollutants by the superoxide radical ($O_2^{\bullet -}$) and the hydoperoxyl radical ($^{\bullet}OOH$) (Equations 1-8 and 1-9)

$$(OR) + OH^{\bullet} \rightarrow \rightarrow CO_2 + H_2O \quad (1\text{-}5)$$

$$O_2^{\bullet -} + H^{+} \rightarrow {}^{\bullet}OOH \quad (1\text{-}6)$$

$$^{\bullet}OOH + {}^{\bullet}OOH \rightarrow H_2O_2 + O_2 \quad (1\text{-}7)$$

$$O_2^{\bullet -} + OR \rightarrow \rightarrow CO_2 + H_2O \quad (1\text{-}8)$$

$$^{\bullet}OOH + OR \rightarrow CO_2 + H_2O \quad (1\text{-}9)$$

(5) Recombination

Photocatalytic activity of semiconductors is limited by the recombination of photogenerated charge carriers. This happens when electrons excited from VB to CB return quickly to the VB, without reacting with the absorbed species. The energy of recombination is emitted as a heat or light (equation 1-10).

$$h^{+}_{(VB)} + e^{-}_{(CB)} \rightarrow \text{heat} \quad (1\text{-}10)$$

Furthermore, recombination could occur on the surface, or in the bulk, of TiO_2.

In general, to be useful for the purpose under discussion here, there are several properties that a photocatalytic semiconductor material should possess. The main ones are:

i) low toxicity and cost

ii) photoactive

iii) chemically and biologically inert

iv) displays photocatalytic behaviour when irradiated by visible and/or UV light

v) resistance toward photocorrosion

One result of this is that titanium dioxide (TiO_2) is considered to be the most interesting photocatalyst semiconductor, particularly because of its non-toxic, low-cost nature and effective properties to light. However, its wide band gap (3.2 eV, anatase; 3.0 eV, rutile) means that it is active under UV radiation only, which is considered an obstacle for visible light applications.[17]

1.3 Enhancing the functions of titanium oxide thin films

The importance of titania stems from its ability to be used in multiple applications, including solar cell devices[18], water splitting[19], self-cleaning[20] and gas sensors.[21] This diversity of application results from factors such as its electronic, optical and structural properties, as well as its reactivity, surface area, morphology and crystallinity.

Specific examples of current applications of titania include commercial products such as self-cleaning glass, which results from the material's high photocatalytic activity, mechanical robustness and low cost. One of the leading companies in this field is Pilkington, which produces a range called Pilkington Activ™ , a self-cleaning glass which not only solves the problem of dirty windows, but reduces the sound of rain impact. The product achieves this by employing photocatalytic activity to break down organic pollutants and its hydrophilic properties to help remove loosened dirt quickly.[22]

In industry, titania is used as a white pigment in products such as paint, paper and some kinds of food.[23] TiO_2 can also be used as a sunscreen, due to its ability to absorb UV, while remaining transparent to visible light.[24] In cosmetics, titania is used as a skin-brightening agent as well as an away of concealing blemishes.[24] Additionally, TiO_2 thin films has been shown to help degrade organic pollutants, bacteria and viruses.[5, 25-27]

As to its structure, titanium dioxide exists in three natural crystalline phases: rutile, brookite and anatase **(Figure 1-2)**.[28-30] The rutile phase is considered to be more

thermodynamically stable in large particles form, compared with anatase and brookite, though the anatase phase is more stable in nanoparticle (ultrafine) form. When Kiedel (1929[31]) studied the photocatalytic activity of TiO_2 he found that a mix of rutile and anatase TiO_2 "titanium white pigment" leads to the chalking of paints when subjected to radiation of visible light frequency. The result was further studies on TiO_2, and, by the end of 1938, another study had demonstrated that the effects reported by Kiedel were due to the degradation of organic material-bonds to the titania (as a result of photocatalytic activity).[32]

When, in 1972, Fujishima and Honda reported for the first time that rutile-TiO_2 and UV light could be used to split water into its component parts (hydrogen and oxygen) there was a dramatic increase in studies of the photocatalytic activity of TiO_2.[19]

1.4 Structure of TiO_2

As we have already noted, the indirect bandgap energies of the rutile and anatase phases of TiO_2 are 3.0 eV and 3.2 eV respectively, a difference which is due to variations in lattice structure. Although both the anatase and rutile phases consist of a tetragonal lattice structure, made up of octahedral TiO_6 building blocks, the Ti atom in both phases is found in the centre of the structure, with an oxygen atom at the vertices. The difference between the structures is their assembly pattern, as each octahedron has a different distortion. The brookite phase has an orthorhombic structure.

In addition, the anatase phase has space group $I_{41/amd}$, and the rutile phase has space group $P_{42/mnm}$ (**Figure1-2).** The most stable planes of anatase and rutile are (101) and (110) respectively. The CB and VB of TiO_2 are different in structure, comprising 3d states on Ti and 2p states on O_2, with titanium and oxygen ions having oxidation states Ti^{4+} and O^{2-}.[33, 34]

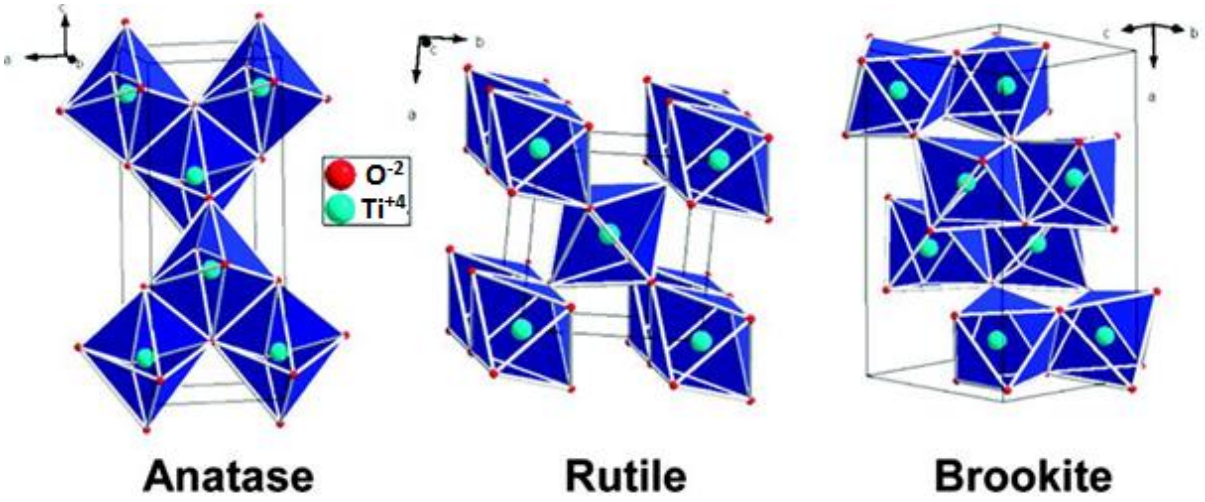

Figure 1.2. TiO_2 structure - rutile, anatase and brookite natural phase. Reproduced with permission from [35].

1.5 Photocatalytic activity

The anatase phase of TiO_2 shows higher photocatalytic activity than the rutile phase, even though it (the anatase phase) has a larger bandgap. This difference may be a result of two principal factors:

(i) Surface behaviour

Both phases are affected by the presence of a peroxo species. However, while the surface of anatase is covered by a layer of a peroxo-species, the rutile phase has only a small amount on the surface during photo-oxidation processes.[36]

ii) The photogenerated carrier recombination rate

This is higher in the rutile phase than in the anatase phase. Transient absorption spectroscopy (TAS) shows that this is due to recombination in the crystal phase rather than surface state. This has important implications for increasing lifetime. [37]

Due to the fact that the anatase phase of TiO_2 has a large band gap (3.2 eV, $\lambda \approx 387$ nm), TiO_2 shows photocatalytic activity when exposed to UV radiation. As previously noted (Section 1.1), this (UV radiation) causes electrons to 'jump' from the VB to CB, creating electron-hole

pairs. This results in a hole in the surface of TiO_2, which can react with, for example, H_2O to produce the hydroxyl radical (OH^-). At the same time, the electron in the conduction band may react with, for example, di-oxygen (O_2) to generate superoxide ($O_2^{\bullet-}$) radicals **(Figure 1.1).** This photocatalytic mechanism of TiO_2 can explain the degradation of organic pollutants on the surface of TiO_2., as reactive species, such as hydroxyl radicals and superoxide groups, are able to oxidise nearby organic pollutants to CO_2 and H_2O (equation 1.11).[38]

$$\text{Organic pollutant} \xrightarrow[\text{ii) } O_2 \\ \text{iii) } hv > Eg]{\text{i) Semiconductor}} CO_2 + H_2O + \text{meneral acids} \qquad 1.11$$

The mechanism by which organic pollutants are degraded by photocatalysis is described by the Langmuir–Hinshelwood kinetic relationship:

$$r_i = \frac{k_S \times S_s \times \Theta_i}{(1 + S_s \times \Theta_i)} \qquad 1.12$$

Where r is the initial reaction rate (organic pollutant degradation), Θ_i is the initial concentration of the organic pollutant, S_s is the rate kinetic constant of organic pollutant to surface absorbed TiO_2 film, and k_s is the kinetic constant of photocatalytic activity. The parameters in this equation are affected by a number of factors, including:

(i) k_s. This is affected by the fraction of oxygen (O_2) absorbed on the surface of TiO_2, as well as the intensity of light absorption (I_0).

(ii) Film thickness. In photocatalytic semiconductors, this plays an important role in understanding the level of photons (I_a) that can be absorbed.

(iii) Bandgap energy. This allows the determination of the region of the solar spectrum in which excitation will occur, thus creating electron-hole pairs.

(iv) Roughness of the film surface. This determines how many active surface sites come into contact with organic pollutants (Θ) to establish radical and superoxide species (k_i).

(v) Recombination and lifetime.

(vi) Crystallinity of semiconductor films. Photocatalysis in semiconductors is affected by crystallinity, as this increases the transfer of photo-generated electron-hole pairs from the material's bulk to its surface (k_s).

1.5.1 The photo-induced hydrophilic effect

The photo-induced hydrophilic effect (PIH) of TiO_2 thin films has been extensively investigated.[39, 40] In their initial state, TiO_2 thin films show a water contact angle (absorption of water molecule on the TiO_2 surface) of about 60^o, which decreases to about 1^o after exposure to UV radiation.[41] There are many applications for this phenomenon, some of which have already been commercially developed, such as anti-fogging mirrors and self-cleaning windows.[20]

However, as PIH occurs when TiO_2 films are exposed to UV radiation, the hole created on the surface of the titania can react with oxygen, leading to the creation of oxygen vacancies as well as the conversion of Ti^{4+} to Ti^{3+}. These oxygen vacancies are absorbed by airborne water molecules, generating the hydroxyl radical (OH^-) on the surface of TiO_2. Further, the presence of Ti^{3+} encourages dissociative H_2O adsorption. As a result, the wettability of the surface increases with the number of hydroxyl groups, as OH^- groups attract H_2O by creating hydrogen bonds **(Figure 1.3)**.[20, 39]

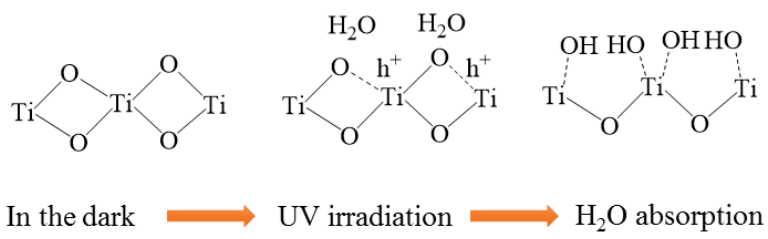

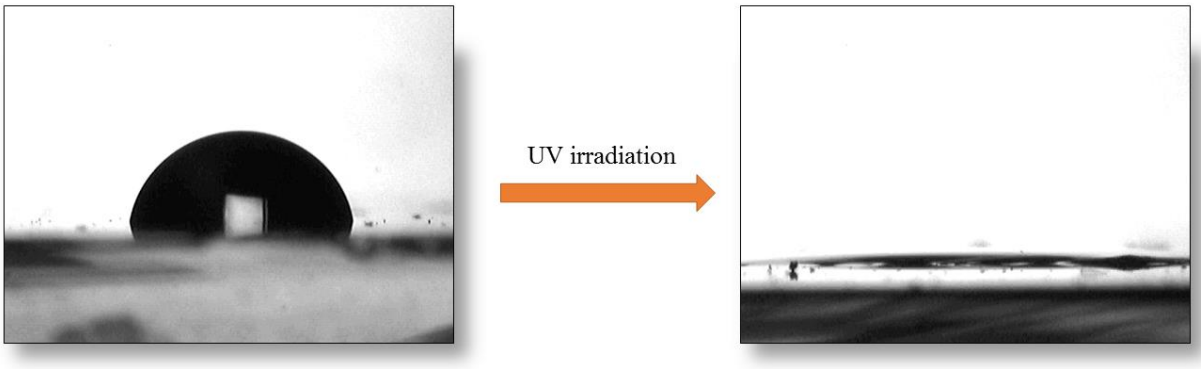

Figure 1.3. The change in water contact angle with TiO_2 thin films before and after exposure to UVA radiation. This film was deposited by AACVD from titanium isopropoxide in ethylacetate at 450°C and then placed under UVA for 24 h.

Many attempts have been made to improve the photocatalytic efficiency of TiO_2, by reducing the band gap of TiO_2 (3.2 eV for anatase) in order to shift absorption to the visible region of the EM spectrum. This would enable more of suns spectrum to be used as a photocatalyst, as well as reduce charge carrier recombination. To achieve this aim, TiO_2 doped with metals and non-metals (e.g., N, S, P, C and F) has been extensively investigated. Doping with metal and/or non-metals have been found to result in high levels of photocatalysis under exposure to visible radiation.

1.5.2 Non-metal doped TiO_2

1.5.2.1 Nitrogen doping

The results of research into nitrogen-doped TiO_2 have been reported by many publications. Asahi *et al.*[42], for example, demonstrated that N-doped TiO_2 improves photocatalytic degradation of gaseous acetaldehyde and methylene blue (MB) using radiation at visible light radiation. They also showed that nitrogen atoms replace oxygen within the lattice of TiO_2, and that this substitution leads to a narrower band gap and higher photocatalytic activity compared with undoped TiO_2. This narrowing of band gap (390-500 nm) could be due to the mixing of oxygen's 2p level with nitrogen's 2p level. However, while the creation of oxygen vacancies

contributes to enhanced photocatalytic activity under visible radiation[43], these oxygen vacancies also work as recombination centres, which may cause a *reduction* in photocatalytic activity under the same radiation conditions.[44]

Another important finding was by Cristiana Valentin *et al*,[45] who reported that, in N-doped TiO_2, where nitrogen substitutes for the lattice oxygen(Ti-N-Ti) or interstitial nitrogen (O-N-Ti), the interstitial N 2p N-O bond was divided into two bonding states: π bonding and π^* bonding. Two bonding states are located below the VB and two anti-bonding states are located above the VB (0.73 eV), while N substitution is above the VB by (0.14 eV).

However, nitrogen precursors also have an effect on photocatalytic activity. This was reported by Parkin *et al*.[46], who investigated the influence of different nitrogen precursors, such as benzylamine, ammonia and tetra-butylamine, on the photocatalytic activity of N-TiO_2 thin films. They found that N-doped TiO_2 thin films show improved photocatalytic activity compared with un-doped TiO_2 thin film, which is consistent with nitrogen concentration (particularly the N-O group) on the surface. They also noted, however, that high nitrogen concentrations in the bulk of the material could work as recombination centres.

1.5.2.2 Sulphur doping

The effects of doping TiO_2 with sulphur have been extensively studied, and it has been found that it enhances photocatalysis under exposure to radiation in the visible part of the spectrum[47,48]. Because sulphur has been found to substitute oxygen in lattice TiO_2 sites to form an S-Ti bond, S-doped TiO_2 may lead to a narrower band gap compared with N-doped TiO_2, as the ionic radius of S^{2-} is bigger than the ionic radius of N^{3-} , and consequently absorbs in visible light.[49] However, photocatalysis in sulphur-doped TiO_2 also depends on oxidation state (S^{2-}, S^{4+} and S^{6+}), as well as precursors and synthetic methods.

T. Ohno *et al*.[50] have demonstrated that cationic sulphur-doped TiO_2 has higher photocatalytic activity under visible radiation than anionic sulphur-doped TiO_2. In addition, Charles Dunnill *et al*.[51] has shown that S-doped TiO_2 thin films, deposited by chemical vapour deposition at 500°C, degrade (by photocatalysis under white light) 2,6-dichloroindophenol and stearic acid very well, compared with pure TiO_2 thin films, prepared under the same conditions. Furthermore, S-doped TiO_2 thin films have been shown to kill E. coli within 24h under white light.[51]

1.5.2.3 Phosphorus doped TiO_2

Phosphorous-doped TiO_2 has been shown to narrow the band gap which leads to photocatalytic activity under visible radiation, due to the creation of an absorption tail in this region of the spectrum.[52] The result is that P-doped TiO_2 enhances the photocatalytic activity of TiO_2. On the other hand, some studies have reported that doping TiO_2 with phosphorus can result in a similar effect in the UV region.[53] Gopal *et al*.[54] reported that P-doped TiO_2 nanoparticles increase photocatalytic degradation of methylene blue under visible radiation due to an increased red shift in the absorption spectra, a decreased particle size and the formation of O-Ti-P linkage. The increased redshift possibly resulted from an increased charge separation. P^{3+} doped TiO_2 thin films were found to give decreased photocatalytic activity compared with P^{5+} doping and un-doped TiO_2 thin films. The P^{3+} species resulted in 6 times higher recompilation of photogenerated charges, compared with P^{5+}, and 20 times higher compared with un-doped TiO_2 thin films.[55]

1.5.2.4 Fluorine doping

Other attempts to enhance the photocatalytic activity of TiO_2 have included adding fluorine into TiO_2. Xu *et al*,[56] found that this was effective, possibly due to the formation of oxygen vacancies on the surface of the TiO_2. It has also been shown that F-doped TiO_2 exhibits a red shift in the band gap. Research by Ho *et al*,[57] found that hierarchical fluorine-doped TiO_2 can degrade 4-chlorophenol under visible radiation. They suggested that photocatalytic activity is a result of the formation of oxygen vacancies, as opposed to a shift in the absorption spectra in the visible region.

1.5.2.5 (S+N) doping

Using two species as dopants - for example, N- and S-doped TiO_2 – has interesting effects in terms of photocatalytic activity in the visible region. When Xiang *et al*.[58] used (S+N) co-doped TiO_2 nanosheets to degrade 4-chlorophenol under visible radiation, they found it was three times more effective compared with pure TiO_2, and twice as effective as Degussa P25. This improvement could be a result of the synergetic effects of N and S and a red shift in absorption. Another study[59] on (S+N) co-doped TiO_2 nanobelts showed that photocatalytic degradation of potassium ethyl xanthate increased with increased concentration of thiourea under exposure to visible radiation, possibly due to a decrease in the recombination rate as well as an absorption shift in the visible region. On the other hand, Ju *et al*[60], found that (S+N) co-doped TiO_2 nanoparticles shows high photocatalytic degradation of methyl blue in the visible region.

1.5.2.6 Hydrogen doping

Hydrogenation of TiO_2 contributes to a shift in band gap to around 1.5 eV, while the colour of the titania turns to black. This is because hydrogenation leads to the creation of Ti^{3+} species and/or oxygen vacancies, causing TiO_2 to absorb nearly 100% of the radiation, from UV to near infrared (a range of approximately 1000 nm).[61] The greatest challenge in the hydrogenation of titania is annealing the TiO_2 with pure hydrogen at high temperatures, as hydrogen is very dangerous at such temperatures. To address this issue, Mao *et al*[62], built a special furnace for working with hydrogen at high temperatures and pressures. After maintaining the temperature at 200˚C for 5 days, they found that the TiO_2 turned black in colour **(Figure 1.4)** and that XPS showed Ti was in the 3+ oxidation state. However, they also found that the black TiO_2 degraded both methylene blue and phenol faster than the white form. In fact, black TiO_2 completely degraded methylene blue in sunlight after just 8 minutes, compared to 1 hour for the white form of TiO_2, while phenol was also degraded significantly faster by the black form. The researchers also found that black TiO_2 produces hydrogen under sunlight, while no hydrogen was produced by white TiO_2 under the same conditions.

Figure 1.4. The colour of TiO_2 before and after hydrogenation at 200 °C for 5 days. Reproduced from [62].

1.5.3 Transition metals doping

Metal doping can lead to a change in the properties of semiconductors due to lattice defects which occur when the lattice is loaded with impurity atoms. There are two types of doping: interstitial and substitutional. The former occurs when the impurity assumes normally occupied sites in the lattice, while the latter occurs when impurity atoms replace host atoms. Metal dopants may be p-type (which acts as acceptor centres) or n-type (which acts as donor centres). Electron-hole recombination is influenced by the type of metal dopant used (p-type or n-type), due to the high charge concentration of electrons on the CB. There are also factors which affect the photocatalytic activity of metal-doped TiO_2. These factors include the type of metal used as dopant, the concentration of dopant and the methods used in the preparation of materials.

1.5.3.1 Copper doping

As already noted, TiO_2 is frequently used in photocatalysis, while copper is used in many other applications, particularly photocatalysis and applications which make use of its antimicrobial properties. The use of Cu-TiO_2 (TiO_2 doped with Cu ions) for photocatalytic degradation of organic pollutants, has been much investigated, as has the antimicrobial behaviour of Cu-TiO_2 under UV and/or visible radiation. The importance of copper as a dopant stems from the fact that the element has high electronic conductivity. In addition, Cu dopants affect the band gap of TiO_2, particularly as Cu exists in different oxidation state (such as Cu_2O and CuO), which results in higher photocatalytic activity, as it leads to electron trapping which reduces charge carrier recombination. Furthermore, Cu dopants create defects and oxygen vacancies in TiO_2. Yang *et al*[63], studied the effect of Cu-doped TiO_2 nanoparticles on the degradation of methylene blue under UV illumination, using different levels of Cu concentration. They found that the nanoparticle band gap decreased as the concentration of copper increased. They also found that the photocatalytic degradation of methylene blue was higher than with pure TiO_2, and they

suggested that this was a result of lower charge carrier recombination in the Cu-doped TiO_2 nanoparticles as well as a decreased band gap.

1.5.3.2 Zinc doping

It has been reported that using zinc as a dopant can affect the photocatalytic performance of TiO_2.[64, 65] Although the band gaps of ZnO and TiO_2 (anatase) are quite similar (3.2 eV), the band gap positions are different. This difference could be one reason for the enhanced separation rate of photoinduced charge and the decreased rate of recombination.[64] However, Nguyen *et al*.[66] found that Zn-doped TiO_2 nanoparticles, prepared by the sol-gel and ammonia-evaporation method, resulted in higher photocatalytic degradation of methylene blue than pure TiO_2 nanoparticles, due to the increase in surface area and different energy levels. In addition, Zn has an effect on the optical band gap of TiO_2. Singla *et al.*[67] found that the band gap of TiO_2 decreased with the addition of zinc, leading to an increase (compared with pure TiO_2) in the photocatalytic degradation, under UV-Vis irradiation, of the dyes Methyl Red and Eriochrome Black T. In another research project, Zhao *et al.*[65], showed that Zn-doped TiO_2 nanoparticles, prepared by the hydrogen-oxygen diffusion flame technique, can degrade the dye Rhodamine B under visible radiation, due to the fact that zinc increases reactive oxygen species on the surface of TiO_2 and promotes electron injection into the CB.

1.5.3.3 Iron doping

Iron-doped TiO_2 is thought to have the ability to enhance the photocatalytic performance of TiO_2, compared with undoped TiO_2. Further, the level of enhancement increases with the amount of Fe in the TiO_2 lattice. Li *et al.*[68] found that Fe doping leads to a shift in the band gap to the visible region. They also found that Fe^{3+} occurs in the lattice of TiO_2 rather than on the surface, and that photocatalytic degradation of methylene blue increased compared to pure

TiO_2. However, Fe precursors also play an important role in photocatalysis. Research shows that the photocatalytic performance of Fe-doped TiO_2 from $FeCl_3$ proved more effective in degrading yellow XRG dye under visible light than Fe-doped TiO_2 from $FeCl_2$ as Fe precursors.[69] As Fe^{3+} and Ti^{4+} are similar in ionic radii, and Fe^{3+} has a good oxidation state for TiO_2 doping[70], photocatalytic performance depends on the incorporation of Fe into TiO_2, which can be substitutional or interstitial. Doping TiO_2 with Fe^{3+} leads to the separation of photogenerated charges, as TiO_2 has a higher dielectric constant compared with the α Fe_2O_3 phase. Consequently photocatalytic performance is enhanced.[71]

1.5.3.4 Au-TiO_2 coupling

Extensive research has been carried out on methods of improving the photocatalytic performance of TiO_2 using nanoparticles (NPs) of noble metals such as silver, gold and platinum. The results have been very encouraging.[72-75] Au nanoparticles have several remarkable properties, including surface plasmon resonance (SPR) which gives an absorption band in the visible region, at around 560 nm. It has been shown that electrons transfer from Au-NPs to TiO_2 at this wavelength.[75, 76] Due to a greater interaction between TiO_2 and Au NPs, the band gap of Au-TiO_2 is lower than that of pure TiO_2 in the anatase and rutile phases[77], though the improvement in photocatalytic performance of Au-TiO_2 is considered due to enhanced charge separation between hole and electron.[78] However, this improvement may also be related to the fact that the Fermi level of Au NPs is lower than the TiO_2 CB. Consequently, photo promoted electrons captured by AuNPs and the hole (h^+) still remain in the VB of TiO_2.[79]

Despite the advantages of the deposition of Au NPs on the surface of TiO_2, there are some drawbacks, too. It has, for example, been observed that, in some reactions, such as the oxidation of cyclohexane, the photocatalytic activity of Au-TiO_2 was reduced, as the presence of Au NPs on the surface of TiO_2 obstructed the formation of reactive oxygen species.[80]

Arabatzis *et al.*[81], tested the photocatalytic performance of Au-TiO_2 thin films on Methyl Orange under visible radiation, and they reported an activity level twice as high as with pure TiO_2. Another study, by Kumar *et al.*[82] found that photocatalytic degradation of Acid Red 88, under visible radiation, by Au-TiO_2 is higher than with pure TiO_2.

1.5.4 Non-metal and transition metal doping

Doping TiO_2 with a mixture of transition metals, such as Cu, Fe, V, Zn, W, Mn and Mo, together with non-metals such as N, F, P, S, has been the subject of considerable research in recent years. As noted in section *1.5.2.1*, nitrogen doping extends the absorption of TiO_2 to the visible region, due to the mixing of the oxygen's 2p states with nitrogen's 2p states. It is also known that transition metal doping leads to a reduced band gap, as a result of hybridization of the metal's 3d state with oxygen's 2p states.[83]

This begs the question of what would the effect be of doping TiO_2 with a mixture of metal and non-metal ions. Parkin et al.[84] reported that if TiO_2 is doped with a mixture of nitrogen and various concentrations of the transition metal nobium, photocatalytic degradation of resazurin dye is enhanced, as are resistivity and water contact angle. Further, Chan-Soo Kim *et al.* [85], reported that N+Cu-doped TiO_2 showed improved photocatalytic degradation of gaseous xylene under visible radiation, compared with TiO_2 doped with N or Cu alone. N+Zn doping of TiO_2 has been studied by Zhang *et al.*[86], who found that 1% Zn doping improved photocatalytic degradation of methylene blue, and suggested that this was due, in large part, to isolated N 2p states and oxygen vacancies, as well as a blue shift in the absorption. When TiO_2 is co-doped with iron and nitrogen, the result is a narrowed band gap, as nitrogen leads to the formation of a new state near the VB, while Fe^{3+} produces a new state near the CB. Furthermore, photocatalytic activity of N+Fe^{3+} doped TiO_2 is enhanced under visible radiation, compared with TiO_2 doped with N or Fe^{3+} alone.[87]

1.6 Antimicrobial activity

Today, there is a huge effort being made to find antimicrobial agents, as they can be used in a wide range of applications, such as air and water purification, food packaging and healthcare. In fact, the rise in frequency of hospital acquired infections (HAIs) has become a major problem in the hospital environment, and has played a significant role in the increasing cost of health care.[88] These infections are propagated in many and various ways, most of which are difficult to protect against, such as the contamination of surfaces such as door handles, keyboards and light switches. Direct patient contact is also a factor.[89,90] The main cause of the problem is a range of bacteria, such as the gram positive bacterium, Staphylococcus aureus (S. aureus) and the gram negative bacterium, Escherichia coli (E. coli). TiO_2, however, offers a solution, as it can be used as an antimicrobial agent, due to its ability to kill pathogenic microorganisms under UV illumination.[26] This was first demonstrated in 1985, when Matsunaga *et al*.[91] found that Pt-TiO_2 powder can sterilize Saccharomyces cerevisiae, Lactobacillus acidophilus and Escherichia coli when incubated with these organisms under UV illumination for 60–120 min. Since then, many reports have been published concerning the antimicrobial properties of TiO_2.

The main problem in the use of TiO_2 in antibacterial applications is its band gap. This is around 3.2 eV, which means – as previously noted - that TiO_2 is effective only under UV radiation. However, this can be addressed by the use of either a metal or non-metal dopant, which extends the effective spectrum into the visible range. Cu-doped TiO_2, for example, is effective in the visible range against Staphylococcus aureus and Escherichia coli.[92] In the case of non-metal doped TiO_2, fluorine doping is particularly effective against Staphylococcus aureus and Pseudomonas aernginosa, compared with un-doped TiO_2, possibly because of the consequent increase in reactive oxygen species and reduced charge carrier recombination.[93] Doping titania with nitrogen has also been shown to be effective against gram positives, such as S. aureus, and the gram negative, E.coli. However, N-doped TiO_2 appears only to be highly

effective under visible light conditions, while (undoped) TiO_2, in contrast, is effective under UV illumination. This could be because, with N-doped TiO_2, nitrogen creates recombination sites and high charge carrier recombination.[94] It is also worth noting that improved antimicrobial activity has been observed using other dopants, such as iodine, carbon and sulfur.[95-97] Other research on enhancing the antimicrobial activity of TiO_2 includes a study of an Ag-TiO_2 composite. Here, the effect of TiO_2 in anatase phase, loaded with silver nanoparticles, on E. coli, was compared with pure TiO_2, both under UV irradiation and in the dark. The effect was found to increase with the amount of Ag used, under UV illumination.[98, 99]

1.6.1 Antimicrobial activity of metal oxide

The mechanism behind the antimicrobial activity of metal oxide and TiO_2 composites is not yet fully understood, despite considerable research on the topic.[100] Much research has also been carried out on the oxidative stress generated by reactive oxygen reactive species (ROS) under UV radiation (ROS are $O_2^{\bullet -}$, $OH^{\bullet}$, and $^1O_2$). As has been noted above ***(Section 1.1)***, when an electron-hole pair is generated by photocatalysis, the electron on the CB reacts with O_2 to generate the superoxide anion $O_2^{\bullet -}$, while H_2O or OH^- reacts with the hole to produce the hydroxyl radical $OH^{\bullet}$. The single oxygen molecule, $^1O_2$ is also usually generated by many steps from aqueous reaction. While $OH^{\bullet}$ can destroy organic biomolecules such as DNA, nucleic acids, protein and lipids, as it is a powerful oxidant compared with other reactive oxygen species, treated tissues can be destroyed by $^1O_2$. The superoxide anion $O_2^{\bullet -}$ is considered to be the weakest oxidant of the three types of ROS, but it also has important biological implications.[101] Some metal oxides (such as TiO_2 and Zn) produce three types of ROS, though others produce only one or two, or even none at all.

The relationship between ROS, metal oxides and antimicrobial activity has been extensively studied. For example, Yongsheng *et al.*[102] investigated the correlation between

antimicrobial activity and the generation of ROS by seven metal oxide nanoparticles (TiO_2, CeO_2, SiO_2, Al_2O_3, ZnO, CuO and Fe_2O_3) under UV light (365 nm) in aqueous solution. They found that TiO_2, CeO_2 and ZnO nanoparticles produce $O_2^{\bullet -}$ on the surface, while Fe_2O_3, TiO_2 and ZnO generate $OH^{\bullet}$. SiO_2, ZnO, TiO_2 and Al_2O_3 all favoured $^1O_2$ production. In addition, the only metal oxides from these seven that were found to produce all three types of ROS were zinc oxide and titania. Moreover, the average ROS concentration generated followed the order: TiO_2 > ZnO > Al_2O_3 > SiO_2 > Fe_2O_3 > CeO_2 > CuO, while the antimicrobial degradation of E.coli under UV light (365 nm) had the order: CuO > TiO_2 > ZnO > Al_2O_3 > SiO_2 > Fe_2O_3 > CeO_2. These results show that, with just one exception, there is a strong connection between ROS generation and antibacterial activity. The exception is CuO, which may be a result of the release of the toxic ion (Cu^{2+}). Furthermore, particle size plays a crucial role in antibacterial activity, which was found to increase as particle size decreases. This is particularly true with Gram-positive bacterial strains.[103] In general, we can conclude that the mechanism of antimicrobial activity may be due to reactive oxygen species or the release of toxic ions such as Cu^{2+} and Ag.[104] In the case of copper, which is considered most effective against bacteria so far, the mechanism, according to Grass *et al*, starts with a Fenton-type reaction between Cu^+ and H_2O_2 which then generates the reactive hydroxyl radical, $^{\bullet}OH$, which plays the main role in destroying the bacteria.

$$Cu^+ + H_2O_2 \longrightarrow Cu^{2+} + OH^- + {}^{\bullet}OH \qquad (1\text{-}13)$$

Copper ions can react with sulfhydryls (RSH) in glutathione or/and cysteines, leading to depletion:

$$2Cu^{2+} + 2RSH \longrightarrow 2Cu^{2+} + RSSR + 2H^+ \qquad (1\text{-}14)$$

$$2\,Cu^+ + 2H^+ + O_2 \longrightarrow 2\,Cu^+ + H_2O_2 \qquad (1\text{-}15)$$

Hydrogen peroxide (H_2O_2) produced in reaction (1-15) can be reused in reaction (1-13) for further production of ($^{\bullet}$OH).[105]

In short, the common type of photocatalytst materials is metal oxide semiconductors for instance TiO_2. To better understand how they contribute to photocatalytic activity, it is necessary to explore the electronic structure and properties of this kind of metal oxide and compare them with those of insulators and conductive metals.

1.7 Electronic structure and band theory in semiconductors

In discrete atoms, electrons occupy orbitals with a specific associated energy, but, in the solid state, atomic orbitals can overlap. Electrons in overlapping orbitals (molecular orbitals) are not linked to specific atoms. This results in low energy (bonding) and high energy (antibonding) orbitals **(Figure 1.5**).[106]

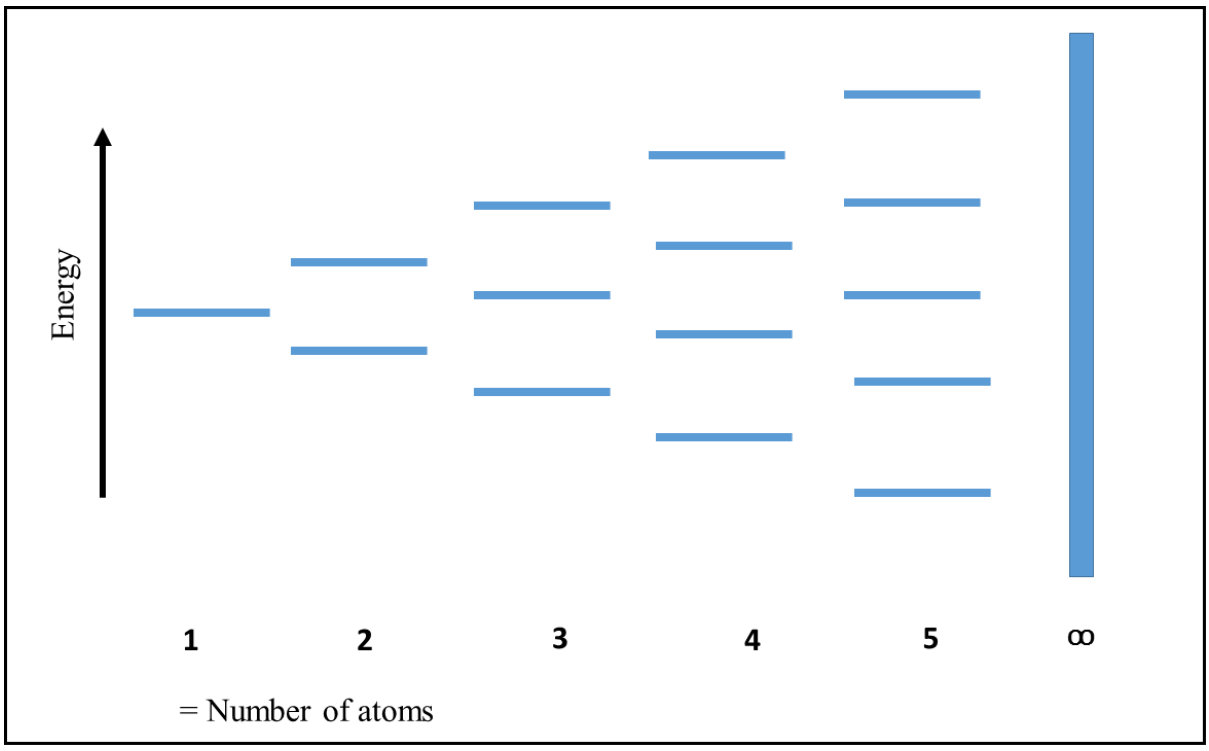

Figure 1.5. Formation of atomic energy levels as the number of atoms increases.

There are three types of solid state: conductors, insulators and semiconductors. The difference between them is a function of band gap, which is the energy gap between the VB and the **CB (Figure 1.6)**. In insulators, the band gap is large (usually greater than 5 eV), so electrons cannot acquire the energy to 'jump' from VB to CB, while in conductors, the VB and CB overlap, so the band gap is zero. In semiconductors, the band gap is non-zero but small, so electrons can be excited from the VB to the CB under certain conditions. Essentially, semiconductors behave like conductors at high temperatures, and insulators at low temperatures.

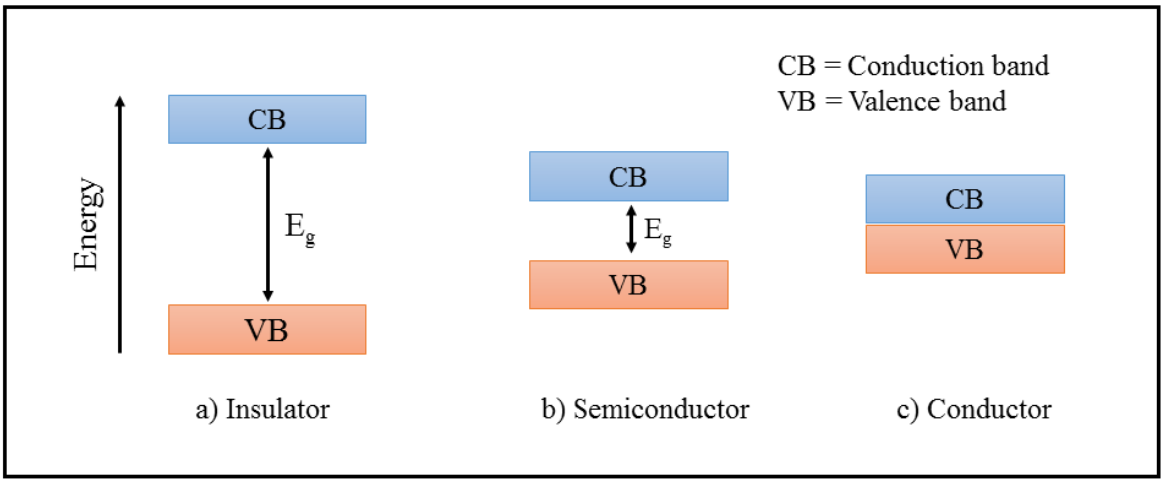

Figure 1.6. The difference in band gap of insulators, semiconductors and conductors

1.8 Semiconductors

Because semiconductors can conduct electricity under certain conditions, they are the basic materials used as transistors, which triggered the electronic age, and ultimately led to the digital revolution. Today, semiconductors are used in applications ranging from the computer to space vehicles. Commonly used semiconductors include germanium, silicon, gallium arsenide and aluminium phosphate.

As we have noted, semiconductors will conduct electricity when electrons acquire enough energy to jump from the VB to the CB. However, the electrical conductivity of a semiconductor is not a fixed value – it can be increased by 'doping' the semiconductor material with suitable impurities (dopants). A pure (undoped) semiconductor is known as an intrinsic semiconductor, while doped semiconductors are called extrinsic semiconductors.

Doping creates two types of semiconductor: n-type (negative) and p-type (positive). In n-type semiconductors, the dopant atoms provide extra electrons to the host material, thus creating an excess of negative charge carriers. In p-type semiconductors, the dopant creates deficiencies of valence electrons, leaving what are effectively positive by charges (holes) in the VB [107]**(Figure 1.7)**.

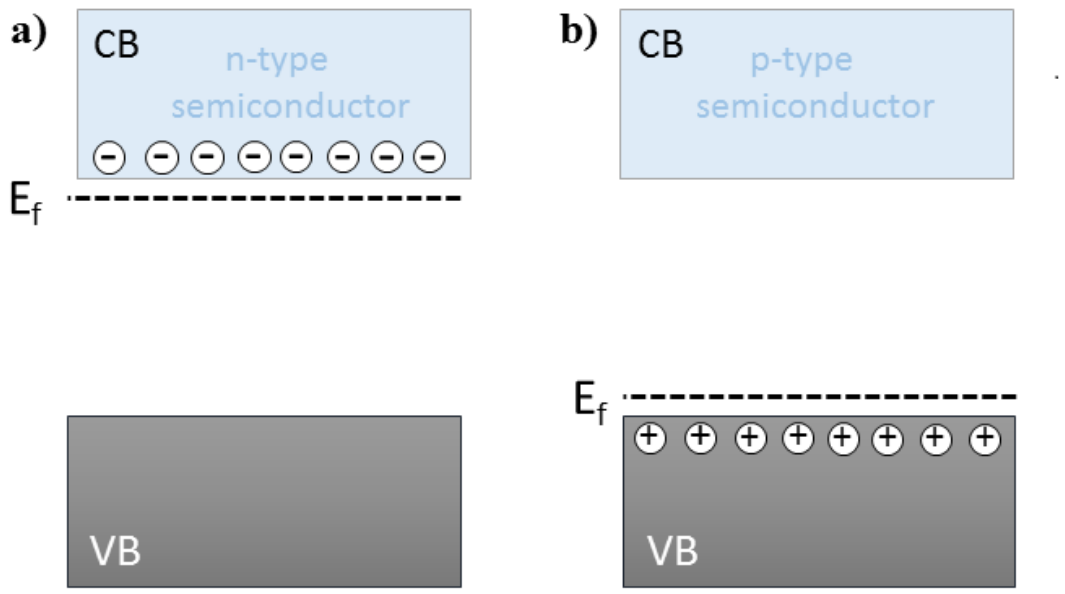

Figure 1.7. Energy band gaps in n- and p-type semiconductors, with donor (n-type) and acceptor levels (p-type).

The Fermi-level (E_f) is an important feature of the electronic band structure and thermal properties of a solid state. This (the Fermi level) is the term used to describe the highest energy

state that is full of electrons at 0 K (absolute zero) **(Figure 1.8)**. However, Fermi level is a result of Fermi Dirac Statistics. According to the fact that electrons obey the Pauli Exclusion Principle, which states that no two electrons can have the same (quantum) state. Thus, if two electrons share the same value for n, l and m, they must have different spin, which means they most have different energy. In a metal, this means that when the temperature is above absolute zero, some electrons must exist above the Fermi level (E_f), which overlaps with the CB, so conductivity is possible. As the temperature increases, more electrons move above the Fermi level, and conduction also increases. In an insulator, the CB is too far, in energy terms, above the Fermi level, so no electrons can acquire the energy required to 'reach' the CB. In semiconductors, there is a small, but non-zero, band gap, so it is relatively easy for electrons to move above the Fermi level to the CB. As (in semiconductors) the Fermi level can be affected by impurities (dopants), it is a very important factor in photocatalysis.

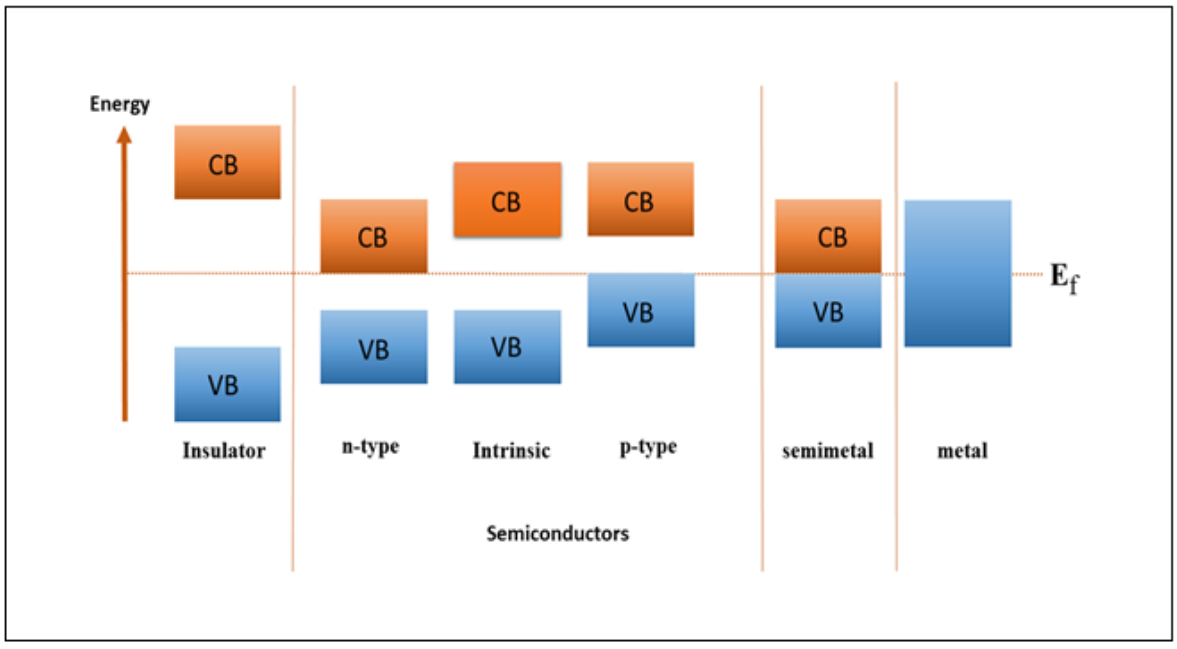

Figure 1.8. Band gap positions in insulators, semiconductors and metals, and the Fermi level (E_f) of each, relative to band gap.

1.9 Methods of fabrication

TiO_2 thin films can be fabricated on different substrates by a number of different methods, including chemical vapour deposition (CVD)[108], molecular beam epitaxy (MBE)[109], atomic layer deposition (ALD) [110], and sol-gel[111] and spin coating. [112]

1.9.1 Chemical vapour deposition

Chemical vapour deposition (CVD) is a method of depositing thin films of metal oxides on substrate materials such as glass, quartz etc. The resulting films are high-performance and high purity, and are used for a wide range of industrial products, such as self-cleaning glass, electronic devices and transparent conducting materials (TCOs). CVD methods are also used for corrosion protection.

It is important to note the difference between chemical vapour deposition (CVD) and physical vapour deposition (PVD). Essentially, the former uses chemical processes[113] to deposit the thin films or layer, while PVD uses only physical forces.

There are various types of CVD, such as atmospheric pressure chemical vapour deposition (APCVD)[38], aerosol assisted chemical vapour deposition (AACVD)[114], plasma enhanced chemical vapour deposition (PLCVD) [115], fluidised bed chemical vapour deposition (FBCVD) [116], metal organic chemical vapour deposition (MOCVD)[117], laser CVD (LCVD)[118] and low-pressure chemical vapour deposition (LPCVD).[119]

The difference between these types of chemical vapour deposition lies in the way that reactions are initiated. In AACVD and APCVD, for instance, reaction is catalysed by heat, while in plasma-enhanced CVD (PLCVD), reactions can be initiated by plasma radiation, or UV radiation in the case of photo-assisted CVD.

In this report, we focus on aerosol assisted chemical vapour deposition (AACVD) as the method of depositing TiO_2 thin films, along with doping TiO_2 with metals/non-metals.

1.9.2 Aerosol assisted chemical vapour deposition (AACVD)

In this deposition technique, the substrate is exposed to one or more involatile precursors which react or decompose on the surface to produce a deposit.[120] First, an aerosol is generated by an ultrasonic humidifier, after which the aerosol is transferred to a reactor via a carrier gas, such as nitrogen or air. The reactor consists of a carbon heating block with two plates (top and bottom) surrounded by a quartz tube **(Figure 1.9)**. Typically, deposition occurs on the bottom plate, though in some cases it occurs on the top plate due to thermophases.[121]

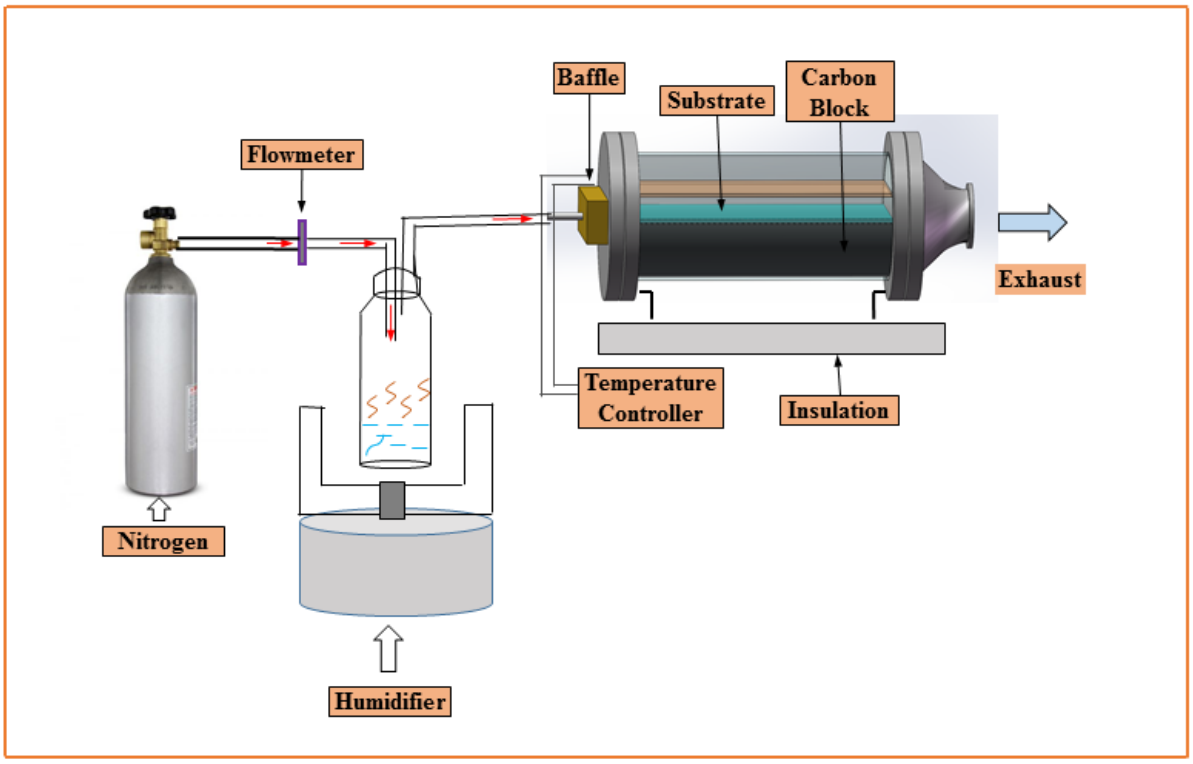

Figure 1.9. An aerosol assisted chemical vapour deposition (AACVD) system.

Aerosol droplet size can be calculated by using Lang's equation (1-16).[122]

$$d = \left(\frac{2\pi\gamma}{\rho f^2}\right)^{1/3} \qquad 1\text{-}16$$

Where d is the droplet diameter, ρ is liquid density, f is the sound frequency and γ is the surface tension of the liquid. It can be seen from Lang's equation that aerosol droplet size increases as the sound frequency decreases.

Mechanical deposition of AACVD starts with the production of a precursor vapour **(Figure 1.10)**. This, along with the solvent vapour, is transferred to the reactor by a suitable gas. Once inside the reactor, the solvent evaporates (due to increased temperature) and the precursor changes to a gaseous state, after which the precursor is adsorbed on the substrate surface.

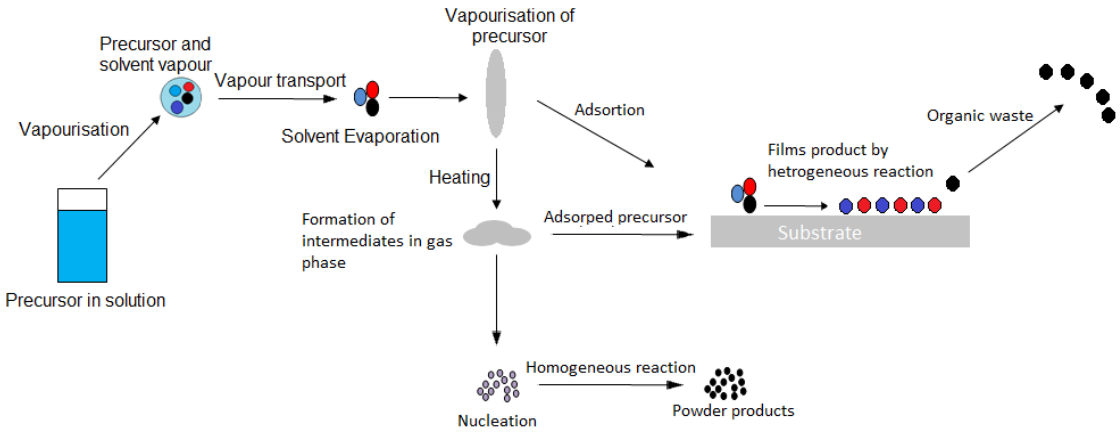

Figure 1.10. The mechanical process of aerosol assisted chemical vapour deposition (AACVD).

There are two explanations for the mechanism of AACVD.[120, 122]

(1) Heterogeneous reaction. After changing to the gaseous state, the precursor decomposes, causing the formation of intermediates. The substrate then adsorbs these

intermediates along with some of the undecomposed precursor. This process of deposition is considered a heterogeneous reaction.[120, 122]

(2) Homogeneous reaction. This occurs at high temperatures, when the precursors are in the gas phase. In this case, chemical reaction and/or decomposition could form powder particles by a homogeneous reaction.[120, 122] However, if these particles are absorbed by the substrate, the chemical reaction changes from homogeneous to heterogeneous due to the creation of external reactive gases and porous films.[120, 122] AACVD offers advantages over conventional CVD methods - the main one being that the method depends on the solubility of the precursors in the different solvents, rather than on volatile precursors. Because of this, AACVD has been investigated using a wide range of precursors that produce high-quality deposition.[122] AACVD can also be used under low or atmospheric pressures.[122] The result is that AACVD is suitable for a wide range of applications, such as the synthesis of powders, coatings, nanotubes and nanocomposite films. Furthermore, AACVD can be used for deposition onto large-scale substrates[123], and can be used to dope metal oxides with nitrogen, or halides such as fluorine, at low temperatures. Noor and Parkin[124] found that when AACVD is used to dope tin oxide with fluorine, the result is high-performing TCOs (transparent conducting oxides) with crystallites, while Diesen *et al.*[125] used AACVD to produce N_2-doped TiO_2 and found that the resulting film had a thickness of 200 nm and a crystal anatase phase. XPS showed that the surface of the TiO_2 film consisted of 0.7% nitrogen, and that doping TiO_2 with nitrogen (using AACVD) decreased the band gap to about 2.85 eV.

However, B. Blackburn *et al.*[126] investigated the gas phase reaction formed during the deposition of TiO_2 from titanium tetraisopropoxide (TTIP) in a CVD reactor. A molecular beam mass spectrometer was used to analyse gas phase products. The deposition was carried

out at 300 °C and 600 °C. The deposition that was carried out at 300 °C gave a range of mass spectra peaks as shown in **Figure (1.11)**.

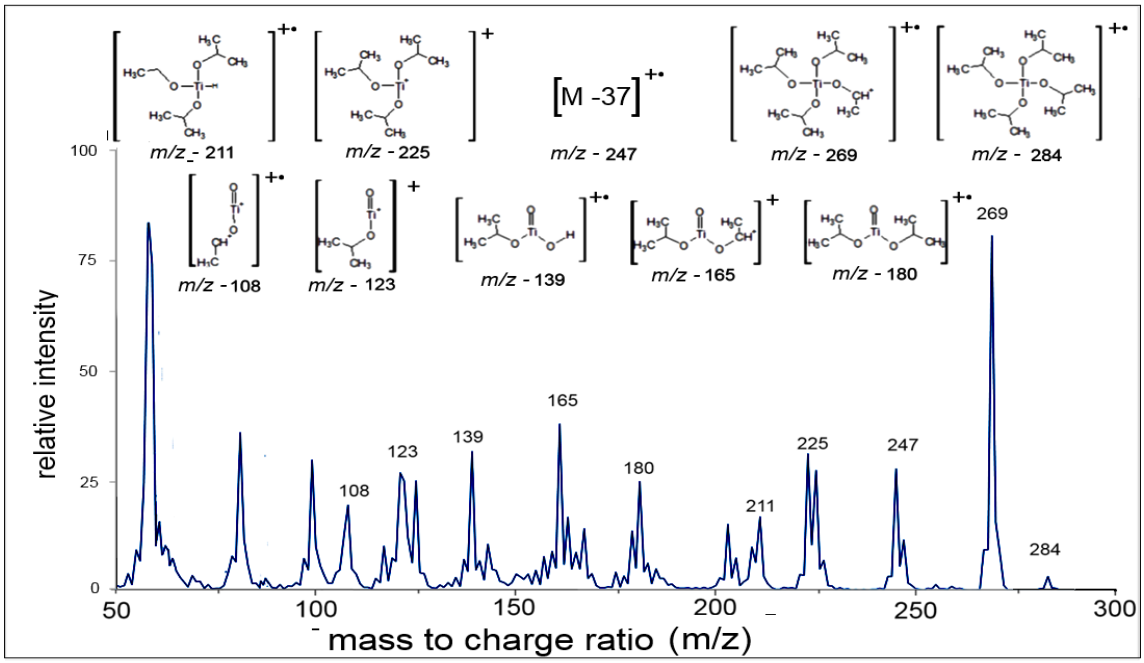

Figure 1.11. Mass spectrum of deposition of TiO_2 from titanium tetraisopropoxide (TTIP) by CVD rig at 300 °C. Reproduced with permission from Ref. 126.

These peaks resulted from a loss of an isopropyl (mass = 59 amu), methyl (mass = 15 amu) and propyl (mass = 43 amu) **Figure (1.12)**.

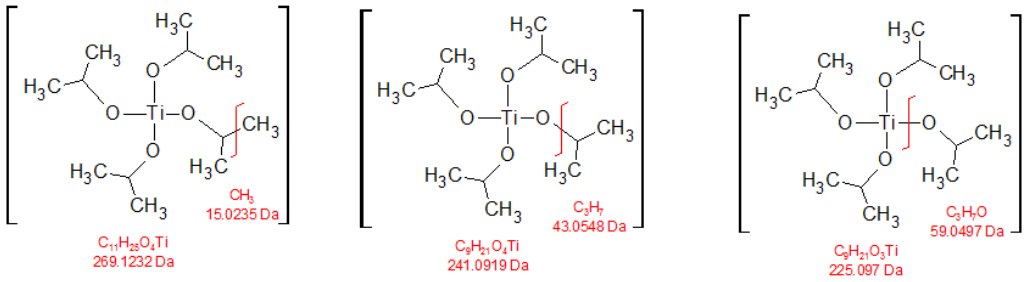

Figure 1.12. Expected fragmentation points on titanium tetraisopropoxide (TTIP). Fragment masses and formulas are shown in red. Reproduced with permission from Ref. 126.

The deposition that was carried out at 600 °C showed some different mass spectra peaks to those obtained at 300 °C, as shown in **Figure (1.13)**. Most of the previous peaks are present, but an increase of isopropoxide ligands was observed, as well as the creation of a dioxo-bridge between the two titanium centres because of the high temperature.

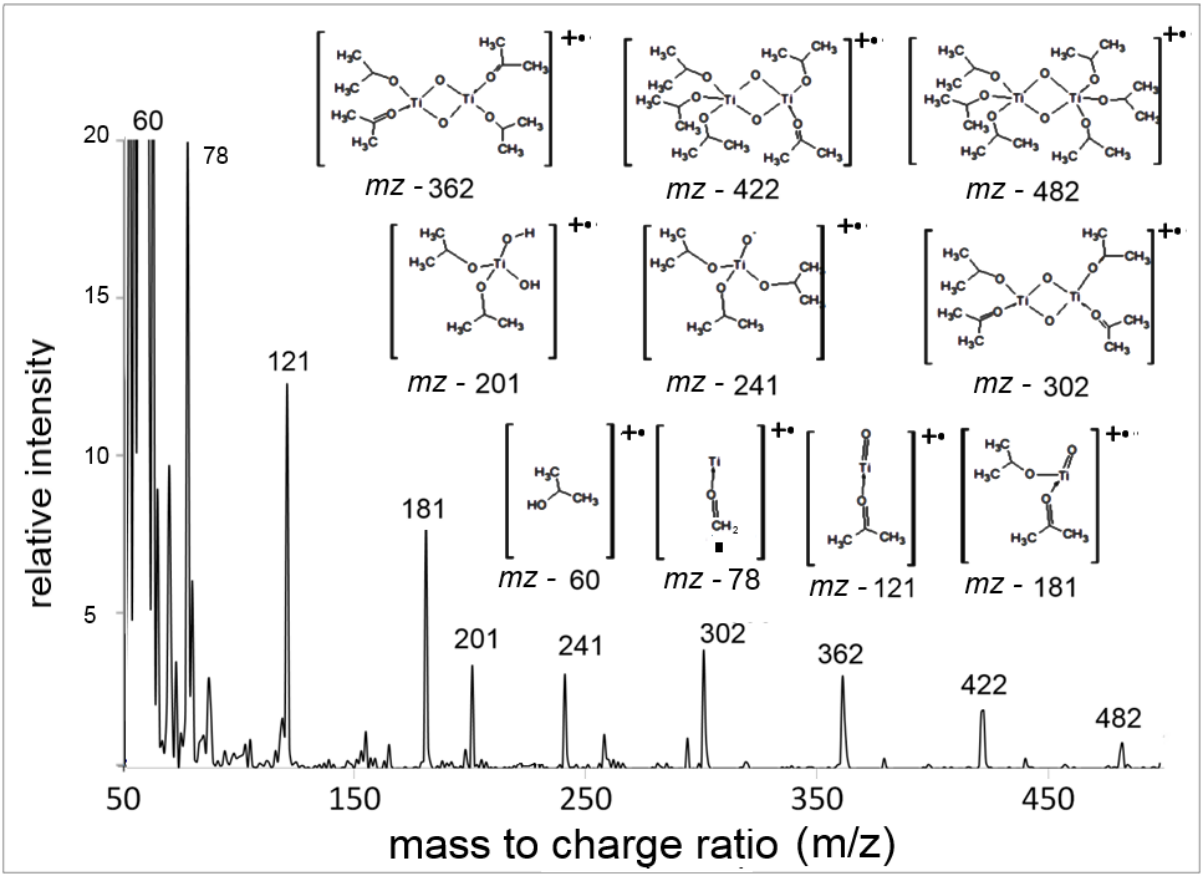

Figure 1.13. Mass spectrum of deposition of TiO_2 from titanium tetraisopropoxide (TTIP) by CVD rig at 600 °C. Reproduced with permission from Ref. 126.

AACVD is an effective way of producing robust and crystalline thin-films, with properties that are essential for photocatalysis properties. However, there are some factors that can affect the process, such as deposition temperature, flow rate, type of precursor or/and precursor concentration, solvent type and ultrasonic sound frequency.

1.9.2.1 Deposition temperature

In the AACVD process, the deposition temperature is a crucial factor in achieving optimum thin film properties. Take, for example, the use of AACVD to create In_2O_3 films using $InMe_3$ in methanol, in the temperature range 400-500 °C. If SEM is used to study the surface morphology of the resulting films **(Figure 1.14)**, clear differences can be seen. At 400 °C the film surface seems flat and featureless. However, as the temperature increases to 500 °C the morphology changes to agglomerated clusters. It seems clear, therefore, that temperature has a significant effect on microstructure.[127]

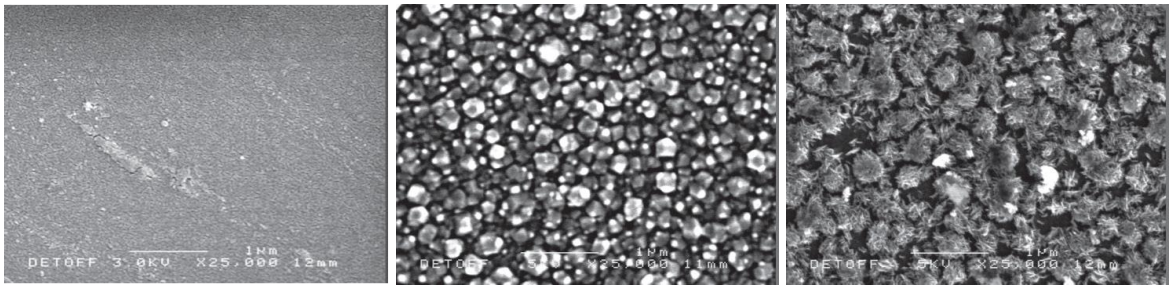

Figure 1.14. SEM images of In_2O_3 thin films deposited by AACVD using InM_3 in methanol at (a) 400 ºC, (b) 450 ºC and (c) 500 °C . Reproduced with permission from Ref.127.

In another example of the effect of temperature on films deposited using AACVD, ZnS films were deposited on FTO glass at different temperatures (375ºC, 425ºC and 475°C) by AACVD using the precursors (a) $[Zn(S_2CNCy_2)_2py]$ and (b) $[Zn(S_2CN(CH_2Ph)Me)_2py]$. At 375ºC the resulting films were cubic phase (as shown in Figure 1.15), but at 425ºC and 475°C the films were hexagonal phase plus partly cubic phase.[128] The morphologies of these films are shown in **Figure 1.16**. Their surface morphology changes with precursor as well as temperature. When ZnS films were deposited using precursor (a), films grown at 370°C were made up of cauliflower-like structures, but when the temperature was increased to 425°C the morphology changed to densely packed globules. At 475°C, the particles resembled a granular compact. With precursor (2), unstructured particles were found at 370°C, but when the temperature

reached 425°C the morphology showed more spherical features, while at 475°C the morphology consisted of large particles.

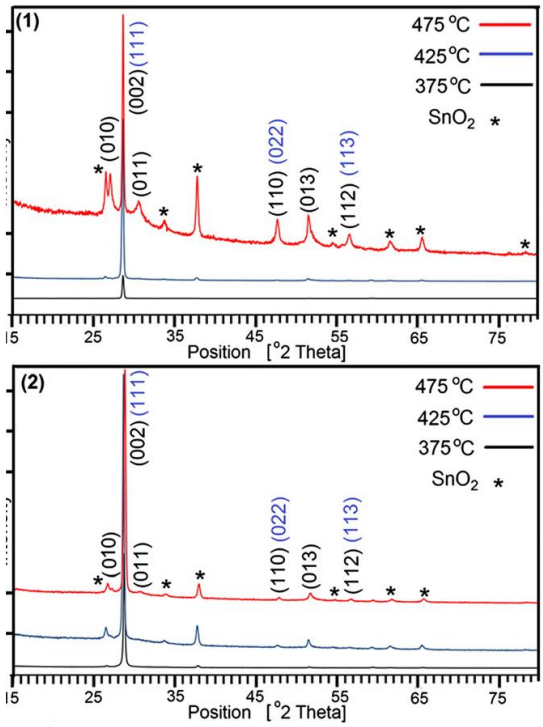

Figure 1.15. XRD of ZnS films deposited by AACVD at different temperatures (375ºC, 425ºC, and 475°C, (a) [Zn(S2CNCy2)2(py)] and (b) [Zn(S2CN(CH2Ph)(Me))2(py)] as precursors. Reproduced with permission from Ref.128.

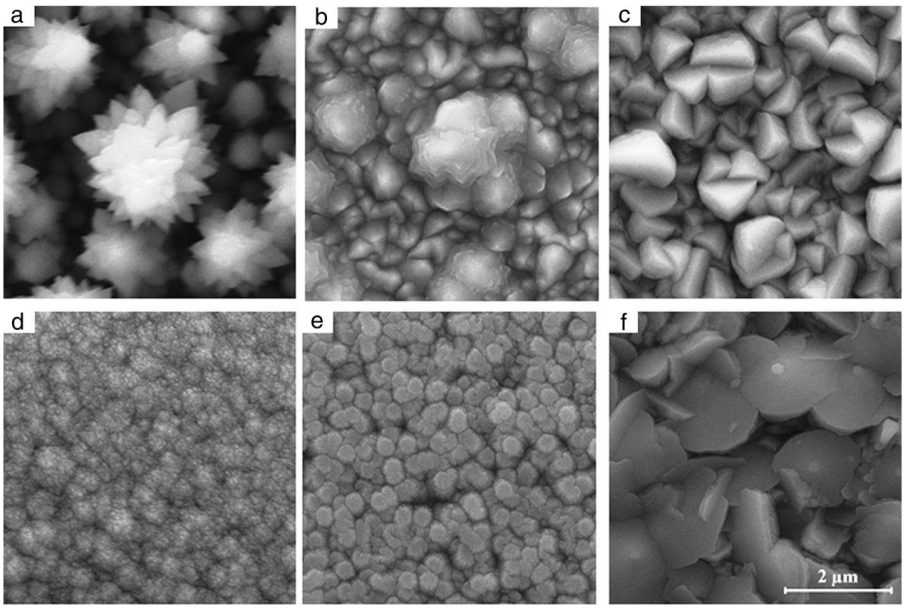

Figure 1.16. SEM images of ZnS films using the precursor [Zn(S2CNCy2)2(py)] at (a) 375ºC, (b) 425ºC and (c) 475 °C respectively, and the precursor [Zn(S2CN(CH2Ph)(Me))2(py)] at the same temperatures (d, e, f, respectively). Reproduced with permission from Ref.128.

1.9.2.3 Precursors

The morphology and properties of films deposited by AACVD are a function of the type of precursor used. For example, ZnS films using the precursor $[Zn(S_2CNCy_2)_2py]$ has an optical band gap of 3.36 eV, but when the precursor is changed to $[Zn(S_2CN(CH_2Ph)Me)_2py]$, keeping other conditions the same, this value increases to 3.40 eV. The concentration of the precursor is also important, as it plays a vital role in the quality of resulting films.[128]

1.9.3 Atmospheric Pressure Chemical Vapour Deposition (APCVD)

This process is used to deposit thin films on substrates such as glass and quartz. The APCVD process differs from AACVD in that, with APCVD, the pure precursor is heated to the vapour state in a suitable bubbler, while, as we have noted **(Section *1.9.2)***, in the AACVD method, the pure precursor is first dissolved in suitable solvents, and an aerosol is generated by ultrasonic sound. In the APCVD process, deposition starts when the precursor has evaporated. It is then transferred to the reaction chamber via an inert gas such as nitrogen. In the reaction chamber, the gaseous products react with each other, and are then absorbed on the surface of the substrate as it is at a higher temperature than the transfer gas. The growth rate of films deposited by APCVD can be monitored by various factors, such as gas flow rate, bubbler temperature, precursor vapour pressure and substrate temperature. It is generally assumed that the precursor species used with APCVD should have a high vapour pressure to encourage the change from liquid to gas.

As the gas flow rate plays a significant role in the growth rate of the film, it is important to be able to calculate this (gas flow) rate. This can done in the following way.

As APCVD works at atmospheric pressure, it is generally considered to follow the ideal gas law of equation 1-17.

$$\frac{N_p}{N_c} = \frac{P_p}{P_c} \qquad (1\text{-}17)$$

Where P_c is the partial pressure of carrier gas, P_p is the partial pressure of precursor reactants, N_c is the concentration of the gas carrier and N_p the amount of precursor reactants. However, as the APCVD system has only precursors and transfer gas, the outlet pressure of the bubbler will be[3]:[129]

$$P_{total} = P_p + P_c \quad (1\text{-}18)$$

$$P_c = P_{total} - P_p \quad (1\text{-}19)$$

Which gives, from equation 1.17

$$N_p = \frac{N_c \times P_p}{P_{total} - P_p} \quad (1\text{-}20)$$

Given that P_{total} is 760 torr (atmospheric pressure), and assuming that 1 mole of gas is equivalent to 22.4 L, we can determine the flow rate of the transfer gas (F_c):

$$F_c = \frac{N_c}{22.4} \quad (1\text{-}21)$$

Which allows us to calculate the flow rate, in L/min of the precursor using the equation:

$$F_{(Precursor)} = \left(\frac{F_c \times P_P}{22.4(760 - P_p)}\right) \quad (1\text{-}22)$$

1.10 Film growth using CVD

When a film starts to develop on the substrate by chemical vapour deposition, it is likely to be amorphous or crystalline. Amorphous films usually result from high growth rate and low

temperature conditions, as gaseous reactants arrive more quickly than the rate of surface division. Crystalline films, on the other hand, usually occurs under opposite conditions - high temperature and low growth rate.

In fact, there are two types of crystalline films: polycrystalline and epitaxial. The former occurs when the lattice planes of the substrate do not match the planes of the film. This is a result of the substrate and film having a different crystal structure and unit cells, causing growth to occur at different surface sites. This leads to growth islands on the substrate.

Epitaxial films occur when the lattice planes of the film match the lattice planes of the substrate. Here, the unit cell and crystal structure of substrate and film are quite similar, so that the rate of absorption of molecules on the substrate is faster than the arrival of precursors.

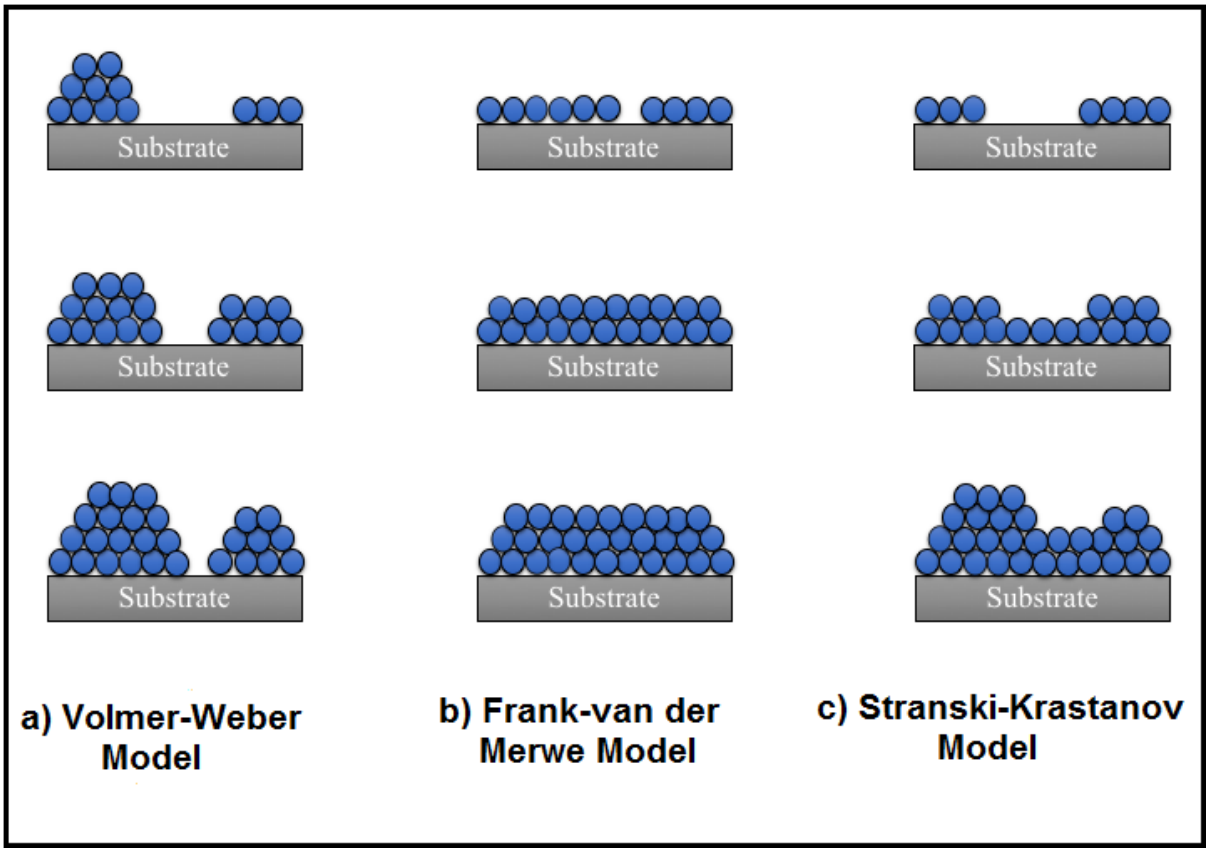

Figure 1.17. The three growth models of chemical vapour deposition.

1.10.1 Growth models of thin films

The growth of films using CVD is generally described by three models.[130] These are:

The Volmer Weber model

Here, the atoms/molecules are more strongly bonded to each other than to the substrate **(Figure 1.17)**, resulting in the growth of 'islands' rather than layers. Factors which affect the growth of these islands include low decomposition temperature and low precursor concentration.

The Frank van der Merwe model

This is essentially the opposite of the Volmer Weber model. In the FvdM model, the molecules/atoms are more attracted to the substrate than each other, so growth occurs layer by layer.

The Stranski-Krastanov model

A combination of the other two models, this model begins with the formation of some monolayers on the substrate, followed by the growth of islands.

1.11 Transient absorption spectroscopy (TAS)

Today, TAS is a set of powerful techniques which can be used to examine transient changes in the absorption of materials on a timescale ranging from femtoseconds (10^{-15} s) to nanoseconds (10^{-9} s). They are used in many fields, such as the study of organic and inorganic materials, as well as the investigation of charge carrier behaviour in semiconductors.

The first pump probe technique (flash photolysis) for studying reaction dynamics at the millisecond level was developed by Eigen, Norrish, and Porter[131], who were awarded the Nobel

Prize in 1967 for their pioneering work. But it was not until 1950 that George Porter employed flash photolysis and spectroscopy to study reactions between free radicals, using gas-filled flash discharge tubes of very high power.[132] Porter's use of flash photochemistry and spectroscopic methods provided many valuable insights on the behaviour of transient intermediates. Following this, in 1970, Porter and Topp published a paper called "nanosecond flash photolysis" [133], in which they described the use of a pulse laser source to investigate events with a duration of a few nanoseconds. This was a massive improvement over conventional flash photolysis, as it was now possible to observe and examine the absorption spectra of singlet and triplet excited states, as well as other chemical events occurring at the nanosecond level. Subsequent improvements in the technique continued to shorten the observable timeframe, so that it is today possible to examine events of durations as short as femtoseconds. The research described in this report makes appropriate use of TAS to investigate charge carrier lifetime and electron-hole recombination.

1.11.1 Determinations of optical density

With metal oxides, and particularly semiconductors, a laser pulse pump beam is usually used to excite electrons from VB to CB, as a laser has a high energy intensity. A probe beam (typically a probe light or steady state lamp) is used to determine the charge carrier concentration by measuring changes in the UV-Vis spectrum **(Figure 1.18)**.

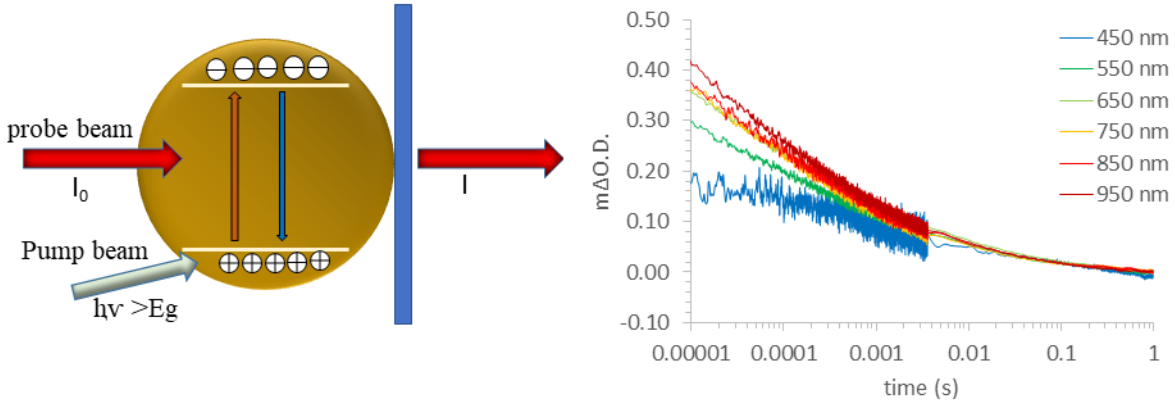

Figure 1.18. Left: the principle of the pump-probe technique. The pump beam (laser pulse) excites electrons from VB to CB, and a probe beam detects changes in the absorption spectrum. Right: Results from an experiment carried out as part of this research project, using Cu-doped TiO_2 thin films.

The optical density (OD), or absorption change, can be expressed as a function of wavelength. Equations 1.23 and 1.24 show OD before and after excitation.

$$O.D_{(no\ ex)} = \log \frac{I_0\ (\lambda)}{I(\lambda)_{noex}} \qquad 1.23$$

$$O.D_{(\ ex)} = \log \frac{I_0\ (\lambda)}{I(\lambda)_{ex}} \qquad 1.24$$

$$\Delta OD = \ O.D_{(ex)} = \log \frac{I_0\ (\lambda)}{I(\lambda)_{ex}} - \ O.D_{(no\ ex)} = \frac{I_0\ (\lambda)}{I(\lambda)_{noex}} = \ log \frac{I_{noex}}{I_{ex}} \qquad 1.25$$

$O.D_{(no\ ex)}$ is the optical density before pump excitation, $O.D_{(ex)}$ is the optical density after pump excitation, and I_0 and I are the intensities of the incident pulse and transmitted pulse respectively.[134-136]

1.11.2 Time-resolved TAS decay at a specific wavelength

We have already described the fundamentals of the TAS process. In principle, it is quite simple. After a fraction of the sample molecules have been promoted to the excited stage with a pump pulse, a (low) intensity probe probe pulse is transmitted through the sample. The difference between the absorption spectrum of the excited sample molecules and the spectrum of the ground-state molecules, can then be calculated. This is known as a difference (delta) absorption spectrum.

Various process contribute to the difference absorption spectrum[137, 138], including:

- Ground state bleaching

Ground state bleaching (GSB) occurs when the pump pulse causes a depletion of carriers in the ground state compared with carriers in the excited state (green colour in Figure *1.196, A).* The result is that the density of molecules in the ground state is lower, so the ground state absorption signal is reduced. This means that the ground state absorption signal in the excited state becomes negative (green colour in Figure *1.19, B).* When the excited molecules return to normal, this negative signal shift disappears.

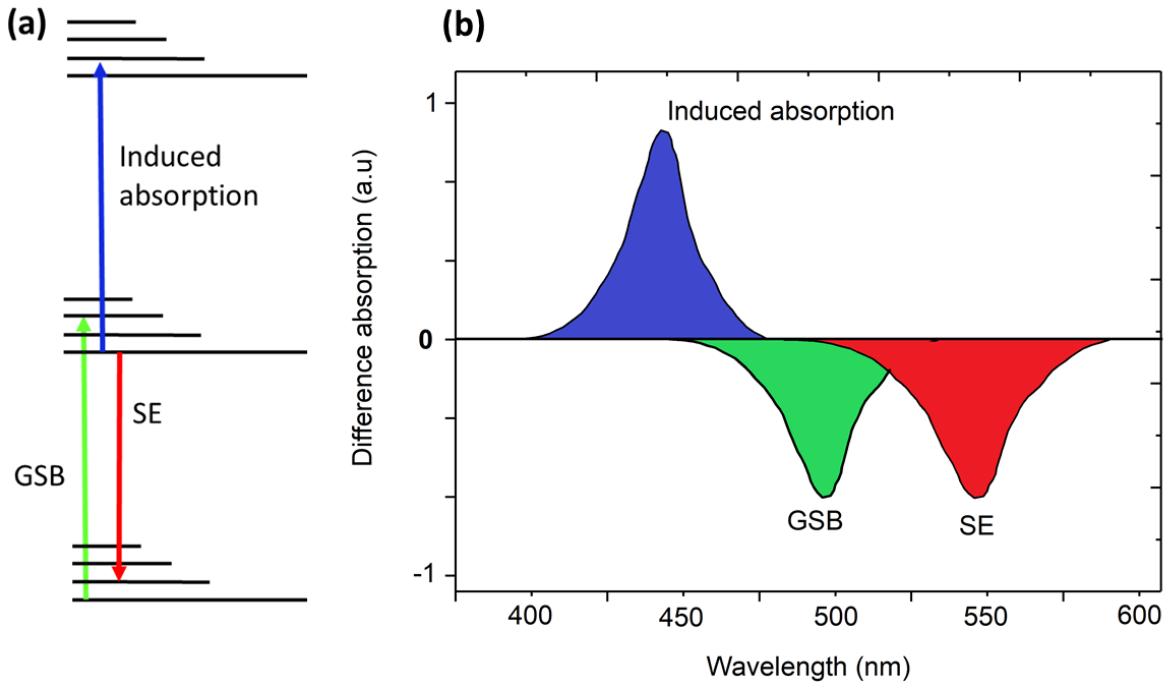

Figure 1.19. (A) Energy level diagram molecules in the difference absorption spectrum, and (B) separate contributions to difference absorption - ground state bleach, stimulated emission, and excited-state (induced absorption).

- Stimulated emission

Stimulated emission (SE) occurs when a photon from the probe pulse interacts with photon of molecules in an excited state. Photon from the excited molecules then drops to a lower energy state ***(red colour in Figure 1.19, A)***, releasing the extra energy in the form of a photon with the same wavelength, phase, polarization and direction as the incident probe photon. As with ground state bleaching, the absorption signal will be negative, and may overlap (with GSB). It can be seen from equation 1.25 that, when the pump pulse is closed, the concentration of photons detected (I_{noex}) is equal to the concentration of photons with no absorption. Further, when the pump pulse is operating, and exciting sample atoms, photon concentration will be a result of photons absorbed by the samples and the photons emitted by the sample. Consequently, the ΔOD signal will be negative, as $I_{ex} > I_{noex}$ (red colour in Figure 1.19, B).

- Excited state absorption (induced absorption)

Induced absorption (IA) occurs when excited molecules absorb photons from the pump pulse, causing further excitation to a higher excited-state (blue colour in Figure 1.19A), resulting in absorption with a positive signal in a particular range of the wavelength spectrum (blue colour in Figure 1.19B).

Transient absorption spectroscopy has been used to investigate charge transfer, recombination, trapping and generation in both the anatase and rutile phases of TiO_2. Charge carriers produced by the laser pulse are absorbed in the visible and near infrared region of the spectrum, and if a sample measurement is made in an inert environment, and then in the presence of a chemical scavenger that can react with one of these charge carriers, the enhancement in charge carrier lifetime of the remaining charge can (if the quantum yield of this process is significant) then be measured. Methanol, for example, is a strong hole scavenger[139], so if hole scavenging occurs at a significant level, the increase in lifetime of photogenerated electrons can be determined. Wang *et al.*[140], studied the kinetic dependence of photocatalysis in titania films, for both the rutile and anatase phase, using TAS measurements on a ms – s timescale and compared the results with the photocatalytic degradation of an intelligent ink, such as resazurin. They found that the rutile phase has recombination kinetics which are 10 times slower than the anatase phase, though anatase showed photocatalytic degradation of intelligent ink 30 times higher than rutile. In addition, the anatase phase has a long electron lifetime of around 0.7 s, as anatase shows hole scavenging of alcohols only. The study concluded, therefore, that the difference in photocatalytic degradation of resazurin is due to the inability of rutile holes to scavenge methanol (oxidised methanol) rather than differences in the recombination rate.

To study photocatalytic activity in rutile:anatase TiO_2 junctions, compared with pure anatase or rutile, TAS measurements were employed. TAS was also used to investigate and compare the migration of trapped charges and hole transfer in rutile:anatas TiO_2 junctions, as well as in the separate anatase and rutile phases. The chemical scavengers used to track electrons and holes were methanol (holes) and aqueous silver nitrate (electrons). In the rutile:anatas TiO_2 composite, the hole was found to transfer from rutile to anatase sites at a particular rutile-anatase ratio, and in sub-microsecond time scales. Thus, for example, at a ratio of 20:80 (rutile:anatase), the amount of holes in anatase grew to 5 times that of rutile. Further, the electron-hole recombination for rutile was 20 ms, while for anatase it was 0.5 ms. For composite (20:80) rutile-anatase it was 4 ms, which is consistent with the composite ratio.[136]

The following chapter shows how AACVD is used to deposit anatase TiO_2 thin films and Cu doped TiO_2 thin films using different Cu concentrations. The photocatalytic and antimicrobial activities of these films are investigated via the degradation of stearic acid as a model of photocatalytic activity. E.coli and S. aureus bacteria were investgated as a model of antimicrobial studies under UV-365 nm. The transient absorption spectra are used to investigate the charge carrier and lifetime of these films.

Chapter 2

Uncovering the Origin of the Enhanced Photocatalytic and Antibacterial Ability of Cu-doped Anatase TiO_2 Thin Films through Theory and Experiment

*"In this chapter, the results of experiments exploring the deposition of a series of Cu doped TiO_2 films using aerosol-assisted chemical vapour deposition (AACVD) are presented; a different concentration of copper co-doping were investigated so that the photocatalytic and antibacterial (*E. coli and S. aureus*) abilities could be determined. Photocatalytic activity was investigated in the destruction of stearic acid as an organic pollutant model. In the results, 5% Cu doped TiO_2 films showed increased photocatalytic activity compared with undoped TiO_2 thin films. Antimicrobial activity was studied against Gram-positive bacteria (*E. coli and S. aureus*) under ultraviolet (UV-365 nm). Transient absorption spectroscopy (TAS) was also used to investigate the charge carrier and lifetime in these films."*

2.1 Introduction:

Anatase TiO_2 is a chemically and biologically stable, inexpensive semiconductor with photosensitive properties for applications in photocatalysis and antibacterial surfaces[28, 141-143]. In fact, the primary application of TiO_2 as a photocatalyst is as a self-cleaning transparent coating on windows to assist in the breakdown of dirt. [144-148]

In order to enhance the photocatalytic activity of TiO_2, it is necessary to investigate doping TiO_2 with transition metals, which can lead to improved photo-efficiency during the electronic process and shift the band gap to the visible region of the spectrum.[149-151] TiO_2 doped with transition metals has been widely investigated for photocatalytic activity, which is caused by the ability of doping centres to trap charge carriers and to improve the separation of photogenerated hole electron pairs.[152, 153] Thus, metal ions help to reduce hole-electron recombination, since the metal ions work as charge-trapping sites.[154, 155] However, the effects of doping on the photocatalytic activity depend on several factors: the type of metal ions used as dopants, the method of doping and the concentrations of dopants.

Among different metal ions doped with TiO_2, copper is important because it occurs in different oxidation states and therefore has a narrow band gap energy (Cu_2O is 2.2 eV and CuO is 1.2 eV).[156] In addition, Cu has high light absorption coefficients. The incorporation of dopant quantities of Cu into the TiO_2 matrix has dual advantages. Not only can Cu be used as an antibacterial agent by itself, through Fenton type reactions[157], but TiO_2:Cu can potentially reduce the recombination of charge carriers which are important for both antibacterial and self-cleaning applications of TiO_2.[123, 158-161]

Preparation of Cu-doped TiO_2 has been carried out *via* solution[162-164] and non-solution[165] based routes in nanoparticulate forms mainly for photocatalytic and ferromagnetic

applications. Sol gel techniques[166] and PVD methods such as magnetron sputtering.[167] have also been used to fabricate thin films.

In this chapter, we demonstrate a novel synthesis of Cu-doped TiO_2 films using an aerosol assisted chemical vapor deposition (AACVD) method. AACVD is a facile technique that places only the limitation of solubility on the precursors *i.e.* there are no volatility concerns as with traditional CVD, thus allowing a wider range of precursors to be employed.[168-173] It is also an atmospheric pressure technique that has been used to grow a wide range of films for various applications with the potential for upscale.[174, 175] Both pure and Cu-doped TiO_2 films were prepared *via* AACVD and their photocatalytic activity to the degradation of a model organic pollutant, stearic acid, and antibacterial activity to bacteria *E. coli* and *S. aureus* were examined under 365 nm radiation and compared. Cu-doped TiO_2 films showed enhanced photocatalytic and antimicrobial activities compared with pure TiO_2. Transient absorption spectroscopy (TAS) studies showed that photogenerated charge carriers were longer-lived in Cu-doped TiO_2 films.

2.2 Experimental Methodology

All chemicals used were purchased from Sigma-Aldrich Chemical Co. and used as received. Deposition were carried out on 150 × 45 × 45 mm SiO_2 (50 nm) coated float-glass (the SiO_2 acts as a barrier layer preventing diffusion of ions from within the glass into the deposited film) which has been supplied by Pilkington NSG. Prior to use the glass substrates were thoroughly cleaned using acetone (99 %), isopropanol (99.9 %) and distilled water and dried in air prior to use.

2.2.1 Deposition procedure

Depositions were carried out under N_2 (BOC Ltd., 99.99% purity) flow using titanium isopropoxide [$Ti(OCH(CH_3)_2)_4$] (99%), copper nitrate (hydrated), [$Cu(NO_3)_2.3H_2O$] (99%) and ethyl acetate (99%).

[$Ti(OCH(CH_3)_2)_4$] (0.5 g, 1.76mmol) was dissolved in ethyl acetate (30 ml) in a glass bubbler. The resulting solution was atomised using a piezoelectric device (Johnson Matthey liquifog®). For the Cu-doped TiO_2 films, [$Cu(NO_3)_2.3H_2O$] (2, 5, 10 and 20 mol.% relative to [$Ti(OCH(CH_3)_2)_4$]) was added to the [$Ti(OCH(CH_3)_2)_4$]/ethyl acetate solution. The precursor flow was kept at 1.4 $L.min^{-1}$. The substrate temperature was 470°C. After the precursor solution had been transferred, the bubblers were closed and the substrate cooled under a flow of N_2 to less than 100 °C before it was removed. Coated substrates were handled and stored in air. The coated glass substrate was cut into *ca.* 1 cm × 1 cm squares for subsequent analysis.

2.2.2 Film characterisation

Powder X-ray diffraction (PXRD) patterns were measured in a modified Bruker-Axs D8 diffractometer with parallel beam optics and a PSD LynxEye silicon strip detector. This instrument uses a un-monochromated Cu Kα source ($K_{\alpha 1}$, 1.54 Å) operated at 40 kV with 30 mA emission current. The incident beam angle was set at 1° and the angular range of the

patterns collected was $10° < 2\theta < 65°$ with a step size of 0.05° counted at 1 s/step. Raman spectroscopy was carried out on a Renishaw 1000 spectrometer equipped with a 514.5 nm laser. The Raman system was calibrated using a silicon reference. Scanning Electron Microscopy (SEM) was performed to determine surface morphology and film thickness using a JEOL JSM-6301F Field Emission SEM at an accelerating voltage of 5 keV. UV-Visible spectroscopy was performed using a Perkin Elmer Lambda 950 UV/Vis/NIR spectrophotometer over a wavelength range of 300 nm to 2500 nm. The spectra were referenced against an air background. X-ray photoelectron spectroscopy (XPS) was performed using a Thermo K alpha spectrometer with monochromated Al K alpha radiation, a dual beam charge compensation system and constant pass energy of 50 eV. Survey scans were collected in the range of 0 – 1200 eV. High resolution peaks were used for the principal peaks of Ti (*2p*), O (*2p*), Cu (*2p*), C (*1s*) and Si (*2p*). The peaks were modelled using sensitivity factors to calculate the film composition. The area underneath these bands is an indication of the element concentration within the region of analysis (spot size 400 µm).

2.2.3 Transient Absorption Spectroscopy

Transient Absorption Spectroscopy (TAS) was used to determine exciton lifetimes at room temperature (~22 °C) from the microsecond to second timescale. Samples were excited using pulsed laser excitation (λ = 355 nm, Opolette 355, pulse width = 6 ns, pulse repetition = 0.8 Hz, laser power = 1.55 $mJ.cm^{-2}$) through a liquid light guide. A quartz halogen lamp (100 W, Bentham, IL 1) with a stabilized power supply (Bentham, 605) was used as the probe light source. To reduce stray light, scattered light and sample emission, two monochromators and appropriate optical cut-off filters were placed before and after the sample. The probe light passing through the sample was detected using a Si photodiode (Hamamatsu Photonics, S1722-

01). This signal was passed through an amplifier (Costronics Electronics) and then measured using the digital oscilloscope. Decays presented are the average of between 100 − 200 laser pulses. Samples were measured inside a gas-tight quartz cell under an argon gas atmosphere.

2.2.4 Photoluminescence

Photoluminescence (PL) spectra from 350-800 nm were performed using an Edinburgh spectroflourometer equipped with maximum average power of 5mW. The excitation wavelength used was 380 nm.

The PL signals from 900-1600 nm were collected through a Newport Oriel monochromator interfaced with a Newport Merlin lock-in amplifier and detected by a TE-cooled Ge photodetector. The samples were excited using a 532-nm diode-pumped solid-state laser. The excitation power was 70 mW. The PL spectra were determined under air and at room temperature.

2.3 Functional testing

The photocatalytic activity was measured by monitoring the photocatalytic decomposition of a model organic pollutant, stearic acid (95%, Sigma-Aldrich). To measure the photocatalytic decomposition of a stearic acid coating, samples were attached to an IR sample holder consisting of an aluminum sheet with a circular hole in the middle. The stearic acid coating was applied from a saturated solution of stearic acid in chloroform (0.05 M) through a dip coating process. Pilkington NSG^{TM} Activ^{TM} glass was used as a benchmark and blank float glass as a control. The breakdown of the C-H bonds in stearic acid was measured using FTIR, between 2800 and 3000 cm^{-1} using a PerkinElmer Spectrum RX1 FTIR spectrometer. Measurements were taken at 0, 1, 2, 3, 4, 18 and 23 h intervals with the samples irradiated using 365 nm UVA lamp.

The C-H bonds in stearic acid absorb at 2958 cm^{-1} (C−H stretch CH_3), 2923 cm^{-1} (symmetric C−H stretch CH_2), and 2853 cm^{-1} (asymmetric C−H stretch CH_2). These peaks can be integrated to give an approximate concentration of stearic acid on the surface using a calibration constant, (where 1 $A.cm^{-1}$ in the integrated area between 2800 and 3000 cm^{-1} corresponds to approximately 9.7×10^{15} molecules cm^{-2}).[176] The rate of removal of stearic acid can thus be measured by monitoring the decrease in IR absorbance. The results are typically expressed in terms of the formal quantum efficiency, ξ, defined as the number of molecules degraded per incident photon (units, molecule × $photon^{-1}$). The light source was a black light-bulb lamp (BLB), 2×8 W (*Vilmer-Lourmat*). The irradiance of the lamp (I = 3.15mW cm^{-2}) was measured using a UVX radiometer (UVP).

E. coli (ATCC 25922) and *S. aureus*(8325-4) strains were maintained by weekly subculture on Brain Heart Infusion (BHI) agar (Oxoid, Basingstoke, UK). Both bacteria were used to inoculate two separate 10 mL aliquots of sterile BHI broths (Oxoid, Basingstoke, UK) and incubated aerobically at 37 °C for 18 hours. Bacteria from the overnight culture were harvested by centrifugation at 13000 × g for 1 minute. The bacteria were then re-suspended in phosphate-buffered saline (PBS) (Oxoid, Basingstoke, UK) and again centrifuged at 13,000 × g for 1 minute. Finally, the bacterial pellet was re-suspended in PBS before use. The turbidity of the bacterial cell suspension was measured at 600 nm using a spectrophotometer and was adjusted to an optical density, which corresponded to approximately 10^5 colony forming units (cfu) per 25 μL aliquot.

Prior to use, the pure TiO_2 and Cu doped TiO_2 slides were cut into 1 × 1 cm sections. A humidity chamber was created to ensure that the suspensions did not dry out. A 25 μL aliquot of the bacterial cell suspension was spread evenly on the surface of each slide and incubated at room temperature (21 ± 2 °C) for the allocated exposure time. For each exposure time (2 and

4 hours), triplicate samples were analyzed and uncoated glass microscope slides were used as a control. The samples were then irradiated for up to 18 hours using a UVA (Vilber-Lourmat, 2 × 8 W, 365 nm, 0.65 ± 0.23 mW cm^{-2}). A further set of samples (in triplicate) was maintained in the dark for the duration of the irradiation time. Each exposure time was also repeated on two separate occasions

After incubation the slides were aseptically transferred to 5 mL PBS and vortexed for 30 seconds to release the bacteria into the solution. Serial dilutions of the resulting bacterial suspensions were prepared in PBS and 100 μL from each dilution was spread on to MacConkey Agar (Oxoid, Basingstoke, UK)) for E.coli and Mannitol Salt agar (MSA, Oxoid Ltd) for S. aureus. Plates were incubated aerobically at 37 °C for 24 hours. After incubation, any bacterial colonies were counted and viable counts of bacteria were calculated.

2.4 Theoretical Methodology (Collaboration with Prof. David Scanlon UCL)

All bulk properties, intrinsic defects and extrinsic dopants together with their respective charge states were simulated using density functional theory (DFT) within the plane-wave code VASP.[177-180] Defect supercells were created from the geometrically optimized bulk parameters of anatase TiO_2 using the hybrid HSE06 (Heyd-Scuzeria-Ernzerhof)[181, 182] functional. Hybrid functionals are an improvement on standard DFT functionals which contain a systematic *self-interaction* error thus underestimating band gaps. HSE06 has been shown to provide a reasonably accurate description of the electronic and geometric properties of all the polymorphs of TiO_2. In order to describe the interactions between the core and valence electrons, the Projector Augmented Wave Method (PAW) was used, this is a method which mimics an all-electron method but with greater computational efficiency.

2.4.1 Optical Emission

Optical emission energies can be evaluated for a given defect. These involve the excitation of an electron from a defect level to the conduction band miminum (E_{abs}) and then the subsequent recapture of an electron (E_{em}). Alternatively a similar analysis can be carried out on hole capture from the valence band. These processes can be matched experimentally through optical photoluminescence measurements, an approach that has been successfully applied to a range of defects and materials.[183-187] The underlying assumption in evaluating the optical transitions is that photoexcitation occurs on a much faster timescale to that of lattice relaxation, as per the Franck-Condon principle.[188, 189] Therefore to calculate these optical processes the unrelaxed excited state (post-absorption) is calculated within the relaxed equilibrium geometry of the ground state, and vice versa for the emission process.[185] The eventual lattice relaxation leads to a release in energy (Franck-Condon shift, E_{rel}) via the emission of phonons. The difference between the equilibrium geometries of the ground and excited states corresponds to the zero-phonon line or the *thermal transition level*, ε(q/q'). The generalised coordinate was calculated by evaluating the mean displacement of atoms in the supercell above a suitable threshold (>0.01 Å displacement) between the equilibrium configurations of the different charge states.

2.5 Results and Discussion:

Pure and Cu-doped TiO_2 films were synthesized from the AACVD reaction of $[Ti(OCH(CH_3)_2)_4]$ and 2, 5, 10 and 20 mol.% of $[Cu(NO_3)_2.3H_2O]$ in ethyl acetate at 470 ^oC. All films had excellent coverage and were well adhered to the substrate, passing the Scotch™ tape test.[190]

2.5.1 X-ray diffraction (XRD) and Raman spectroscopy

The powder X-ray diffraction (PXRD) patterns (**Figure 2.1a**) showed all films to be phase pure anatase apart from 20% TiO_2:Cu, where Cu solubility limits were possibly reached in the TiO_2 lattice causing the formation of a separate Cu metal phase; as evidenced from reflections at 43.3º (111) and 50.4º (200). The line width of the (101) peak increased with dopant concentration, indicating a reduction in crystallinity due to lattice imperfections caused by Cu doping.[191] However, there was no noticeable shift in the anatase reflection peak positions for the Cu doped films, even at higher concentrations. This cannot be said for the Raman spectra (**Figure 2.1b**) where the principal E_g vibrational mode of anatase (caused by symmetric O-Ti-O stretching vibrations in TiO_2) at 141.5 cm^{-1} for pure TiO_2 shows an increasing blue shift with Cu concentration, corresponding to an expansion in the anatase unit cell and providing some evidence for the formation of a solid solution.[192] The discrepancy between the XRD and Raman data here could be due to the Raman technique being more surface sensitive. This suggesting that perhaps bigger changes to the TiO_2 lattice occurred at the material surface. Our XPS analysis showed that Cu (I) and Cu (II) species were present. As such, this expansion in the unit cell was expected, as the ionic radii of Cu (I) and Cu (II) in six coordination are 0.77 and 0.73 Å respectively, which are substantially larger than the ionic radii of Ti (0.60 Å). Additional low intensity modes at 396.5 cm^{-1} (B_{1g}, caused by symmetric bending vibration of O-Ti-O), 514.5 cm^{-1} ($A_{1g,}$ caused by asymmetric bending vibration of O-Ti-O) and 636.9 cm^{-1} (E_g) were also observed, which can all be assigned to anatase TiO_2.[192]

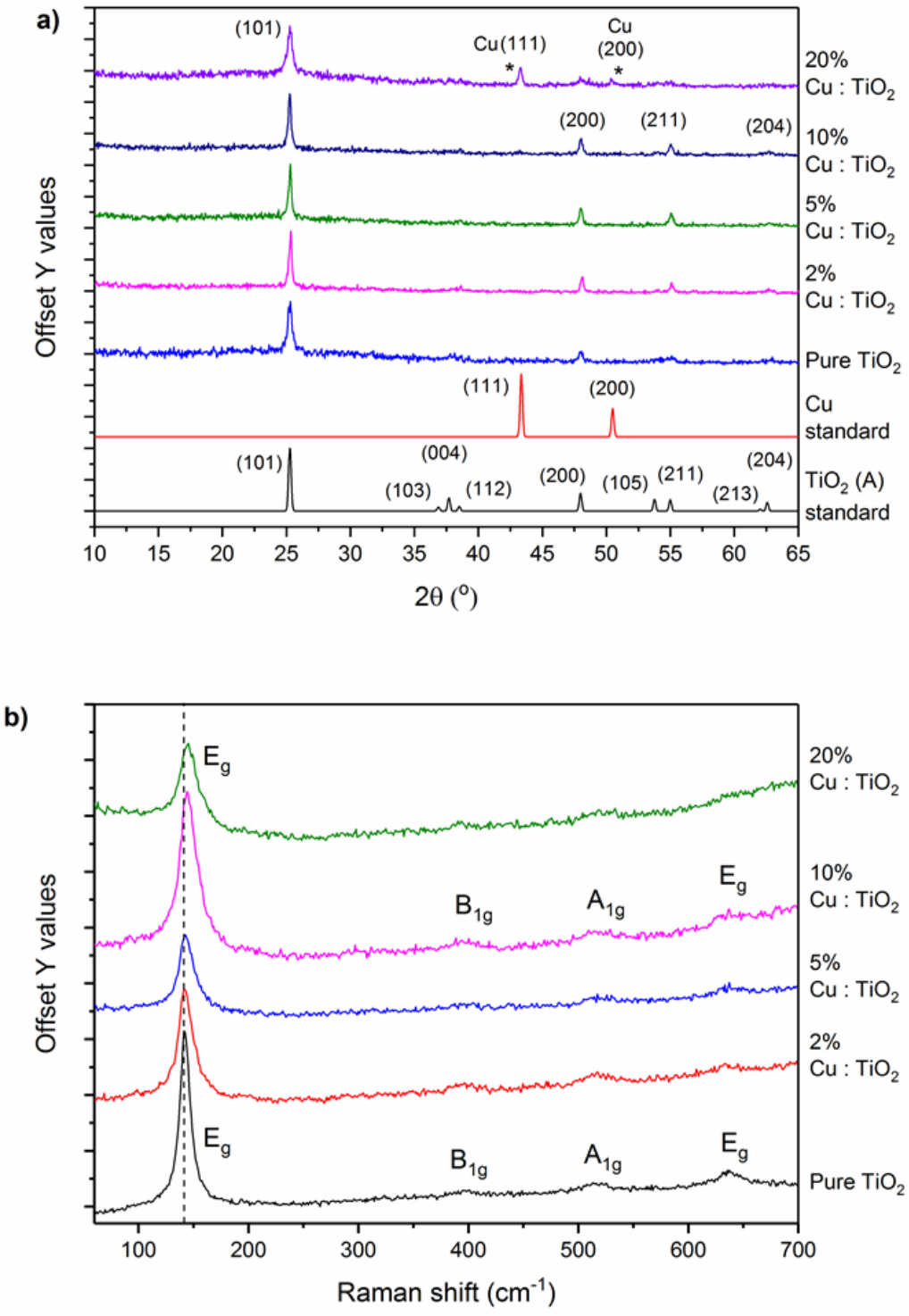

Figure 2.1: a) The PXRD patterns and b) Raman spectra matching anatase TiO_2 for the pure and Cu- TiO_2 films grown via AACVD at 470 ºC from ethyl acetate solutions of $[Ti(OCH(CH_3)_2)_4]$ and $[Cu(NO_3)_2.3H_2O]$ under a N_2 flow.

2.5.2 UV-Vis spectroscopy

Figure 2.2a shows the UV-vis spectra for the pure and Cu-doped films. The spectra are quite similar for pure TiO_2 and 2% Cu-doped TiO_2, with transmittance in the visible region at 70%. The transmittance in the visible region decreases systematically with increasing Cu concentration reaching 30% for the 20% Cu-doped TiO_2 film. The indirect optical band gap, calculated using the Tauc plot, remained at 3.3 eV for the pure, 2%, 5% and 10% films, For the 20% Cu-doped TiO_2 film however, there was small shift to 3.2 eV. This concurs with previous reports where a shift towards the visible was only observed at very high dopant levels.

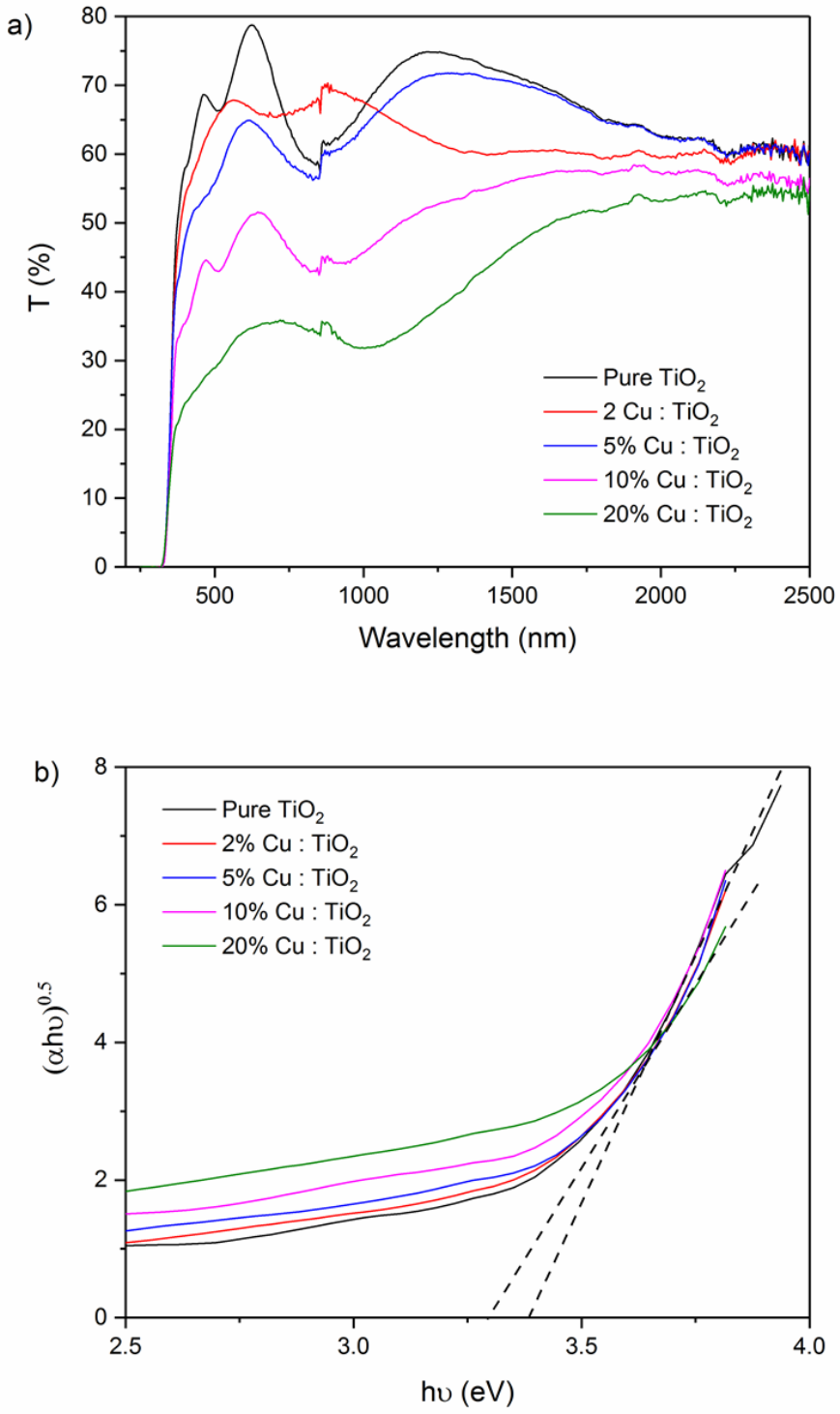

Figure 2.2: a) Transmittance spectra encompassing the UV, visible and near infrared wavelengths for the AACVD grown pure and Cu doped TiO_2 films. b) Shows the indirect optical band gaps of the films as calculated using the Tauc method.

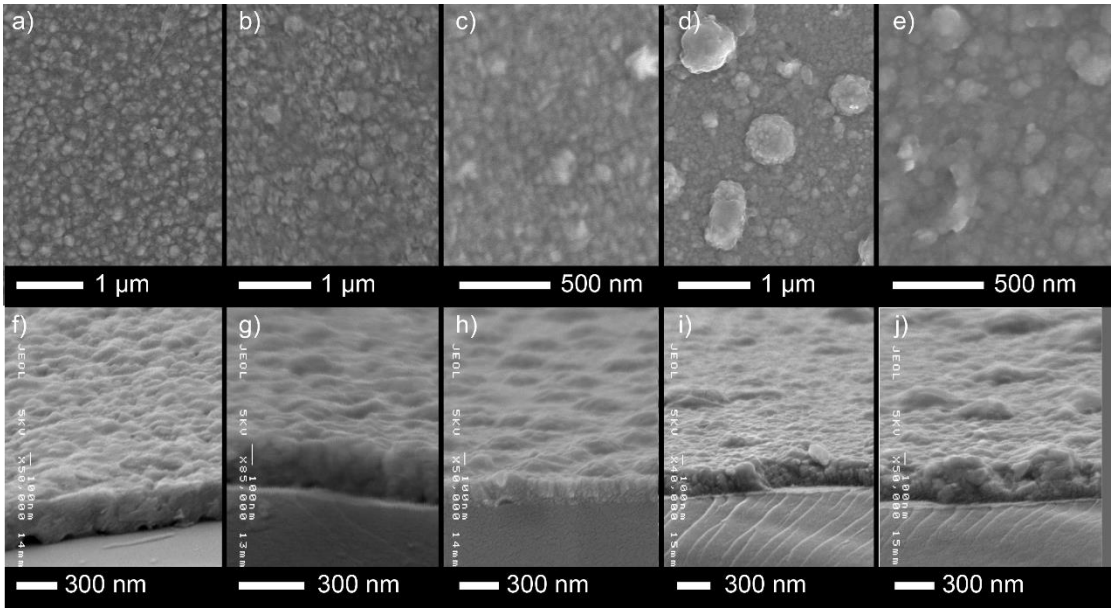

Figure 2.3: SEM images of the a) pure TiO_2, b) 2% TiO_2:Cu, c) 5% TiO_2:Cu, d) 10% TiO_2:Cu and e) 20% TiO_2:Cu grown via AACVD from $[Ti(OCH(CH_3)_2)_4]$ and $[Cu(NO_3)_2.3H_2O]$. The side-on SEM images also presented show the thickness of the films.

2.5.3 Scan electron microscopy (SEM)

Figure 2.3 shows the top down and side on scanning electron microscopy (SEM) images for TiO_2 thin films of various Cu concentration. The pure TiO_2 (**Figure 2.3a**), 2% and 5% doped TiO_2:Cu films have very similar morphology consisting of densely packed particles *ca.* 150 nm wide with no signs of pin holes, voids or cracks. All films were *ca.* 300 nm thick. At the higher doping levels (10% and 20%), large globular features are present.

2.5.4 X-ray photoelectron spectroscopy (XPS)

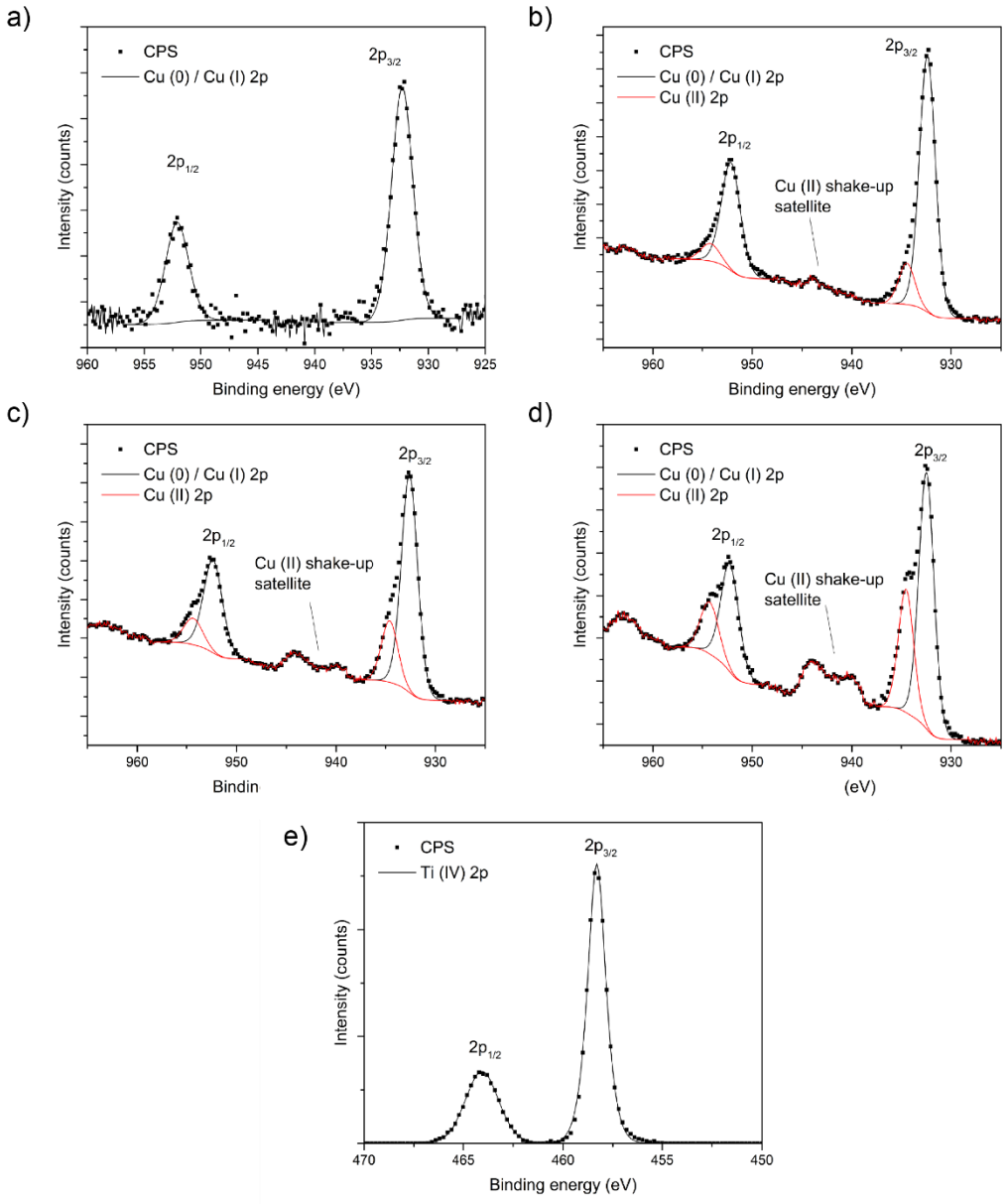

Figure 2.4: a-e) Core level XPS spectra for the AACVD grown pure and Cu-doped TiO_2 films. Cu 2p spectra show peak positions matching Cu (0) and/or Cu(I) for all doped films. Peaks for Cu (II) appear at higher doping levels. Ti was in the +4 oxidation state for all films with $2p_{3/2}$ peaks centred around 458.3 eV.

Core level X-ray photoelectron spectroscopy (XPS) for Cu *2p* (**Figure 2.4a-d**) nd Ti *2p* (**Figure 2.4e**) regions for the pure and Cu-doped TiO_2 films is shown in **Figure 2.4**. The 2% Cu doped

film, the Cu $2p_{3/2}$ peak is centered at 923.3 eV, matching the transition for Cu (0) and/or Cu (I) (due to heavy peak overlap, it is difficult to distinguish between Cu (0) and Cu (I) from the Cu 2p region alone).[193, 194] The lack of the Cu (II) shake-up satellite peak that is normally found around 945 eV indicates the absence of Cu (II) in this film. However, as the Cu concentration is increased to 20%, the Cu $2p_{3/2}$ peak shows an asymmetrical line shape that can be deconvoluted to two environments corresponding to a primary peak at 932.4 eV matching to Cu(0)/Cu(I) and a secondary peak at 394.5 eV that is assigned to Cu (II).[193, 194] There is also the resultant Cu (II) shake up feature at 945 eV. For all films, the Ti 2p transition is very similar with the expected doublet separated by 5.76 eV. The Ti $2p_{3/2}$ peaks are generally centered at 458.3 eV and can be assigned to Ti in the 4+ oxidation state. The ratio of Ti to Cu on the surface was 35:1, 2:1, 3:1 and 3:1 for 2%, 5%, 10% and 20% suggesting surface segregation of Cu on the surface of the TiO_2 films.

Valence band spectra for the pure and TiO_2:Cu samples show the valence band edge with respect to the Fermi level of the material at 0 eV, shown in **Figure 2.4f**. It consists of a broad peak between 2 and 10 eV that is itself made up of two smaller peaks centered at 5 eV and 7 eV originating from π (non-bonding) and σ (bonding) O 2p orbitals.[195]

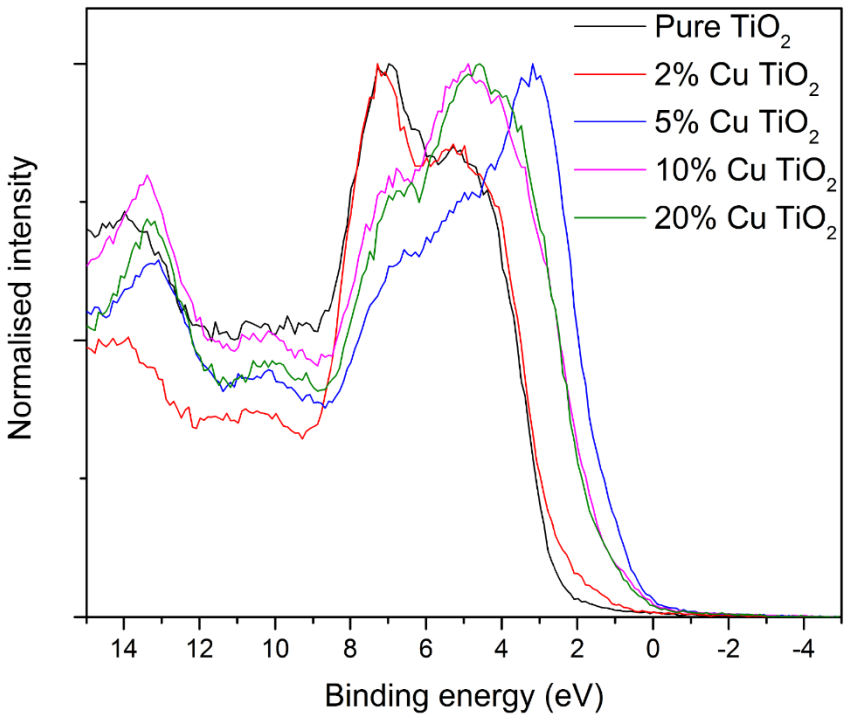

Figure 2.4f: The valence band XPS of the pure and Cu doped TiO2 films. Valence band spectra show a decrease in the band onset at high Cu dopant concentrations.

The Fermi level in TiO_2 (showing *n* type conductivity) is dependent on the carrier concentration but is typically found 0.3 eV below the conduction band minima (CBM). Therefore in theory the difference in energy between the valence band maxima (VBM) (determined by simple extrapolation of the low energy edge) and the Fermi level plus 0.3 eV corresponds to the band gap.[28, 196] However, for the AACVD grown films in this case, the difference in energy between the VBM and the Fermi level is, for undoped TiO_2, 2.7 eV. Upon doping with Cu this energy difference reduces even further. A similar observation was made by Cheng *et al.* for TiO_2 powders where they reported an optical band gap of 3.2 eV and a valence band maximum of 2.18 eV) and Parkin *et al.* with TiO_2 thin films grown from $[Ti(OEt)_4]$ and toluene that showed a band gap of 3.2 eV measured by UV-vis spectroscopy and a valence band maximum of 2.3

eV.[197, 198] The difference in the optical band gaps and the the XPS valence band calculated band gaps could also be due to the surface segregation of Cu in the films that may have shifted the reference point of the Fermi level.

2.5.5 Photoluminescence

The further study on the emission of Cu doped TiO_2 films in the UV-Vis and infrared region were carried out by photoluminescence (PL). PL spectral emission can be used to study of charge carrier recombination and to investigate the efficiency of charge carrier trapping, migration, separation and transfer in semiconductors.[199-201] PL emission spectra result from radiative recombination of a photoexcitation, where a higher PL intensity shows a higher degree of radiative recombination.[164, 199-201] There have been examples of materials displaying strong photoluminescence and high photocatalytic activity.[202]

Photoluminescence emission spectra of Cu doped TiO_2 at different Cu doping concentrations (2, 5, 10 and 20%) in the wavelength range from (350 to 800 nm) with excitation wavelength 405 nm revealed in **Figure 2.5(A)**. All the samples have a peak at 380-430 nm, which could be due to band-gap, defects or surface trapping of electrons. There are broad peaks from around 500 to 650 nm which intensify with increasing Cu doping, the peaks located around 520 nm are thought to be due to a self-trapping of electrons by the TiO_6 octahedra.[164]

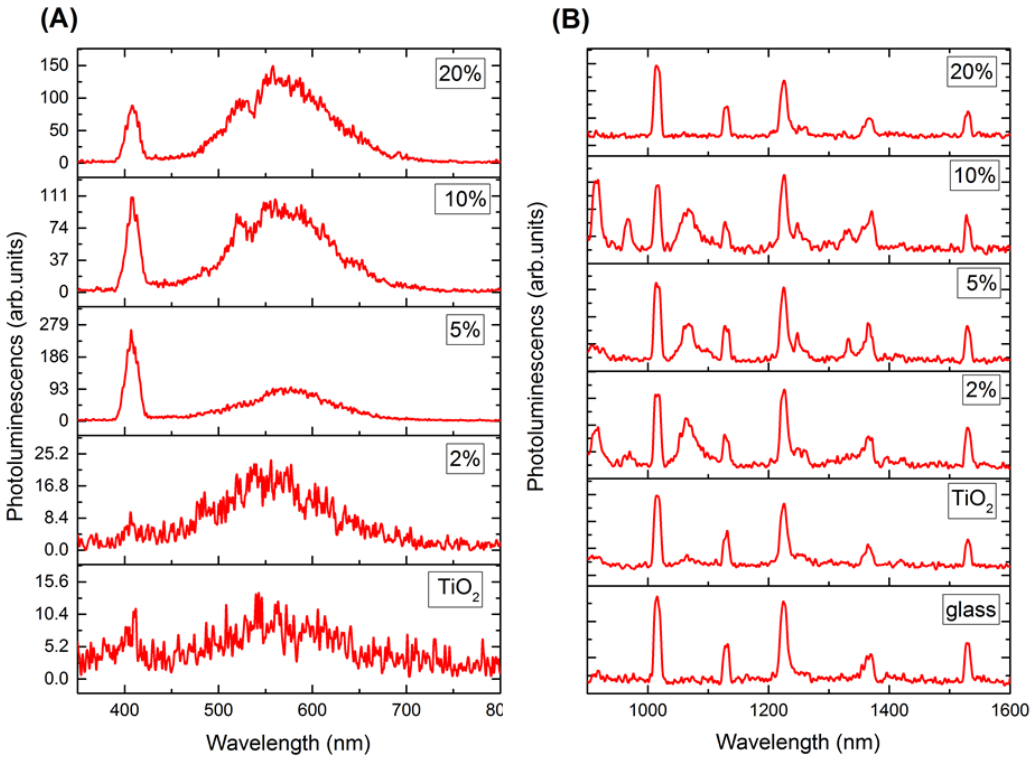

Figure 2.5, Room temperature photoluminescence (PL) spectra of Cu-doped TiO_2 at different Cu doping concentrations (2, 5, 10 and 20%). Figure 5(a) shows PL spectra in the wavelength range form (350-800 nm) for all samples. .Figure 5(b) shows PL spectra in in wavelength range from (900-1600 nm) with excitation wavelength of 532 nm.

In the PL spectra (900-1600 nm; **Figure 2.5B**). Emission peaks with wavelengths of 1010 nm, 1128 nm, 1230 nm, 1340 and 1525 nm are found to originate as normal glass emissions.

In undoped anatase TiO_2, the non-glass peaks exist as low intensity peaks, in particular peaks around 920nm, and 1050nm likely due to defect centred emissions. In 2%, 5% and 10% Cu doped anatase, the peaks present in anatase (non-glass) are observed here albeit more pronounced. In 2%, 5% and 10% TiO_2:Cu, additional peaks exist such as the emission at 960nm 1250nm and 1400nm. 20% Cu, however appears more like undoped anatase, with the glass peaks dominating the spectrum. To understand these results, theoretical calculations on the photoluminescence of Cu-doped anatase are given below.

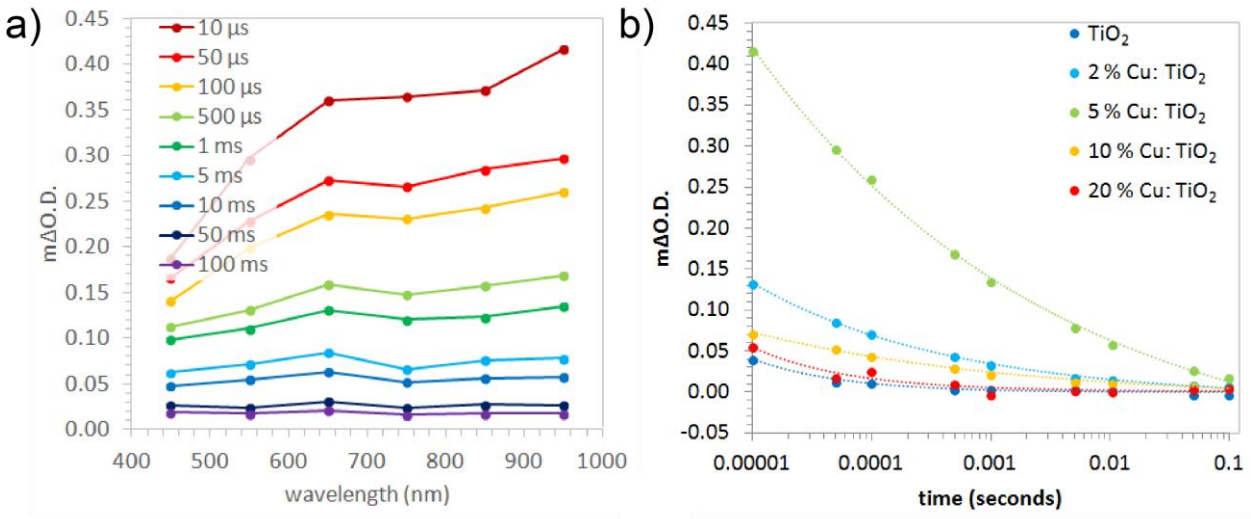

Figure 2.6: (a) The transient absorption spectra at select times for the 5% Cu doped TiO_2 thin-film. (b) The recombination kinetics at 950 nm for all samples, where the dashed lines represent a fit to a power law decay model ($f(t) = a.t^b$, where t is time and a and b are variables).

2.5.6 Transient absorption spectroscopy (TAS)

Transient absorption spectroscopy (TAS) is a form of laser flash spectroscopy that can monitor the generation, recombination, trapping, charge transfer *etc* of photo-generated charges in semiconductors.[203, 204] The dynamics of photo-generated charges can be studied by tracking transient changes in absorbance at particular wavelengths,[205] where it has been shown that the electrons and holes in anatase TiO_2 absorb in the visible.[136, 140] The technique has primarily been used to study charge transfer processes in solar cells (organic-organic or inorganic-organic)[206-208] but has also been used to study charge transfers in heterojunction photocatalysts (inorganic-inorganic)[209] as well as the kinetics of photocatalytic processes.[210-212]

In this study, the kinetics of electron-hole recombination for the series of Cu doped anatase TiO_2 samples were investigated using TAS. Samples were excited using a UVA laser (355 nm, 1.55 $mJ.cm^{-2}$.per pulse) and the transient changes in absorption were measured from 450 – 950 nm. Previous studies have shown that the photo-generated electrons and holes in anatase show broad absorptions centred at ~ 800 and 450 nm respectively.[140] An example TAS spectrum of

the 5% Cu doped TiO_2 sample is shown in **Figure 2.6a**, which shows an extended absorption across the visible typical of anatase TiO_2. The decay kinetics did not change with probe wavelength. This showed that charge transfer processes were not occurring within the material. For instance, it has typically been cited that phase segregated metal dopants in TiO_2, such as Cu, may act as electron sinks.[213] If Cu was indeed acting as an electron sink, our TAS studies would show a difference in decay kinetics in the electron region (~ 800 nm) compared with the hole region (~ 450 nm). This wasn't the case for any Cu doped sample studied herein. As the samples were studied in an argon atmosphere, no photo-chemistry could occur. This meant that the transient decay of our absorption signals was due solely to electron-hole recombination. The kinetics of electron-hole recombination were compared across all samples (**Figure 2.6b**). These kinetics could be fit to power law decays, typical of the trap/de-trapping movement of charge found in anatase TiO_2.[214] The rate of recombination was quantified, by finding the time where half the initial absorption was lost ($t_{50\%}$). In the 5% Cu doped TiO_2 sample, recombination was the slowest ($t_{50\%}$ ~ 110 ms), followed by the 2 % ($t_{50\%}$ ~ 26 ms), 10% ($t_{50\%}$ ~ 19 ms), 20% ($t_{50\%}$ ~ 3 ms) and undoped sample ($t_{50\%}$ ~ 1 ms). In the undoped sample, the timescale of recombination was typical of anatase TiO_2.[6] Moreover, our TAS results showed that Cu doping resulted in an enhancement in charge carrier lifetime. Substantial differences in the initial absorption were also observed (**Figure 2.6b**). This indicated that there were critical differences in ultra-fast timescale recombination between samples, not observable on the timescale of these measurements. What was clear was that the 5 % Cu doped TiO_2 sample possessed the greatest number of photo-generated charges from 10 μs (followed by the 2%, 10%, 20% and undoped TiO_2 sample). This trend was analogous to the lifetime of photo-generated charge, where the 5% Cu doped TiO_2 samples showed the both the most charges from 10 μs and the slowest rate of electron-hole recombination.

2.5.7 Photocatalytic activity

The photocatalytic activities of the as-synthesised were evaluated against the degradation of a model organic pollutant, octadecanoic (stearic) acid, under ultraviolet (UVA) illumination (*I*= 3.15 mW cm^{-2}). Stearic acid is highly stable under UV light (in the absence of an underlying effective photocatalyst) and can be easily monitored on transparent materials *via* infrared spectroscopy. Its photocatalytic degradation can be monitored following the disappearance of characteristic C-H modes at 2958, 2923 and 2853 cm^{-1} (**Figure 2.7b**). The photocatalytic rates were estimated from linear regression of the initial steps (30 – 40 %) of the curve of integrated area *vs.* illumination time. The corresponding rates were expressed as formal quantum efficiencies (FQE), defined as molecules of stearic acid degraded over incident photons (units, molecule × $photon^{-1}$) (**Figure 2.7a**). The variation in FQE values was discarded to be due to differences in physical properties of the films, since all films investigated showed comparable thicknesses and crystallinity, based on XRD and SEM analyses (**Figures 2.1 and 2.3**). In addition, a blank piece of glass (as a control) and Pilkington Activ™ self-cleaning glass (15 nm TiO_2 anatase coating) were also tested for comparison.

The pure TiO_2 sample showed a destruction rate of 1.2 x 10^{-2} molecules. $photon^{-1}$, upon doping the 2% and 5% of Cu the rate increases to 1.6 x 10^{-2} molecules. $photon^{-1}$ and 1.8 x 10^{-2} molecules. $photon^{-1}$ (a higher rate than Activ™, 1.6 x 10^{-2} molecules. $photon^{-1}$) respectively. At higher concentrations of Cu (10% and 20%) the stearic acid destruction rate decreases to 1.1 x 10^{-2} molecules. $photon^{-1}$ and 3.6 x 10^{-3} molecules. $photon^{-1}$ respectively. The film photocatalytic activities observed (**Figure 2.7a**) could be correlated directly with photo-generated charge carrier lifetimes (**Figure 2.6**), where high lifetime resulted in high photocatalytic activity. These observations were attributed to the kinetics of the typical processes associated with photocatalysis on TiO_2. It is commonly accepted that photocatalysis on TiO_2 occurs through the reaction of: i) holes with surface H_2O producing highly reactive

hydroxyl radicals which subsequently degrade nearby organics and ii) electrons with O_2 forming highly reactive superoxide radicals which also degrade nearby organics.[208] These two processes occur on different time-scales, where it has been demonstrated that holes can react with H_2O within ~2 μs and electrons react with O_2 from 10 – 900 μs.[209] Our TAS studies showed that the sample with longest-lived photo-generated charge carrier was 5% Cu-doped TiO_2, which showed both the slowest rate of recombination and the highest number of photo-generated charges.

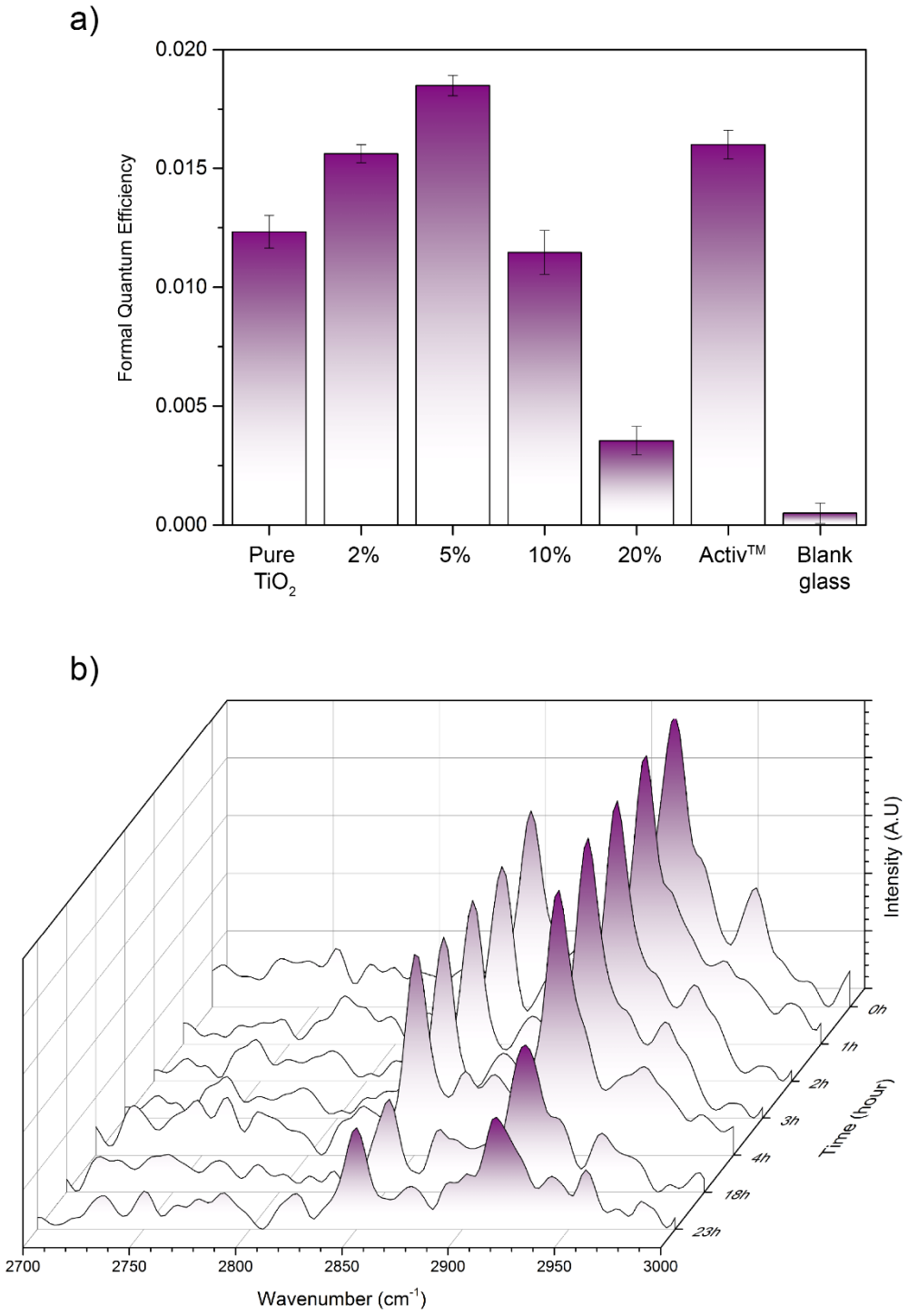

Figure 2.7: a) Formal quantum efficiencies obtained during degradation of stearic acid under UVA irradiation of Cu:TiO_2 and undoped thin films. Blank glass and Actic™ samples are included for comparison. b)IR spectra of stearic acid upon UVA illumination (I = 3.15 mW cm^{-2}) on a typical Cu-doped TiO_2 film, 5 % Cu:TiO_2.

2.5.8 Antimicrobial activity

Since 5% Cu doped TiO_2 sample showed the best photocatalytic results, this sample was chosen along with pure TiO_2 for antimicrobial activity testing against a Gram negative bacterium, *E. coli*, and Gram positive bacterium, *S. aureus*, under dark and UVA irradiated conditions. In the case of *E. coli*, there was no significant reduction in the colony counts for the pure TiO_2 sample under darkness from 2 to 4 hours (**Figure 2.8a and 2.8b**). A small reduction was observed under UVA irradiation, this is likely to be due to the oxidative stress caused by the generation of reactive oxygen species (ROS). This was also observed when the pure TiO_2 sample was tested against *S. aureus* (**Figure 2.8c and 2.8d**). However for the Cu doped sample, there was a small decrease in the colony counts of both *E. coli* and *S. aureus* under dark conditions which we think is primarily due to the Fenton type reactions that Cu is known to undergo. Under UVA irradiation for 4 hours, there was a rapid decrease in bacterial numbers, to below or almost below detectable levels, for *S. aureus* and *E. coli* respectively (**Figure 2.8b and 2.8d**). We attribute this to the generation of ROS that attack organic matter when TiO_2 is irradiated with energy above its band gap. The activity was higher in the Cu doped TiO_2 film compared to the undoped film due, as previously observed from TAS measurements and discussed, to the Cu states acting as trapping sites that can reduce charge carrier recombination. The lifetimes of the charge carrier are important as they have to travel to the surface of the semiconductor before they can undergo reactions with water and oxygen to produce ROS that then go on to destroy bacterial cells. The secondary reason for the superior activity of the doped samples over the undoped is due the presence of Cu that has its own antibacterial properties, *via* Fenton type reactions as discussed in the introduction.

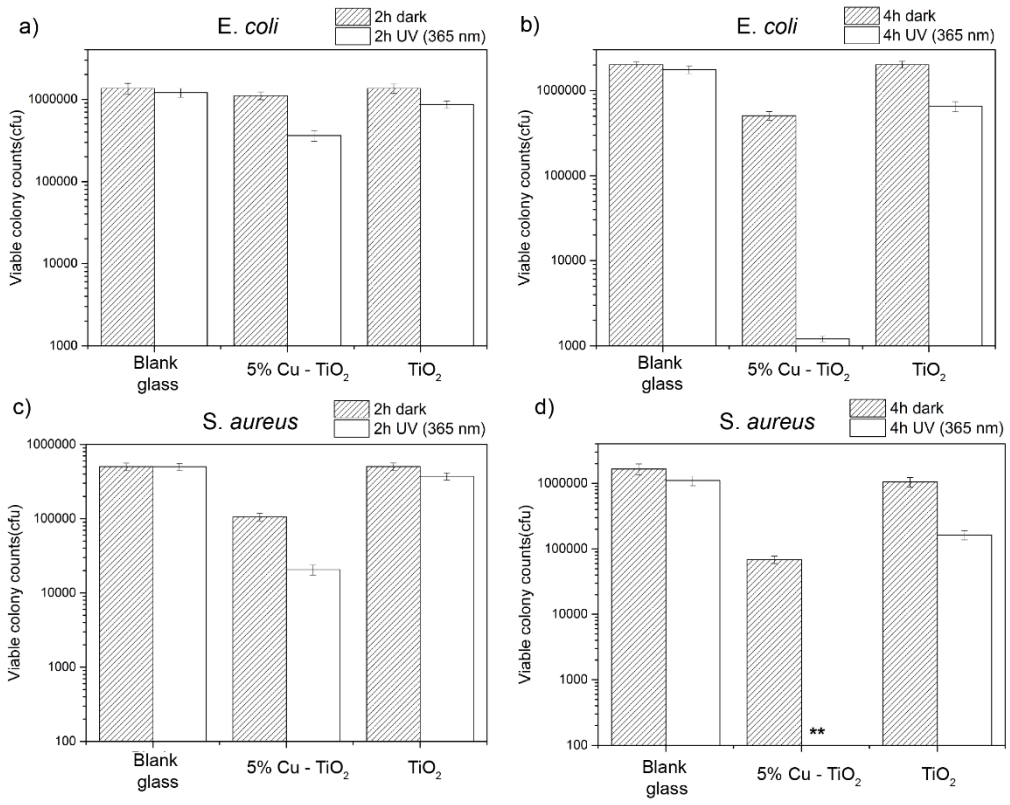

Figure 2.8: Antimicrobial test results for pure and 5% doped films under dark and UVA conditions for 2 hours (a and c) and 4 hours (b and d) against gram negative E.coli (a and b) and gram positive S. aureus (c and d) bacteria.

2.6 Dopant-Centered Optical Properties:

The theoretical studies and data analysis in this section **(Section, 2.6)** were carried out in collaboration with Prof. David O. Scanlon.

The optical transitions for all defects were evaluated and are shown for substitutional and interstitial Cu in **Figure 2.9.**

Figure 2.9a shows that Cu_{Ti} undergoes optical absorption from Cu_{Ti}^{2-} to Cu_{Ti}^{1-} and from Cu_{Ti}^{1-} to Cu_{Ti}^{0} in the near UV (490 nm) and the UV (375 nm) regions respectively for the excitation of an electron to the conduction band. These absorptions will occur within the absorption edge of anatase TiO_2, and thus is not expected to be distinguishable experimentally. Cu_{Ti} can also undergo hole ionisation from the VBM as is shown in **Figure 2.9c** where the absorptions occur in the near-IR (886nm; $Cu_{Ti}^{0} \rightarrow Cu_{Ti}^{1-}$) and the green portion (525nm; $Cu_{Ti}^{1-} \rightarrow Cu_{Ti}^{2-}$) of the visible spectrum. These results can be seen in the transmission data in **(Figure 2.2a)** by the dip around the absorption edge and ~525 nm compared to undoped *pure* anatase and is shown to be quite pronouced in the 10% Cu samples, signifying larger concentrations of substitutional Cu.

Figure 2.9b and **2.9d** display the electron and hole ionisation transitions for interstitial Cu (Cu_i) respectively. **Figure 2.9b** indicates that the optical excitation of an electron to the CBM results in the absorption of a photon in the near IR (969 nm) for $Cu_i^{1+} \rightarrow Cu_i^{2+}$. From the transmission data in **(Figure 2.2a),** broad troughs are seen ~900-1200nm for the 10% and 20% Cu samples, suggesting that an increased incorporation of interstitial Cu is present. The broad troughs are indicative of a large relaxation energy[187] (E_{rel}) which, for Cu_i^{1+} to Cu_i^{2+} is ~0.91eV. A small dip in the transmission occurs for 5% Cu and none at all for 2% Cu leading to the conclusions that the 2+→1+ transition may be suppressed (ie. increased Cu_i present as Cu(I) and decreased Cu_{Ti}) film). It is not expected that an optical transition will occur from the 1+ to the 0 charge

states as *thermal* ionisation occurs in the conduction band and so has been omitted from this diagram. The capture of an electron by Cu_i^{2+} (from the VBM) facilitates the absorption of a photon in the near-UV with a wavelength of which, as with Cu_{Ti}, is not expected to be distinguishable experimentally due to its position in the absorption edge of TiO_2.

2.6.1 Emission:

The emission energies present for electron (**Figure 2.9a)** and hole (**Figure 2.9c)** ionisation of Cu_{Ti} range from the mid-IR region to the red portion of the visible spectrum. In **Figure 2.9a** the transition of $Cu_{Ti}^{0} \rightarrow Cu_{Ti}^{1-}$ and the subsequent transition of Cu_{Ti}^{1-} to Cu_{Ti}^{2-} gives rise to photoluminescence peaks at ~634 nm and ~1252 nm respectively. Upon the release of a hole to the VBM, two photoluminescence peaks are expected around 1512 nm ($Cu_{Ti}^{2-} \rightarrow Cu_{Ti}^{1-}$) and ~31µm ($Cu_{Ti}^{1-} \rightarrow Cu_{Ti}^{0}$). The latter absorption is expected to be *non-radiative* due to the very small emission energy and will thus be dissapated through the anatase lattice as phonons.[184] Similar behaviour is seen in acceptor defects such as V_{Zn} in ZnO [183] as well as V_{Ga} in GaN.[184] It is expected that these peaks will be broad, due to the relatively large E_{rel} values (~0.7eV). Due to the glass emission at 1525 nm in **Figure 2.5b**, it is hard to tell whether this peak is present in the AACVD-made Cu-doped TiO_2 thin films.

Cu_i will only photoluminesce after the capture of an electron from the valence band. **Figure 2.9d** depicts this with a value of 599 nm and a broad peak (E_{rel} = 0.91eV). This is seen in the room-temperature photoluminescence data in (**Figure 2.5a)** from ~450 nm – 625 nm. The highest intensity photoluminescence occurs in the 20% Cu sample, which, together with the transmission data in **(Figure 2.2a)** indicates that the presence of interstitial Cu is more substantial. **Figure 2.9b** shows that Cu_i will not photoluminesce after electron ionisation due to the *thermodynamic* resonance of Cu_i^{1+} in the conduction band. Instead, it is likely that Cu_i^{1+}

will *readily* capture an electron with an energy barrier of 0.005eV to return to the 2+ charge state.

The presence of interstitial Cu in the anatase lattice together with substitutional Cu is likely beneficial to both the photocatalytic activity and the electron-carrier separation lifetimes. The mechanism of this is possibly due to the synergistic effect of *deep*-acceptor/*shallow*-donor pairs whereby an excited electron from Cu_{Ti} can be readily accepted by an interstitial Cu defect thereby increasing the separation. Electron capture by substitutional Cu occurs in the visible/near-IR portion of the spectrum, ($Cu_{Ti}^{0} \rightarrow Cu_{Ti}^{1-}$; E_{abs} = 886 nm), and electron excitation of Cu_i also occurs in the visible/near-IR portion ($Cu_i^{1+} \rightarrow Cu_i^{2+}$; E_{abs} = 969 nm) aiding the visible light enhanced photocatalytic activity. It is possible that competition between these defects may arise with increased Cu incorporation favouring the formation of interstitial Cu over substitutional Cu thereby losing the beneficial synergistic effect. This is evidenced through the detrimental effect to the carrier separation lifetimes in **Figure 2.6** and to the decrease in photocatalytic activity (**Figure 2.7a)** towards higher doping levels where the Cu_{Ti}:Cu_i ratio is suggested to be higher (10% and 20%).

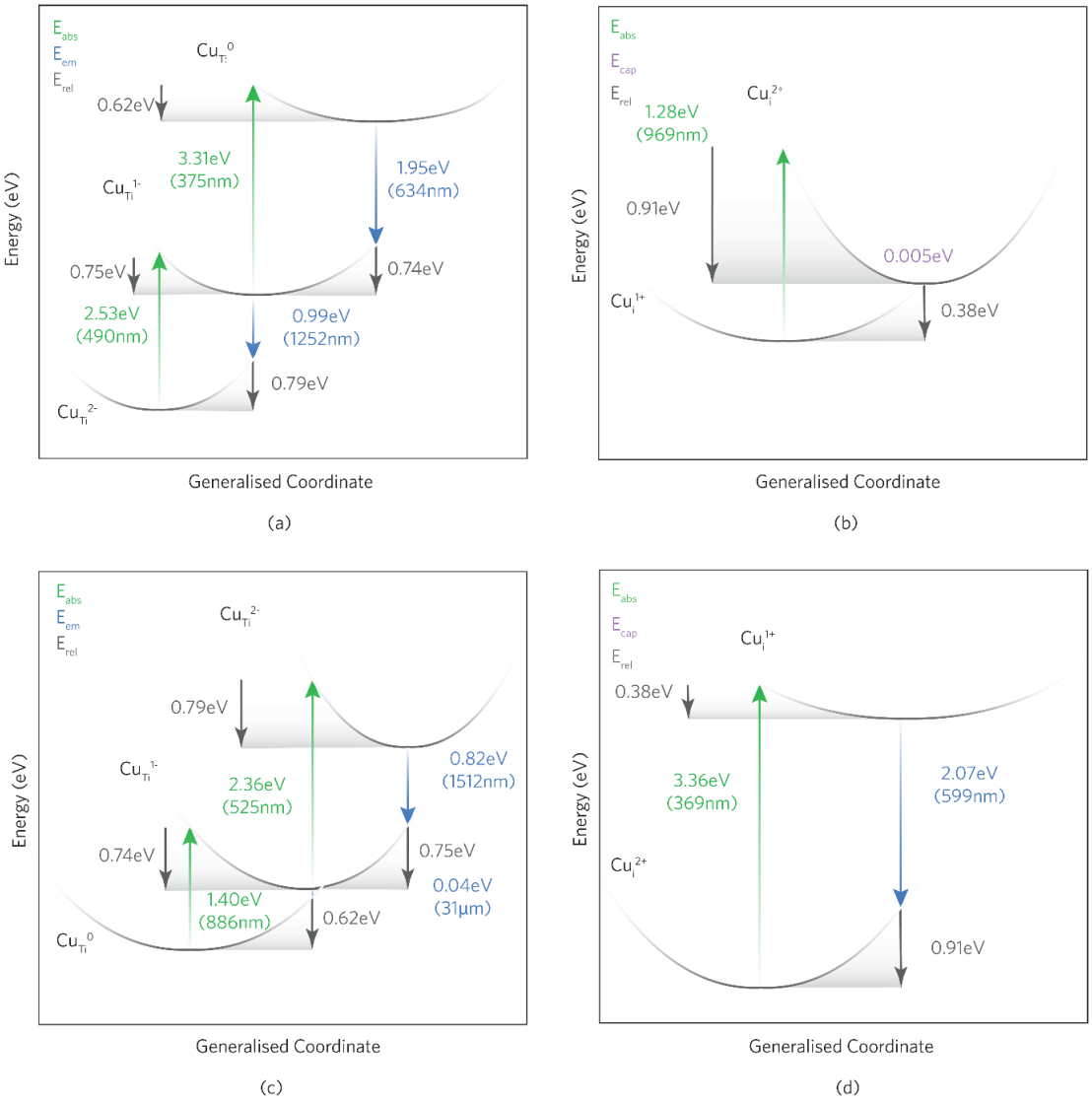

Figure 2.9A one-dimensional configurational coordinate diagram for (a), (c) Cu_{Ti} and (b), (d) Cu_i under electron and hole ionisation respectively. In each example the absorption and emission energies are independent of the chemical potentials and therefore the growth conditions.

2.7 Conclusion:

Titanium dioxide is a versatile material that displays multifunctionality. Here, highly photoactive thin films of Cu-doped TiO_2 were successfully fabricated on glass substrates using aerosol assisted chemical vapour deposition (AACVD). This is the first example, to the best of our knowledge, of TiO_2:Cu thin films grown in this manner. A range of copper concentrations (2, 5, 10 and 20%) were investigated so that the photocatalytic and antibacterial *(vs S.Aureus and E.Coli)* abilities could be determined. Transient absorption spectroscopy (TAS) was carried out on both pure and Cu-doped TiO_2, with Cu-doped films displaying *extended* exciton lifetimes relative to pure TiO_2 that correlated with photocatalytic activity. Hybrid density functional theory calculations, carried out in this work, help us to better understand the mechanism for the enhanced UV/visible light photoactivities observed. Interactions between substitutional and interstitial Cu in the anatase lattice may also explain the enhancement in exciton lifetimes and confirmed by optical transmission and photoluminescence experiments.

In the next chapter, pure Rutile-TiO_2 films and Cu doped rutile-TiO_2 were deposited onto a large of ZrO_2 at 500 °C by aerosol assisted chemical vapour deposition (AACVD). Photocatalytic activity of pure rutile and Cu doped rutile-TiO_2 films at different copper concentrations were compared by the degradation of Stearic acid under white light and UVA irradiation. The Cu doped rutile TiO_2 thin films exhibited surface plasmonic resonance (SPR) bands at ~ 613 and 629.5 respectively.

Chapter 3

Cu doped Rutile TiO_2 Plasmonic thin films

'In this chapter, the results of experiments which explore the deposition of Rutile TiO_2 films and Cu doped Rutile TiO_2 films by aerosol assisted chemical vapour deposition (AACVD) are present. Pure rutile TiO_2 films were deposited on ZrO_2 films at 500 °C. A series of different Cu concentration doped rutile TiO_2 films will be studied to investigate their impact on photocatalytic degradation of stearic acid under UVA and white light. Surface plasmon resonance (SPR) was observed with high Cu concentration such as 10 and 20%Cu doped TiO_2 thin films'.

3.1 Introduction

Titanium dioxide (TiO_2) is a well-known photocatalytic semiconductor with applications in water/air purification systems, water splitting devices and self-cleaning surfaces as it is inexpensive, chemically stable and non-toxic.[28, 114, 141, 142] The rutile form is one of the three commonly occurring polymorphs of TiO_2, however with a difficult synthetic procedure and poorer transport of bulk excitons to the surface compared to the anatase phase, it is less well investigated for use in photocatalysis.[215] The indirect optical band gap of rutile is 3.0 eV, which means (much like anatase) it is activated by only 4% of solar radiation. The band gap can be red shifted in an effort to capture more than the 43% of light energy that lies in the visible portion of the solar spectrum. This is often achieved through cation (eg. Cu, Fe or W)[216-219] or anion (C, S or N) doping.[50, 51, 55, 94, 220-224]

As previously mentioned, despite rutile being the most naturally abundant polymorph it is difficult to synthesis particularly in the thin film form at large scale due to the high preparation temperature. Typically synthetic routes to rutile films involve temperatures above 950 ^oC alternatively rutile can be fabricated through post synthetic calcination of anatase films or powders again at very high temperatures.[215] As a result it is even more difficult to produce doped rutile films as post deposition calcination of doped anatase films can result in phase separation. This has limited the potential of rutile TiO_2 thin films in many applications including photocatalysis.

In this chapter we lay the foundations for a facile route to both pristine and Cu doped rutile TiO_2 thin films at 500 ^oC using aerosol assisted chemical vapour deposition – a high throughput, easily scalable technique that can employ a wide range of volatile and non-volatile precursors. This was achieved by preparing a thin layer of ZrO_2. We found that this layer promoted rutile-TiO_2 growth while inhibiting the anatase polymorph. The Cu doped films

showed enhanced photocatalytic activity under both UV and visible light irradiation. This is presumably due to a reduction in charge carrier recombination as dopant species act as electron traps.[225-227] In addition, surface plasmon resonance (SPR) plays a vital role in activity with increased copper concentration.

3.2 Experimental Section

3.2.1 Materials

Titanium (IV) butoxide [$Ti(OCH_2CH_2CH_2CH_3)_4$], zirconium acetylacetonate [$Zr(acac)_4$], [$Cu(NO_3)_2.3H_2O$] and stearic acid 95%, were purchased from Sigma-Aldrich Chemical Co; absolute methanol and toluene from Merck Chemicals. All chemicals were used as received.

3.2.2 AACVD

All films were deposited by aerosol assisted chemical vapour deposition (AACVD). A Pico-Health™ ultrasonic humidifier was used to generate the aerosol mist and a N_2 (99.99% from BOC) flow at a rate of 1.5 $Lmin^{-1}$ to deliver the mist into the CVD reactor. The reactor includes a carbon block containing a Whatmann cartridge heater. The reactor has a bottom and top plates (8 mm separation) to promote laminar flow. A Pt–Rh thermocouple was used to monitor the temperature on the substrate. The glass substrates were washed by distilled water, isopropanol and acetone then allowed to dry in a 100 ^oC oven. The deposition was carried out in a cold-walled horizontal-bed CVD at 500 °C for Rutile. ZrO_2 was deposited at 450 °C onto glass substrate. The aerosol was transferred into the reactor by N_2 with flow rate 1.5 L min^{-1}. The glasses after the depositions were left to cool under nitrogen until room temperature.

3.2.3 ZrO_2 substrates

$[Zr(acac)_2]$ (0.5 g = 1.025 mmole) was dissolved in methanol (20 mL) and the resulting solution was atomised using a Pico-Health™ ultrasonic humidifier. The precursor flow was kept at 1.5 $Lmin^{-1}$. The substrate temperature was kept at 450 ^oC. After the deposition the bubblers were closed and the substrates were cooled under a flow of nitrogen then annealed at 500 °C to remove carbon contamination.

3.2.4 Pristine and Cu doped rutile films

$[Ti(OCH_2CH_2CH_2CH_3)_4]$ (0.5g =1.5 mmole) was dissolved in MeOH (20 ml) and $[Cu(NO_3)_2.3H_2O]$ was added in dopant amounts (0, 2, 5, 10 and 20 mol.%). The resulting solution was then atomised. The precursor flow was kept at 1.5 $L.min^{-1}$. The substrate temperature was kept at 500 °C.

3.3 Characterization of the films

Scanning Electron Microscopy (SEM) was performed to determine surface morphology and film thickness using a JEOL JSM-6301F Field Emission SEM at an accelerating voltage of 5 keV.

Fourier infrared spectroscopy (FT-IR) was used by a Perkin Elmer RX-I transform infrared (FTIR) spectrometer. An FTA-1000 drop shape instrument was used to measure water contact angle by using 5 µl droplet of water on the samples and the drop of water image was captured by A Fujiflm Finepix HS25 EXR camera at 1000 frames per second.

3.4 Photocatalytic test

Prior to using the samples for photocatalytic performance, the samples were washed by distilled water, rinsed in isopropanol and acetone then placed under UVA irradiation overnight to clean and activate the surface. (0.05 M) of stearic acid in chloroform was prepared. The films were

coated by stearic acid as thin films. The photocatalytic test was carried out under photo reactor for visible and light Black-light blue (BLB) lamps (Vilber-Lourmat, 2 × 8 W, 365 nm, 1.2 mW cm^{-2}) for UVA, as well as, under white light experiments were carried out using (General Electric 28 W Biax 2D compact fluorescent lamp). FT-IR was used to show the degradation of the over the stearic acid in the range 2700–3000 cm^{-1}. Integrate area of characteristic C–H bands at 2853, 2958 and 2923 cm^{-1} were calculated.

3.5 Results and Discussion

Thin films of pristine and Cu doped rutile TiO_2 were deposited on ZrO_2 coated glass substrates *via* AACVD at 500 ^oC using N_2 as the carrier gas. A pristine rutile film was prepared from a methanol solution (20 mL) of $[Ti(OCH_2CH_2CH_2CH_3)_4]$ (0.5 g, 1.5 mmol) while for the Cu doped rutile films, dopant concentrations (2, 5, 10 and 20 mol.%) of $[Cu(NO_3)_2.3H_2O]$ in methanol (20 mL) were used. This is, to the best our knowledge, the first example of the formation of phase pure TiO_2 thin films in the rutile phase formed by AACVD at 500 ^oC as well as the doped rutile thin films. The films were well adheared to the substrate passing the Scotch^{TM} tape test. Visually all films were translucent with an increase in coloration with increasing Cu concentration.

3.5.1 X-ray diffraction (XRD) and Raman spectroscopy

Figure 3.1 showed XRD analysis of ZrO_2 thin films with peaks that match the cubic phase of zirconia along with the standard patterns of ZrO_2. Peaks were centred at 30.3, 35.3, 50.6 and 60.3° corresponding to the (111), (200), (220) and (311) planes.[228] The ZrO_2 thin films was deposited by AACVD surprisingly matched to cubic phase because it is not common to form this phase at this temperature.

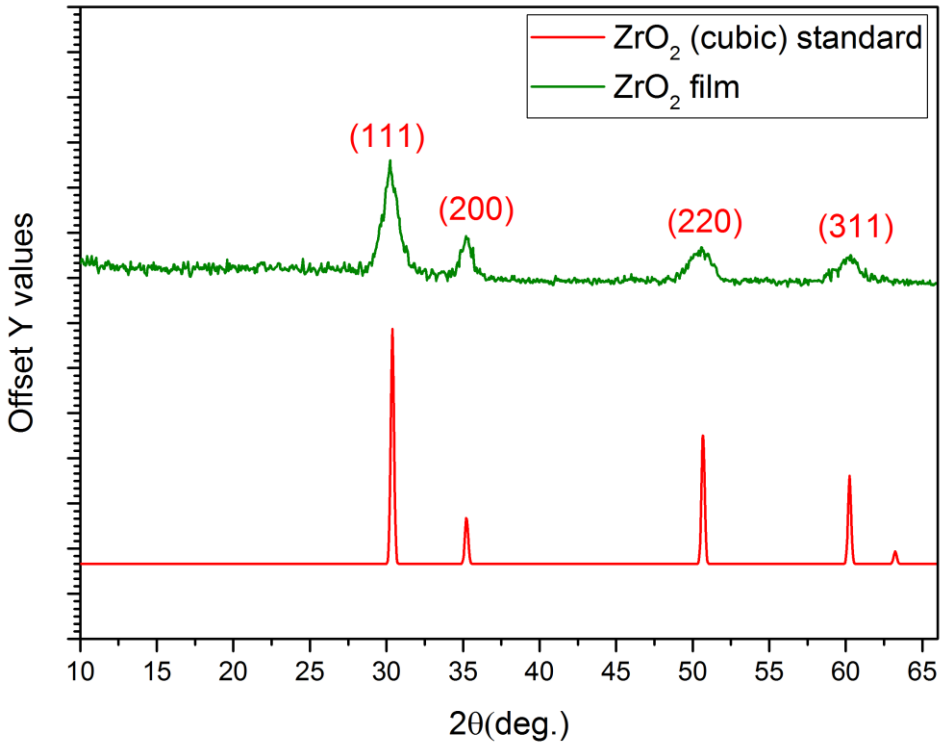

Figure 3.1 shows XRD patterns of ZrO_2 thin films grown via AACVD at 450 ºC and then annealed at 500 ºC from [$Zr(acac)_4$] in methanol. XRD show the films to be phase pure cubic.

XRD analysis of the films showed patterns with peaks that match the tetragonal rutile phase of TiO_2 **(Figure 3.2)**. Peaks were centred at 27.5, 36.1, 39.2, 41.3, 44.1, 54.3, 56.7, 62.8 and 64.1º corresponding to the (110), (101), (200), (111), (210), (211), (220) (002) and (311) planes.[229] The lack of peaks for any copper or copper oxide phases suggests the successful formation of solid solution with successful doping taking place or that a secondary copper phase was X-ray amorphous. It is important to note that due to the low thickness of the ZrO_2 under layer, no peaks are observed in the XRD.

Compared to the standard pattern (JCDPS no. 21-1276). There was no noticeable change in preferred orientation for the AACVD grown films even with Cu doping. The crystallinity,

determined by using the Deby - Scherrer equation, of the films does however change upon incorporation of Cu into the rutile lattice as evident from an increase in crystallite size from ca. 25 nm to a consistent ca. 40 nm for the doped films. This has previously been observed in previous literature examples of cation doped TiO_2 powders and films.[114, 230]

Raman spectroscopy, which unlike XRD is a surface sensitive technique, also confirms the films to be phase pure rutile **(Figure 3.2b)** with no crystalline or amorphous copper oxide phases. Three peaks were seen at 143, 447, 610 cm^{-1} corresponding to the B_{1g}, E_g, A_{1g} and B_{2g} first order fundamental modes. A broad second order scattering feature at 232 cm^{-1} was seen for the pure and 2% Cu doped films, indicating that at high concentrations of Cu in the rutile unit cell results in a suppression of this peak that results from a multi-photon process. The peak positions of all the observed first and second order peaks correlate well with literature reports.[231]

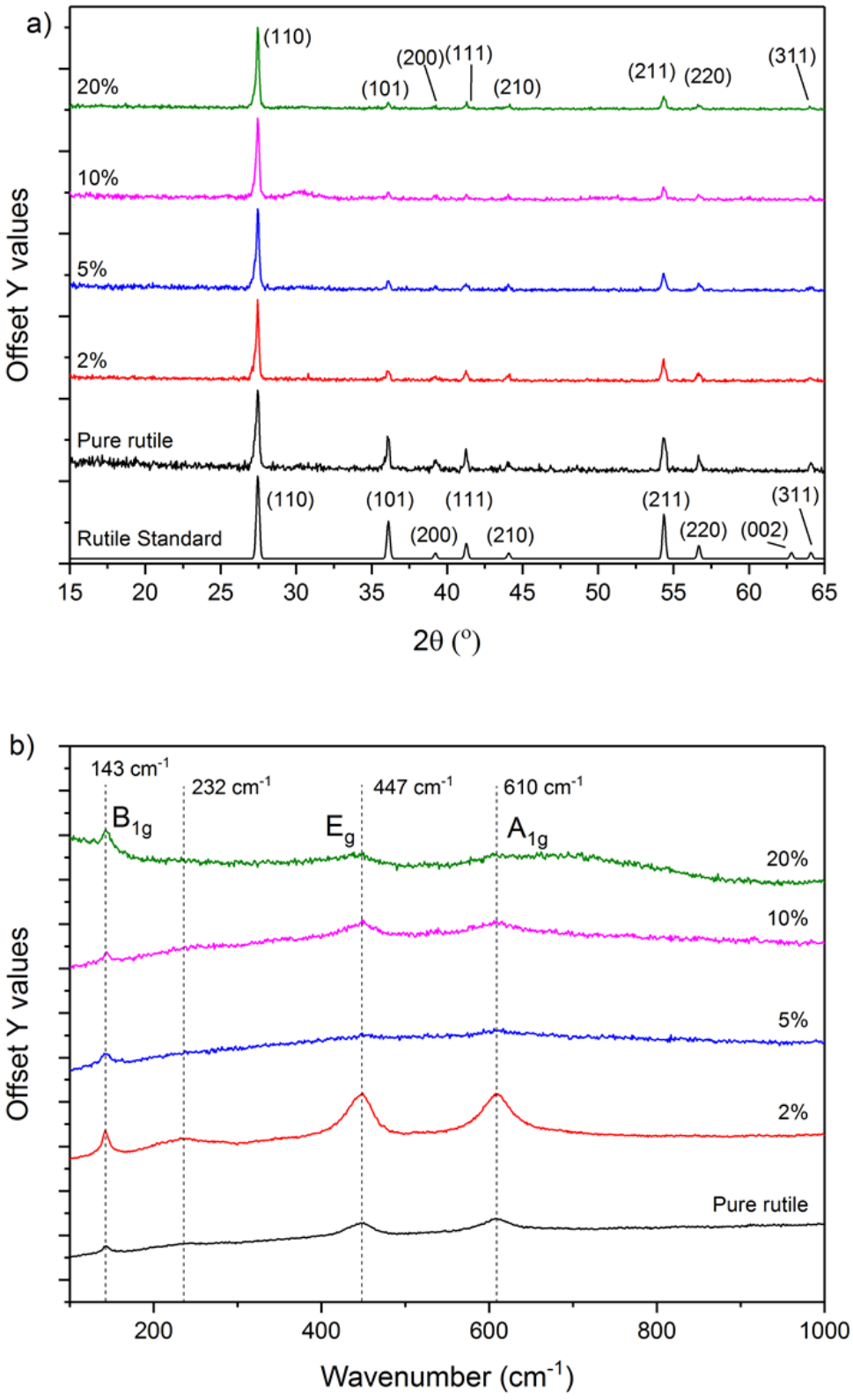

Figure 3.2: a) XRD patterns and b) Raman spectra of the pure and Cu doped rutile TiO_2 films grown via AACVD at 500 ºC. Both sets of data show the films to be phase pure rutile.

3.5.2 X-ray photoelectron spectroscopy (XPS)

Oxidation state of Zr in ZrO_2 thin films was determined by XPS spectra. Zr appeared in the 4+ oxidation state with $3d_{5/2}$ peak centred at 182.5 eV **(Figure 3.3).**[232]

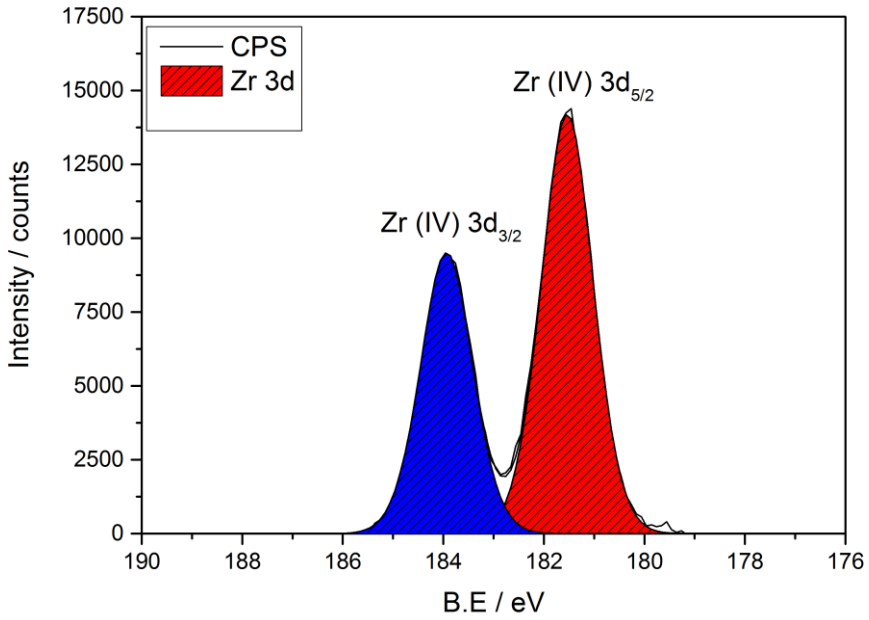

Figure 3.3 shows XPS spectra of ZrO_2 thin films grown via AACVD at 450 ºC on glass substrate

Figure 3.4a-e shows the core level XPS spectra for the prepared thin films. The Ti $2p_{3/2}$ transition was centred at 458.3 eV corresponding to Ti (IV) and this remains consistent through the different Cu doping regimes. For the 2% and 5% Cu doped sample the single to noise ratio for the Cu 2p spectra was relatively low. However modelling of the data reveals single symmetrical peaks in the $2p_{3/2}$ region at 932.8 eV (2%) and 932.7 eV (5%) indicating the presence of either Cu (0) and/or Cu (I).[233, 234] It is difficult to differentiate from Cu (0) and Cu (I) from XPS alone due to heavy peak overlap. Upon increased Cu loading at 10% and 20% the $2p_{3/2}$ peak shapes become asymmetrical and were modelled to a peak at 932.7 eV (10%)

and 932.8 eV (20%) matching to Cu (0) and/or Cu (I) and a peak at 934.8 eV (10%) and 934.4 eV (20%) assigned to Cu (II). The appearance of the satellite shake-up peaks between 940-945 eV in the XPS spectrum for the 20% sample is indicative of the presence of Cu (II). The Ti $2p_{3/2}$ peaks are generally centered at 458.3 eV and can be assigned to Ti in the 4+ oxidation state.[235] XPS spectra was used to calculate the ratio between Ti and Cu. The ratio of Ti to Cu on the surface was 77:1, 34:1, 10:1 and 4:1 for 2%, 5%, 10% and 20% suggesting surface segregation of Cu on the surface of the TiO_2 films.

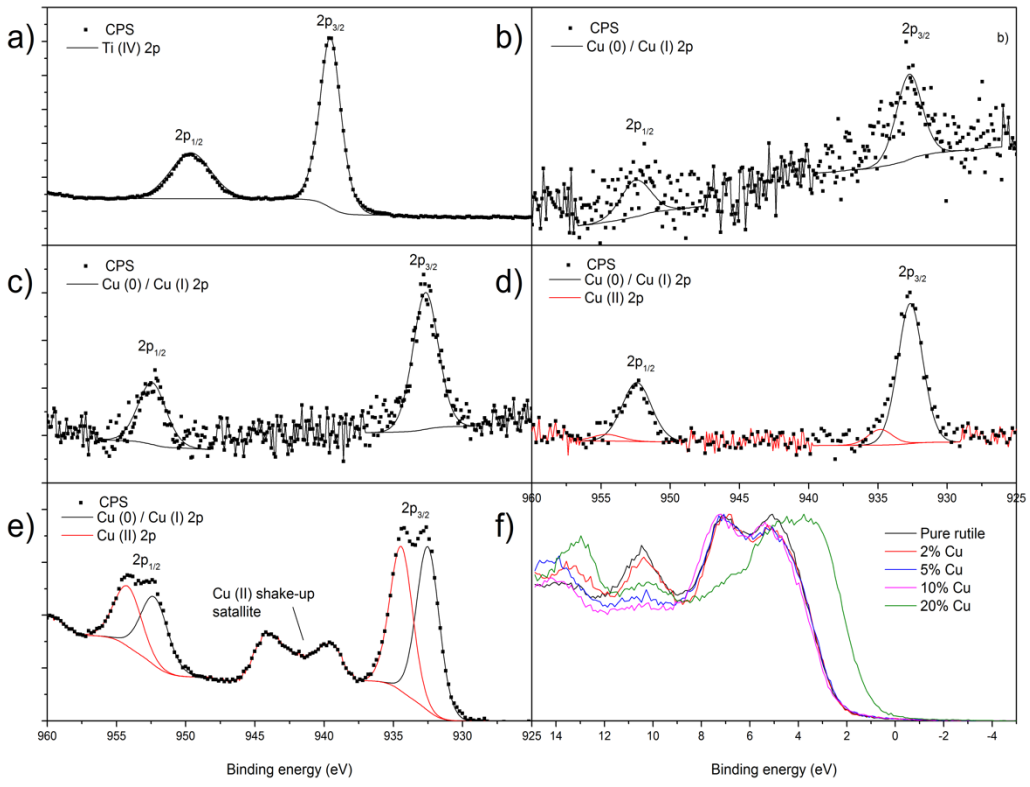

Figure 3.4: The core level XPS spectra for the a) Ti and b-e) Cu 2p transitions for the Cu doped rutile thin films. f) Shows the valence band XPS.

Figure 3.4f shows the valence band XPS spectra for the pure and Cu doped films. The O 2p derived valence band of rutile TiO_2 is broad in character (ca. 8 eV) and is itself made up of two smaller peaks at ca. 5 and 7 eV. The onset of the valence band was at 2.5 eV and was simply determined by extrapolating the leading edge of the main peak. Upon copper doping up to 10% the rutile valence band structure remains mostly unchanged but at 20% Cu the valence band is shifted to by 2 eV giving rise to the leading edge appearing at 0 eV.

3.5.3 UV-Vis spectroscopy

Figure 3.5a shows the UV-Vis transmission spectrum of rutile TiO_2 thin film, and Cu doped rutile-TiO_2 thin films at different concentrations of copper. The transparency of pure rutile-TiO_2 films is between 55 to 65 % in the visible region (360 to 800 nm) and there is a slight increase in the near infrared region (800 to 1600 nm) between 65 to reach 75 % in the (1600 to 2400 nm) there is slightly decreased from 75 to 55%. The transparency of 2 and 5% Cu doped rutile TiO_2 is increased from 25 to 40% in the visible region (350 to 800 nm) then increased in the infrared region to reach 65% at 2000 nm then slightly decreased. The lowest transparency for 20% Cu doped rutile TiO_2 is between 20 to 25% in the visible region then increased to reach 50% in the near infrared region (800 to 2400 nm).

Using the UV-Vis spectra and the Tauc method[236] the band gaps for the pure and Cu doped films were calculated to be 3.1 eV and corresponding well to literature reports for the indirect allowed transition of rutile TiO_2 **(Figure 3.5b)**.

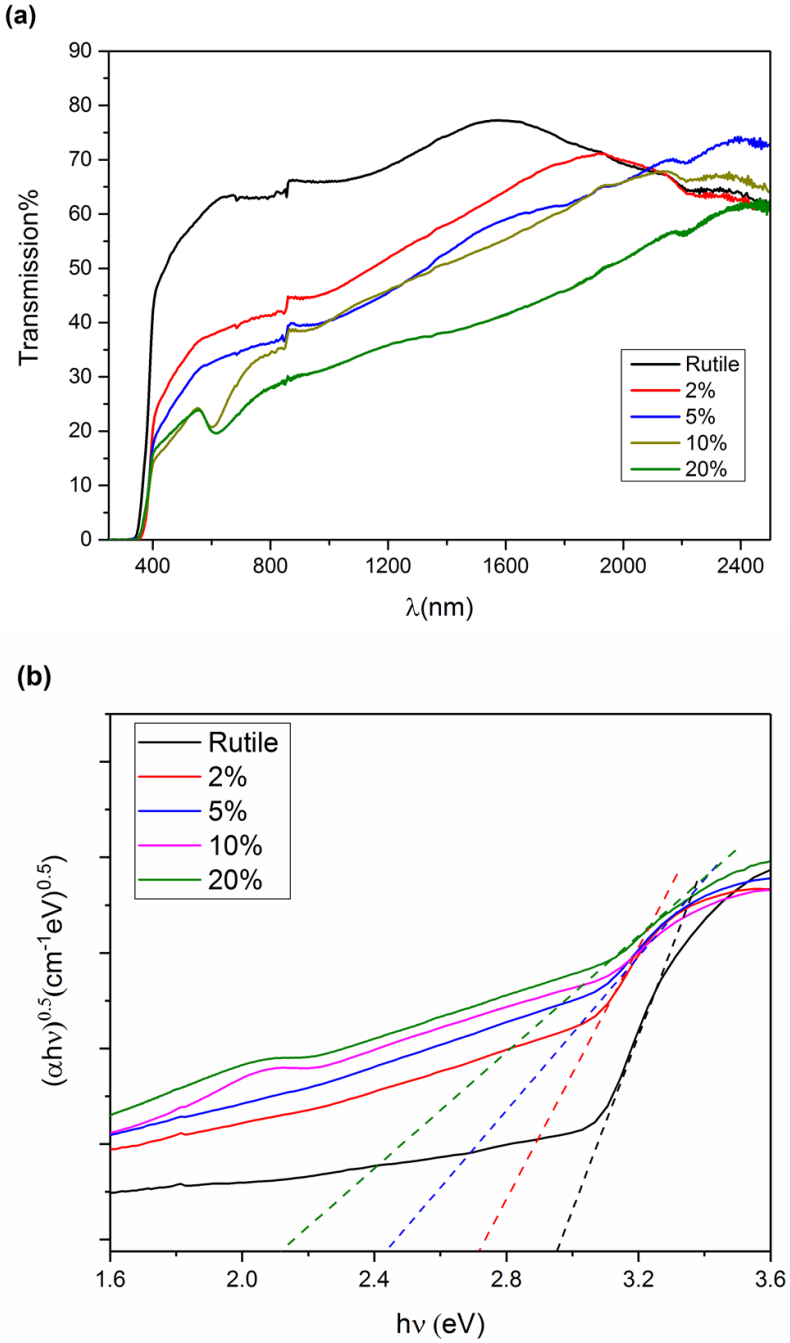

Figure 3.5: a) The UV-visible spectra a) transmission of Rutile TiO_2 and Cu doped Rutile with different concentrate of Cu, and b) corresponding Tauc plots for the pure and copper doped films grown via AACVD.

Interestingly, for the heavily doped samples, 10 and 20% Cu, an absorption peak appears at 600 and 620 nm respectively. This is too sharp to be an interference fringe that usually occurs in TiO_2 thin films that have a thickness gradient. The peak positions are indicative of surface plasmon resonance of Cu nanoparticles. Although, XRD and Raman spectroscopy showed no

presence of any phases apart from rutile in the bulk or surface small amounts of Cu nanoparticles would go undetected by these two techniques. Evidence for Cu nanoparticles on the surface of the 20% film is possibly given by both core level – peak at 932.8 eV which might correspond to Cu (0).

3.5.4 Scanning electron microscopy (SEM)

The morphology of cubic ZrO_2 thin films was studied by scanning electron microscopy (SEM) **(Figure 3.6)**. The ZrO_2 morphology consists of square-shaped particles with an average size around 100 – 300 nm **(Figure 3.6a)**. The side on micrographs reveal that the pure ZrO_2 on glass substrate and its thickness are between 160 and 250 nm **(Figure 3.6b)**.

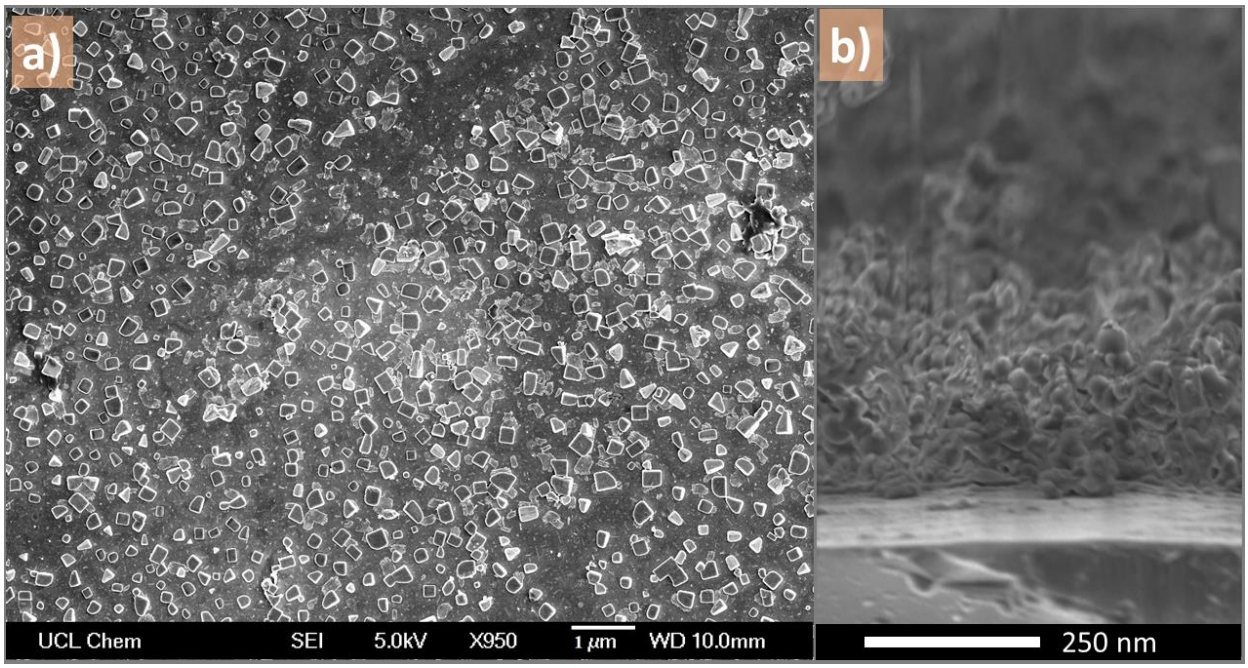

Figure 3.6 shows SEM image of ZrO_2 thin films on glass substrate and the thickness was presented by side-on SEM image.

The morphology of rutile TiO_2 thin films and Cu doped rutile-TiO_2 thin films with different copper concentrations that were deposited at 500 °C onto ZrO_2 thin films by AACVD was

investigated by scanning electron microscopy (SEM) **(Figure 3.7)**. All the films show similar morphology. SEM of pure rutile consists of pyramidal features of TiO_2 ranging from 100 to 500 nm in size protruding from the substrate. With increasing Cu concentration the features coalesce together where at 20% Cu film an over layer is present. The side on micrographs reveal the layered nature of the film with the ZrO_2 seeding layer being ca. 150 nm in thickness while the rutile layers above are between 300 and 400 nm.

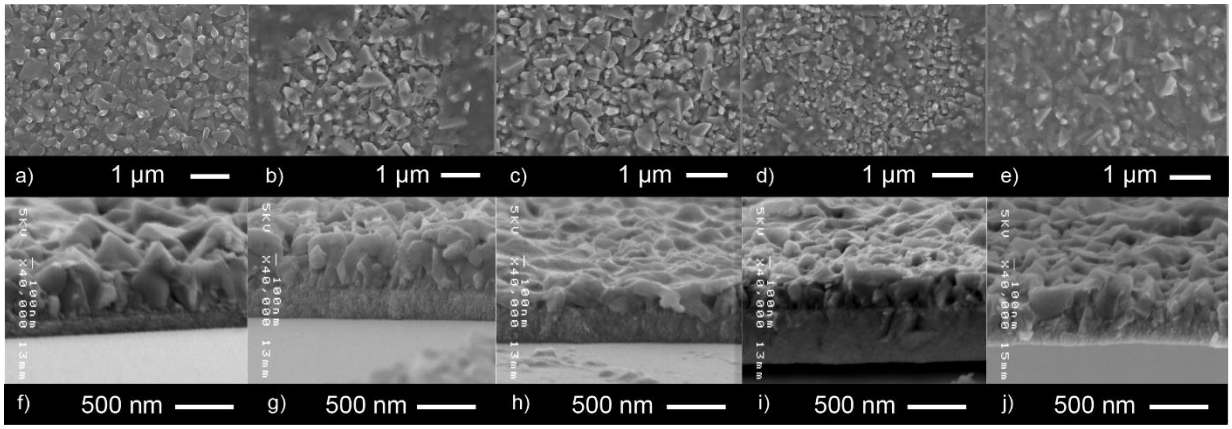

Figure 3.7: SEM images of the A) pure Rutile, (B),(C),(D) and (E) Cu dopedTiO_2 thin film at different copper concentrations (2,5,10 and 20% respectively). The thickness was presented by side-on SEM images.

3.5.5 UV-visible measurements (UV-Vis) for SPR

UV-Vis absorption spectroscopy was used to study surface plasmon resonance (SPR) of Cu doped TiO_2 thin films. **Figure 3.8**, illustrates the absorption of the Cu doped TiO_2 thin films that were prepared by AACVD on the ZrO_2 thin films as substrate from different copper concentrations (2, 5, 10 and 20%). SPR peaks appear with 10 and 20% Cu doped TiO_2 thin films at ~ 613 and ~ 629.5nm respectively **(Figure 3.8)**. The peak positions were shifted towards the red region for the peaks SPR due to increase of Cu concentration and also contribute to the average size of Cu:TiO_2. The pure rutile TiO_2 and copper concentrations (2 and 5%) did not show signals in the 500–800 nm region for SPR peaks. However, Jong Min

Kum and et al found the SPR peak is located at 450 nm and they found that the surface plasmon resonance (SPR) enhanced of photocatalysts of Cu/TiO_2 NPs of water splitting under visible light compared with pure TiO_2 NPs.[237] The shift in the SPR peak position towered the red region in the UV-Vis spectrum was observed when the concentration of copper ion increased into Ag-Cu NPs.[238] Yeshchenko found that the SPR of Cu nanoparticles embedded in SiO_2 glass were located at 570-580 nm and SPR peak shifted towards the red region with temperature they also rated a shift that depends on the temperature as well as particles size of the Cu NPs.[239]

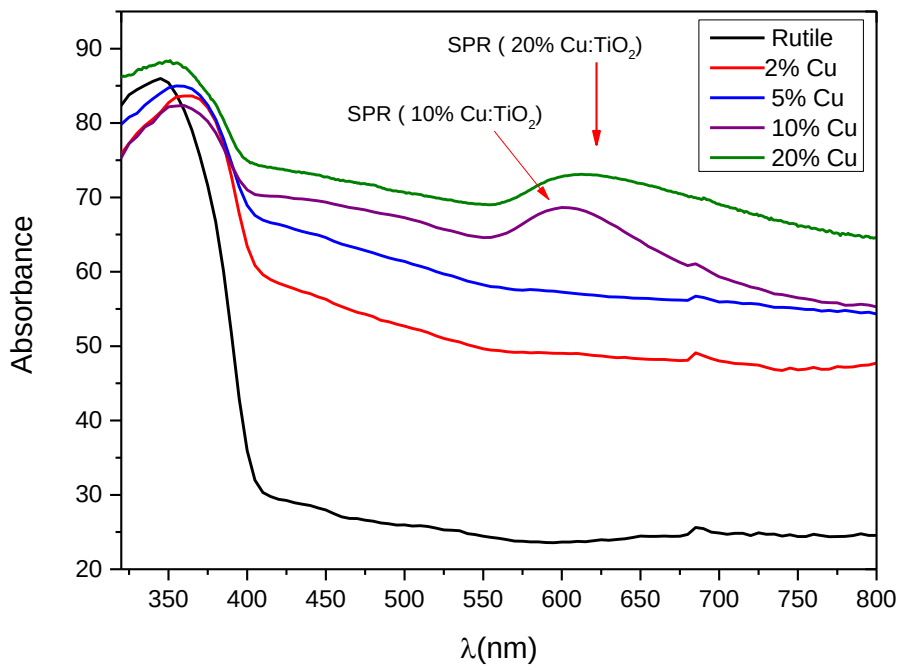

Figure 3.8: shows UV-Vis, Absorbance of Rutile TiO_2 and Cu doped Rutile with different amount of Cu. All films were deposited onto ZrO_2 thin films at 500 by AACVD from Titanium butoxide and $Cu(NO_3)_2 3H_2O$ as precursors, the films at initial copper concentration (10 and 20%) exhibited SPR peaks at ~ 613 and 629.5 respectively.

3.6 Functional testing

3.6.1 Photocatalytic activity

The photocatalytic activity of rutile-TiO_2, 2, 5, 10 and 20% Cu doped rutile-TiO_2 thin films were investigated under the same conditions by degradation of stearic acid. Prior to the photocatalysis test the samples were cleaned by distilled water rinsed in isopropanol and acetone and placed under UV (254 nm) irradiation for 30 minutes to activate the surface. The white light was used to induce a photoreduction reaction of un-doped and Cu doped rutile TiO_2 thin films and was observed by FT-IR in the region 2950 to 2850 cm^{-1} for the peaks, 2958 cm^{-1} C-H stretch (CH_3), 2923 cm^{-1}stretch (CH_2) and 2853 cm^{-1} stretch C-H (CH). The samples were dipped into stearic acid solution (0.05 M) then withdraw by dip coating apparatus at a steady rate 130 cm min^{-1} then the samples were left to dry overnight. All samples were examined under white light. Optivex was used to prevent UV light to that comes from the white light. **Figure 3.9**, illustrates the spectral distribution diagram for the white light lamp used in the photocatalytic test.

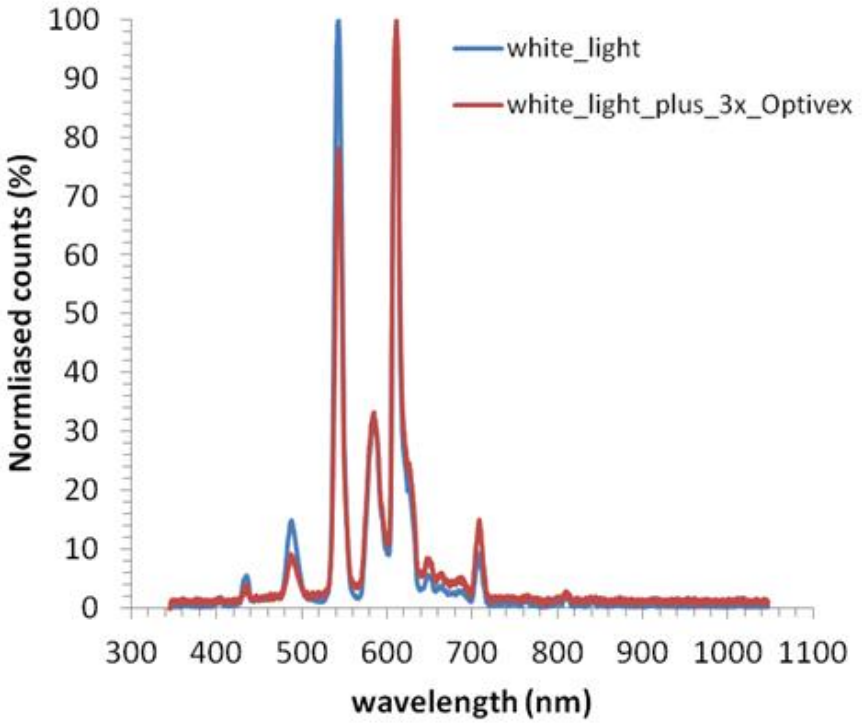

Figure 3.9 shows the spectral power distribution chart for the lamp of white light source

The rate of degradation of pure rutile-TiO_2 and Cu doped rutile TiO_2 thin films at different initial copper concentrations were compared. The overall photocatalytic activity of stearic acid can be summarised as follows:

$$CH_3(CH_2)_{16}CO_2H + 26O_2 \xrightarrow{TiO_2(h\nu \geq Eg)} 18CO_2 + 18H_2O \qquad (3.1)$$

During the photocatalytic activity, the degradation of stearic acid FT-IR peaks can be used to assess the number of molecules of stearic acid following Mills et al report.[176] Mills estimated that 9.7×10^{15} molecules of stearic acid correspond to 1 cm^{-1} of integrated area. The degradation rates of stearic acid are estimated from linear regression of the initial 30-40% drop in integrated area versus irradiation time. Hence 1 cm^{-1} of integrated area correspond to 9.7×10^{15} molecules

Figure (3.10) shows the rate of degradation of stearic acid onto the thin films by white light and the experiment was read over 197 hours. However, the rate of degradation increased with

copper concentrate starting from 2% to 20 % and the highest degradation was seen for the 20% Cu doped rutile-TiO_2 thin film followed by 10% Cu **(Figure 3.10 and 3.11)**. These results are in agreement with the UV-Vis spectra, due to the surface plasmon resonance (SPR) the films at initial concentration (10 and 20%) exhibit good photocatalytic activity of degradation of Stearic acid under visible light.

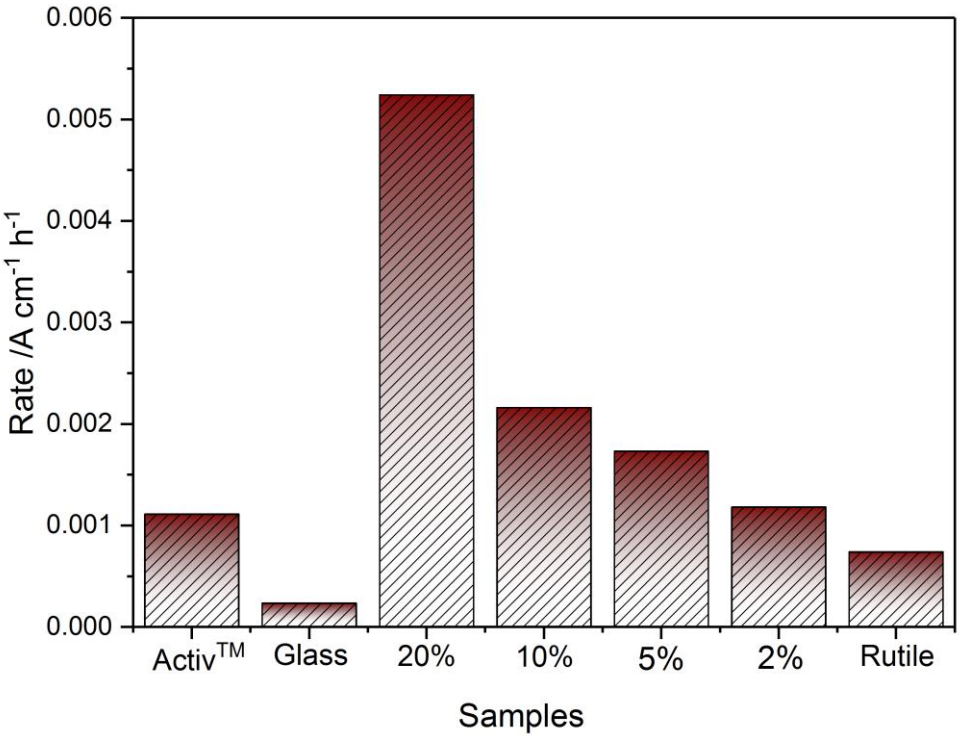

Figure 3.10 illustrates the rate of degradation of stearic acid on the surface of Rutile, and Cu doped Rutile TiO_2 films at different concentration of copper by white light

The photocatalytic activities of the as-synthesised were evaluated against the degradation of a model organic pollutant, octadecanoic (stearic) acid, under ultraviolet (UVA) illumination (*I*= 3.15 mW cm^{-2}) as well. Its photocatalytic degradation can be monitored following the disappearance of characteristic C-H modes at 2958, 2923 and 2853 cm^{-1}. **Figure (3.11a)** shows

the photocatalytic activity under UV-365 nm. The corresponding rates were expressed as formal quantum efficiencies (FQE) (**Figure 3.11b**), defined as molecules of stearic acid degraded over incident photons (units, molecule × photon^{-1}). Rutile TiO_2 thin film showed a destruction rate of 7.4 x 10^{-4} molecules photon^{-1}, upon doping the 5% and 10% of Cu the rate increases to 5.6 x 10^{-3} molecules photon^{-1} and 2.0 x 10^{-3} molecules photon^{-1} (a higher rate than Activ^{TM}, 1.0 x 10^{-3} molecules photon^{-1}) respectively. At concentrations of Cu (2% and 20%) the stearic acid destruction rate decreases to 1.8 x 10^{-3} molecules. photon^{-1} and 2.5 x 10^{-4} molecules. photon^{-1} respectively. This improvement in photocatalytic properties could be correlated directly with photo-generated charge carrier lifetimes as dopant species act as electron traps. Transient absorption spectroscopy (TAS) was used to investigate charge carrier recombination in these films but unfortunately could not get reliable results as the samples have low transparency (less than 40%), making observation difficult.

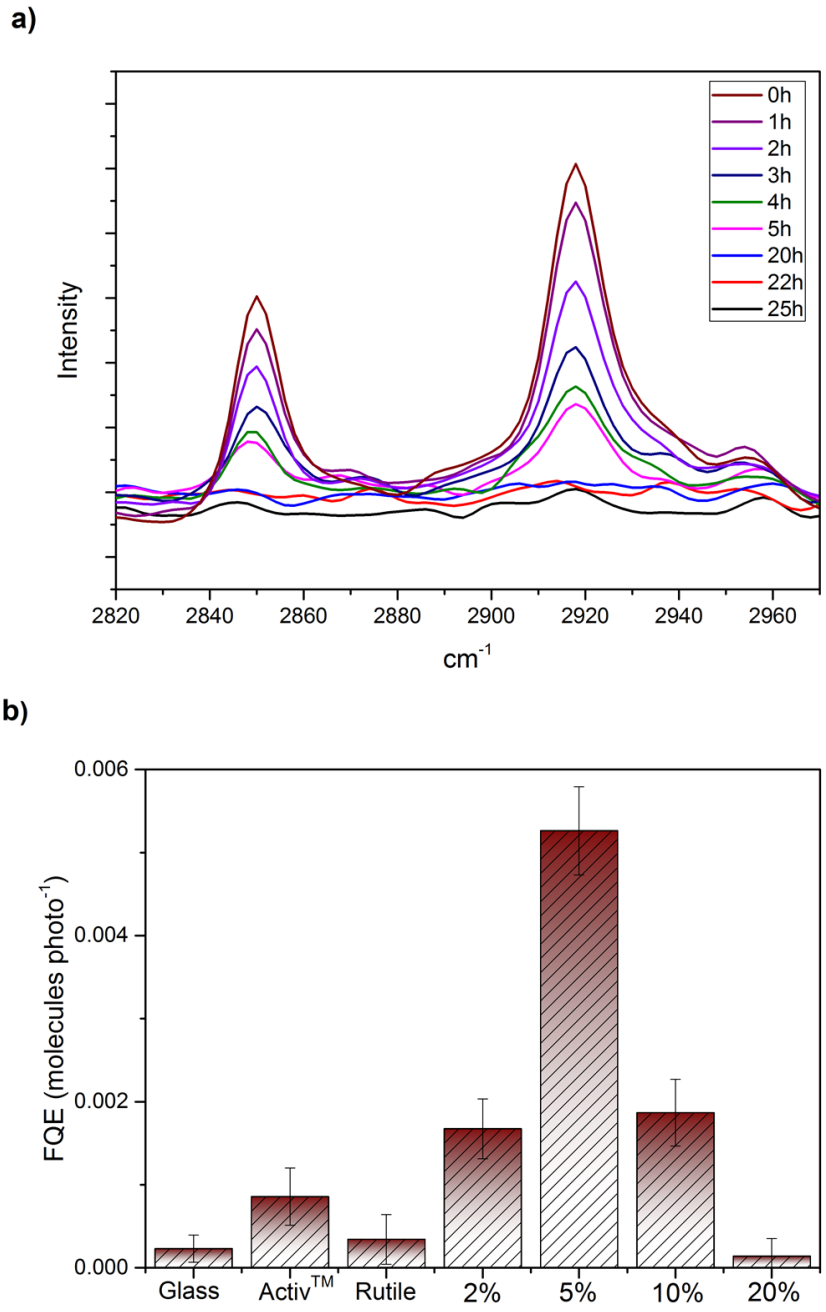

Figure 3.11: shows a) the degradation of stearic acid on the surface of 5% Cu doped TiO_2 thin film b) the formal quantum efficiencies for the destruction of stearic acid on Cu doped r-TiO_2 thin films at different copper concentration by UVA irradiation for 25 hours.

3.7 Photoinduced Wettability

Water drop contact angle of rutile TiO_2 films and series of Cu doped TiO_2 films are shown in **Figure 3.12** . Further, Water conatact angle was measured before and after UVA irradiation for 10 h using 5 µl droplet of water on the samples (flux = 3.67 10^{14} photons per cm^2 per s). A significat change in water contact angle was obsreved after Cu doping. Pure rutile TiO_2 showed water contact angle is 74° pre-irradiation **(Fig.3.12 a)**. Upon doping the 5% and 10% of Cu the water contact angle increases to 96 and 88° respectivily (Fig.10, c and d). At concentation of Cu (2 and 20%) the water contact angle is smiliar to pure rutile (Fig.10, b and e). On the other hand, post irradiation for 10 h, there was decreased in water contact angle as shown in (Figure 10, f-j). A significant change was observed with 2% Cu doped TiO_2 thin films, which is a superhydrophilic film was achieved, water contact angle is (> 3°) **(Figure 3.12 g).**

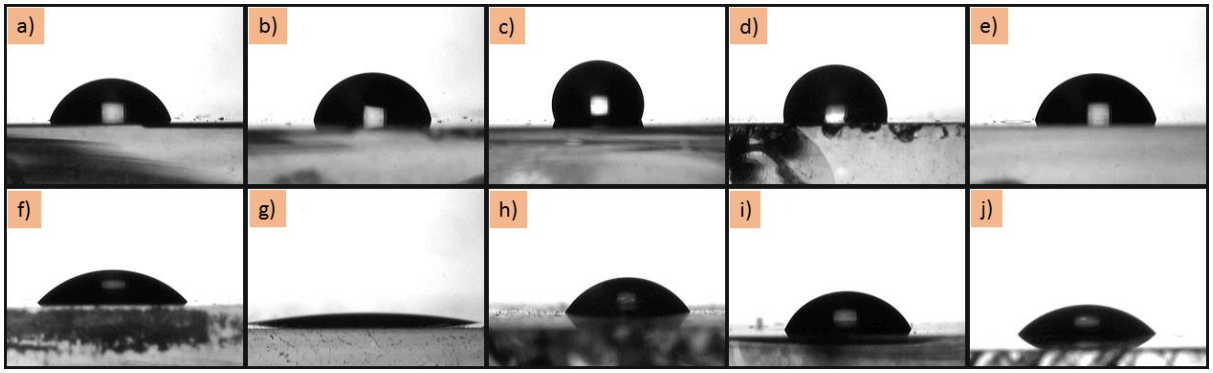

Figure 3.12: Water contact angle of pre-irradiation a) rutile TiO_2 and (b, c, d and e) Cu dopedTiO_2 thin film at different copper concentrations (2, 5, 10 and 20% respectively). Post irradiation with UVA radiation f) rutile TiO_2 thin film and (g, h, i and j) Cu dopedTiO_2 thin film at different copper concentrations (2, 5, 10 and 20% respectively).

3.8 Conclusion

ZrO_2 thin film was deposited on a glass substrate for the first time by AACVD at 450 °C using $[Zr(acac)_4]$ as a precursor. This film showed pure cubic-phase and high transparency compared with pure rutile TiO_2 thin films.

On the other hand, TiO_2 thin films in the pure rutile phase and Cu doped rutile TiO_2 were prepared by AACVD at low temperature (500 °C) onto ZrO_2 thin film as a substrate. Photocatalytic activity of all films was investigated by degradation of stearic acid under UVA and white light.

All films exhibited photocatalytic activity under white light and UVA. The 20% Cu doped rutile TiO_2 thin films shows high activity in the visible light and could be due to surface plasmon resonance (SPR) and 5% Cu doped rutile TiO_2 thin films shows high activity under UV light.

In the following chapter, AACVD will be used to prepare brookite TiO_2 thin films. Photocatalytic activity of brookite TiO_2 thin films well be investigated by degradation of stearic acid as model of photocatalytic activity. Transient absorption spectroscopy will be used to investigate charge carrier lifetime.

Chapter 4

Pure brookite thin films obtained via aerosol-assisted chemical vapour deposition

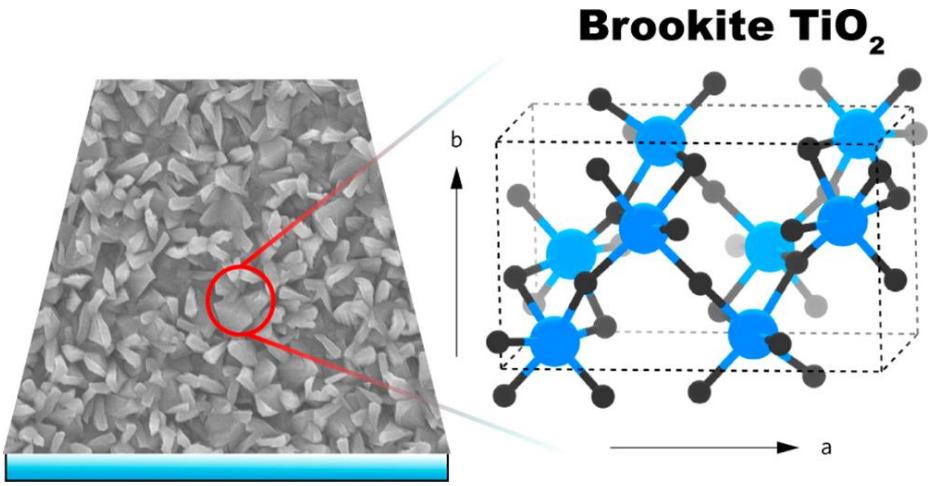

*In this chapter, the results of experiments exploring the deposition of brookite TiO_2 films on a glass substrate using aerosol-assisted chemical vapour deposition (AACVD) are presented; the pure brookite films were determined using Raman spectra and X-*ray diffraction. *The photocatalytic properties of brookite were examined using stearic acid under UVA (365 nm) irradiation, and superior photocatalytic activity was exhibited compared with the anatase form. The direct band gaps of brookite were calculated using the Tuc plot and shown to be 3.4 eV. Transient absorption spectroscopy (TAS) was used for investigating the innate hole−electron recombination dynamics in brookite and anatase form in a methanol and argon atmosphere.*

Cover image for chapter 4

SEM image of brookite TiO_2 film that was deposited by AACVD matched with unit cell brookite TiO_2. Ti atoms are represented in blue and O atoms are represented in dark grey. This image is reused with permission from our paper. Chemistry of Material. 2018, 30, 1353−1361. © 2018, American Chemical Society.

Chapter 4 figures

All figures in this chapter except Figure 4.3 are reused with permission from Ref. A. M. Alotaibi et al., Chemistry of Material. 2018, 30, 1353−1361. © 2018, American Chemical Society.

4.1 Introduction

As previously mentioned, titanium dioxide (TiO_2) has three crystal structures, namely the rutile, anatase and brookite forms. The rutile (tetragonal) form is considered thermodynamically stable compared with the other forms. The brookite (orthorhombic) and anatase (tetragonal) structures are almost metastable; the anatase and brookite phases are easily transferred to the rutile phase at high temperatures (>950°C).[205, 240] The importance of TiO_2 arises from its use in a wide range of applications, such as water purification via the photocatalytic degradation of organic compounds, water splitting and killing bacteria.[19, 205] Furthermore, TiO_2 is well known, as it is the most widely investigated photocatalyst particularly in the anatase structure; further, it is stable, mechanically robust, chemically inert, environmentally friendly and naturally abundant.[28, 141] In addition, the anatase and rutile forms are easy to prepare. Hence, these two forms have been synthesised in both structures for thin films and powders using numerous preparation methods.[241] Comparing between the different forms concerning the photocatalyst, a wide range of studies have reported that the anatase form typically has more photocatalytic activity than the rutile form does.[241-243] There have still been relatively few studies on the brookite form, but some reports have mentioned that the brookite phase exhibits more activity than the anatase phase does. In contrast, other studies have stated that the brookite phase is inactive under UV irradiation for some photocatalytic degradations, such as the degradation of some dyes.[244-247]

It is clear from the discussion above that the photocatalytic process of the brookite phase is still a contested issue. This lack of consensus also relates to the difficulty of preparing pure brookite in both the film and powder phases. While the indirect band gaps of anatase and rutile are 3.2 and 3.0 eV, respectively, the band gap value of the brookite phase is not accurately known.[244-248] However, Some studies reported that the band gape of brookite range from 3.1 to 3.4 eV.[249]

Recently, the interest in the brookite form has risen dramatically, and it has been identified as a promising candidate for photocatalytic applications. **Figure 4.1** shows the number of papers published on the pure and mixed brookite forms from 2000 to 2017. This number exhibits a remarkable increase in interest in brookite. Most of the papers focussed on the preparation methods and some photocatalytic applications.

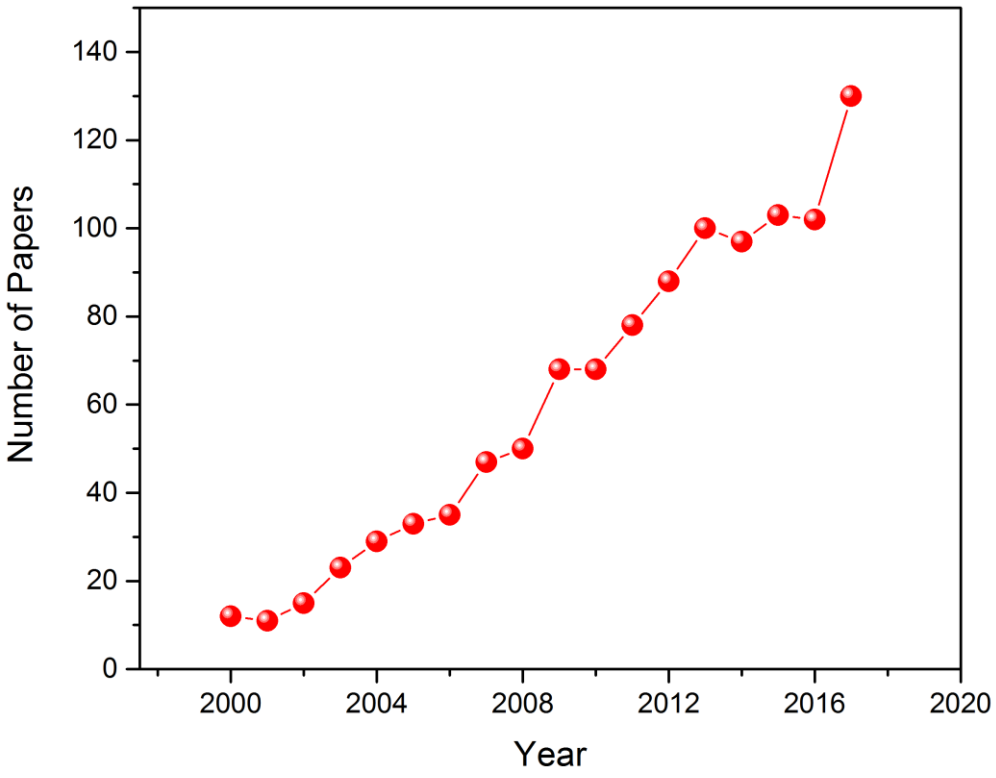

Figure 4.1 Number of papers published on the brookite phase in 2000–2017. The data were obtained from the ISI Web of Knowledge database on 10 September 2018.

The most common methods that have been used for the synthesis of the brookite form in the structure of films and powders are hydrothermal treatments with titanium precursors in organic or aqueous medium at a high pressure and temperature.[250] To the best of our knowledge, the first paper on the synthesis of pure brookite was published in 1950s.[251] Since then, many efforts

have been made to control the pure and mixed phases of brookite with another phase, such as anatase or rutile.

Recently, brookite TiO_2 thin films have been prepared by atomic layer deposition (ALD) on an yttria-stabilised zirconia (YSZ) substrate.[252] Another attempt was made to obtain brookite thin films via pulsed laser deposition (PLD), and a high fraction (95%) of brookite thin films was obtained by this method.[253]

In this chapter, we lay the foundations for a facile route of obtaining pure brookite TiO_2 thin films using aerosol-assisted chemical vapour deposition (AACVD). The phase purity of brookite films was determined by Raman spectroscopy and XRD. Both pure brookite and anatase films were prepared via AACVD, and their photocatalytic activity to the degradation of a model organic pollutant and stearic acid were examined under UVA (365 nm) radiation and compared using a commercial self-cleaning NSG Activ coating as reference. Transient absorption spectroscopy (TAS) was used to study the kinetics of the charge carrier recombination in brookite and anatase using methanol as a hole scavenger.

4.2 Experimental Section

Titanium butoxide and methanol were purchased from Sigma-Aldrich Chemical Co. and used as received. Deposition was carried out on a 150 × 45 × 45 mm SiO_2 (50 nm) coated float glass supplied by Pilkington NSG. (The SiO_2 acts as a barrier layer preventing diffusion of ions from within the glass into the deposited film). Prior to use, the glass substrates were thoroughly cleaned with acetone (99%), isopropanol (99.9%) and distilled water and dried in air.

4.2.1 Deposition procedure

For the deposition procedure, 0.5 g (1.46 mmol) of titanium butoxide [$Ti(OCH_2CH_2CH_2CH_3)_4$] (99%) was dissolved in 20 mL of methanol and put in a glass bubbler under N_2 (BOC Ltd., 99.99% purity). The resulting solution was atomised using a piezoelectric device (Johnson Matthey Liquifog®). The precursor flow was kept at 1.4 $L.min^{-1}$. The substrate temperature was 550°C. After the precursor solution was transferred to the reactor using nitrogen (BOC Ltd., 99.99%), the bubblers were closed and the substrate cooled to less than 100°C under a flow of N_2 before the substrate was removed. Coated substrates were handled and stored in air. The coated glass substrate was cut to squares of approximately 2 × 2 cm for subsequent analysis. The film was annealed at 500°C in the air to remove carbon contamination. Anatase phase was deposited by AACVD and titanium isopropoxide [$Ti(OCH(CH_3)_2)_4$] (0.5 g, 1.76mmol) was dissolved in ethyl acetate (30 ml) in a glass bubbler at 470 °C.

4.2.2 Computational Section

Hybrid density functional theory (HDFT) simulation was calculated using the Vienna ab initio simulation package (VASP)[177-180] on the structure and electronic properties of brookite TiO_2 *(Pbca)*. Hybrid functional theory is well known to accurately describe and predict the electronic structures and compare these simulations with experimental results.[254-260]

Calculations of the structure and electronic properties of TiO_2 polymorphs was carried out by the Heyd–Scuzeria–Ernzerhoff functional (HSE06).[182, 198, 261-265] The aim of HSE06 is to fix the self-interaction error (SIE) immanent to standard functionals. The exchange interaction can be divided into two parts, namely 1) the short-range (SR) and 2) the long-range (LR) parts, with 25% of the exact nonlocal Fock exchange substituting the SR Perdew−Burke−Ernzerhoff (PBE) functional.[266]

The Coulomb potential can be divided into two parts, namely the SR and LR parts, using a screening factor of 0.207 $Å^{-1}$, as follows:

$$E_{xc}^{HSE0} = E_x^{HSE06,SR} + E_x^{PBE,LR} + E_c^{PBE} \quad 4.1$$

where

$$E_x^{HSE06,SR} = \frac{1}{4}E_x^{Fock,SR} + \frac{3}{4}E_x^{PBE,SR} \quad 4.2$$

The valence band of brookite TiO_2 obtained by XPS was simulated using the atomic orbital photoionisation cross-sections explored by Lindau and Yeh and using weighting of the calculated DOS. In addition, a Gaussian broadening of 0.47 eV was employed to match the experimental broadening. This process showed accurate calculations of the electronic states that formed the XPS data.[171, 257, 267-269]

4.2.3 Photocatalytic activity

The photocatalytic activity was measured by monitoring the photocatalytic decomposition of a model organic pollutant, stearic acid (95%, Sigma-Aldrich). To measure the photocatalytic decomposition of a stearic acid coating, samples were attached to an IR sample holder consisting of an aluminium sheet with a circular hole in the middle. The stearic acid coating was applied from a saturated solution of stearic acid in chloroform (0.05 M) through a dip-coating process. Pilkington NSG Activ™ glass was used as a benchmark and blank float glass as a control. The breakdown of the C–H bonds in stearic acid was measured using FTIR between 2800 and 3000 cm^{-1} with a PerkinElmer Spectrum RX1 FTIR spectrometer.

Measurements were taken at the intervals of 0, 15, 30, 45, 60, 75, 90, 115, 130, 145, 160, 175 and 190 min with the samples irradiated using a 365-nm UVA lamp.

The C–H bonds in stearic acid absorb at 2958 cm^{-1} (C−H stretch CH_3), 2923 cm^{-1} (symmetric C−H stretch CH_2) and 2853 cm^{-1} (asymmetric C−H stretch CH_2). These peaks can be integrated to give an approximate concentration of stearic acid on the surface using a calibration constant, where 1 $A.cm^{-1}$ in the integrated area between 2800 and 3000 cm^{-1} corresponds to approximately 9.7 × 1015 molecules cm^{-2}).[176] Thus, the rate of removal of stearic acid can be measured by monitoring the decrease in IR absorbance. The results are typically expressed in terms of the formal quantum efficiency (FQE), defined as the number of molecules degraded per incident photon (units, molecule × $photon^{-1}$). The light source was a black light-bulb (BLB) lamp, 2 × 8 W (Vilmer-Lourmat). The irradiance of the lamp (I = 3.15 mW cm^{-2}) was measured using a UVX radiometer (UVP).

4.2.4 Transient absorption spectroscopy (TAS)

TAS was used to determine exciton lifetimes at room temperature (~22°C) from the microsecond to second timescale; it was performed in either diffuse reflection or transmission. The brookite form was investigated in the diffuse reflection mode because brookite is highly scattering; the anatase form was assessed in the transmission mode, as anatase is highly transparent.

As mentioned in Chapter 2, samples were excited using pulsed laser excitation (λ = 355 nm, Opolette 355, pulse width = 6 ns, pulse repetition = 0.8 Hz, laser power = 1.55 $mJ.cm^{-2}$) using a liquid light guide. A quartz halogen lamp (100 W, Bentham, IL 1) with a stabilised power supply (Bentham, 605) was used as the probe light source. To reduce stray light, scattered light

and sample emission, two monochromators and appropriate optical cut-off filters were placed before and after the sample.

The probe light passing through the sample was detected using a Si photodiode (Hamamatsu Photonics, S1722-01). This signal was passed through an amplifier (Costronics Electronics) and then measured using a digital oscilloscope. Decays presented are the average of 100−200 laser pulses. Samples were measured inside a gas-tight quartz cell under an argon gas atmosphere or methanol degassed with argon. Because the changes of photo-induced reflectance/transmittance were low (1.0%), it was assumed that the concentration of excited species was directly proportional to the transient signal.

4.3 Results and Discussion

Pure brookite TiO_2 thin films were prepared by AACVD at 550°C on a glass substrate using titanium butoxide and methanol as precursors. It is worth mentioning that methanol is used not only as a solvent for generating the aerosol, but it also has a significant role in the formation of active reagents in AACVD reactions. It was found that deposition of TiO_2 by AACVD under the same conditions, but using different solvents, such as ethylacetate, hexane, toluene and ethanol, generated the anatase form at 550°C. Unexpected results have been found when methanol is used to deposit the films by AACVD. For example, Crick and Parkin[270] deposited metallic Cu films from copper nitrate by AACVD when they used methanol, whereas, when they used other solvents, such as ethanol, they obtained Cu_2O and $Cu-Cu_2O$ composite films. They ascribe this to the 'in situ' production of hydrogen catalysed by the copper thin films. As mentioned above, most brookite phase TiO_2 has been prepared using hydrothermal processes, and the mechanisms of preparation are still under debate. Some studies have mentioned that specific acidic and basic conditions are extremely important for brookite preparation.[271-273]

From our AACVD results, we can suggest that, in the presence of acidic conditions, the use of a methanol solvent may help to form the pure brookite phase. Here, the brookite TiO_2 film was hazy due to its nanostructure; moreover, it exhibited excellent coverage and adhered well to the substrate, passing the Scotch tape test.[190]

The PXRD pattern indicated an orthorhombic brookite phase with high crystallinity **(Figure 4.2)**. All diffraction peaks matched well with the standard diffraction data of the brookite TiO_2 crystal structure (JCPDS No. 29-1360). The diffraction patterns for the (210) plane overlapped with the (111) plane at 2θ values of 25.3 and 25.7°, while the diffraction patterns for the (221), (102), (021), (202), (302), (321) and (312) planes did so at 2θ values of 30.8, 36.24, 37.3, 40.0, 42.5, 46.0, 48.1 and 49.1°, respectively **(Figure 4.2a)**. In contrast, the anatase films showed diffraction patterns for the (101), (004), (200), (105), (211) and (204) planes at 2θ values of 25.1, 38.6, 48.0, 54.3, 55.1 and 62.7°, respectively **(Figure 4.2b)**.

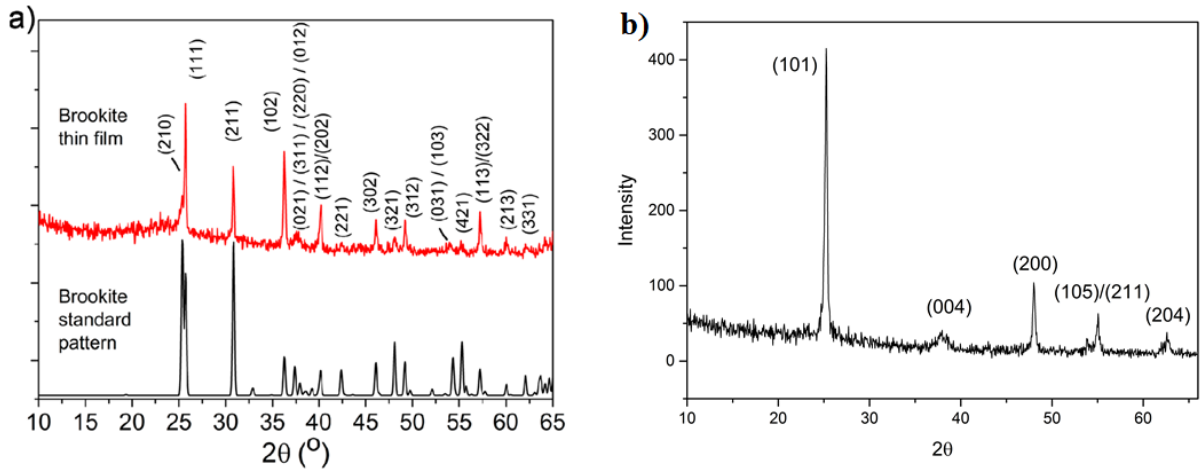

Figure 4.2 XRD patterns of (a) the brookite phase and (b) anatase phase grown by AACVD on glass substrates. Brookite phase was deposited using titanium butoxide [$Ti(OCH_2CH_2CH_2CH_3)_4$] in methanol at 550 °C and anatase phase was deposited using titanium isopropoxide [$Ti(OCH(CH_3)_2)_4$] in ethyl acetate at 470 °C

As shown in **Table 4.1**, there is an excellent agreement between the calculated HSE06 results for the lattice parameters and literature results (<0.4% difference). The lattice parameters of brookite TiO_2 were calculated by HSE06, and the experimental results are illustrated in parentheses.

Table 4.1, Structural Parameters of Brookite Calculated by HSE06

	a (Å)	**b (Å)**	**c (Å)**	**α = β = γ (o)**
TiO_2	9.21 (9.17)	5.46 (5.44)	5.15 (5.14)	90 (90)

It should be noted that the brookite phase has (210) and (111) reflections at 2θ values of 25.25° and 25.72°, and these reflections overlap with the anatase (101) reflection at a 2θ value of 25.25°.[250] Accordingly, it may be difficult to use only XRD to determine the purity of brookite. Therefore, the use of Raman spectroscopy is necessary for confirming and removing any doubt about the purity of brookite deposited by AACVD, as Raman spectroscopy is a sensitive technique for investigating the presence of the brookite phase. As shown in **Figure 4.3a**, the Raman spectrum of brookite revealed 15 vibrational bands at 125.7, 151.1, 170.2, 192.6, 211.9, 244.3, 284.5, 319.5, 365, 410, 458.1, 501.5, 540.4, 581.0 and 636.5 cm^{-1}, which are related to the four (A_{1g}, B_{1g}, B_{2g} and B_{3g}) modes.[274] No peaks were observed for the rutile or anatase phase. In an attempt to prove the brookite form and avoid any doubt, the main peak of brookite (A_{1g}) was modelled to obtain an accurate peak position, which was observed at 151.00 cm^{-1}. There is an excellent agreement between this value and the literature results for the brookite principle (A_{1g}) band at 152 cm^{-1}.[275] Although this value is close, it is quite different from the nearest value to the anatase band (E_g)[276] at 141 cm^{-1} **(Figure 4.3b)**.

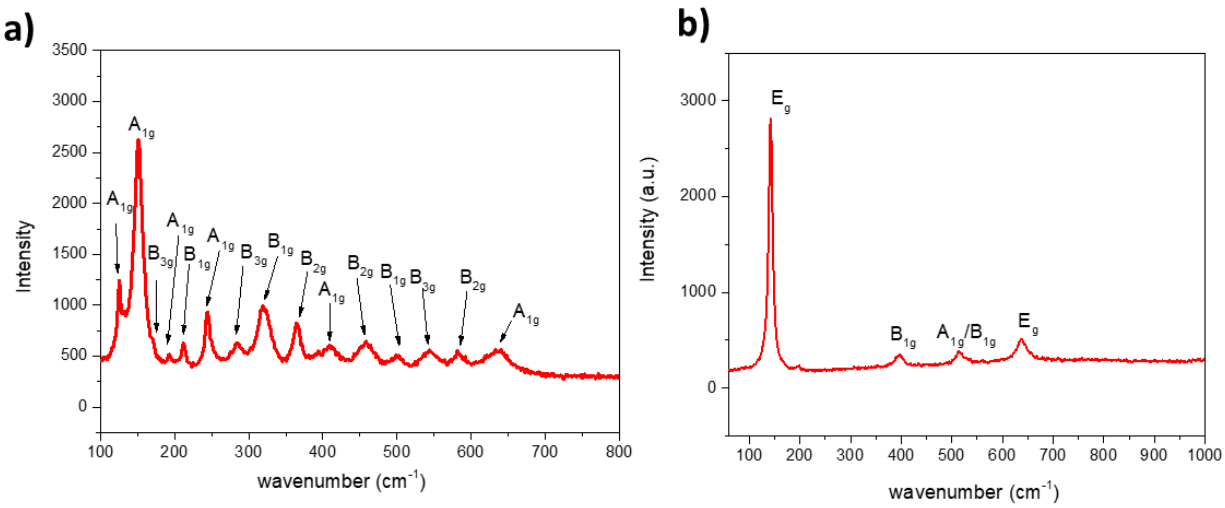

Figure 4.3 Raman spectroscopy of (a) the brookite phase and (b) anatase phase; Raman spectra used with a 633 nm laser.

4.3.1 X-ray photoelectron spectroscopy (XPS)

XPS was used to investigate the oxidation state of brookite thin films (as shown in **Figure 4.4**). The Ti $2p_{3/2}$ and $2p_{1/2}$ peaks are generally centred at 457.9 and 463.6 eV, respectively, and can be assigned to Ti in the 4+ oxidation state. No peak corresponding to Ti in the 3+ oxidation state was observed.

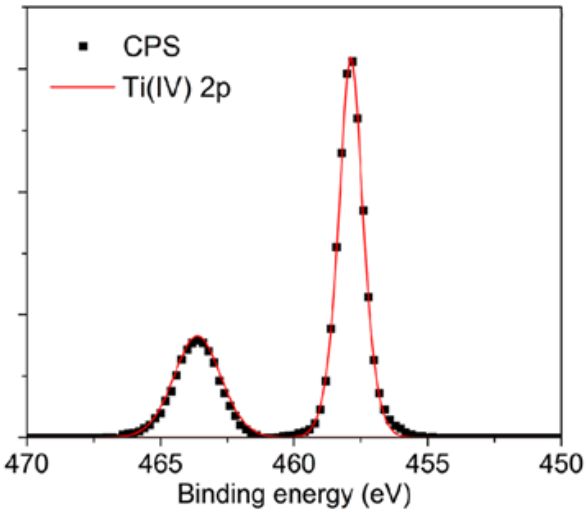

Figure 4.4 XPS spectra of brookite TiO_2 films showing the Ti $2p_{3/2}$ and $2p_{1/2}$ transitions.

4.3.2 Scanning electron microscopy (SEM)

The morphology of brookite TiO_2 thin film was studied using SEM. **Figure 4.5a** demonstrates that the morphology consisted of narrow pyramidal features protruding from the substrate, with a rough width of 20–50 nm and length of 250–300 nm. This morphology is similar to the previous morphology of SnO_2–TiO_2 composite thin films published by Calmert et al.[226] However, the surface area of brookite TiO_2 thin film on the glass substrate was calculated by AFM, and it was 44.5 μm^2. In addition, the morphology of the anatase phase was investigated by SEM **(Figure 4.5b)** and compared with the brookite phase morphology. The anatase phase was grown by AACVD using titanium isopropoxide [$Ti(OCH(CH_3)_2)_4$] in ethyl acetate at 470 °C, and the results showed a compact dome morphology with a surface area that was found to be 29.1 μm^2 by AFM; this is smaller than the surface area of brookite.

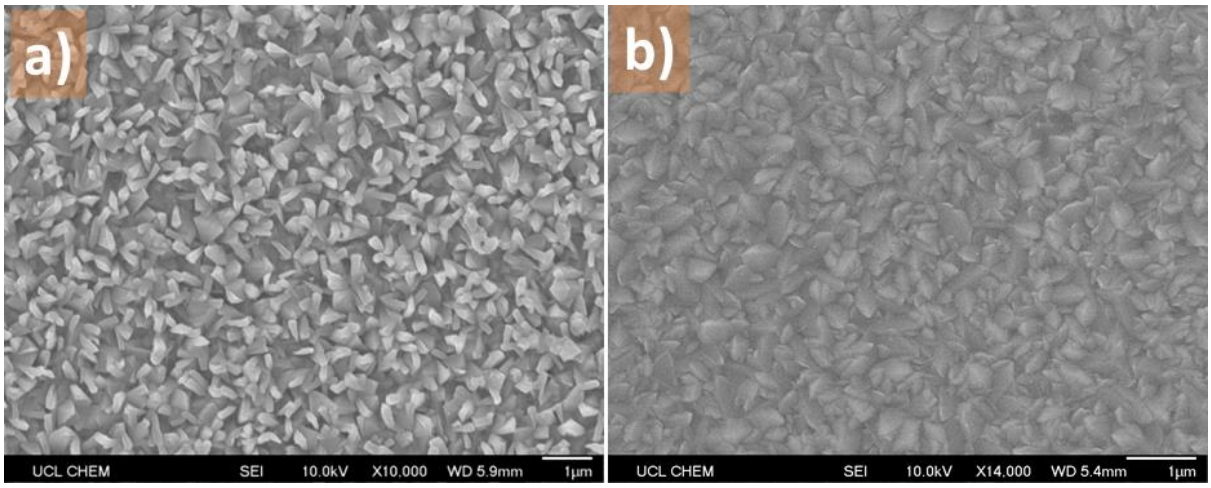

Figure 4.5 SEM images of (a) brookite TiO_2 films and (b) anatase TiO_2 films; both films were grown by AACVD on a glass substrate under the same conditions.

4.3.3 Optical properties of brookite

UV-Vis spectra of brookite thin films were used to investigate the films' optical properties **(Figure 4.6).** As was observed through the surface structure of brookite **(Figure 4.5)**, the protruding features are too small to scatter the light in the near-IR region. In contrast, they are large enough to scatter the light in the visible region. Hence, the transmittance was high in the near-IR region, at above 80%, and it dropped to 55% in the visible wavelength. This is evidence from the UV-Vis spectra that explains the hazy white appearance of brookite thin films. The optical band gap of brookite was calculated using a Tauc plot; **Figure 4.6** shows that the direct band gap of brookite was 3.4 eV.

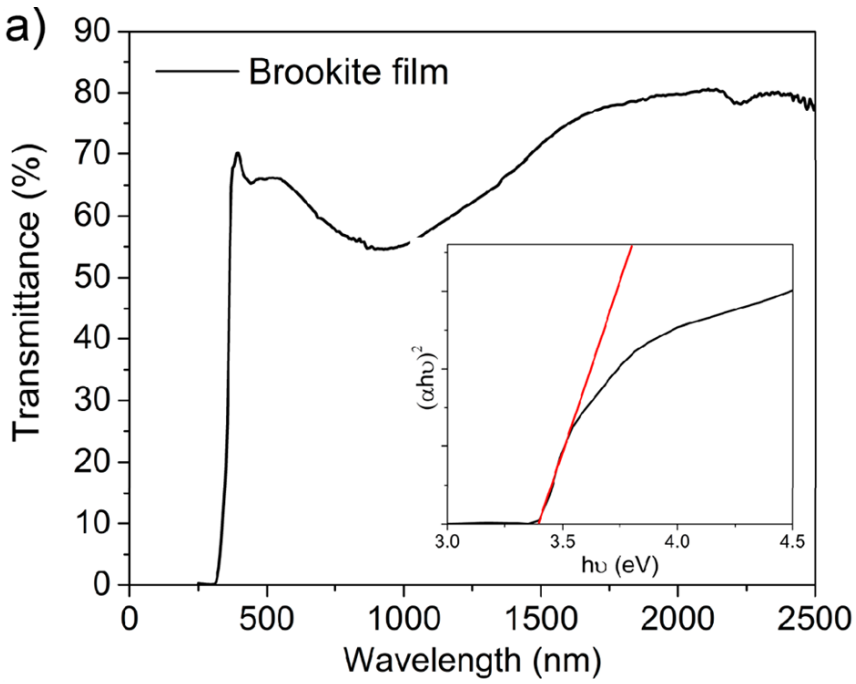

Figure 4.6 UV-Vis spectra of brookite films; the direct band gap was represented using a Tauc plot.

4.3.4 Theoretical studies

The theoretical studies and data analysis in this section **(Section, 4.3.4)** were carried out in collaboration with Prof. David O. Scanlon.

The theoretical results for the brookite's band structure are shown in **Figure 4.7a**, revealing a direct band gap of 3.45 eV at the Γ point. The HSE06 calculated band gap of brookite showed an excellent agreement with the optical band gap calculated from the experimental results for brookite thin films deposited by AACVD. The theoretical calculations by HSE06 for brookite thin films are close to the range of band gap values that have been obtained experimentally (3.26−3.40 eV)[241, 250, 262, 277, 278], as well as from theoretical studies (2.38−3.86 eV).[242, 262, 279, 280]

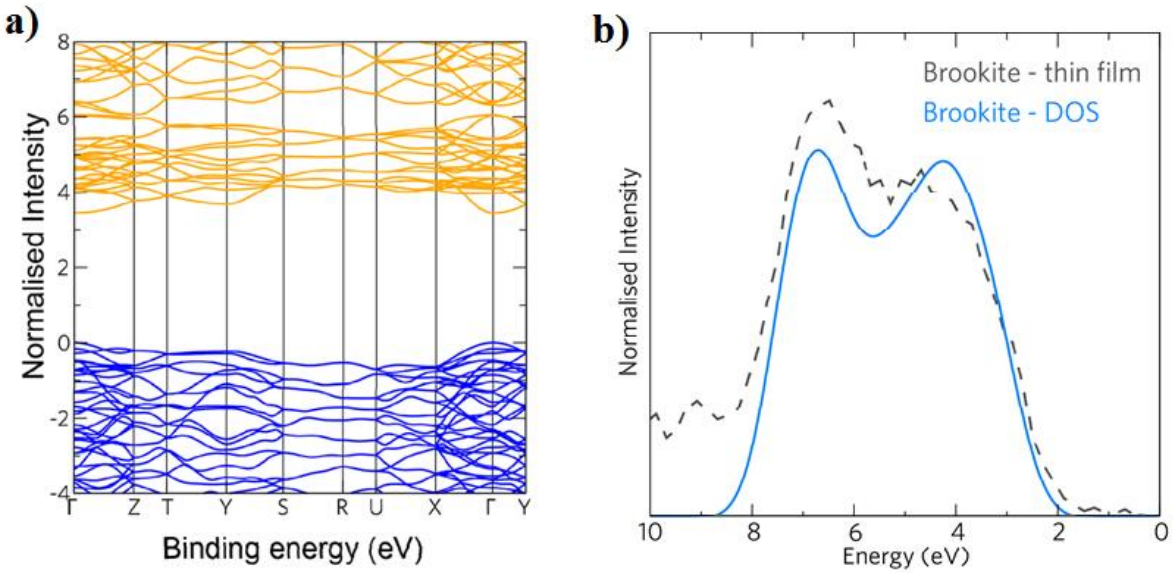

Figure 4.7 (a) Band structure of the brookite form using the hybrid HSE06 functional; b) valance band of brookite from XPS (dashed black) with the simulated XPS (blue line) using the HSE06 functional.

The XPS valence band of brookite TiO_2 was simulated using the atomic orbital photoionisation cross-sections devised by Lindau and Yeh.[281] These results were compared with the experimental data from VB-XPS (as shown in **Figure 4.7b**). The VB-XPS experimental results are consistent with the simulated data. The valence band of brookite shows a peak width of ~6 eV, and a small cavity at ~5.5 eV could be due to a lack of density of states **(Figure 4.7b)**.

4.3.5 Photocatalytic activity

The photocatalytic activities of brookite and anatase TiO_2 thin films were evaluated under UVA illumination (I = 3.15 mW cm^{-2}) for the photodegradation of stearic acid, as in the following equation:[38]

$$CH_3(CH_2)_{16}CO_2H + 26O_2 \xrightarrow{TiO_2(h\nu \geq Eg)} 18CO_2 + 18H_2O \qquad (4.3)$$

A model organic pollutant, octadecanoic (stearic acid), was employed in these tests, as stearic acid is stable under UVA irradiation, and it is easy to follow its degradation by monitoring the loss in the FTIR peaks (C–H) at 2958, 2923 and 2853 cm^{-1} **(Figure 4.8a)**. Formal quantum efficiencies (FQE), which mean that molecules of stearic acid degrade over incident photons (unit, molecule × $photon^{-1}$) FQE are given by the following equation:[176]

$$\text{FQE} = \frac{\text{rate of removal of stearic acid (molecules/s)}}{\text{rate of incident light (photons/s)}} \qquad (4.4)$$

In these tests, a glass slide coated with stearic acid was used as a control to ensure that any loss of stearic acid occurred due to TiO_2 rather than by photoinduced degradation or evaporation. The concentration of stearic acid on the glass slide remained constant, and no significant

degradation of stearic acid was observed during the test period, as in previous research reported by Mills and Wang.[176] However, the brookite films exhibited an FQE of 5.81×10^{-4} molecules/incident photon **(Figure 4.8b)**. Further, two charges (hole, electron) are created by one photon, and a hole and an electron contribute either indirectly or directly to the degradation of stearic acid; considering this, stearic acid will take 104 electron transfers for each molecule to be degraded. In this case, the FQE can be expressed by $5.81 \times 10^{-4} \times (104/2) = 3.02 \times 10^{-2}$ charges that can contribute to the photocatalytic activity per incident photon. (alternatively, it can be expressed as 3.02% of charges contributing to the photocatalytic activity per 100 incident photons). The pure anatase phase was tested under the same conditions, and the anatase films exhibited an FQE of 1.17×10^{-4} molecules per incident photon. Surprisingly, the photocatalytic activity of the brookite films is nearly four times higher than the activity of anatase films. In addition, commercial self-cleaning glass (NSG Activ, the industry benchmark thin film photocatalyst) showed an FQE of 2.64×10^{-4} molecules per incident photon. This means that the FQE of brookite was more than twice that of NSG Activ glass. NSG Activ glass is typically used for comparison when a photocatalyst is studied for thin films. The precise mechanism of photocatalytic activity of stearic acid by TiO_2 is not yet known, but as previously mentioned, a general mechanism is assumed where photogenerated electrons reduce dioxygen into superoxide ($O_2^{-\bullet}$) and possibly react with H_2O to generate further radicals, such as $HO_2^{\bullet}$, H_2O_2, $OH^{\bullet}$ and HO_2^{-}, while photogenerated holes (h^+) oxidise H_2O or OH groups on the TiO_2 surface to hydroxyl radicals ($OH^{\bullet}$); these radicals, created on the TiO_2 surface, can oxidise stearic acid to CO_2 and mineral acids in the presence of UVA irradiation.

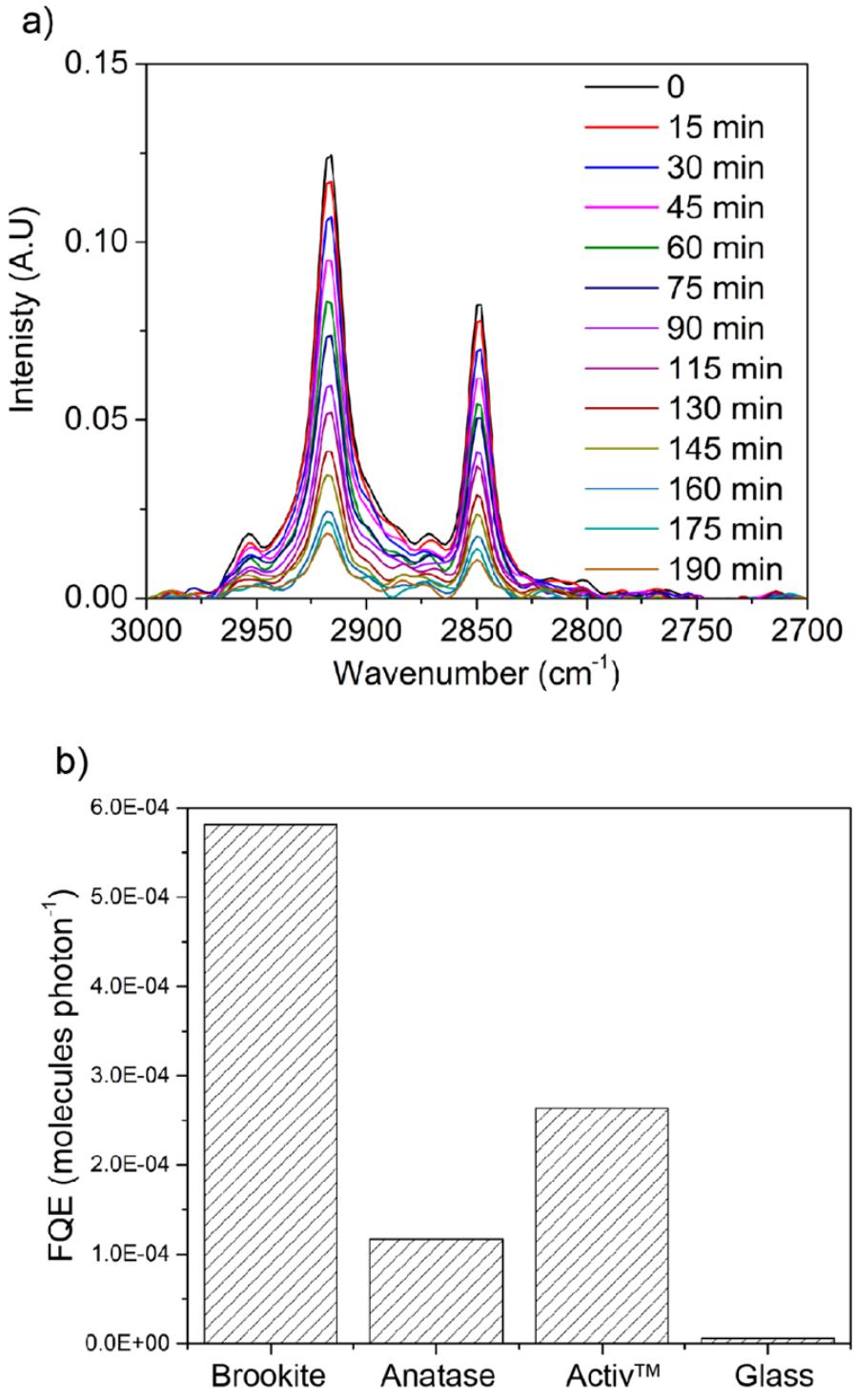

Figure 4.8 Disappearance of the infrared-peaks of stearic acid (C–H) at 2958 cm^{-1} (C−H stretch CH_3), 2923 cm^{-1} (symmetric C−H stretch CH_2) and 2853 cm^{-1} (asymmetric C−H stretch CH_2) for (a) brookite and (b) the formal quantum efficiencies (FQE) for the degradation of stearic acid on anatase, brookite, a glass control and NSG Activ™ under UVA (365 nm); the lamp's irradiance is I = 3.15 mW cm^{-2}.

4.3.6 Photo-induced Wettability

The photo-induced superhydrophilicity of TiO_2 under UV irradiation was discovered in 1997 by Wang et al.[282] Since then, extensive attention has been directed toward this phenomenon, as it can be used in many applications, such as antifogging, self-cleaning, stain-proofing and antibacterial agents. This phenomenon occurs due to increased hydroxyl groups on the titanium dioxide surface by UV irradiation.

In this work, the water drop contact angles of brookite and anatase TiO_2 thin films are shown in **Figure 4.9**. An FTA-1000 drop shape instrument was used to estimate the water contact angles using 5-µl droplets of water in the samples; the images of the drops of water were captured by a Fujifilm Finepix HS25 EXR camera at 1000 frames per second. Surprisingly, the brookite thin films exhibited superhydrophilic properties prior to any irradiation (**Figure 4.9a**). Moreover, the anatase films exhibited the expected 70° value prior to any UV light irradiation (**Figure 4.9b**). The superhydrophilic properties of TiO_2 by non-UV light irradiation were previously observed, and they were attributed to the surface roughness of TiO_2 films. In our work on brookite films, this may be the primary case, with hydroxyl groups increasing on the surface of the brookite films as well (**Figure 4.10**).

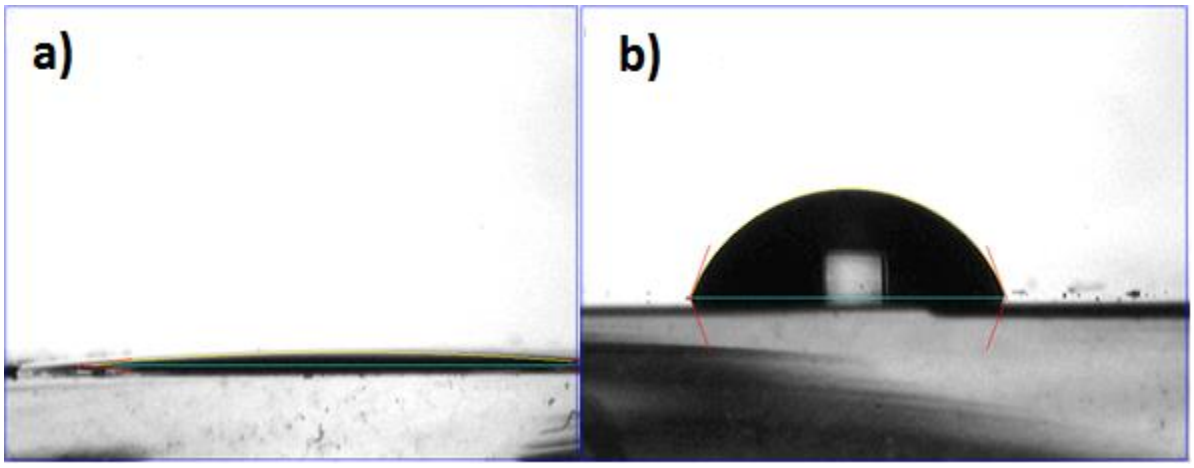

Figure 4.9 Water contact angle prior to any UV light irradiation of (a) brookite thin films and (b) anatase TiO_2 thin films; both films were deposited by AACVD under the same conditions.

4.3.7 Atomic force microscopy (AFM)

For further morphological study, atomic force microscopy (AFM) was used to investigate the surface topography of brookite and anatase TiO_2 thin films, as illustrated in **Figure 4.10**. AFM showed the surface area of brookite thin films to be 44.5 μm^2 (**Figure 4.10a and c [3D]**) and surface area of anatase thin films to be 29.1 μm^2. Thus, the surface area of brookite thin films was larger than that of anatase thin films. However, the surface area of brookite TiO_2 thin films, as calculated by AFM, showed an increase compared with a flat surface; this was calculated as follows:

$$\frac{\text{Surface area}-\text{projected area}}{\text{projected area}} \times 100 = \frac{44.5\mu m^2 - 25\mu m^2}{25\mu m^2} \times 100 = 101\% \quad (4.5)$$

In addition, the surface area of anatase TiO_2 thin films was increased compared with a flat surface, as calculated by AFM:

$$\frac{\text{Surface area} - \text{projected area}}{\text{projected area}} \times 100 = \frac{29.1\mu m^2 - 25\mu m^2}{25\mu m^2} \times 100 = 16.4\% \quad (4.6)$$

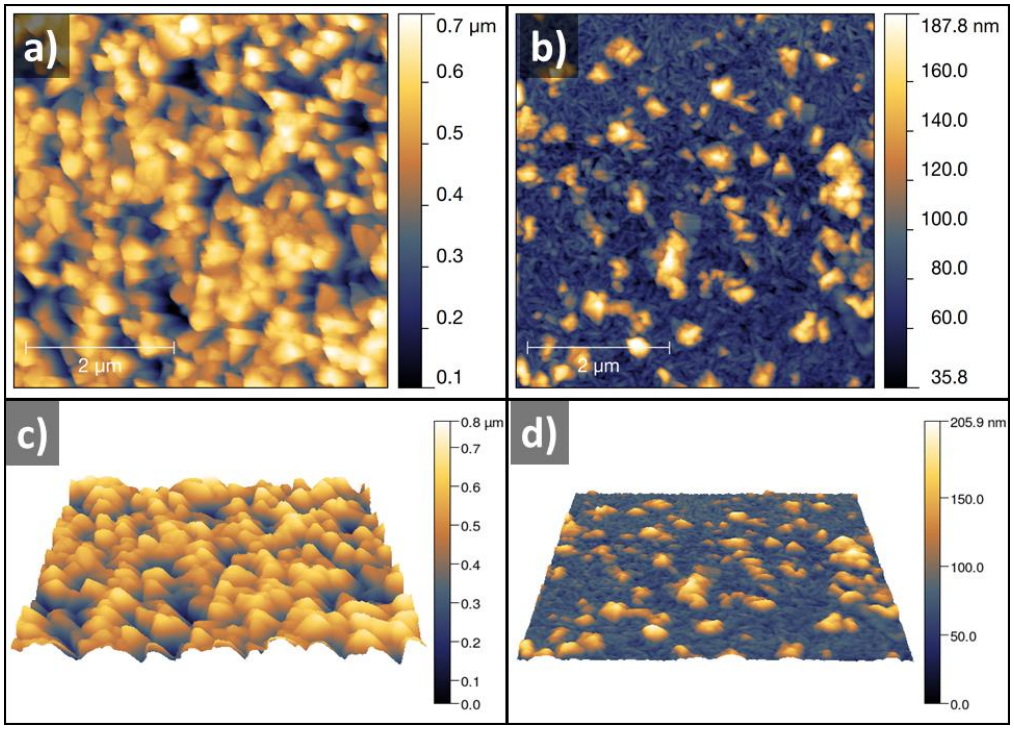

Figure 4.10 AFM images of (a and c) brookite films and (b and d) anatase thin films deposited by AACVD under the same conditions.

4.4 Transient absorption spectroscopy (TAS)

TAS measurements of the brookite sample were carried out alongside those of the anatase sample for comparison. As previously mentioned, the brookite sample was hazy due to its nanostructure, and the anatase sample was highly transparent, owing to its flat and densely packed structure. To the naked eye, there appears to be a huge difference in the surface area. In the TAS measurements, the samples were fired by a laser pulse (355 nm light, 1.5 $mJ.cm^{-2}$ per pulse, 6–ns pulse width). The time-resolved change in absorption at a given wavelength was measured from the microsecond to the second. For TiO_2, the charge carriers formed by this laser pulse absorb in the visible and near-IR region of the electromagnetic spectrum. If the samples were measured in an inert environment, the recombination rate of these charge carriers could be monitored. However, if the samples were measured in the presence of a chemical scavenger that would react with one of these charge carriers (and the quantum yield of this process is sizeable), the enhancement in the charge carrier lifetime of the remaining charge could be monitored. For example, methanol is a strong (hole) scavenger, so if the hole scavenging is sizeable, we can monitor the increase in lifetime of photogenerated electrons.

In the TAS measurements for brookite and anatase TiO_2 thin films grown by AACVD, TAS measurement was carried out in an inert atmosphere (Ar) and in contact with a hole scavenger (methanol). TAS measurements of brookite thin films were carried out in the reflection mode, as it was too scattering to look at in transmission mode. In contrast, the anatase sample was not reflective enough to be looked at in the reflectance mode, so the TAS measurements of anatase thin films were carried out in the transmission mode.

In the transmission mode, the real change in absorbance was determined. However, in the reflectance mode, percentage changes in absorbance versus the initial absorbance were only measured. In our case, this did not affect the analysis of the results. This is because we do not

know the extinction coefficient of electrons or holes in brookite, and thus, we cannot translate our observed transient changes in absorption into a carrier density. Notably, this is not the case for anatase, as it has been well studied via TAS, and the extinction coefficients of electrons and holes have been determined.

To our knowledge, there has only been one recently published study of the TAS of brookite.[283] As such, the charge carrier dynamics of brookite is certainly not as well understood as that of anatase.

The transient absorption spectra and decay kinetics of brookite thin films in argon are shown in **Figure 4.11**. The results are similar to those of previous studies on brookite mesoporous films.[283] In addition, the hole–electron recombination in brookite thin films exhibits a $t_{50\%}$, which is the time to reach 50% of the signal from the start of the measurement, of 100 µs.

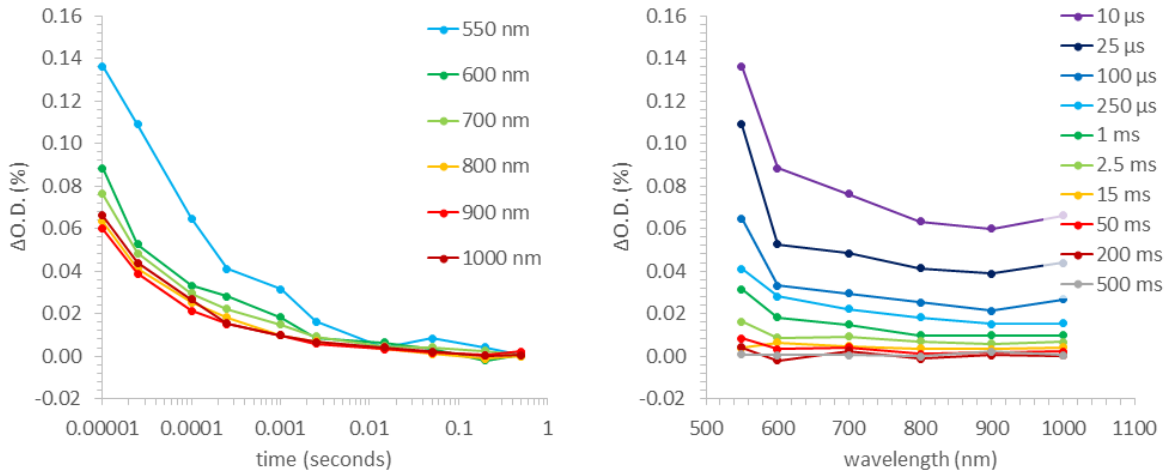

Figure 4.11 (a) Transient absorption decay and (b) transient absorption spectra of brookite TiO_2 films grown by AACVD at 550°C on a glass substrate. TAS measurements were taken under an Ar atmosphere using the diffuse reflection mode.

Anatase TiO_2 thin films grown by AACVD under the same conditions as brookite were used for comparison. The transient absorption spectra and decay kinetics of anatase thin films were investigated, as shown in **Figure 4.12**. The hole–electron recombination in anatase thin films exhibited a $t_{50\%}$ of 100 µs, illustrating that the electron–hole recombinations in anatase and brookite films occurred at similar rates. This is no surprise, as it has previously been observed in the literature for both materials.[283, 284]

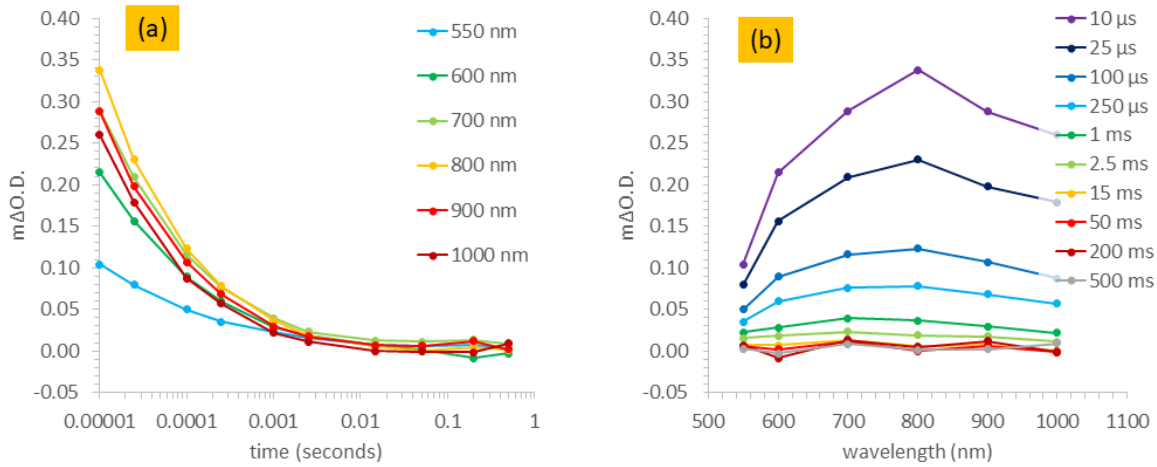

Figure 4.12 (a) Transient absorption decay and (b) transient absorption spectra of anatase TiO_2 films grown by AACVD at 550°C on a glass substrate; TAS measurements were carried out in an Ar atmosphere using transmission mode.

The TAS measurements in both films were investigated using the hole scavenger methanol. The comparison of the TAS decay kinetics in methanol and argon for brookite (left) and anatase (right) is given in **Figure 4.13**.

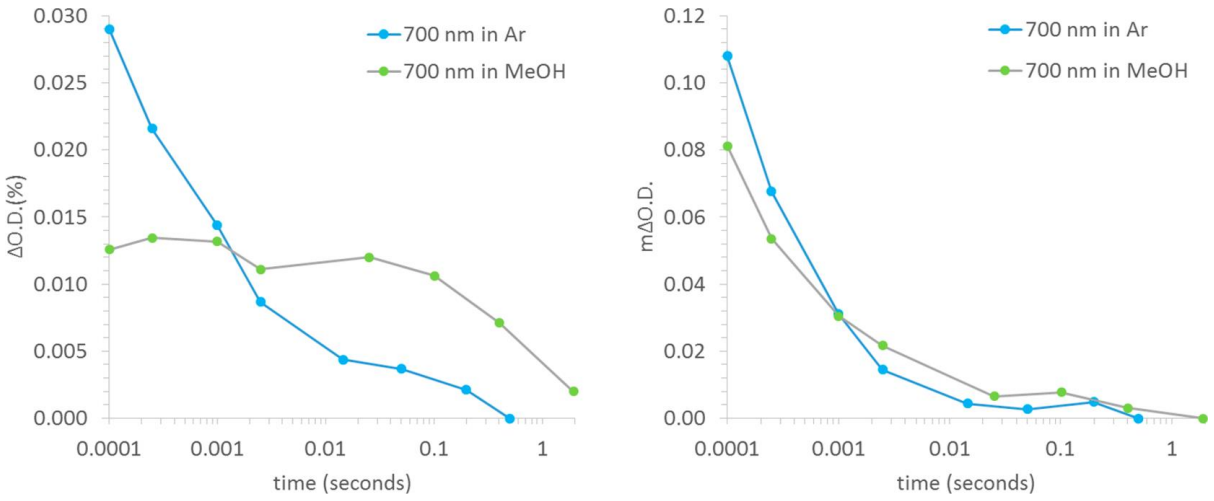

Figure 4.13 TA decays of brookite (left) and anatase TiO_2 films (right); TA decay was carried out at a probe wavelength of 700 nm in methanol (MeOH) and argon (Ar).

As we can see, there is a substantial effect in methanol for the brookite sample. This shows that there is strong hole scavenging by the brookite sample, resulting in long-lived electron carriers. There is no observed effect for the anatase sample. This is not because holes in anatase cannot be scavenged strongly by methanol; indeed, they can, and nanopowders or mesoporous structures often show a strong hole scavenging effect. However, in the case of a flat and dense sample, the quantum yield of this interaction is too low to see an overall effect (since bulk electron–hole recombination simply dominates).

Overall, the results of the TAS measurements exhibited that the hole–electron recombination dynamics in both anatase and brookite are comparable. Further, the higher photocatalytic properties of brookite are not due to an innate increase in the charge carrier lifetime. However, due to the nanostructure and higher surface area of brookite thin films, near the surface, a higher percentage of charge carriers was generated that reacted with the surface organics (such as methanol). In contrast to this, the anatase thin films showed a densely packed, highly flat structure; as a result, most of the charge carriers were generated in the bulk of the anatase that could not react with the surface organics.

4.5 Conclusion

In this chapter, pure brookite TiO_2 films were deposited by AACVD. The direct optical band gap of brookite was calculated using the Tauc plot as 3.4 eV, and this result is in good agreement with the HDFT calculations.

The photocatalytic activity of brookite films was investigated by measuring the destruction of stearic acid under UV light irradiation. Anatase TiO_2 films were used here for comparison. Pure brookite TiO_2 films exhibited excellent photocatalytic properties compared with active glass (NSG Activ), as well as pure anatase films. The water drop contact angles of brookite and anatase TiO_2 thin films were compared, and the brookite films showed superhydrophilic properties prior to any irradiation.

TAS was employed to investigate the hole–electron dynamics in both brookite and anatase films; both films showed similar hole–electron dynamics. The high photocatalytic activity of brookite could have been due to the nanostructure giving a higher surface area of brookite.

In the next chapter, AACVD is used to prepare TiO_2 thin films and (N, Zn) doped TiO_2 thin films using different Zn concentrations. The photocatalytic and antimicrobial activities of these films are investigated via the degradation of stearic acid as a model of photocatalytic activity and *E.coli* as a model of antimicrobial studies under white light. The transient absorption spectra are used to investigate the charge carrier and lifetime of these films.

Chapter 5

Aerosol-assisted chemical vapour deposition of (N, Zn)-doped TiO_2 thin films: photocatalytic and antimicrobial studies

*"In this chapter, the results of experiments exploring the deposition of a series of (N,Zn)-doped TiO_2 films using aerosol-assisted chemical vapour deposition (AACVD) are presented; a different concentration of zinc and nitrogen as cation and anion co-doping were investigated so that the photocatalytic and antibacterial (*E. coli*) abilities could be determined. Photocatalytic activity was investigated in the destruction of stearic acid as an organic pollutant model. In the results, 0.2% Zn, N–doped TiO_2 films showed increased photocatalytic activity compared with N-doped TiO_2 thin films. Antimicrobial activity was studied against Gram-positive bacteria (*E. coli*) under ultraviolet (UV) A and white light conditions comparable to those found in a clinical environment. Single oxygen realised from the surface of thin films under UVA (365 nm) was evaluated using a 2,3-bis(2-methoxy-4-nitro-5-sulfophenyl)-5-[(phenylamino)carbonyl]-2H-tetrazolium sodium salt (XTT) indicator. Transient absorption spectroscopy (TAS) was also used to investigate the charge carrier and lifetime in these films."*

5.1 Introduction

As discussed previously, titanium dioxide (TiO_2) is well known as the best semiconductor for photocatalysts so far, due to its photosensitive properties.[42, 43, 141-143] However, the photocatalytic performance of TiO_2 shows high activity compared with other metal oxides under UV light because of its wide band gap (3.2 eV), leading to extensive studies aimed at improving the photocatalytic activity of TiO_2 under visible light.[285-289]

Efforts to use co-dopants with metal and/or non-metal materials have been prominent in the literature. As mentioned in Chapter 1, nitrogen-doped TiO_2 shows photocatalytic activity under visible light and shifts the band gap toward the visible region. Asahi et al.[42] demonstrated that the photocatalytic activity of TiO_2 improved under visible light irradiation after doping TiO_2 with nitrogen (N) and studying the degradation of methylene blue MB and gaseous acetaldehyde. It was found that the oxygen sites substituted with N atoms in the TiO_2 lattice were responsible for the shift band gap and photocatalytic activity under visible light. Other non-metal dopants such as F, S, P and C have been investigated for their visible light activity within anatase TiO_2.[48, 50, 55, 221, 290, 291] To further enhance the photocatalytic properties of TiO_2, a wide range of studies looked at modifying TiO_2 photocatalytic activity by co-doping TiO_2 with N and another metal or non-metal. N doped Au-TiO_2 showed high photocatalytic performance under visible light compared with undoped and N-doped TiO_2.[292] Cong et al.[87] fabricated N- and Fe-doped TiO_2 nanoparticles. They suggested that the Fe ion and N led to the formation of a new energy state closed to conduction and the valence band, respectively. In addition, these dopants reduced the band gap energy and enhanced the photocatalytic activity under visible light compared with pure TiO_2.

Zhang et al.[86] prepared (Zn, N) co-doped TiO_2 nanoparticles using the sol-gel method with a particle size of around 15 nm; they found that the photocatalytic activity was enhanced at the 1% Zn-doped level for the degradation of methylene blue MB. Zhao et al.[65] reported that incorporating Zn with TiO_2 led to the enhanced photodegradation of Rhodamine B dye under visible light irradiation.

In investigations of the bactericidal and photocatalytic activity of reactive oxygen species (ROS) generated from metal oxides[101, 102], it was found that the correlation between generated ROS and bactericidal activity is linear. The OH^- radical can damage DNA, nucleic acids and amino acids due to its stronger oxidation[293]. In addition, $^1O_2$ has a short lifetime compared with OH^- or superoxide ($O_2^{\bullet -}$), but it can damage the tissue, leading to degradation of the membrane[12].

Detection of ROS generated from metal oxides has been extensively investigated. The 2,3-bis(2-methoxy-4-nitro-5-sulfophenyl)-5-[(phenylamino)carbonyl]-2H-tetrazolium sodium salt (XTT), 3-(4,5-dimethyl-2-thiazol)-2,5-diphenyl-2H-tetrazolium bromide (MTT) and nitroblue tetrazolium (NBT) were used to detect the superoxide ($O_2^{\bullet -}$) anion radical. XTT sodium salt has been extensively used due to the ability to reduce it to XTT formazan reduction using superoxide ($O_2^{\bullet -}$). For instance, Chen and et al.[102], used XTT sodium salt to detect superoxide ($O_2^{\bullet -}$) anion radicals generated from metal oxide nanoparticles like TiO_2, CeO_2, SiO_2, Al_2O_3, ZnO, CuO and Fe_2O_3 under UVA irradiation (365 nm). Wang and Zhao[294] also used XTT sodium salt and NBT as probes for detecting superoxide ($O_2^{\bullet -}$) radicals generated under UV by histidine. Moreover, Zhao and Jafvert[295], used XTT sodium salt for detecting the generation of superoxide from graphene oxide (GO) under UV irradiation.

In this chapter, the films were deposited by AACVD under the similar conditions, with the dopant nitrogen and zinc incorporated into the lattice of TiO_2 thin films, which led to obtaining a narrowing band gap. The films' functional properties were studied to understand the effect of dopant (nitrogen and zinc) concentration on photocatalytic and bactericidal activity. Transient absorption spectroscopy (TAS) was used to investigate photogenerated hole-electron recombination in these samples.

5.2 Experimental section

5.2.1 Material and deposition procedure

Titanium butoxide and ethanol were purchased from Sigma-Aldrich Chemical Co. and Zinc-2-ethylhexanoate,1%diethylene glycol monomethyl ether from Strem Chemicals, Inc.; they were used as received. Depositions were carried out on 150 × 45 × 45 mm SiO_2 (50 nm)–coated float-glass supplied by Pilkington NSG. The SiO_2 acts as a barrier layer, preventing diffusion of ions from within the glass into the deposited film. Prior to use, the glass substrates were thoroughly cleaned using acetone (99%), isopropanol (99.9%) and distilled water and dried in air.

Titanium butoxide [$Ti(OCH_2CH_2CH_2CH_3)_4$, 0.5 g = 1.5 mmol] was dissolved in 25 ml of ethanol in a glass bubbler, and 3.6 mmol of butylamine [$CH_3(CH_2)_3NH_2$] was added to the solution. For the Zn, N–doped TiO_2 thin films, [$C_{16}H_{30}O_4Zn$] (0.2, 0.5, 1.0 and 2.0 mol.%) relative to [$Ti(OCH_2CH_2CH_2CH_3)_4$] was added in ethanol.

AACVD was used to deposit the films. The mist was transferred to the reactor by nitrogen (BOC Ltd., 99.99%) with a flow rate of 1.4 L min^{-1}, and the deposition was carried out at 500°C for 40 min. After the deposition, the reactor was left to cool to room temperature under N_2 before the films were removed.

5.2.2 Film characterisation

Optical spectra were taken using a Perkin Elmer Fourier transform Lambda 950 spectrometer over a wavelength range of 250 nm to 2500 nm. This range encompasses the UV, visible and near infrared (NIR) regions. The spectra were referenced against an air background.

5.2.3 Detection of $O_2^{\bullet-}$ by XTT

In the study, 100 μM XTT sodium salt was used as the indicator for $O_2^{\bullet-}$; the samples were cut (2 × 2 cm) and placed in the tube of glass, following which, 2.5 ml of XTT sodium salt was added to the samples[9]. After UV (365 nm) illumination for different periods, 1 mL of the solution was used to measure the change in the colour due to XTT's reduction to XTT-formazan.

5.2.4 Photocatalytic activity

Stearic acid (0.05 M, 95%, Sigma-Aldrich) was used as a model for photocatalytic performance, and this was prepared by dissolving stearic acid in chloroform. The samples were coated by a thin layer of stearic acid; Pilkington NSG™ Activ™ glass was used as a benchmark and blank float glass as a control. The photocatalytic activity of the films was monitored by Fourier transform-infrared (FT-IR) spectroscopy using a PerkinElmer RX-I instrument. The IR spectrum of each acid overlayer was recorded over the range 3000–2700 cm^{-1}, and the areas of the peaks between 2950 and 2870 and 2870 and 2830 cm^{-1} were integrated. These peaks respectively represent the C–H antisymmetric and symmetric stretches of stearic acid and can be directly related to the concentration of stearic acid on the film's surface.[296] The samples were irradiated using a 365 nm (I = 3.15 mW cm^{-2}) UV lamp. The IR spectrum of each acid-over layer was then recorded over the same range 3000–2700 cm^{-1}. The peaks integrated in the same manner at each interval are proportional to the stearic acid present in unit's molecules in

cm^{-2}. Using a predetermined conversion factor (9.7×10^{15} molecules, 1 $A.cm^{-1}$, where A is absorption) allows a reaction rate to be expressed in units degraded molecules ($cm^{-2}.s^{-1}$).[296]

5.2.5 Antimicrobial activity

One colony of *Escherichia coli* (ATCC 25922) was inoculated into 10 mL of brain heart infusion (BHI; Oxoid, Basingstoke, UK) and incubated with shaking at 200 rpm at 37 °C for 18 h. The culture was centrifuged at 3000 g for 15 min to recover the bacteria and washed in phosphate-buffered saline (PBS; 10 mL; Oxoid), then centrifuged at 3000 g for 15 min and resuspended in 10 mL of PBS. Finally, suspensions of the bacteria were diluted in 10 ml of PBS to give an inoculum containing approximately 10^6 colony-forming units (CFU). The samples with control glass were cut into 2 × 2 cm pieces. PBS (5 ml) was added to each petri dish to make a humid atmosphere and prevent the suspensions from drying out. A 25-µL aliquot of the bacterial cell suspension (*E. coli*) was spread evenly on the surface of each sample and incubated at room temperature for 8 h under UV (365 nm) illumination and after 18 h under white light. After incubation, the slides were transferred to 5 mL of PBS and vortexed for 40 s. Serial dilution of the resulting bacterial suspensions was prepared in PBS, and 100 µL from each dilution was spread onto MacConkey agar for *E. coli*. All the plates were incubated for 24 h at 37 °C. After incubation, any bacterial colonies were counted, and viable counts of bacteria were calculated[170].

5.3 Results and discussion

5.3.1 X-ray diffraction (XRD)

Powder XRD (PXRD) of undoped TiO_2, N:TiO_2 and (Zn, N):TiO_2 films with varying dopant amounts of zinc are presented in **Figure 5.1**. PXRD exhibited a typically anatase crystalline phase of TiO_2, with reflections at (101), (112), (200) and (204) at 2θ values of 25.3, 38.6, 48.0,

55.1 and 62.8° respectively. No secondary peaks were observed for ZnO or TiN. This does not mean to exclude the presence of small amounts of zinc, as the intensity of these peaks is small, and thus, they are not visible in the presence of high-intensity TiO_2 peaks.

A slight increase in the peak (101) intensity of the (N, Zn) doped TiO_2 compared with undoped TiO_2 was observed. This increase could be attributed to the substitution of Zn^{2+} with Ti^{4+} rather than nitrogen or preferred orientation. It has been reported that there are two kinds of doping, substitutional and interstitial, due to Zn^{2+} ion larger than Ti^{4+}; the substitutional situation may be more difficult to bring about, and interstitial zinc is more likely. If substitution Zn^{2+} ion with Ti^{4+} does occur, an expansion of crystal lattice of TiO_2 would be expected.

The General Structure Analysis System (GSAS) and Experiment Graphical user Interface (EXPGUI) suite were used to calculate the lattice parameters of all the thin films by fitting a Le Bail model with the XRD patterns, as shown in **Table 5.1**. The standard peak was obtained from the Inorganic Crystal Structure Database (ICSD). However, the expansion of the unit cells was observed as a comparison between the series (N, Zn)–doped TiO_2 films, standard TiO_2 and undoped TiO_2 thin films, and it was increased with the zinc contents in the films. This expansion could be due to the substitution of Zn^{2+} (0.74 Å) with Ti^{4+} (0.61 Å) site. No expansion in the unit cell of N-doped TiO_2 was observed compared with undoped TiO_2 film because the ionic radii of nitrogen is not large enough to cause expansion.

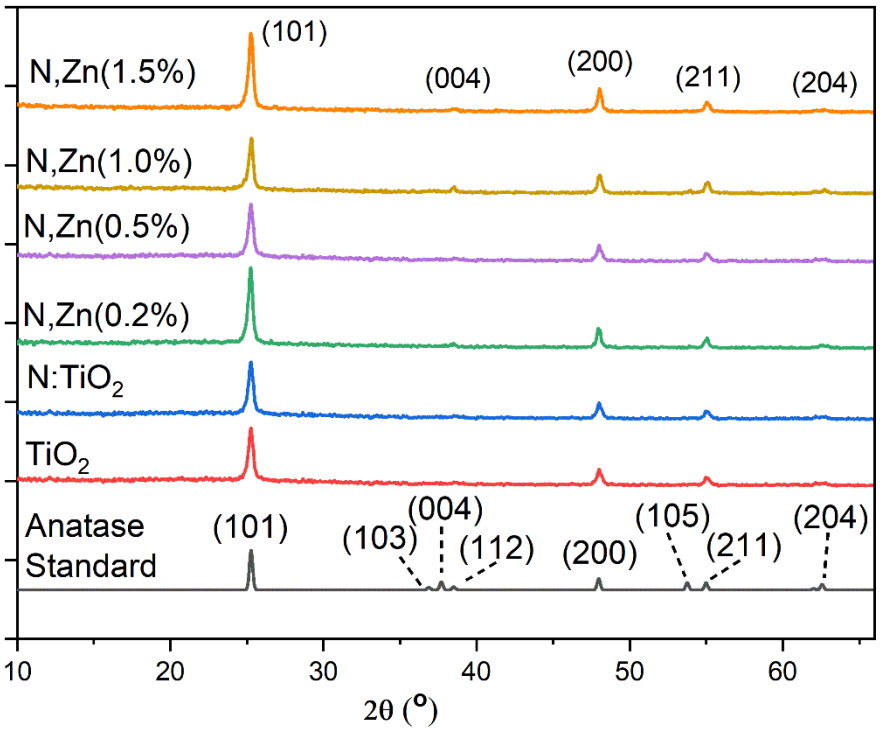

Figure 5.1. X-ray diffraction (XRD) of N-doped titanium dioxide (TiO_2) thin films and 0.2, 0.5, 1.0 and 1.5% (Zn, N)–doped TiO_2 thin films. All films were deposited by aerosol-assisted chemical vapour deposition (AACVD) on the glass substrate at 500°C under N_2 atmosphere.

Table 5.1 Unit cell parameters of titanium dioxide (TiO2), N:TiO_2 and (N,Zn):TiO_2 thin films with different dopant concentrations of zinc

Samples	*a* /Å	*c* /Å	Unit cell volume /Å^3
Undoped TiO_2	3.78	9.52	136.76
N:TiO_2	3.78	9.52	136.76
0.4%	3.78	9.53	136.83
1.0%	3.79	9.51	136.77
1.4%	3.79	9.54	137.20
2.9%	3.79	9.55	137.24

5.3.2 Raman spectroscopy.

The Raman spectra of undoped TiO_2, N:TiO_2 and (N,Zn):TiO_2 thin films with varying dopant amounts of zinc showed anatase structures with 141.5 cm^{-1} (E_g), 397 cm^{-1} (B_{1g}), 514 cm^{-1} (A_{1g}) and 635 cm^{-1} (E_g), as shown in **Figure 5.2.** This result is in good agreement with the XRD analysis. No secondary phases were detected for example ZnO or TiN.

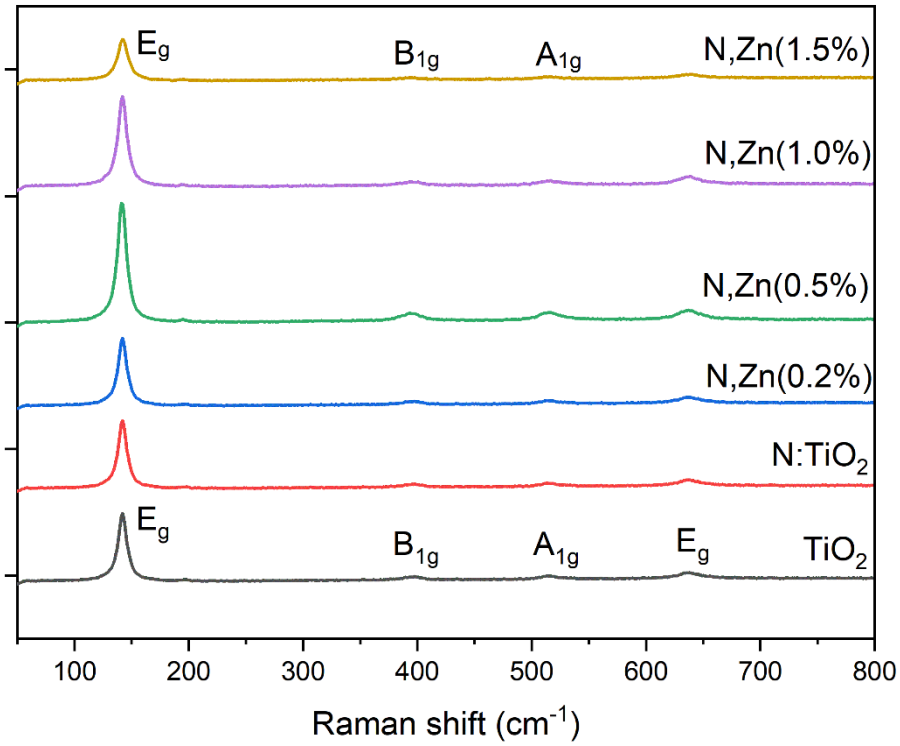

Figure 5.2 Raman spectra for (0%) N:titanium dioxide (TiO_2), 0.2% N,Zn:TiO_2, 0.5% N,Zn:TiO_2, 1.0% N,Zn:TiO_2 and 1.5% N,Zn:TiO_2 thin films.

5.3.3 UV-Vis spectroscopy

The transmittance and reflectance properties of the undoped TiO_2, N:TiO_2 and N,Zn:TiO_2 films were investigated by UV-Vis spectroscopy, as shown in **Figure 5.3a**. The transmittance of all the films showed low transparency across the visible region. N:TiO_2 and N,Zn(0.4%):TiO_2 film

had transparency of around 60% at 600 nm, whereas N,Zn (1.0, 1.4 and 2.9%)–doped TiO_2 films were slightly below this. The reflectance of all films is displayed in **Figure 5.3a**, all the samples showed poor reflectance in the UV-Vis region, which fluctuated between 15 and 20%. The interference fringes observed in the reflectance spectra were a function of film thickness, which resulted from a thickness variation across the thin film; in addition, multiple reflections arose as a result of the interface between thin films and air, as well as the thin films and the glass substrate.

The indirect optical band gap was calculated using the Tauc plot calculations, as shown in **Figure 5.3b**; the undoped TiO_2 thin film had the expected indirect band gap of 3.25 eV. The decrease in the band gap was observed in N doped TiO_2 and series Zn,N-doped TiO_2 films, where the sample with N,Zn (1.5%)–doped TiO_2 film displayed the lowest indirect band gap ~ 3.0 eV. However, the red shift of the band gaps was observed after zinc or nitrogen doping.[42, 65] The decrease in the band gaps may be attributed to the interfacial coupling effect between TiO_2 and ZnO_2, as well as that the sub-band transitions are closely related to the presence of oxygen vacancies.[297] Furthermore, Zn-Ti-O and N-Ti-O could be attributed to creating new energy states. For Zn doping, new states were created below the CB and above the VB by nitrogen doping.[298] As a result, a narrow band gap was obtained and led to decrease in recombination of photoelectrons and holes, as well as an enhanced charge-separation state, as shown in **Figure 5.11**. The films thickness were carried out using the Filmetrics F20 thin-film analyser using reflectance model and against supplied SiO_2 standard in air. In this method, the amount of light reflected from the film was measured over wavelengths 300 – 1000 nm. Fast Fourier transform (FFT) technique was used to compute the data. In these measurements, a series of measured reflectance data for a silica standard substrate was used to calibrate the data. The resulting graph of this analysis was fitted to a theoretical model. **Table 5.2** showed the

film thickness of un-doped TiO_2, N:TiO_2 and series of (N,Zn) doped TiO_2 films. It was found that the film thickness increased with zinc content.

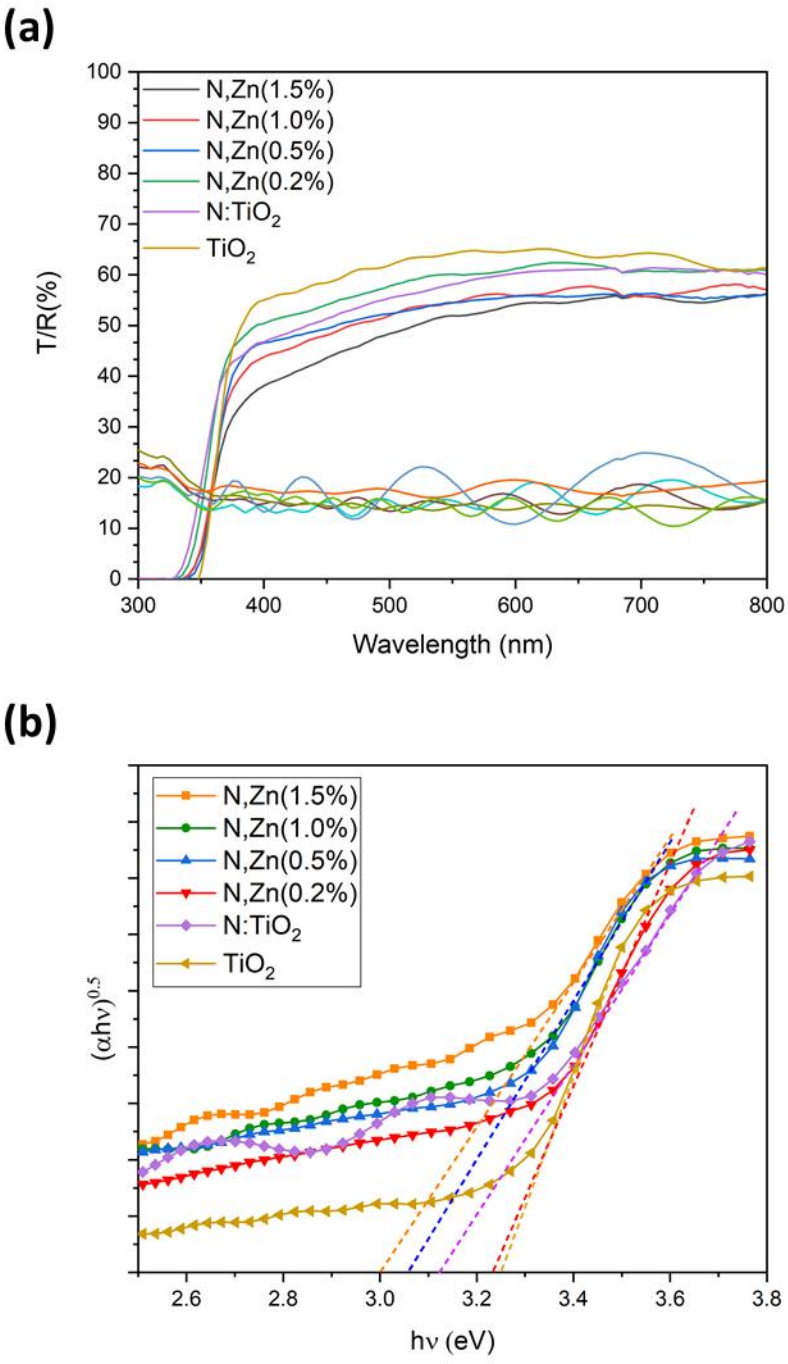

Figure 5.3. Ultraviolet–visible (UV-Vis) spectra of (N,Zn)-doped titanium dioxide (TiO_2) thin films at different zinc concentrations: (a) Transparency and reflectance spectra, (b) indirect band gaps were calculated by Tauc plots. All the films were deposited by aerosol-assisted chemical vapour deposition (AACVD) at 500°C, using butylamine and zinc-2-ethylhexanoate,1%diethylene glycol monomethyl ether, 99%, for the N and Zn precursors.

Table 5.2, the films thickness values of undoped TiO_2, N:TiO_2 and series (N, Zn) doped TiO_2 films

Sample	film thickness (nm)
Undoped TiO_2	350
N doped TiO_2	350
N, Zn (0.2%)	453
N, Zn (0.5%)	531
N, Zn (1.0%)	550
N, Zn (1.5%)	595

5.3.4 Scan electron microscopy (SEM)

The surface morphology of the samples was investigated using a scanning electron microscope, as shown in **Figure 5.4**. Surface morphology is an important factor when photocatalytic activity is discussed, because the surface area can change when the surface morphology is changed.

From the scanning electron microscopy (SEM) images, there are no apparent void spaces, and the particles are well connected. The morphology of undoped TiO_2 films consists of needles with a length of around 100 nm (**Figure 5.4a**). The addition of nitrogen changes the surface morphology; perhaps the most prominent alterations are an increase in the particle size and change to a star shape compared with undoped TiO_2. The morphology is similar to that of N,Zn:TiO_2 film at low dopant levels (0.4 and 1.0%). The addition of zinc dramatically changes the particles' size and the shape, especially at a high zinc concentration. The morphology of N,Zn(1.4 and 2.9%)–doped TiO_2 films consists of a mixture of irregular shapes and densely packed particles that are about 300 nm wide (**Figure 5.4e,f**).

Energy-dispersive X-ray spectroscopy (EDX) was used to analyse the zinc concentrations in the films; the results showed that, when the initial concentrations of zinc (concentrations in the solution) increased, the zinc concentrations in the films increased, as shown in **Table 5.2**. In addition, we could not detect nitrogen concentrations in the films by EDX due to overlaps between the nitrogen peak and other peaks.

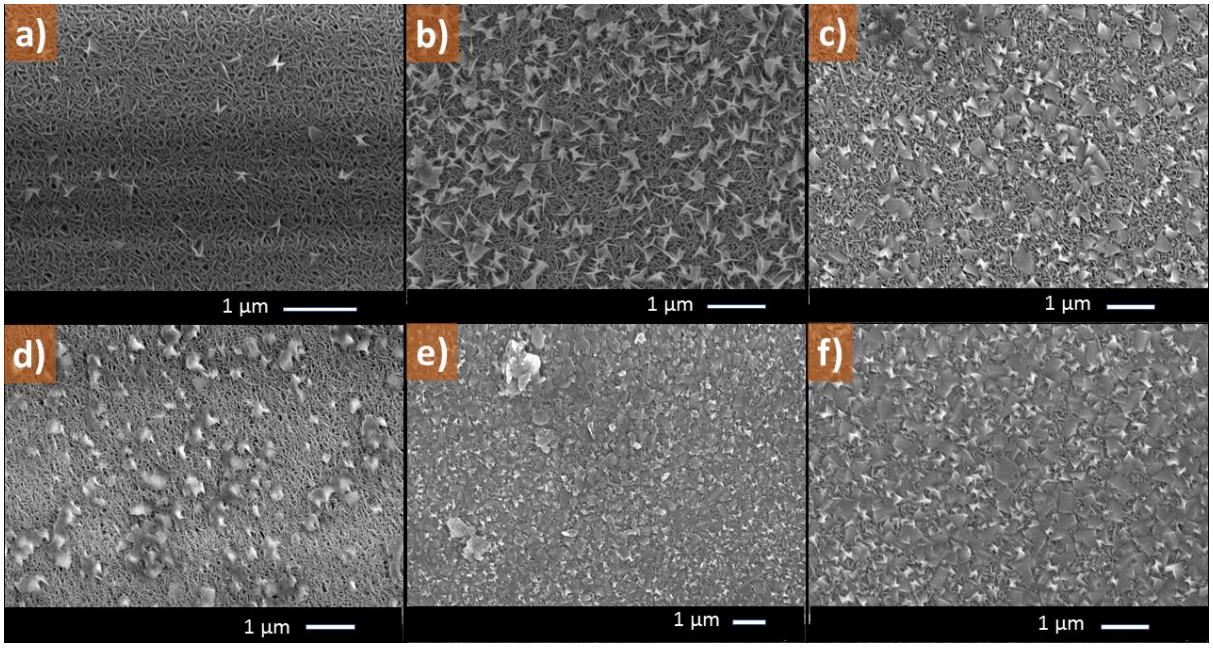

Figure 5.4 Scanning electron microscopy (SEM) images of (N, Zn)–doped TiO_2 thin films at different zinc concentrations: (A) 1.5%, (B) 1.0%, (C) 0.5%, (D) 0.2% and (C) for N-doped titanium dioxide (TiO_2) thin film.

Table 5.2 Relationship between mol% in solution and at.% of zinc in the film obtained by dispersive X-ray spectroscopy (EDX)

Sample	mol% in the solution	At. % obtained by EDX
N,Z:TiO_2	0.2%	0.4%
N,Z:TiO_2	0.5%	1.0%
N,Z:TiO_2	1.0%	1.4%
N,Z:TiO_2	1.5%	2.9%

5.3.5 X-ray photoelectron spectroscopy (XPS)

The oxidation states of the Ti, N and Zn species in the films on the surface and in the bulk were studied using XPS. The XPS spectra of all the films showed the Ti 2p binding energies corresponded to Ti^{4+}, with the $2p_{3/2}$ and $2p_{1/2}$ peaks centred at 458 and 463.6 eV, respectively[235],

as shown in **Figure 5.5a** [from bottom to top: are N:TiO_2, N,Zn(0.4%):TiO_2, N,Zn(1.0%):TiO_2, N,Zn(1.4%):TiO_2, N,Zn(2.9%):TiO_2]. Furthermore, the XPS results illustrated that nitrogen and Zn(II) dopants were present. Nitrogen was detected on the surface in the N:TiO_2 films and series (N,Zn):TiO_2 films [**Figure 5.5b**, from bottom to top: N:TiO_2, N,Zn(0.2%):TiO_2, N,Zn(0.5%):TiO_2, N,Zn(1.0%):TiO_2, N,Zn(1.5%):TiO_2]. As previously stated, nitrogen can be doped into the TiO_2 structure in a substitutional or interstitial manner, depending on binding energies of ~400 eV for the interstitial (N_i) and ~398.5 eV for substitutional (N_s) form, by XPS analysis.[38, 299, 300] our films showed binding energy at ~ 399 eV, which could be assigned to substitutional (N_i) position, as well as to chemisorbed nitrogen (γ-N_2).

The serial (N, Zn)–doped TiO_2 films showed the zinc 2p spectra on the surface, as illustrated in **Figure 5.5c** [from bottom to top: N:TiO_2, N,Zn(0.2%):TiO_2, N,Zn(0.5%):TiO_2, N,Zn(1.0%):TiO_2, N,Zn(1.5%):TiO_2]. The Zn $2p_{3/2}$ and $2p_{1/2}$ transitions occurred at 1021.3 and 1044.08 eV, respectively [229, 301, 302], and in the +2 oxidation state.

The VBs of N:TiO_2 and serial (N,Zn)–doped TiO_2 films were investigated by XPS, as shown in **Figure 5.5d**. The VB consisted of two peaks between 2 and 9 eV, which corresponded to the O 2p orbitals σ (bonding) and π (non-bonding). The VBs were shifted toward low-energy binding when the zinc level increased compared with N:TiO_2 film. However, the shift in the VB gap may have corresponded to nitrogen and/or zinc dopants forming new energy states above VB.

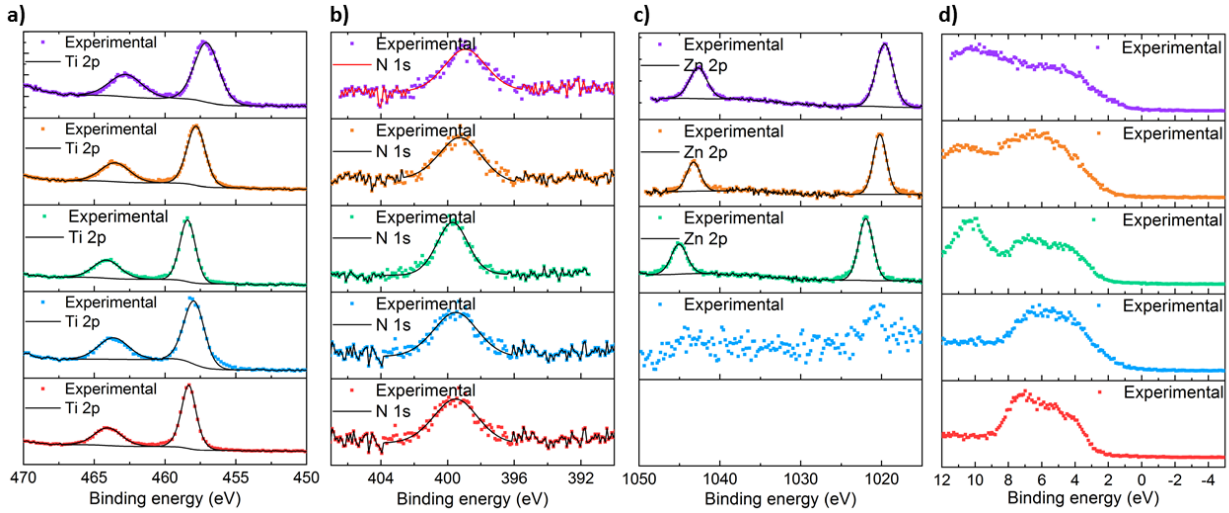

Figure 5.5 Surface X-ray photoelectron spectroscopy (XPS) spectra of N: titanium dioxide (TiO_2) and series (N,Zn):TiO_2 films showing (a) Ti $2p_{3/2}$ and $2p_{1/2}$ peaks, (b) N 1s peak, (c) Zn $2p_{3/2}$ and $2p_{1/2}$ peaks and (d) valence band (VB) XPS spectra for the aerosol-assisted chemical vapour deposition (AACVD)-grown N-doped TiO_2 and series (Zn,N)–doped TiO_2 films. All the peaks in this figure, from bottom to top, are N:TiO_2, N,Zn(0.2%):TiO_2, N,Zn(0.5%):TiO_2, N,Zn(1.0%):TiO_2, N,Zn(1.5%):TiO_2).

The depth profiles of all the films (etched for 150 seconds) showed that the zinc and nitrogen contents were consistent throughout the film. At the same time, the zinc contents in the bulk were slightly less than those on the surface, while the nitrogen content was almost equal on the surface and in the bulk, as shown in **Figure 5.6a** and **b**.

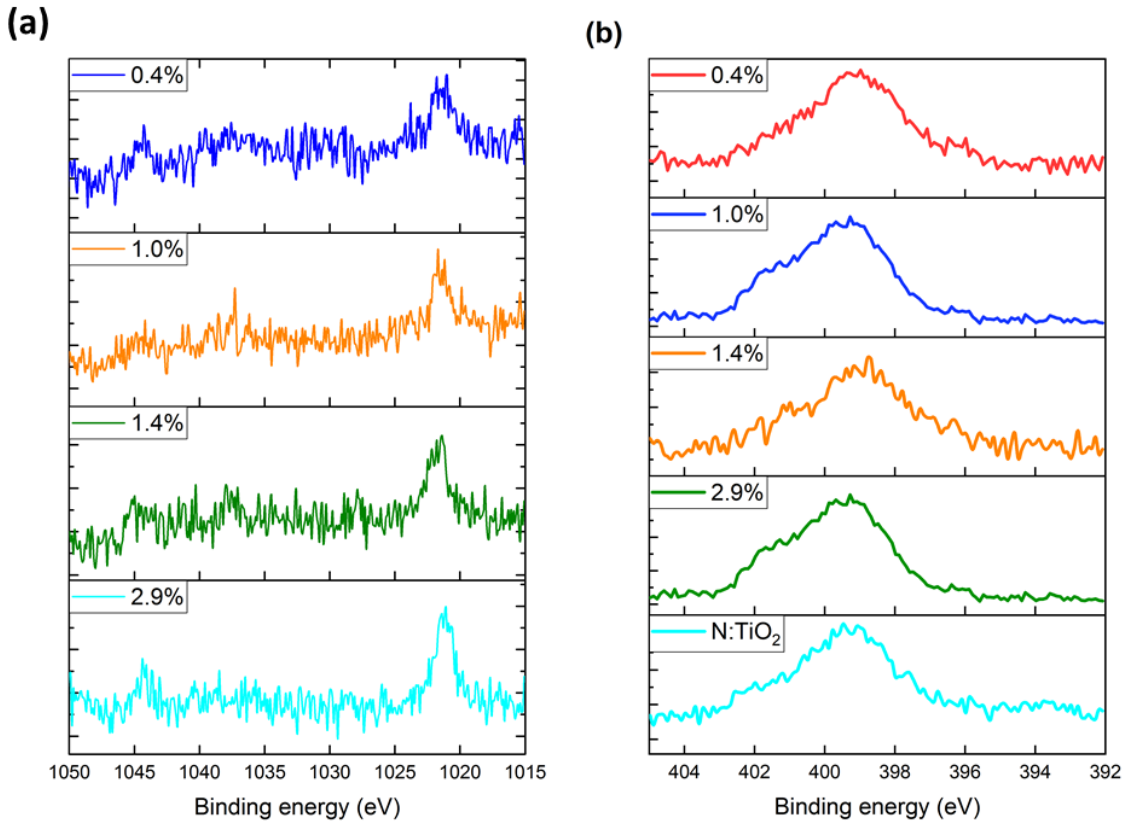

Figure 5.6 X-ray photoelectron spectroscopy (XPS) spectra of all N,Zn (0.2, 0.5, 1.0 and 1.5%)–doped TiO_2 films showing the depth profile of (a) Zn and (b) N content in the films.

5.3.6 Reactive Oxygen Species (ROS)

Generation of superoxide ($O_2^{\cdot-}$) radical

ROS, like superoxide, single oxygen and hydroxyl radicals, play an important role in antimicrobial activity. In this study, the generation of the superoxide anion radical ($O_2^{\bullet-}$) from the surface of the films was investigated by using a reduction of 100 µM XTT sodium salt.

The samples were cut (2 × 2 cm) and placed in small glass tubes. Following this, 2.5 ml of 100 µM XTT sodium salt was added and all samples were placed under UVA light irradiation simultaneously at room temperature. The control sample was normal glass in 2.5 ml of 100 µM XTT sodium salt. The control glass was used to make sure that the reduction of 100 µM XTT

sodium salt was due to the generation of superoxide anion radical ($O_2^{\bullet -}$) from the surface of the films and not the effects of UV irradiation on 100 µM XTT sodium salt. The change in the absorption spectra at 470 nm after 44 h under UV-365 nm irradiation indicates that the 100 µM XTT sodium salt was reduced to XTT formazan by the superoxide anion radical ($O_2^{\bullet -}$), as shown in **Figure 5.7**. All the films generated reactive superoxide radical under UV light irradiation compared with the control sample (**Figure 5.8**). However, The samples with initial zinc concentrations (0.2% and 1.0%) illustrated the highest ($O_2^{\bullet -}$) generation, followed by (N, Zn(0.5%))–doped TiO_2 film. In addition, (N,Zn(1.5%))–doped TiO_2 thin films showed the lowest ($O_2^{\bullet -}$) generation compared with the other thin films.

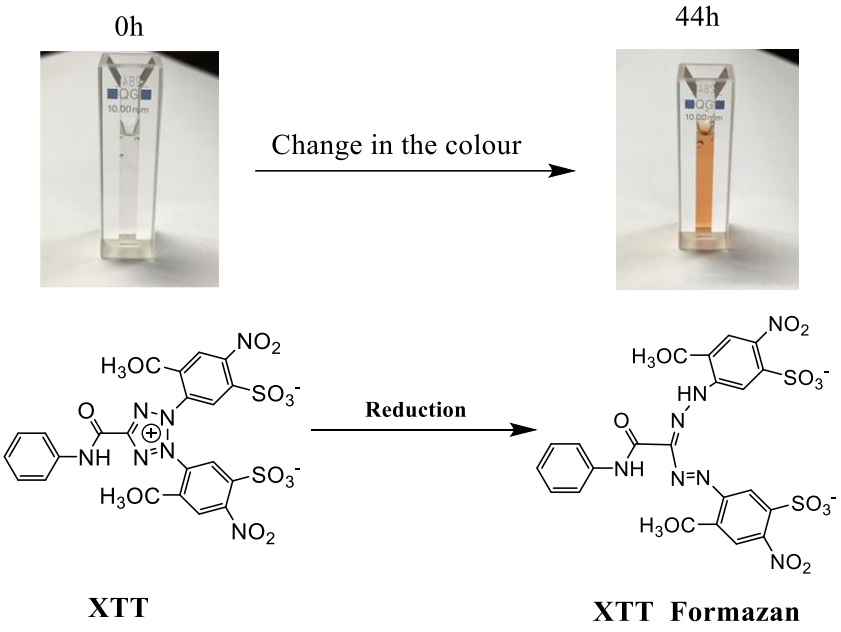

Figure 5.7 Structure of reduction of 2,3-bis(2-methoxy-4-nitro-5-sulfophenyl)-5-[(phenylamino)carbonyl]-2H-tetrazolium sodium salt (XTT) sodium salt to XTT formazan by super oxide ($O_2^{\bullet -}$) was generated from the films with different zinc concentrations under ultraviolet (UV) irradiation.

$$A = \varepsilon \times b \times c, \qquad (5.1)$$

where A is the measured absorbance at 470 nm; ε is the wavelength-dependent molar absorptivity coefficient for XTT at 470 nm, 2.16×10^4 M^{-1} s^{-1}; c is the analytic concentration; and b is the cell length.

The Beer-Lambert law (**eq. 5.1**) was used to calculate the superoxide concentrations at different periods at λ = 470 nm, with coefficients for XTT of 2.16×10^4 M^{-1} s^{-1} at 470 [303]. **Figure 5.9** exhibits the average ($O_2^{\bullet -}$) molarity for all the samples as calculated from this law. The sample with an initial zinc concentration of 0.2% generated nearly 3.28×10^{-5} M of ($O_2^{\bullet -}$), while the sample with 1.0% generated 3.22×10^{-5} M. The film with a high initial zinc concentration (1.5%) generated 9.3×10^{-6} M of reactive superoxide radical.

However, the increased contents of superoxide anion radical ($O_2^{\bullet -}$) from the surface of (N, Zn)–doped TiO_2 films compared with undoped TiO_2 film may be due to the following factors:

- The contribution of zinc contents in the films;

- Improved charge transfer after zinc dopant application (**Figure 5.11**);

- Different concentrations of OH groups on the film surfaces before UV irradiation; this is the most likely explanation, as when the samples were annealed at 500°C after deposition, no reduction was observed for XTT even after 44 h. It is worth mentioning that other assays were used to investigate other ROS (e.g. OH^- and $^1O_2$), using Furfuryl alcohol (FFA) and p-Chlorobenzoic acid, but we did not notice any change in the absorption spectrum by using UV-Vis spectroscopy. Therefore, the use of other techniques in the future such as high-performance liquid chromatography (HPLC) with gas chromatography (GC) and EPR will be necessary for studies generating OH^- and $^1O_2$.

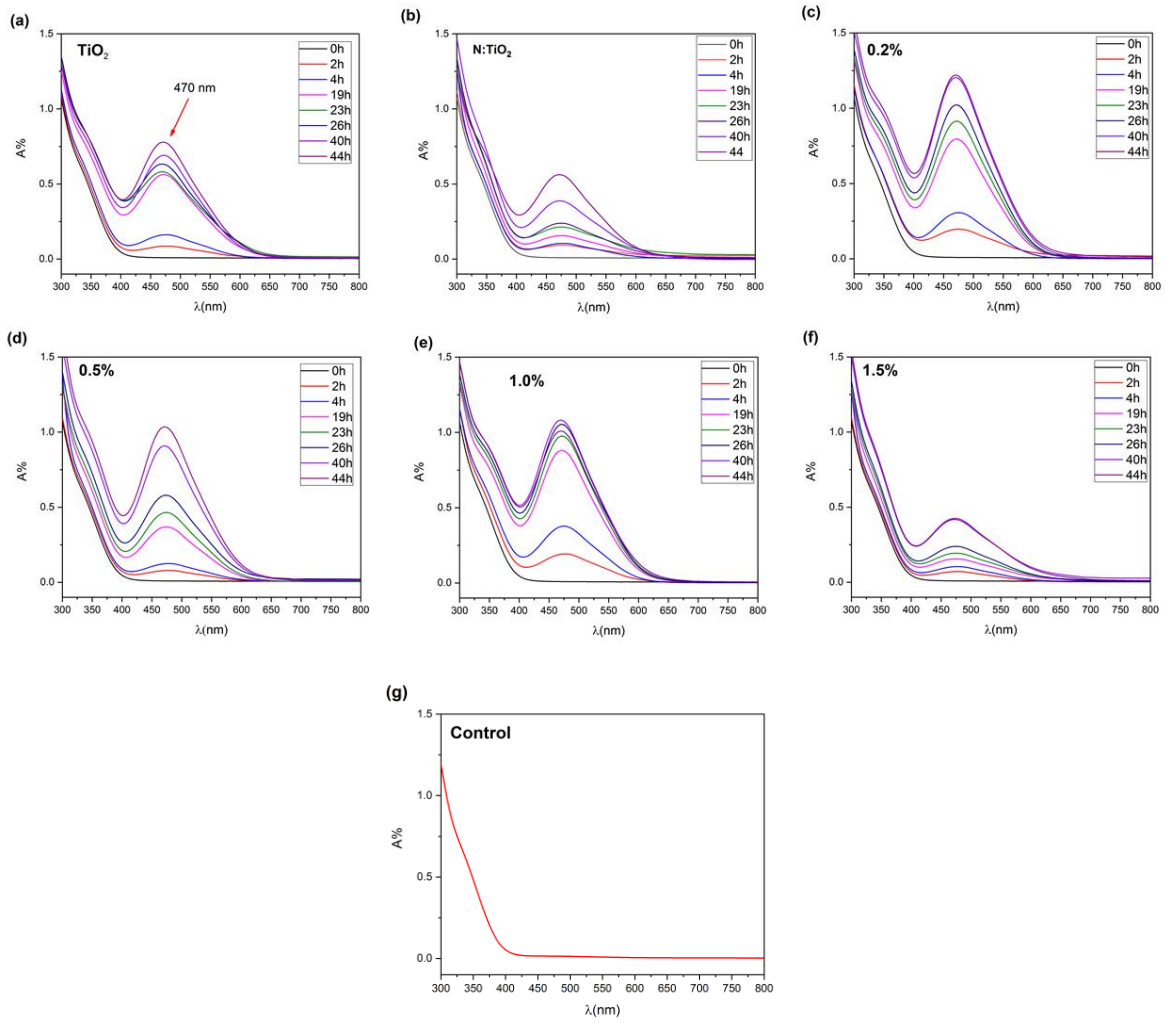

Figure 5.8, Reduction of 100 µM 2,3-bis(2-methoxy-4-nitro-5-sulfophenyl)-5-[(phenylamino)carbonyl]-2H-tetrazolium sodium salt (XTT) sodium salt by superoxide (O_2^-) radical under UV-360 nm irradiation for 44 h on (a) N: titanium dioxide (TiO_2) , (b) 0.2% Zn,N:TiO_2, (c) 0.5% Zn,N:TiO_2, (d) 1.0% Zn,N:TiO_2, (e) 1.5% Zn,N:TiO_2 and (f) control. The room temperature is ~22°C, the UV intensity is 3.15 mW cm^{-2}; all films were deposited on normal glass by aerosol-assisted chemical vapour deposition (AACVD) at 500°C. The samples were placed in the tubes and 2.5 ml of 100 µM XTT sodium salt was added; after the exposure time, 1 ml of suspension was taken, and after UVA illumination for different periods, the concentration of the organic colour of the reduction of XTT sodium salt to XTT formazan was measured.

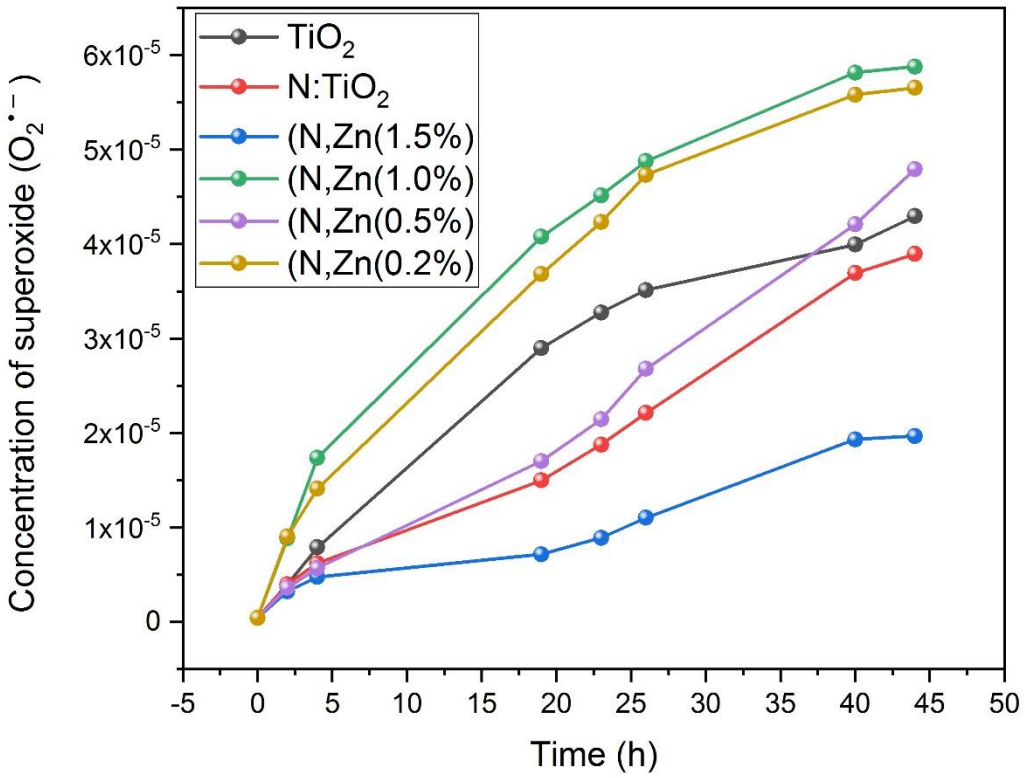

Figure 5.9, Superoxide ($O_2^{\bullet -}$) concentrations of N:TiO_2, N,Zn(0.2%):TiO_2, N,Zn(0.5%):TiO_2, N,Zn(1.0%):TiO_2, N,Zn(1.5%):TiO_2; the concentrations were calculated using the Beer-Lambert law.

5.3.7 Photocatalytic activity

The photocatalytic activities of undoped TiO_2, series (N, Zn):TiO_2 and N:TiO_2 films were investigated for degradation of a model organic pollutant, octadecanoic (stearic acid), under UVA irradiation. Here, 0.05 M stearic acid solution in chloroform was used to coat the films in a thin layer, using a dip coater. All the films were placed under UVA irradiation (I = 3.15 mW cm^{-2}). Activ^{TM} glass was used for comparison. Blank glass (control) coated with stearic acid was also used to make sure any loss of stearic acid occurred due to the photocatalytic properties of films and not side interventions occurring as a result of evaporation or

photoinduced degradation; no loss was observed in the concentration of stearic acid on the control.

The photocatalytic test was employed to monitor the decreased intensity of the characteristic C-H infrared bands at 2958, 2923 and 2853 cm^{-1}.[304, 305] The photocatalytic rates were estimated from the linear regression of the initial steps (30–40%) of the curve of integrated area versus illumination time. Formal quantum efficiencies (FQE), defined as molecules of stearic acid degraded over incident photons (units, molecule × $photon^{-1}$), were used to express the photocatalytic rate; the undoped TiO_2 film exhibited an FQE of 0.15×10^{-14} molecules per incident photon and the FQE increased slightly to 0.21×10^{-14} molecules per incident photon for N:TiO_2 film, as shown in **Figure 5.10**. The FQE increased with the zinc dopant; N,Zn(0.4 and 1.0%) doped TiO_2 showed dramatically increased in FQE values, reaching 0.33×10^{-14} and 0.25×10^{-14} respectively. At high zinc levels, the FQE decreased, to reach 0.07×10^{-14} and 0.03×10^{-14} for N,Zn(1.4 and 2.9%)–doped TiO_2 films, respectively. Furthermore, the (N, Zn(0.4%))–doped TiO_2 displayed more than twice the activity of undoped TiO_2, as well as higher activity than NSG Activ™ did at 0.20×10^{-14}. Surprisingly, these photocatalytic activities correlated directly with the superoxide generated, as we can see from **Figures 5.8 and 5.9**. For instance, the sample showed that the second highest superoxide generation exhibited the highest photocatalytic rate, while the sample that revealed the lowest photocatalytic rate showed the lowest superoxide generated. As previously mentioned, the photocatalytic mechanism on the surface of TiO_2 usually occurred when the TiO_2 absorbs the radiation, leading to create hole and electron on the VB and CB respectively, the hole (h^+) can result in oxidation of H_2O and produce OH^- radicals, the electron (e^-) can reduce O_2 and produce reactive superoxide radicals ($O_2^{\cdot -}$). OH^- radicals and reactive superoxide radicals ($O_2^{\cdot -}$) contribute in degrading nearby organics.[6, 306]

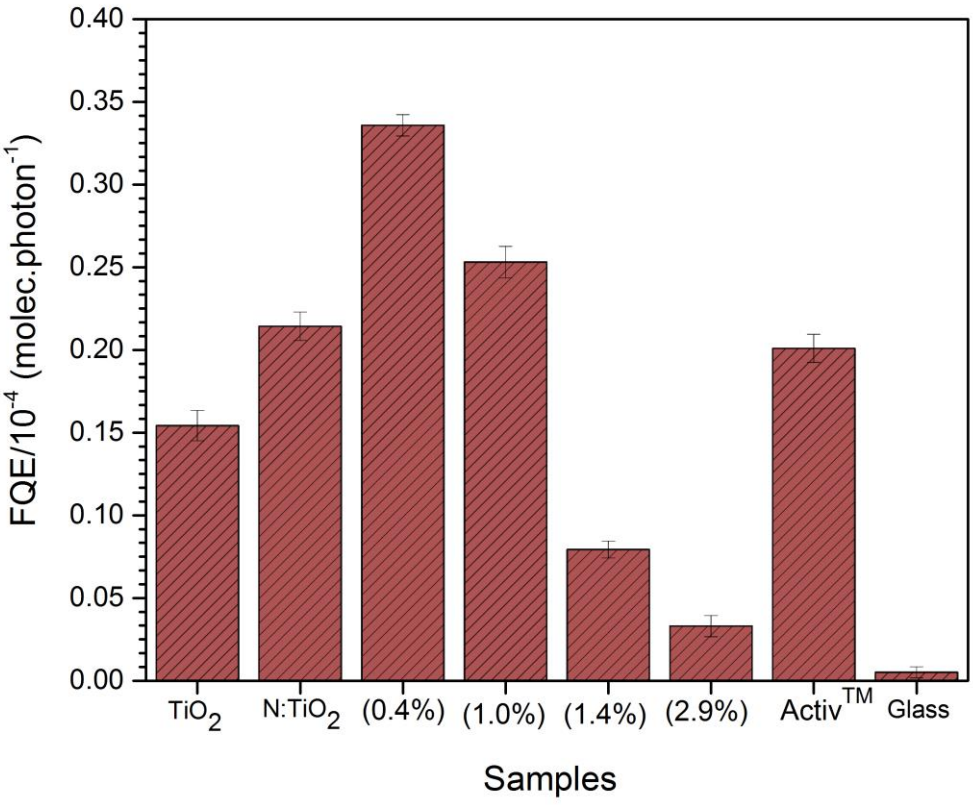

Figure 5.10 Formal quantum efficiencies (FQE) obtained during photocatalytic activity of the undoped titanium dioxide (TiO_2), N:TiO_2, series (N,Zn) doped TiO_2 films and Activ™ glass, as well as blank glass. Stearic acid was used as model of photocatalytic test under ultraviolet (UV) A for the exposure time.

5.3.8 Antimicrobial activity

The bactericidal tests of undoped, N:TiO_2 and serial (N, Zn)–doped TiO_2 films were performed against the Gram-negative bacterium *E. coli*. Bactericidal activity was carried out by incubating the samples with bacteria at 37°C for 8 and 18 hours under UV-365 nm and white light, respectively, to investigate whether doping TiO_2 with Zn and N increased the antimicrobial activity compared with that of undoped TiO_2 film. The bactericidal tests were carried out under UVA (365 nm) and white light at the same time. The results revealed that the (N, Zn)–doped TiO_2 films had good antimicrobial activity against the Gram-negative bacterium *E. coli*

compared with undoped TiO_2 film. **Figure 5.11a**, shows the viable counts of bacteria after incubation of the samples under UVA irradiation (I = 3.15 mW cm^{-2}) and under dark conditions for 8 h. All the films revealed a significant reduction in the number of viable bacteria under UVA irradiation; in contrast, no significant reduction was observed under dark conditions. The (N, Zn(0.5%)) doped TiO_2 films showed the highest reduction under UVA for 8 h, followed by N,Zn(1.0%) doped TiO_2 and (N,Zn(0.2%)) doped TiO_2 films under the same conditions. However, doped TiO_2 with Zn and N was found to improve antimicrobial activity against *E. coli*. This is likely due to the oxidative stress caused by the generation of ROS. All the samples tested under the white light were comparable to those found in a clinical environment, specifically, in UK hospitals. The intensity of the white light was measured to range between 6000 and 9000 lux, at a distance of 30 cm from the lamp (28-W fluorescent lamp) using a lux meter (LX-101, Lutron Inc., Coopersburg, PA).

The results indicate that (N, Zn)–doped TiO_2 films displayed a significant reduction in the viable counts of bacteria after incubation in the serial (N,Zn)-doped TiO_2 after 18 h under white light illumination **(Figure 5.11b)**. The (N,Zn(0.5%))–doped TiO_2 showed the highest bactericidal activity, followed by (N,Zn(0.2%))–doped TiO_2 film, which was comparable to undoped TiO_2.

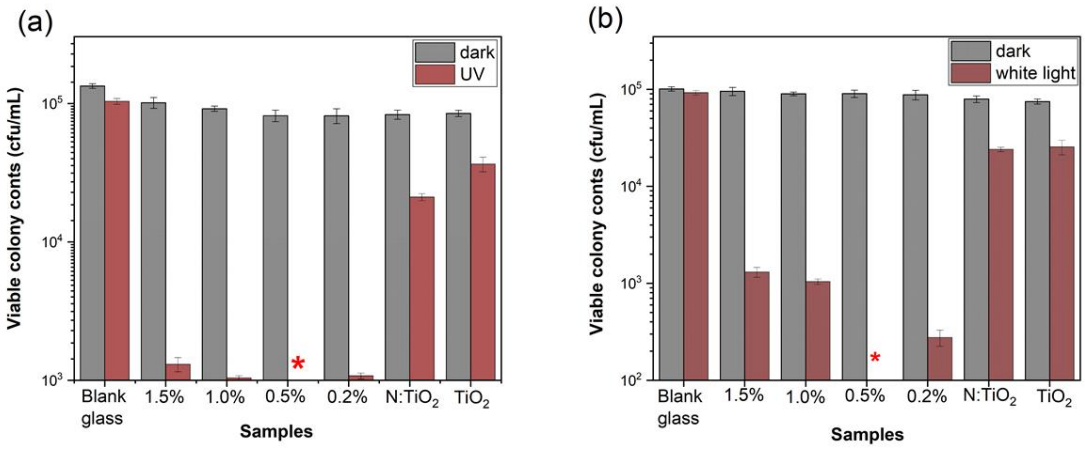

Figure 5.11 Viable counts of bacteria after incubation on Zn,N–doped titanium dioxide (TiO_2) at different zinc concentrations for *Escherichia coli* under ultraviolet (UV) A and white light. All the films were able to reduce the *E. coli* number to below the limits of detection after 8 h under UVA and the 0.5%Zn,N–doped TiO_2 was able to reduce the bacterial number to below the limits of detection after 18 h under white light.

5.3.9 Transient absorption spectroscopy (TAS)

TAS measurements were carried out under the same conditions discussed in chapters 2 and 4. The transient absorption spectra and decay of isolated undoped TiO_2, N:TiO_2 and the series of (N, Zn)–doped TiO_2 films were monitored in Ar atmosphere (i.e. an inert environment) in the wavelength range of 450–1000 nm; the samples were excited by a UVA laser (355 nm, 1.55 $mJ.cm^{-2}$.per pulse) and an inert atmosphere to prevent any chemical surface reactions (**Figures 5.12 and 5.13**). The TA decay kinetics of undoped anatase TiO_2 films are relatively similar to other TA decay data of anatase films that were examined previously.[140]

In undoped TiO_2 films, the highest signal was observed at wavelength 800 and 600 nm followed by 500 and 1000 nm respectively (**Figure 5.12(a)**) and the maximum absorption of undoped TiO_2 was ~0.31 mΔO.D. In addition, the recombination rate was slow at 600 and 800 nm compared with recombination rate at 500 nm. The highest recombination rate was at a wavelength of 1000 nm.

For N-doped TiO_2 and serial (N,Zn) doped TiO_2 films with different Zn concentrations, the highest absorption was observed at 500 nm; this decreased dramatically when the probe wavelength was increased. The maximum absorption of N-doped TiO_2 was ~0.17 mΔO.D. at 500 nm (**Figure 5.12b**), which is lower than that of undoped TiO_2. This decrease of the TA signal could be due to slow hole (h^+)–electron (e^-) recombination, and N-doped TiO_2 films showed a slower rate of decay in the photogenerated charge carrier than undoped TiO_2 thin films did; this could also be due to recombination occurs from an electron tunnelling process.

In series (Zn, N) doped TiO_2 films with different Zn concentrations (e.g. 0.2, 0.5, 1.0 and 1.5%). All the films showed increased absorption compared with undoped TiO_2 films at the examined wavelength.

The sample with (N,Zn(0.5%)) doped TiO_2 films revealed the highest absorption (~1.4 mΔO.D.) at 500 nm (**Figure 5.12d**), followed by the sample with N,Zn(1.0%)–doped TiO_2 films (~1.2 mΔO.D.). The samples with (N,Zn(0.2 and 1.5%)–doped TiO_2 films showed maximum absorptions at 500 nm of ~0.6 mΔO.D. and ~0.48 mΔO.D., respectively (**Figure 5.12c,f**).

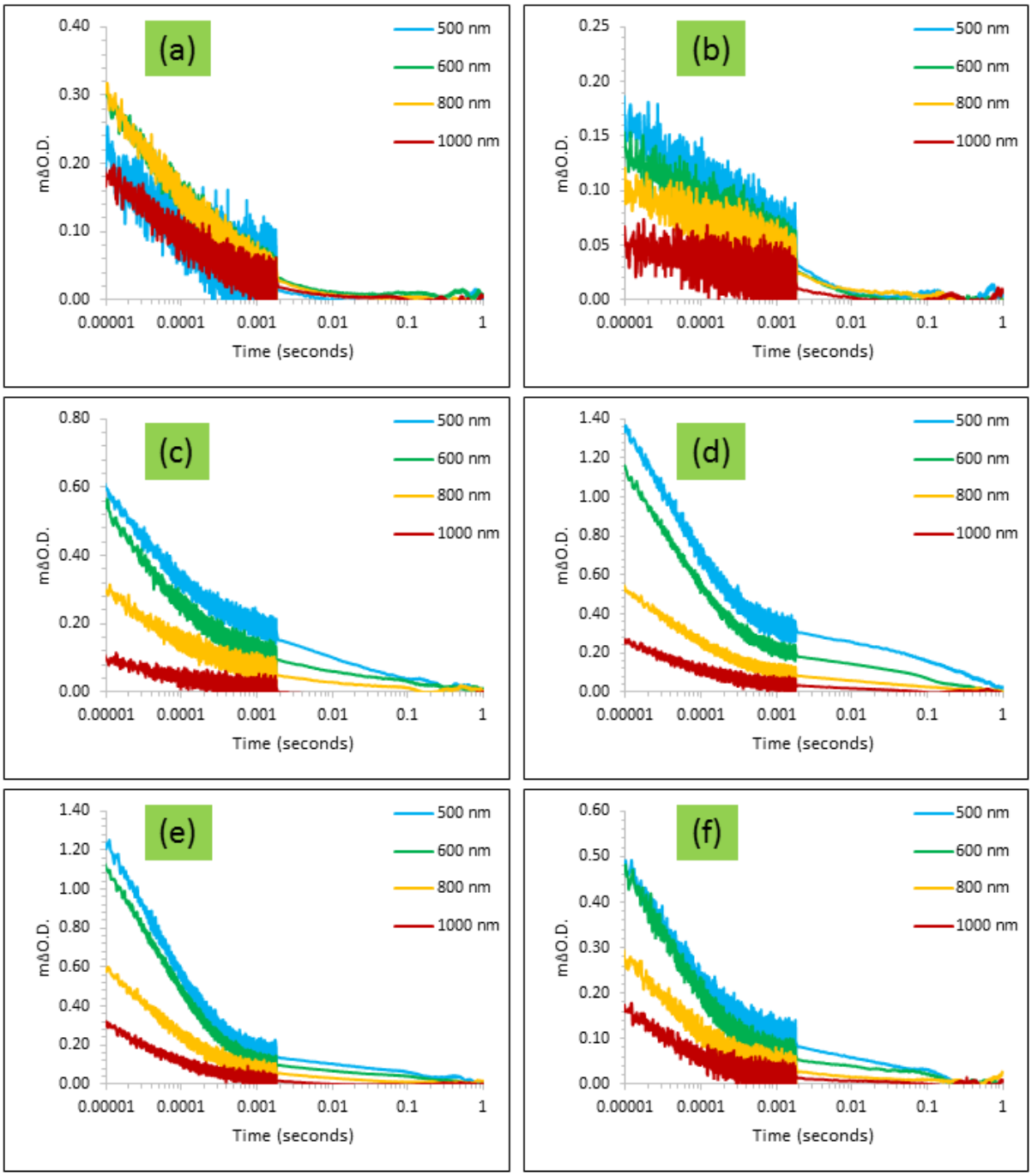

Figure 5.12. Transient absorption decay traces monitored in Ar, 355 nm laser (approx. 1 mJ.cm^{-2}, per pulse; pulse rate = 0.65 Hz), probe 500–1000 nm of (a) TiO_2, (b) N-TiO_2 and (Zn, N)–doped TiO_2 thin films with different Zn concentrations (0.2, 0.5, 1.0 and 1.5%; c, d, e and f).

Figure 5.13 shows the transient absorption decay at select wavelengths (450, 500, 600, 800 and 1000 nm). The highest absorption was for N,Zn(0.5)-TiO_2 along the timescale; the second

highest absorption was for N,Zn(1.0)-TiO_2 at a short time, and after 100 µs, the absorption of N,Zn(0.2)-TiO_2 increased. The decay kinetics of undoped TiO_2, N-TiO_2 and N,Zn(1.5)-TiO_2 were similar, which showed that the electron-hole recombination in these samples occurred at a similar rate at this wavelength.

At 500 nm, the decay kinetics was similar to that at 450 nm, but the decay kinetics of N,Zn(1.5)-TiO_2 increased compared with undoped TiO_2. The decay kinetics of N, Zn(0.5)–TiO_2 were similar to those of N,Zn(1.0)-TiO_2 at 600, 800 and 1000 nm; the only change was shown with undoped TiO_2. The rate of recombination was quantified, by finding the time where half the initial absorption was lost ($t_{50\%}$) at 800 nm. In the N doped TiO_2 sample, recombination was the slowest ($t_{50\%}$ ~ 294 µs), followed by the N,Zn(0.2%) ($t_{50\%}$ ~ 93 µs), N,Zn(0.5%) ($t_{50\%}$ ~ 80 µs), undoped TiO_2 ($t_{50\%}$ ~ 73 µs), N,Zn(1.0%) ($t_{50\%}$ ~ 55 µs) and N,Zn(1.5%) ($t_{50\%}$ ~ 53 µs).

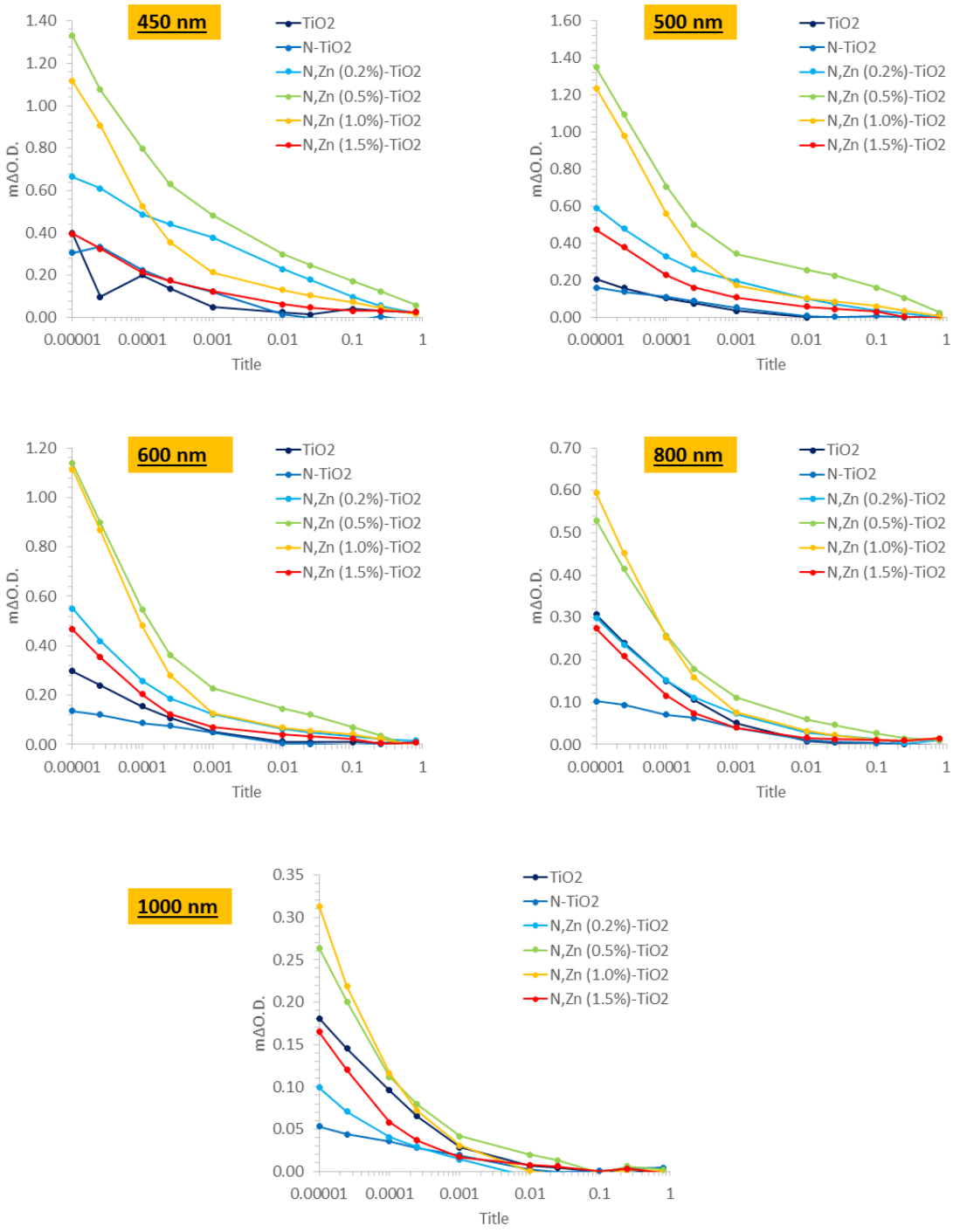

Figure 5.13 Comparison of transient absorption decay of al; samples at selected wavelengths, monitored in Ar, 355 nm laser (approx. 1 mJ.cm^{-2}, per pulse, pulse rate = 0.65 Hz).

Figure 5.14 shows transient absorption spectra of TiO_2, N-TiO_2 and the series of (N,Zn)–doped TiO_2 films recorded in an Ar atmosphere in the range of 450–1000 nm. The TA spectra were investigated at selected timescales (10 µs, 25 µs, 100 µs, 250 µs, 1 ms, 10 ms, 25 ms, 100 ms, 250 ms and 800 ms). In this study, the kinetics of electron–hole recombination was investigated by TAS. The transient changes in absorption were measured at 450–1000 nm. As mentioned above, studies have shown that the photogenerated electrons and holes in anatase exhibited broad absorptions centred at ~800 and 450 nm, respectively. All the samples showed an extended absorption across the visible spectrum that was typical of anatase TiO_2. The maximum absorption was at 450 nm for undoped, N-TiO_2 and (0.2% Zn, N)–doped TiO_2 films, and at 500 nm for (0.5, 1.0 and 1.5%Zn, N)–doped TiO_2 films **(Figure 5.14)**. Using chemical scavengers, a previous study showed that the absorption in this area is due to the presence of photogenerated holes.[140, 307] The increase in the absorption at longer wavelengths is due to the photogenerated electron around 800 nm for the anatase phase. By TAS measurement, we can follow the degree of hole transfer and find the holes' yields. However, the changes in the hole (h^+) yields was observed on the premeasurement/submicrosecond timescale. These spectra are similar to the literature on anatase, which typically shows a flatter spectrum over the visible region. The initial undoped TiO_2 thin films hole yields were lower than those of (Zn, N)–doped TiO_2 could be due to a lower extinction coefficient [136]**,** and at long select times of 10 ms, 25 ms, 100 ms, 250 ms and 800 ms, no recombination was observed.

Doping TiO_2 with Zn led to a decrease in the TA signal when the wavelength was increased, especially with 0.5% Zn dopants (**Figure 5.14c**). This was attributed to the zinc contribution in forming the photogenerated hole.

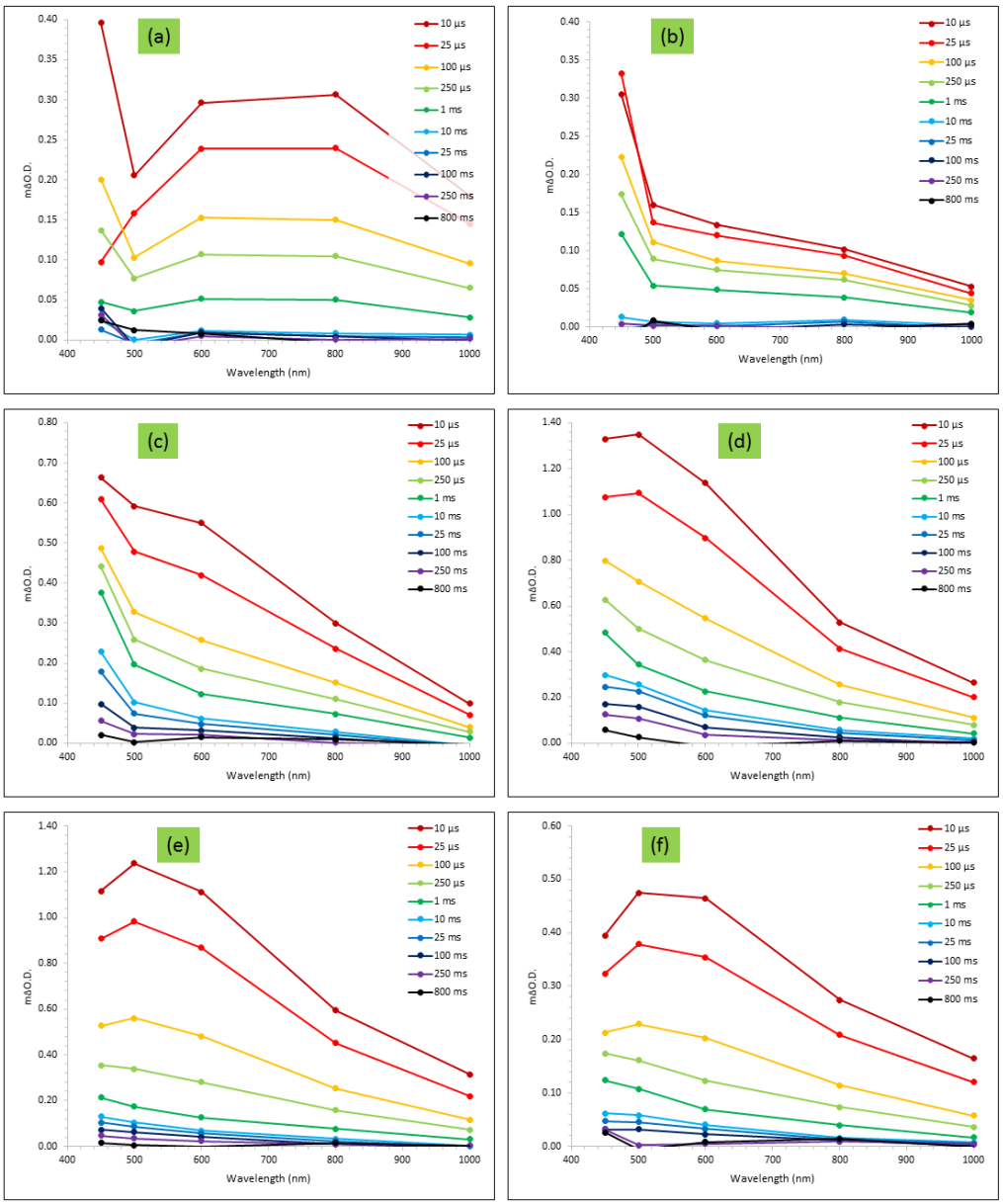

Figure 5.14 Transient absorption spectroscopy (TAS) spectra at select times for (a) TiO_2, (b) N-TiO_2 and (Zn, N)–doped TiO_2 thin films with different Zn concentrations (0.2, 0.5, 1.0 and 1.5%; c, d, e and f.

Figure 5.15 reveals the comparison of the samples for the transient absorption spectra for select times (10 µs, 1 ms and 250 ms) at a short pulse (10 µs). The N,Zn(0.5):TiO_2 and N,Zn(1.0):TiO_2 samples had similar photogenerated electron hole recombination. The N-TiO_2 thin films showed the lowest photogenerated electron hole recombination at this pulse. At a

high pulse (1 ms and 250 ms), the photogenerated electron hole recombination of N,Zn(0.5)-TiO_2 was increased compared with that of the other samples.

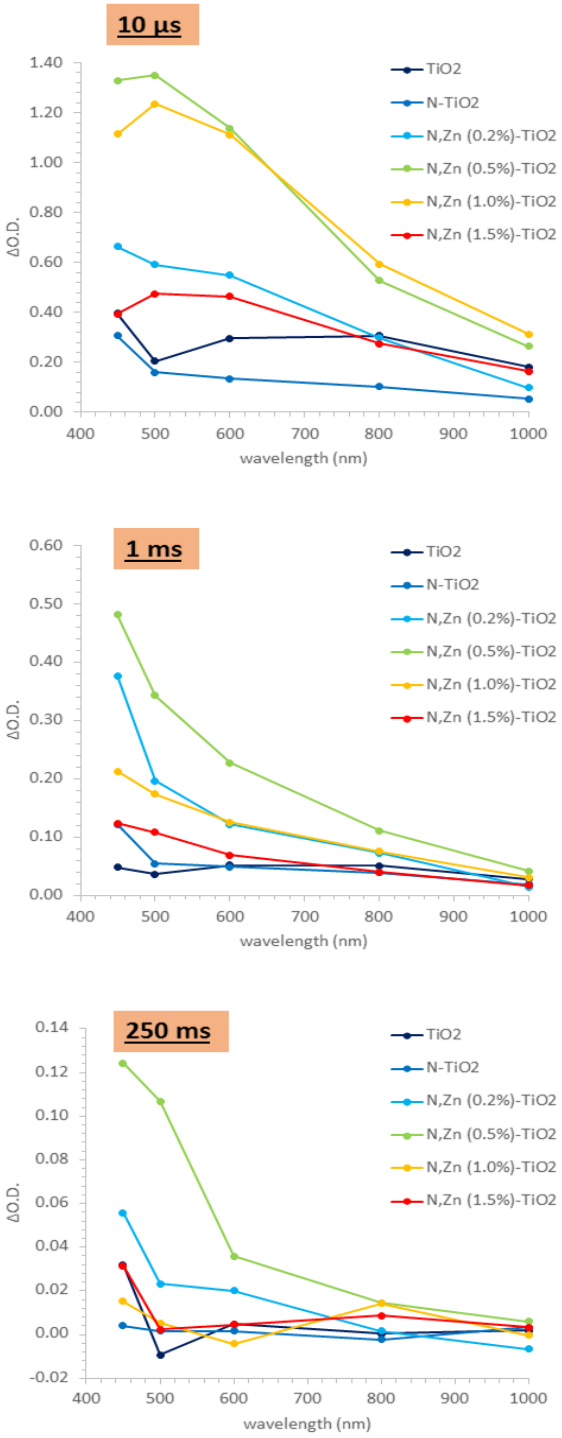

Figure 5.15 Comparison of transient absorption spectroscopy (TAS) spectra at select times (10 µs, 1 ms and 250 ms) of undoped TiO_2, N-TiO_2, N,Zn(0.2)-TiO_2, N,Zn(0.5)-TiO_2, N,Zn(1.0)-TiO_2 and N,Zn(1.5)-TiO_2 thin films.

As we can see in **Figure 5.16**, the N, Zn (0.5%):TiO_2 film showed a higher absorption at 10 μs than any other samples did. This absorption decay (due to the recombination of charge carriers) occurred in a bifunctional way, initially showing power law decay dynamics and later exhibiting a stretched exponential tail of decay. This may be attributed to the distribution of trap state energies in the material, with some being deeper in energy, resulting in a very long-lived photogenerated charge. Nevertheless, the charge carriers were longer lived in this co-doped system, with the optimal doping level being 0.5%. If we plot the absorption at 10 μs versus the doping level, we see the trend exhibited below.

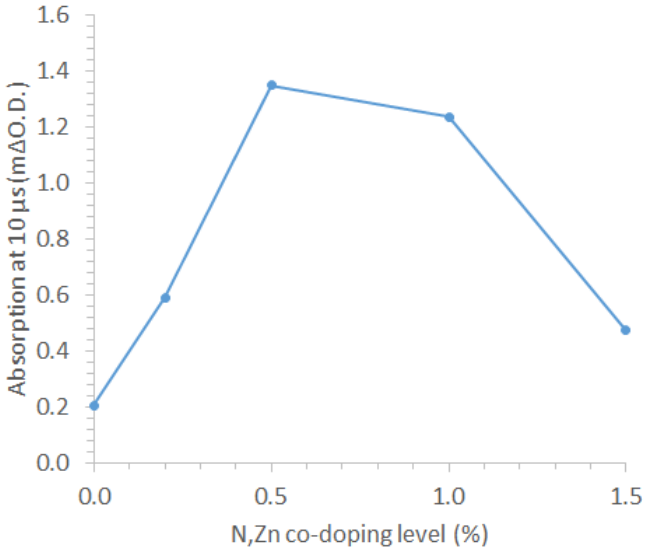

Figure 5.16. Transient absorption at 10 μs versus level of N, Zn co-doping %.

5.4 Conclusion

First, undoped TiO_2, N-doped TiO_2 and a series of (N,Zn)-doped TiO_2 thin films with different zinc concentrations were grown by AACVD on glass substrate at 500°C. Using N and zinc co-doped TiO_2 films, it was found that changes occurred in the functional properties of TiO_2, including physical properties, crystal structures and band gap. Excellent photocatalytic activity was achieved for the destruction of stearic acid as an organic pollutant due to zinc doping compared with undoped and N-doped TiO_2 under UVA light irradiation. In addition, good bactericidal activity was observed for killing *E.coli* under UVA and white light. The generation of superoxide ($O_2^{\bullet -}$) radicals from the surfaces of the samples was investigated using the reduction of XTT under UVA irradiation. An increased concentration of superoxide ($O_2^{\bullet -}$) from the surfaces of the (N, Zn)–doped TiO_2 thin films was observed; these were strongly linked to the bactericidal results. TAS was used to study the recombination kinetics and lifetime of all the thin films. The TAS results confirmed that the lifetime and charge carrier of the thin films were enhanced after zinc doping.

The next chapter, chapter 6, is divided into two parts. In the first part, AACVD is used to deposit Fe_2O_3 films on a glass substrate. TiO_2/Fe_2O_3 films are deposited on a glass substrate using the APCVD and AACVD methods, resulting in different TiO_2 thicknesses. The photocatalytic activities of these films are investigated via the degradation of stearic acid as a model of photocatalytic activity. The antimicrobial activities of these samples are tested against *E. coli* and *Staphylococcus aureus* under white light. In the second part of chapter 6, the films are deposited on FTO instead of a glass substrate. In this part, water splitting of these samples were examined and compared with the results for TiO_2 films. The transient absorption spectra are used to investigate the charge carrier and lifetime in these films.

Chapter 6

A study of the Influence of different TiO_2 Thicknesses on The Photocatalytic Efficiency of TiO_2/α-Fe_2O_3 Films

"In this chapter, the results of experiments which explore the deposition of TiO_2/α-Fe_2O_3 films on a glass substrate using aerosol-assisted chemical vapour deposition (AACVD), and atmospheric pressure chemical vapour deposition (APCVD) are presented. Different thicknesses of TiO_2 on α-Fe_2O_3 were studied to investigate their impact on photocatalytic and antimicrobial activity compared with pure hematite and titania. "In this chapter also, the extent to which different thicknesses of TiO_2 on α-Fe_2O_3 impact water splitting and the stability of hematite are investigated. A significant improvement in photocurrent density of the TiO_2/ α-Fe_2O_3 heterojunction was observed, and its stability was increased to 16 hours. Charge carrier recombination and lifetimes of TiO_2/α-Fe_2O_3 films were investigated using transient absorption spectroscopy (TAS). Compatibility between PEC results and TAS measures was seen."

A study of the Influence of different TiO_2 Thicknesses on the Photocatalytic and antimicrobial activity of TiO_2/ α-Fe_2O_3 Films

6.1 Introduction

Titanium dioxide (TiO_2) is well known, as it is the most widely researched photocatalytic semiconductor. This is due to its use in a wide range of applications, such as water splitting, degradation of organic pollutants, antimicrobial activity and water purification.[19, 142, 143, 308-311] It also has many advantages, including the fact that it is cheap, corrosion resistant, environmentally friendly and abundant.[312] TiO_2 has three amorphous structures, anatase, rutile and brookite,[253] and the optical bandgaps of anatase and rutile are relatively large (3.2 and 3.0 eV respectively),[28] resulting in photoreaction under UV illumination but not under the visible portion of sunlight. Another obstacle to its use as a photocatalyst is the high level of electron-hole recombination and low rate of photoreaction with reactants.[313] Surface area, crystallinity and particle size also play an important role in photocatalytic performance.[314]

Over the last few decades, extensive studies have been made on ways to decrease these bandgaps (anastase, rutile) and recombination rates. One useful approach to achieving a suitable bandgap and improving electron-hole separation, is to combine TiO_2 with metal or metal oxides. This is because, in photocatalytic activity, contact between two or more components tend to encourage the mobility of charge carriers between the semiconductors and promote separation, resulting in an improvement in photocatalytic activity compared with a single semiconductor. As α-Fe_2O_3 has a lower optical bandgap (2.1 eV)[315], combining or doping α-Fe_2O_3 with TiO_2 gives improved morphological and optical properties, as well as leading to a shift in bandgap toward the visible region. Such a coupling is therefore a promising approach for enhancing the efficiency of TiO_2 for photocatalytic activity. Possible mechanisms are:

i) Under visible light, electrons cannot be excited from the VB to CB of TiO_2 to generate electron/hole pairs. This, however can happen with α-Fe_2O_3 (2.2 eV) under visible light. Consequently, electrons from the CB of α-Fe_2O_3 can be transferred to the CB of TiO_2. Furthermore, holes which accumulate in the valence band of Fe_2O_3 will react with OH^- species to product active hydroxyl radicals ($^{\cdot}OH$), while electrons on the CB band of TiO_2 can react with O_2 to generate hydrogen peroxide (H_2O_2) and superoxide anions (O^{2-}).[316]

ii) Under UV irradiation, electron-hole pairs will be generated on the VB and CB of TiO_2 respectively. The charge transfer from the CB of TiO_2 to the CB of Fe_2O_3 in the interface region, due to the CB edge of TiO_2 (- 0.12 V vis NHE at pH = 0) is more negative than that of Fe_2O_3 (0.46 V vis NHE at pH = 0).[317] In addition, photogenerated holes transfer to the VB of Fe_2O_3, because Fe_2O_3 acts as a recombination centre.[315, 317]

Various synthetic methods were used to synthesise TiO_2, including chemical vapour deposition techniques[318-320], sol-gel,[321-324] electrochemical deposition[325], hydrothermal[326] and spray pyrolysis[327]. However, it is important to note that the deposition of TiO_2 or Fe_2O_3 by chemical vapour deposition has many advantages, such as the use of a single source, good crystallinity, excellent uniformity and high purity.[120]

In this chapter, we demonstrate a new way of synthesising TiO_2/α-Fe_2O_3 films using one-step, aerosol-assisted chemical vapour deposition (AACVD) for α-Fe_2O_3 films, and *atmospheric pressure chemical vapour deposition (APCVD)*, for TiO_2 films. As AACVD depends on solubility rather than the volatility of precursors, it allows a wider range of precursors to be employed. It is also a technique that has been used, at atmospheric pressure, to grow a wide range of films for various applications with the potential to upscale. It should also be noted that APCVD has been used to make different thicknesses of TiO_2 by using different deposition times.

6.2 The experiments

6.2.1 General procedure

All chemicals used in these experiments were supplied by Sigma-Aldrich Chemical Co. and were used as received. Deposition was on 150 × 45 × 45 mm float-glass, supplied by Pilkington NSG, coated with SiO_2 (50 nm). This acts as a barrier layer, preventing the diffusion of ions from within the glass into the deposited film. Prior to use, the glass substrates were thoroughly cleaned using acetone (99 %), isopropanol (99.9 %) and distilled water, then dried in air.

6.2.2 Deposition conditions

[0.23 g, 0.905 mmol] of Iron(II) acetylacetonate $Fe[CH_3COCH=C(O)CH_3]_2$ was dissolved in 60 ml of ethylacetate in a glass bubbler. Aerosol-assisted chemical vapour deposition (AACVD) was then used to deposit α-Fe_2O_3 thin films on a glass substrate **(Figure 6.1)**. The mist was transferred to the reactor using nitrogen (BOC Ltd., 99.99%) with a flow rate of 1.4 L min^{-1} , and deposition continued for 40 minutes at 450°C. After deposition, the reactor was left to cool, in N_2, to room temperature before the films were removed and then annealed at 500ºC in nitrogen at 2 L.min-1 for 30 mins to remove carbon contamination.

At this stage, 40 ml of Titanium(IV) isopropoxide $[Ti(OCH(CH_3)_2]_4$ was added in a glass bubbler. atmospheric pressure chemical vapour deposition *(APCVD)* was used to deposit TiO_2 films on a glass substrate and α-Fe_2O_3 films as a second layer. At the same time, Titanium(IV) isopropoxide was heated in a glass bubbler to approx. 120°C and the vapour transferred to the reactor via nitrogen (BOC Ltd., 99.99%) with a flow rate 4 L $min^{-1.}$ Deposition was allowed to continue at 450 °C for TiO_2 and TiO_2/α-Fe_2O_3 for different deposition times (4, 8 and 12 min) on glass substrate then annealed at 500°C for 30 mins **(Figure 6.1)**.

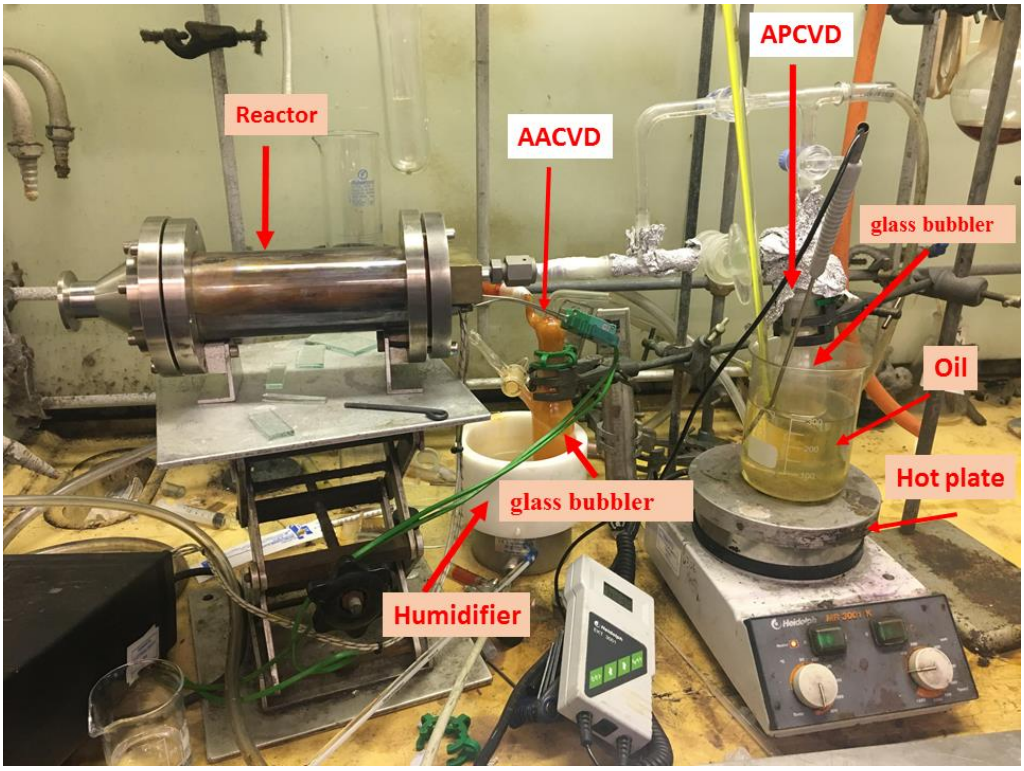

Figure 6.1. The AACVD rig used for hematite deposition and APCVD rig used for titania deposition.

6.3 Film characterization

Photoluminescence (PL) spectra from 350-800 nm were obtained using an Edinburgh spectroflourometer with an average power of 5mW. The excitation wavelength used was 380 nm.

6.4 Photocatalytic activity

0.05 molar of stearic acid (95%, Sigma-Aldrich), dissolved in chloroform, was used as a model for photocatalytic performance. Samples were coated with a thin layer of this solution using a bespoke apparatus. Pilkington NSG^{TM} Activ^{TM} glass was used as a benchmark, and blank float glass as a control. The samples were left for one hour to evaporate of chloroform before use. Photocatalytic activity of films was monitored by Fourier transform-infrared (FT-IR) spectroscopy using a PerkinElmer RX-I. The IR spectrum of each acid-over layer was recorded

over the range 2700 - 3000 cm^{-1} and the areas of the peaks between 2870 - 2950 cm^{-1} and 2830 - 2870cm^{-1} were integrated. These peaks respectively represent the C–H antisymmetric and symmetric stretches of stearic acid and can be directly related to the concentration of stearic acid on the film's surface. The samples were illuminated using white light with an intensity of 4500 Lux. The IR spectrum of each acid-over layer was then recorded over the same range (2700 - 3000 cm^{-1}).

6.5 Antimicrobial performance

Two species of bacteria were used to investigate the bactericidal activity of the samples - *S. aureus* (8325-4) and *E. coli* (ATCC 25922). A single colony of both bacteria was used to inoculate two separate (10 mL) aliquots of sterile BHI broths (Oxoid, Basingstoke, UK), which were incubated aerobically for 18 hours at 37°C, with shaking at 200 rpm. Bacteria from the overnight culture were centrifuged at 3000 x g for 15 minutes to harvest the bacteria, then washed in 10 mL of PBS (phosphate-buffered saline) sourced from Oxoid (Basingstoke, UK), and again centrifuged at 3000 x g for 15 minutes before being re-suspended in 10 ml of PBS. Suspensions (10µL) of the bacteria were then added to 10 ml of (PBS) to give approximately 10^6 CFUs (colony forming units) per mL for each 25 µL aliquot.

Prior to use, α-Fe_2O_3, TiO_2 and TiO_2/α-Fe_2O_3 film and glass controls were cut into 1.5 x 1.5 cm sections, and a humidity chamber was created to ensure that the suspensions did not dry out. For each exposure time (4 and 8 hours), three samples were placed in the humidity chamber, and 25 µL of the suspensions spread evenly on the surface of each slide and incubated at room temperature (21 ± 2°C). The samples were then exposed to white light for 4 and 8 hours, while another set of samples were placed in the dark for the same time periods. The intensity of the white light ranged from 6000 to 9000 Lux **(Figure 6.12)**. After exposure, the samples were added to 5 mL of PBS and blended using a vortex mixer. 100 µL of the bacterial suspension was then plated on agar (mannitol salt agar for S. aureus; MacConkey for E. coli)

for viable counts, and incubated aerobically at 37°C for 24 hours. After incubation, the bacterial colonies were counted and viable counts calculated.

6.6 Results and discussion

Figure 6.2 shows the films that were deposited using AACVD and APCVD. TiO_2 films had rainbow-like colouring, due to birefringence (left), while α-Fe_2O_3 appeared reddish (right). However, all films showed good stability in common solvents such as ethanol, methanol, chloroform and isopropanol. In addition, they had a good stability when stored for a long time under ambient conditions and remained firmly adhered to the substrate, passing the Scotch tape test.

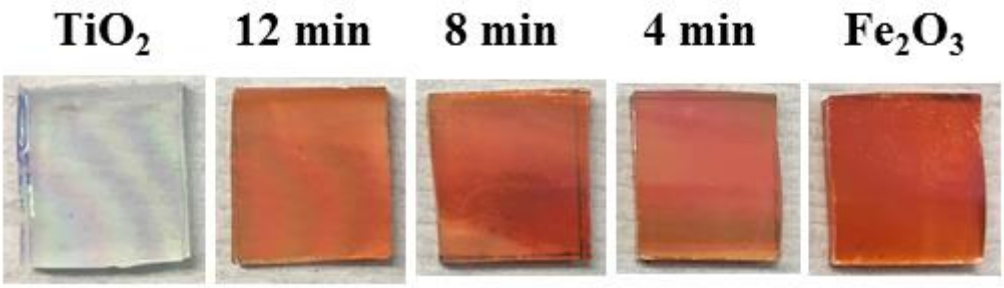

Figure 6.2 TiO_2, α-Fe_2O_3 films and a series of TiO_2/ α-Fe_2O_3 layers with deposition times of 4, 8 and 12 min on glass. All samples were deposited at 450°C and annealed at 500°C.

6.6.1 X-ray diffraction (XRD) and Raman spectroscopy

Powder X-ray diffraction (PXRD) was used to analyse the TiO_2/α-Fe_2O_3, pure α-Fe_2O_3 and pure TiO_2 films **(Figure 6.3a)**. These showed iron oxide in the α-Fe_2O_3 phase, with reflections at (012), (104), (110), (113), (024), (116) and (214) at 2θ values of 24.2°, 33.1°, 35.5°, 40.8°, 49.4°, 54.1° and 62.5° respectively. These results are in a good agreement with reference data for the α-Fe_2O_3 phase.[328, 329] No peaks for other iron oxide phases were observed. PXRD results for pure TiO_2 showed a typical anatase phase, with reflections at (101), (112), (200) and (204) at 2θ values of 25.3 °, 38.6 °, 48.0 °, 55.1 ° and 62.8° respectively.[226] The TiO_2/α-Fe_2O_3 films,

with different thicknesses of TiO_2, showed a TiO_2 anatase phase, and no peaks were observed for α-Fe_2O_3 films with deposition times of 8 and 12 min. For the film with a deposition time of 4 min, a peak for α-Fe_2O_3 was seen as TiO_2 layer was thin enough to see the α-Fe_2O_3 peak.

Figure 6.3b shows Raman spectra of TiO_2/α-Fe_2O_3, pure α-Fe_2O_3 and TiO_2 films. Raman peaks of Fe_2O_3 films appeared at 225 cm^{-1} (A_{1g}), 245 cm^{-1} (E_g), 292 cm^{-1} (E_g), 410 cm^{-1} (E_g), 502 cm^{-1} (A_{1g}), 497 cm^{-1} (E_g) and 612 cm^{-1} (E_g). TiO_2 films in the anatase phase showed peaks at 141.5 cm^{-1} (E_g), 397 cm^{-1} (B_{1g}), 514 cm^{-1} (A_{1g}) and 635 cm^{-1} (E_g). The TiO_2/α-Fe_2O_3 films showed peaks for TiO_2 in the anatase phase and for α-Fe_2O_3. However, Raman spectra is consistent with XRD results for iron oxide in the hematite phase and TiO_2 in the anatase phase.

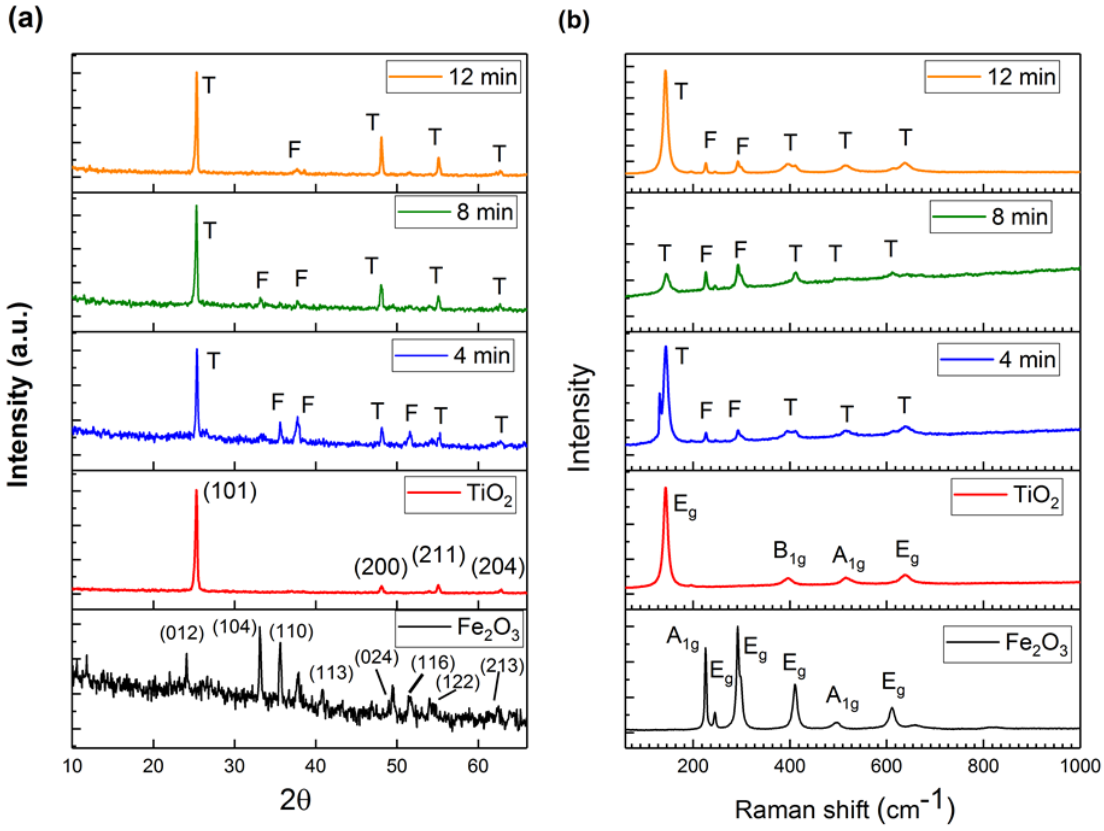

Figure 6.3, (1a). Powder x-ray diffraction (PXRD) patterns of α-Fe_2O_3, TiO_2, TiO_2/α-Fe_2O_3 layers film with different TiO_2 thicknesses. (1b) illustrates Raman spectra (using a laser wavelength of 633 nm) of all these films. The α-Fe_2O_3 film was deposited by AACVD at 450 °C on glass substrate and annealed at 500°C, while the pure TiO_2 and TiO_2 on α-Fe_2O_3 films were deposited by APCVD at 450°C and annealed at 500°C with different deposition times (4, 8 and 12 min)

6.6.2 Scanning Electron Microscopy (SEM)

SEM was used to investigate the morphology of samples (**Figures 6.4A-E**). The results showed that α-Fe_2O_3 films had a flat surface consisting of spherical particles with an average diameter of 150 - 300 nm**,** while TiO_2/α-Fe_2O_3 (4 min deposition time) films were an aggregation of spherical particles with average diameter of 500 – 850 nm. TiO_2/α-Fe_2O_3 (8 min deposition time) consisted of particles with an average size of around 100 – 200 nm**,** while TiO_2/α-Fe_2O_3 (12 min deposition time) films were quite similar, in morphological terms, to the TiO_2/α-Fe_2O_3 (4 min) sample, with an average particle size of around 300 – 500 nm. Pure TiO_2 showed densely packed particles ranging from 200 to 400 nm**.**

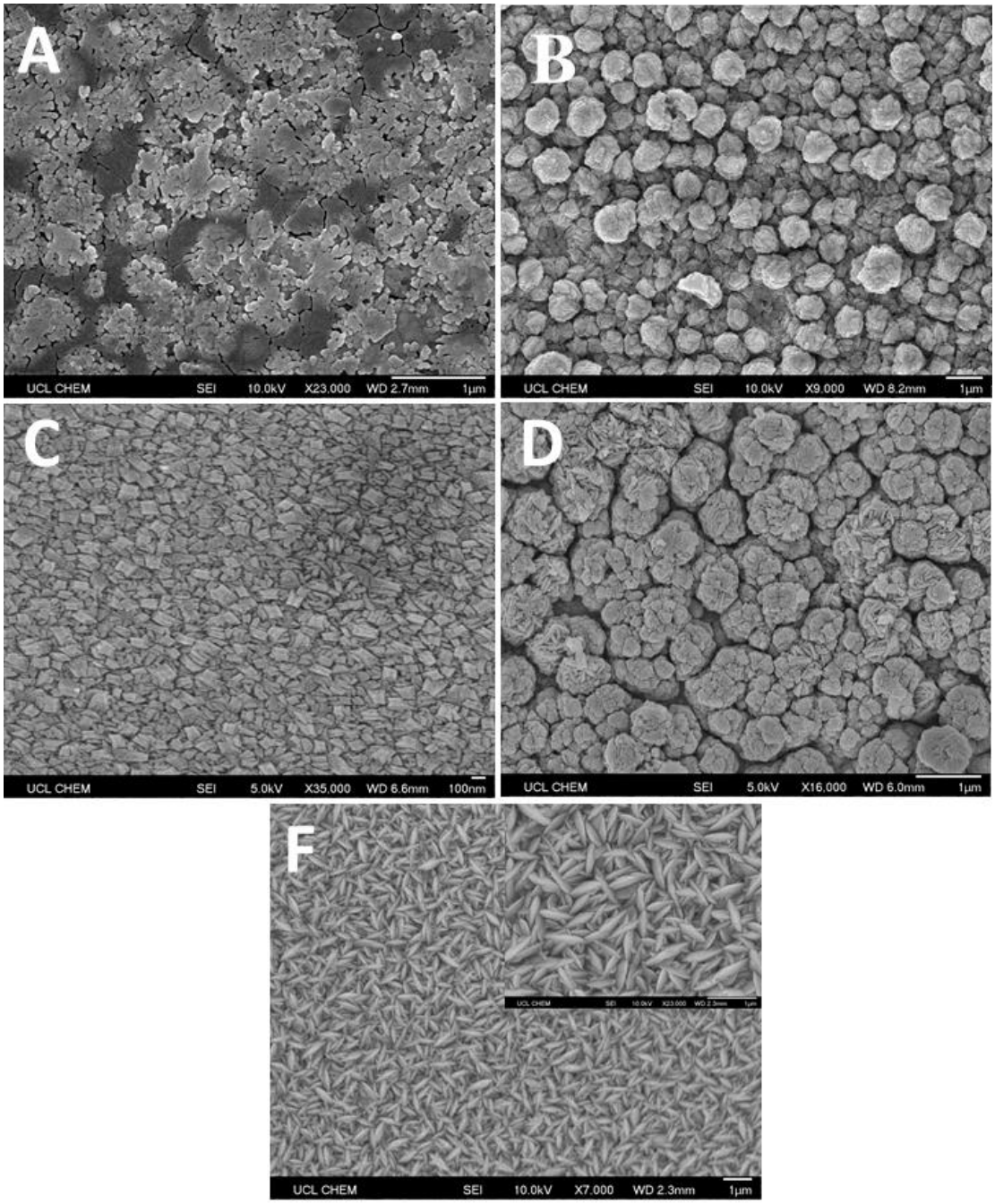

Figure 6.4: SEM images of A) pure α-Fe_2O_3, B) TiO_2/α-Fe_2O_3 (4 min), C) TiO_2/Fe_2O_3 (8 min), D) TiO_2/α-Fe_2O_3 (12 min)e) and pure TiO_2, grown using AACVD and APCVD from [$Ti(OCH_2CH_2CH_2CH_3)_4$] and $Fe[CH_3COCH=C(O)CH_3]_2$.

6.6.3 UV-Vis spectroscopy

The optical properties of the series of TiO_2/Fe_2O_3 films, and pure Fe_2O_3 and TiO_2 films, were studied by UV-Vis spectra, **Figure 6.5(A)**, shows the bandgaps of these films, calculated using Tauc plots.[236] The bandgaps of Fe_2O_3 and pure TiO_2 are approximately 1.95 eV and 3.2 eV

respectively, while the TiO_2/Fe_2O_3 films have bandgaps of 2.1, 2.1 and 1.78 eV for deposition times of 4, 8 and 12 min respectively. **Figure 6.5(B)**, shows the absorption spectra of all films. Absorption of pure TiO_2 occurs around 380 nm, as expected, while pure Fe_2O_3 and TiO_2/Fe_2O_3 films with deposition times of 4 and 8 min absorb at around 600 nm, with absorption extending across the visible region. Absorption for the TiO_2/Fe_2O_3 film (12 min) showed a slight shift towards the visible region, to around 650 nm.

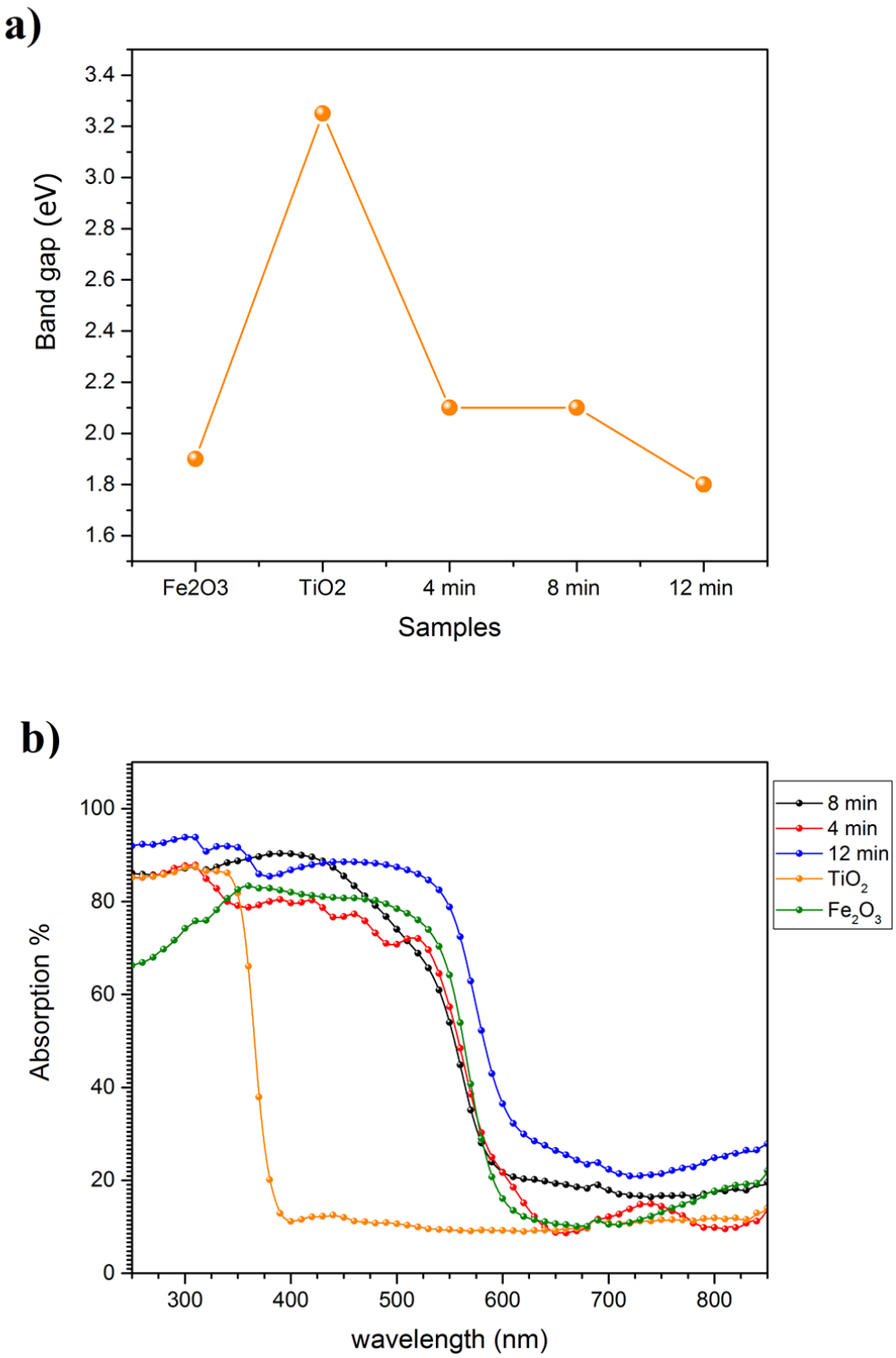

Figure 6.5. UV-Vis spectra of pure α-Fe_2O_3 , TiO_2 and TiO_2/α-Fe_2O_3 layers films, a) Shows bandgaps calculated by Tauc plots, b) shows the absorption spectra of all films - pure TiO_2 absorbs around 380 nm and pure α-Fe_2O_3 around 600 nm.

Figure 6.6 shows UV-Vis transmission spectra for all samples, showing expected interference fringes for TiO_2 and α-Fe_2O_3 based films. Transmission of TiO_2 films is around 72% for wavelengths between 380 – 780 nm, but this increases to about 83% in the near infrared. The transparency of hematite deposited by AACVD shows a transparency lower than TiO_2 films in the visible region, while, in the near infrared, it fluctuates between 72 – 63%. The transmission spectra of TiO_2/α-Fe_2O_3 films with a deposition time of 12 min show the lowest transparency value in the visible region (500 – 760 nm), while the TiO_2/α-Fe_2O_3 (4 min) sample shows a slight increase in transparency value in the region 700 -2500 nm, compared with pure TiO_2 films.

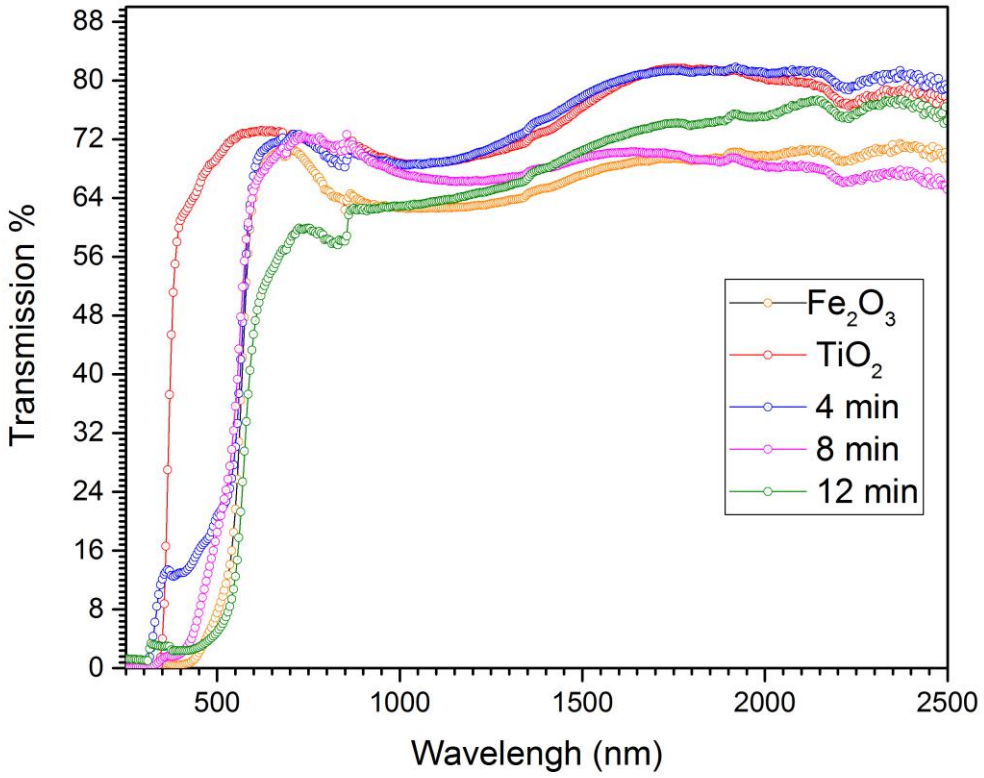

Figure 6.6 Transmission spectra of α-Fe_2O_3, TiO_2 and TiO_2/α-Fe_2O_3 layers films on glass substrate

6.6.4 X-ray Photoelectron Spectroscopy (XPS)

X-ray Photoelectron Spectroscopy (XPS) was used to study chemical states and valence bands of all Fe and Ti films, at surface level. The high-spin $2p_{2/3}$ peak in Fe^{2+} and Fe^{3+} is considerably broader than the low-spin Fe^{2+} or $Fe^{(0)}$ [330]. This broadening has been shown by Gupta and Sen to be caused by:

(1) Unpaired 3d electrons of the photo-ionised Fe cation

(2) Spin orbit coupling between the 2p core hole

(3) The inclusion of crystal field and electrostatic interactions[331, 332].

According to the Gupta and Sen Study, supported by others[333, 334], Fe $2p_{3/2}$ peaks were fit using the multiplet structure calculation. They found that the Fe $2p_{3/2}$ envelope in α-Fe_2O_3 can be fit to four spectra - 709.8, 710.7, 711.4 and 712.3 eV. Additionally, a satellite peak is found at approximately 719 eV, caused by charge transfer processes and shake- up[333]. A surface peak, caused by surface structure, is located at ~715 eV.

The Fe spectrum fitted with the Gaussian–Lorentzian function, and exhibiting Fe 2p binding energies, corresponded to Fe^{3+}, with $2p_{3/2}$ centered at 709.2, 710.1, 710.6, 711.7 and 712.7 eV, with pre-peak at 708.1 and a satellite peak at 719.1 eV. This compared well with our samples, as shown in (**Figure 6.7a).**

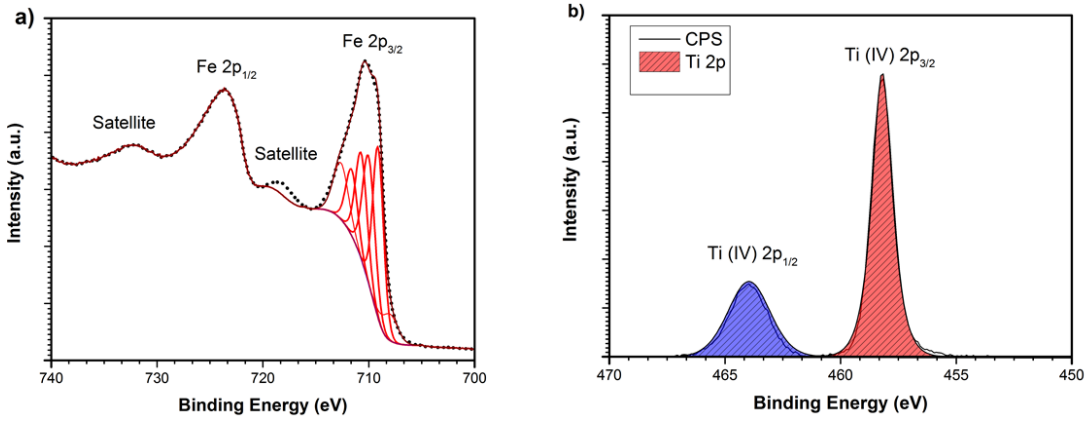

Figure 6.7 Surface X-ray photoelectron spectra (XPS) in the Fe 2p environment of: (A) α-Fe_2O_3, (B) Ti was in the 4+ oxidation state for all films with $2p_{3/2}$ peaks cantered around 458.3 eV.

The XPS results for Ti 2p in pure TiO_2 and the α-Fe_2O_3 series showed peaks at binding energies of 458.9 eV and 464.6 eV which corresponded to Ti-O bonds of Ti^{4+} in the TiO_2 lattice (**Figure 6.7b)**. The $2p_{3/2}$ peaks were higher than the $2p_{1/2}$ peaks, due to the fact that $2p_{1/2}$ has degeneracy in two states, while $2p_{3/2}$ has four states in spin orbit (j–j) couplings. In addition, no Ti^{3+} peak was seen in any of the samples. In future work, it will be necessary to confirm the chemical environment of the atoms, using, for example, X-ray absorption fine structure spectroscopy (EXAFS).

Figure 6.8 shows XPS spectra of the VB region of Fe_2O_3, TiO_2 and TiO_2/α-Fe_2O_3 films with different TiO_2 thicknesses. While all VB spectra consist of a main band from 0 to around 10 eV, the VB spectra of the α-Fe_2O_3 film also has three bands at approximately 2.3 , 4.8 and 7.5 eV, which is compatible with the VB of α-Fe_2O_3[334] . The VB spectra of TiO_2 and TiO_2/α-Fe_2O_3 films with different deposition times (4, 8 and 12 min) consist of two peaks (at approximately 4.2 and 7.5 eV), with a slight shift in the binding energy when the TiO_2 film thickness is greater than with pure TiO_2 film. The most notable difference between the VB spectra of α-Fe_2O_3, TiO_2 and TiO_2/α-Fe_2O_3 samples is the intensity. The VB intensity of α-Fe_2O_3 is higher than that of TiO_2 or TiO_2/α-Fe_2O_3, though, in the case of α-Fe_2O_3, the VB shows a Fe 3d (t_{2g} and e_g orbital symmetry) and O 2p hybridised state, as well as the O 2p valence state. Furthermore, the two peaks at the lowest energy (2.3 and 4.8eV) correspond to excitations of $3e_g$ and $2t_g$ orbitals respectively. The third peak is located at around 7.5 eV, which is the $2e_g$ orbital[334]. In addition, the O 2p peaks overlap with 4d orbitals, which is the O 2p state located at around 7.0 eV, and the O 2p σ, overlap with e_g peaks[335] . On the other hand, the VB spectra of TiO_2 films consist of the e_g and t_{2g} states, located at 7.5 and 4.2 eV respectively, as a result of O 2p orbitals[336]**.**

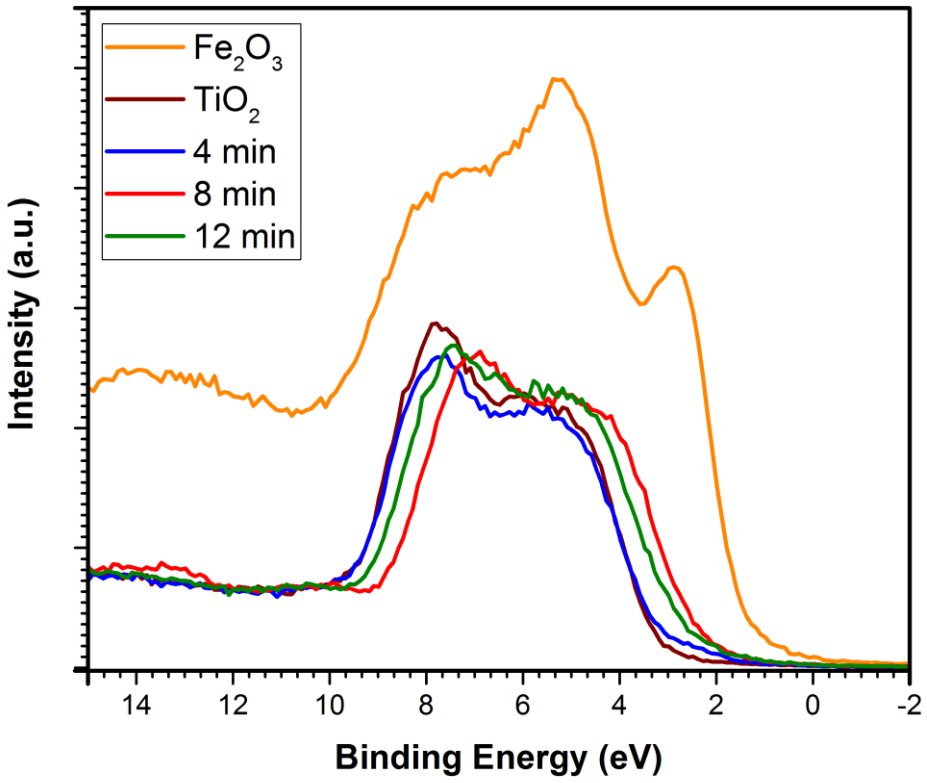

Figure 6.8 The valence band XPS of pure Fe_2O_3, TiO_2 and TiO_2/Fe_2O_3 films with deposition times of 4, 8 and 12 min. VB spectra show a decrease in the band onset at high TiO_2 thickness.

6.6.5 Photoluminescence spectra (PL)

The steady state photoluminescence (PL) spectra of α-Fe_2O_3 and TiO_2/α-Fe_2O_3 films are shown in **Figure 6.9**, in the wavelength range from 450 to 900 nm, with an excitation wavelength of 405 nm. All films exhibit three broad peaks, centered at approximately 525, 570 and 815 nm. The peak centered at 570 nm (2.1 eV) could be due to normal band edge emission, which implies radiative recombination (t_{2g} e_g), while the peak at 525 nm (2.3 eV) is due to the size-induced quantum confinement effect[337]. The peak at 815 nm (1.5 eV) can be attributed to oxygen vacancy that leads to electron traps, or electronic band structure[338].

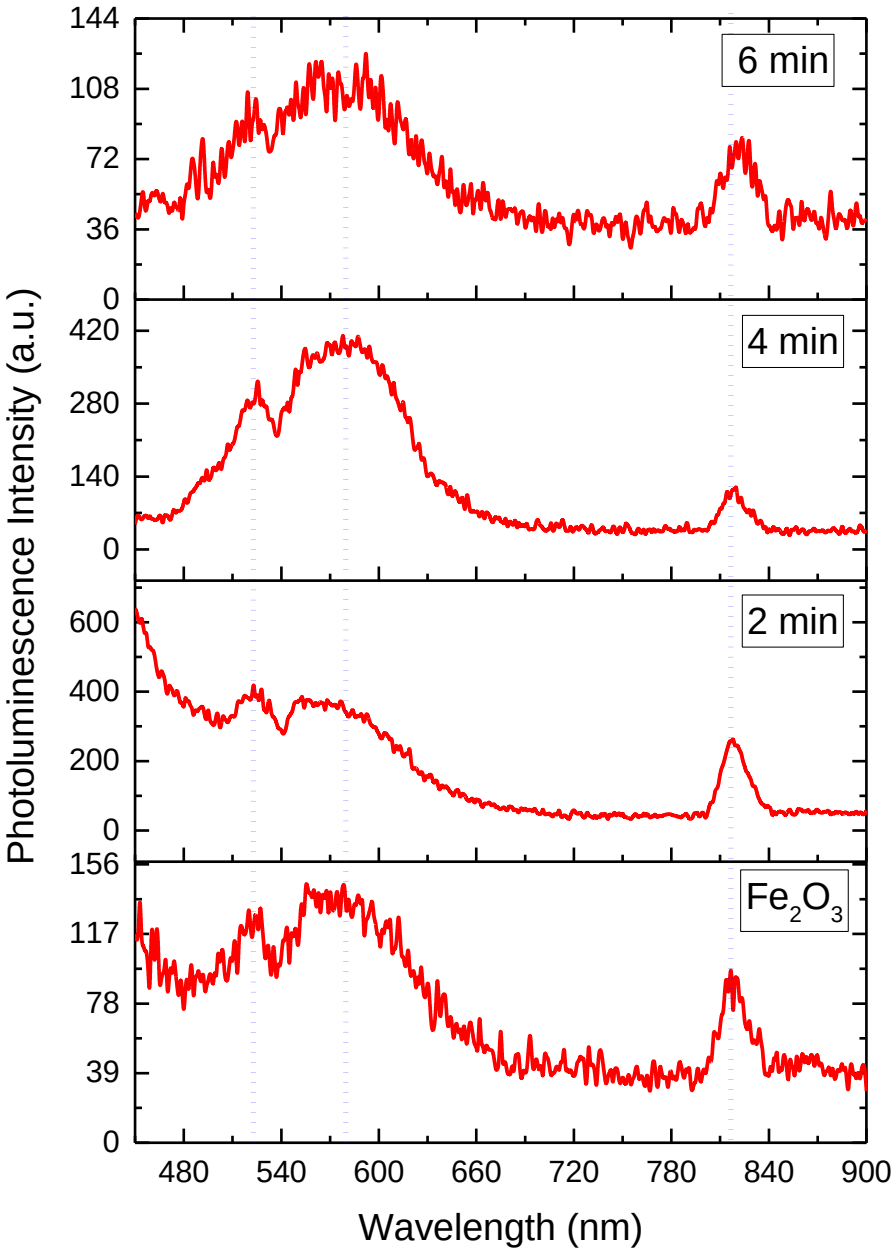

Figure 6.9 The PL spectra of α-Fe_2O_3 and TiO_2/α-Fe_2O_3 with different thicknesses of TiO_2 films. Excitation wavelength was 405 nm.

6.6.5.1 Time Resolved Photoluminescence Spectra (TRPL)

For further study, the photogenerated kinetic TRPL spectra of α-Fe_2O_3 and TiO_2/α-Fe_2O_3 films were used to investigate the PL lifetime. The PL spectra was fitted to a bi-exponential decay function, using equation (1).

$$f(t) = \sum A_i \exp(-t/\tau_i) + K \qquad (1)$$

Here, τ_i is the time of decay, A_i is the amplitude of decay and the constant K is the baseline offset. TRPL spectra showed that the decay time of pure hematite is 4 ns **(Figure 6.10)**. The TiO_2/α-Fe_2O_3- (4 min) sample had a similar decay time (to hematite), while the longest decay time (8ns) was found to be for TiO_2/α-Fe_2O_3- (12 min). The TiO_2/α-Fe_2O_3- (8 min) sample had a decay time of around 7 ns. However, decay time depends on the density of TiO_2/Fe_2O_3, rather than Fe_2O_3, as TiO_2/Fe_2O_3 leads to better charge separation. So TiO_2/Fe_2O_3 films have a longer decay time than pure Fe_2O_3. This is a key insight to the improvement of photocatalytic activity.

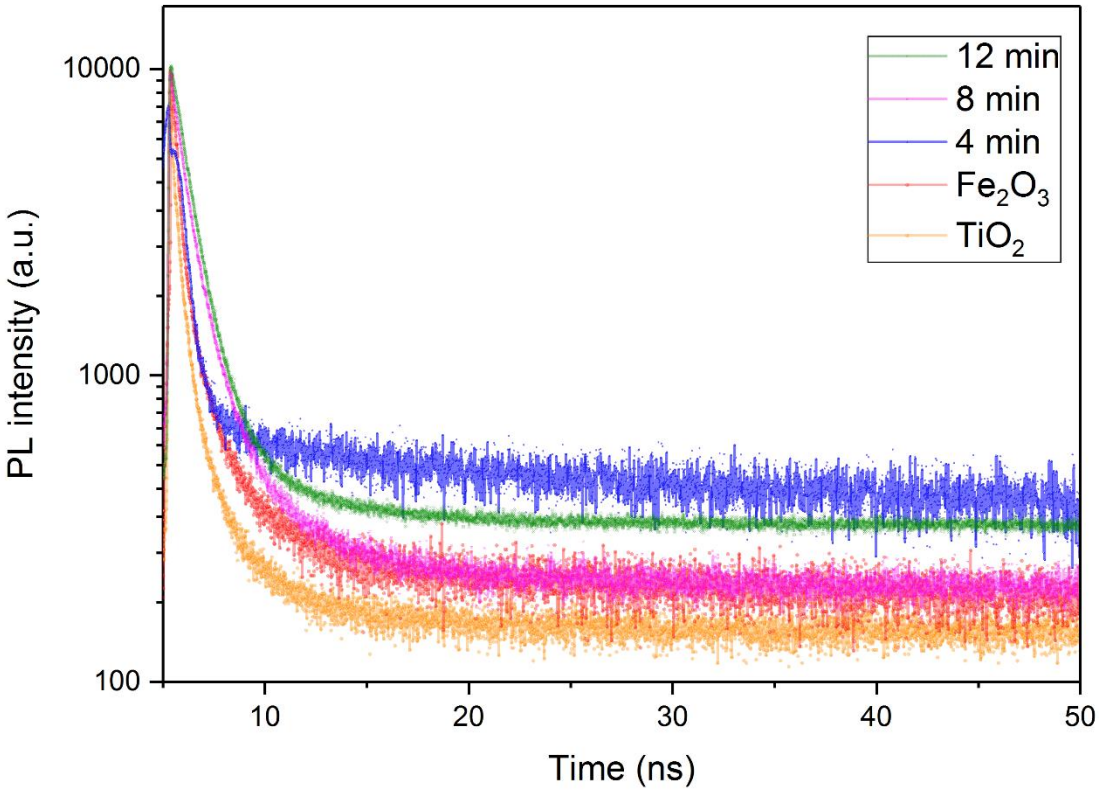

Figure 6.10: Time-resolved photoluminescence spectra for α-Fe_2O_3, TiO_2 and TiO_2/α-Fe_2O_3 films with different deposition times (4, 8 and 12 min).

6.6.6 Functional properties

6.6.6.1 Photocatalytic activity

Photocatalytic properties of α-Fe_2O_3, TiO_2 and TiO_2/α-Fe_2O_3 films with different deposition times (4, 8 and 12 min) were determined by the destruction of stearic acid by exposure to white light. Stearic acid was used due to its high stability under white light and UV illumination. The destruction of stearic acid was followed by a reduction, over time, in area of the characteristic peaks at 2958, 2923 and 2853 cm^{-1}. The reaction can be described by:

$$CH_3(CH_2)_{16}CO_2H + 26O_2 \xrightarrow{TiO_2(hv \geq Eg)} 18CO_2 + 18H_2O \quad (6.2)$$

Photocatalytic rates were estimated from linear regression of the initial steps (30 – 40%) of the graph of area *vs.* illumination time. A (blank) piece of glass was used as a control, and Pilkington Activ^{TM} self-cleaning glass (with 15 nm TiO_2 anatase coating) was also tested for comparison.

The sample TiO_2/Fe_2O_3 films with different deposition time (4, 8 and 12 min) showed improved photocatalytic efficiency compared with pure TiO_2 and α-Fe_2O_3 under exposure to white light **(Figure 6.11)**. The best photocatalytic performance was observed for the TiO_2/α-Fe_2O_3 sample with a deposition time of 12 min. This performance was 9 times better than that of pure TiO_2 films.

This is not surprising when we consider that the depositon of TiO_2 on α-Fe_2O_3 films leads to a shift in the absroption spectra to the visible region **(Figure 6.5,b)** and increases both particle size and crystallinity, as seen with SEM **(Figure 6.4)**. In addition, photocatalytic performance correlates directly with photo-generated charge carrier lifetimes, as shown in the PL results (**Figure 6.10**), where high lifetime resulted in high photocatalytic activity.

However, as has already been noted, photocatlaytic acitivty of TiO_2 usually occurs when electrons are excited (by UV, or sometimes visible light) from VB to CB , generating electrons and holes. The hole on the surface reacts with H_2O producing hydroxyl radicals, which degrade nearby organic molecules. Also, the electrons on the CB react with O_2, producing superoxide, which also degrades nearby organics. These mechanisms occur at different time scales – holes react with H_2O within about 2 μs, faster than electrons react with oxygen (from 10 – 900 μs).

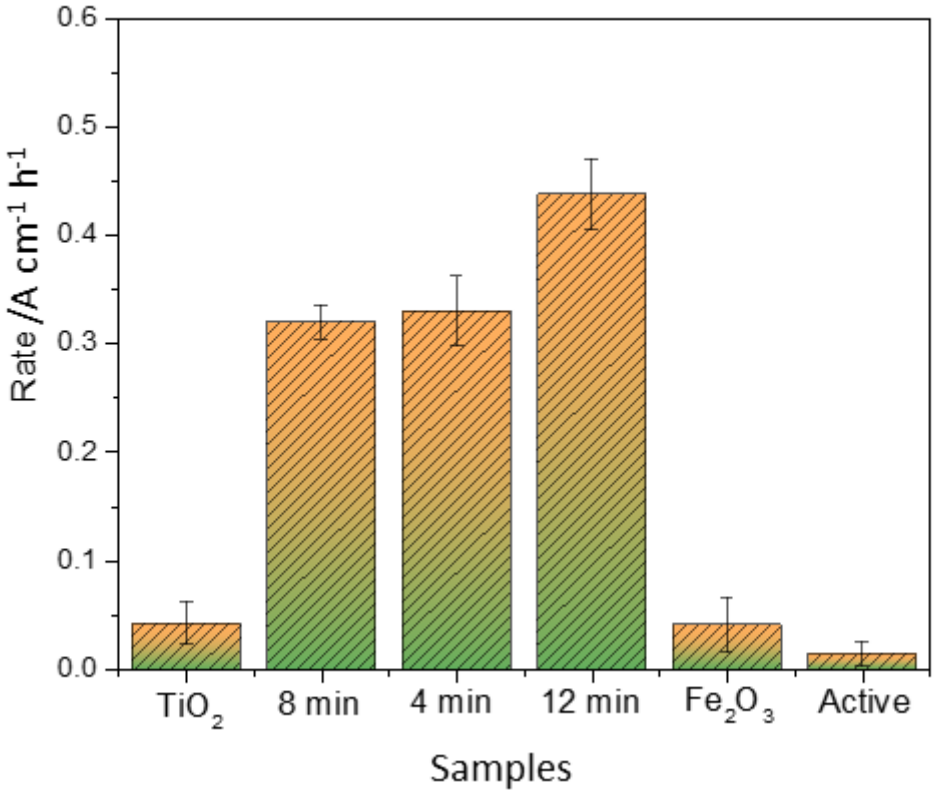

Figure 6.11 Photocatalytic activity of α-Fe_2O_3, TiO_2 and TiO_2/α-Fe_2O_3 films with different deposition times (4, 8 and 12 min). Photocatalytic rates were obtained during degradation of stearic acid under white light. Blank glass and Actic™ samples are included for comparison.

6.6.6.2 Antimicrobial activity

The antimicrobial activity of α-Fe_2O_3, TiO_2 and TiO_2/α-Fe_2O_3 films deposited by AACVD and APCVD was investigated using a representative strain of the gram-positive bacteria, Staphylococcus aureus (S.aureus) and gram-negative bacteria, Escherichia coli (E.coli) under white light and dark conditions. After irradiation, 25 µL of bacterial suspension was smeared on the surface of these samples at room temperature and placed under white light or incubated in the dark. The white light intensity was measured at distances up to 30 cm from the source (a 28W fluorescent lamp) by a lux meter (LX-101, Lutron Inc., Coopersburg, PA, USA), and found to range between 6000 and 9000 Lux. The results are shown in **(Figure 6.12).**

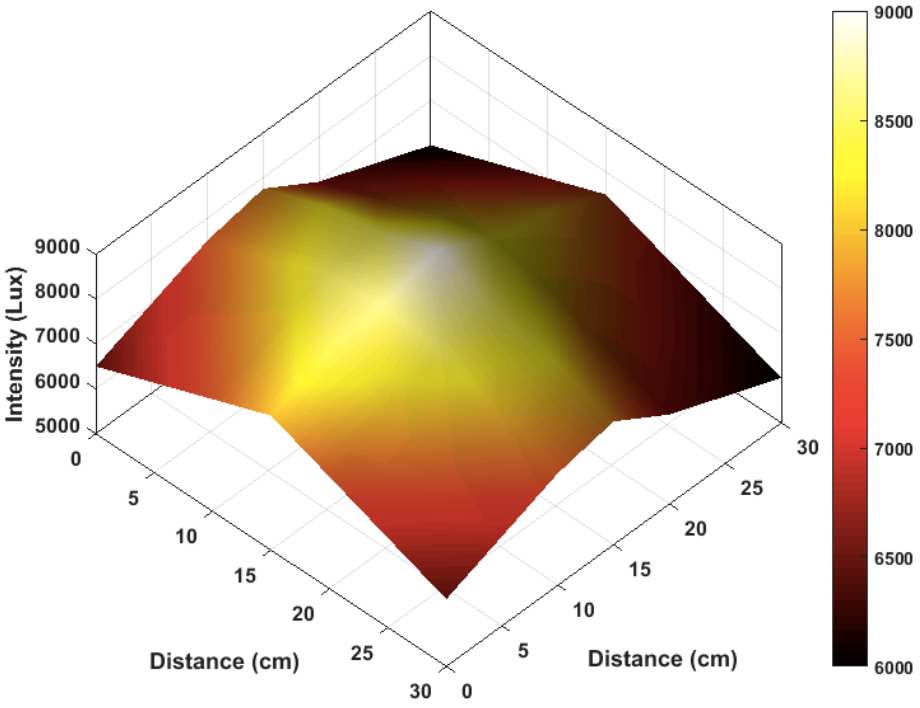

Figure 6.12. Intensity distribution of the white light to which TiO_2, α-Fe_2O_3 and TiO_2/α-Fe_2O_3 samples were exposed. A lux meter was used to measure intensity at distances up to 30 cm from the source (a 28 W hospital fluorescent lamp). The scale bar shows intensity values from 6000 lux (black) to 9000 lux (light yellow).

Figure 6.13 shows the antimicrobial activity of the samples and control against *E.col* **(Fig.6.13a)** and *S.aureus* **(Fig.6.13b)** after being incubated under white light for 4 and 8 hours, and in the dark for 8 hours. A glass slide was used as a control in these tests, and no reduction in the number of viable bacteria was seen on the surface of this control under either white light or in the dark for either E.coli or S.aureus. As can be seen in Figures 10a and 10b, all the samples showed antimicrobial activity against Gram-negative and Gram-positive bacterial strains under white light.

Against *E.coli*, a significant reduction in the numbers of viable bacteria was seen on the TiO_2/α-Fe_2O_3- (4 min) samples after 8 hours of incubation, and pure Fe_2O_3 films showed a stronger bacterial degradation under white light than pure TiO_2 films after 8h. Under dark

conditions, against E.coli, only α-Fe_2O_3 films exhibited a decrease in viable bacteria after 8 hours.

When the samples were tested against *S. aureus*, α-Fe_2O_3 showed a significant reduction in viable bacteria after 8 hours under white light, to a level below the detection limit. TiO_2/ Fe_2O_3 film with deposition times of 4 and 8 min showed similar antibacterial activity under white light (2 and 4 hours) and also in dark conditions. Both TiO_2 and TiO_2/Fe_2O_3 (with deposition time 12 min) showed lower antimicrobial activity against S. aurreus.

TiO_2 and Fe_2O_3 are well-known for their antimicrobial activity and, in a previous study, this activity was affected by particle size and shape. In fact, it has been established that antimicrobial activity significantly increases when the particle size is less than 50 nm[339]. However, the antimicrobial mechanism of metal oxides typically relates to the oxidative stress induced by the formation of reactive oxygen species (ROS) such as ($^{\bullet}OH$, $^1O_2$, H_2O_2 and $O_2^{\bullet -}$) and the release of metal ions. The antimicrobial activity of Fe_2O_3 is not thought to be connected to the release of Fe ions , and may be attributed to the oxidative stress produced by the particles $^{\bullet}OH$ and $O_2^{\bullet -}$[340] and Fenton reaction.

S.aureus and *E.coli* are among the most common causes of infections. These infections can be local (e.g. wounds or postoperative infection) or prosthetic (e.g. as a result of the use of endotracheal tubes or catheters). These types of bacteria also have the ability to resist antibiotics such as methicillin, penicillin, erythromycin and tetracycline. It is therefore very important to find an alternative treatment for these bacterial infections.

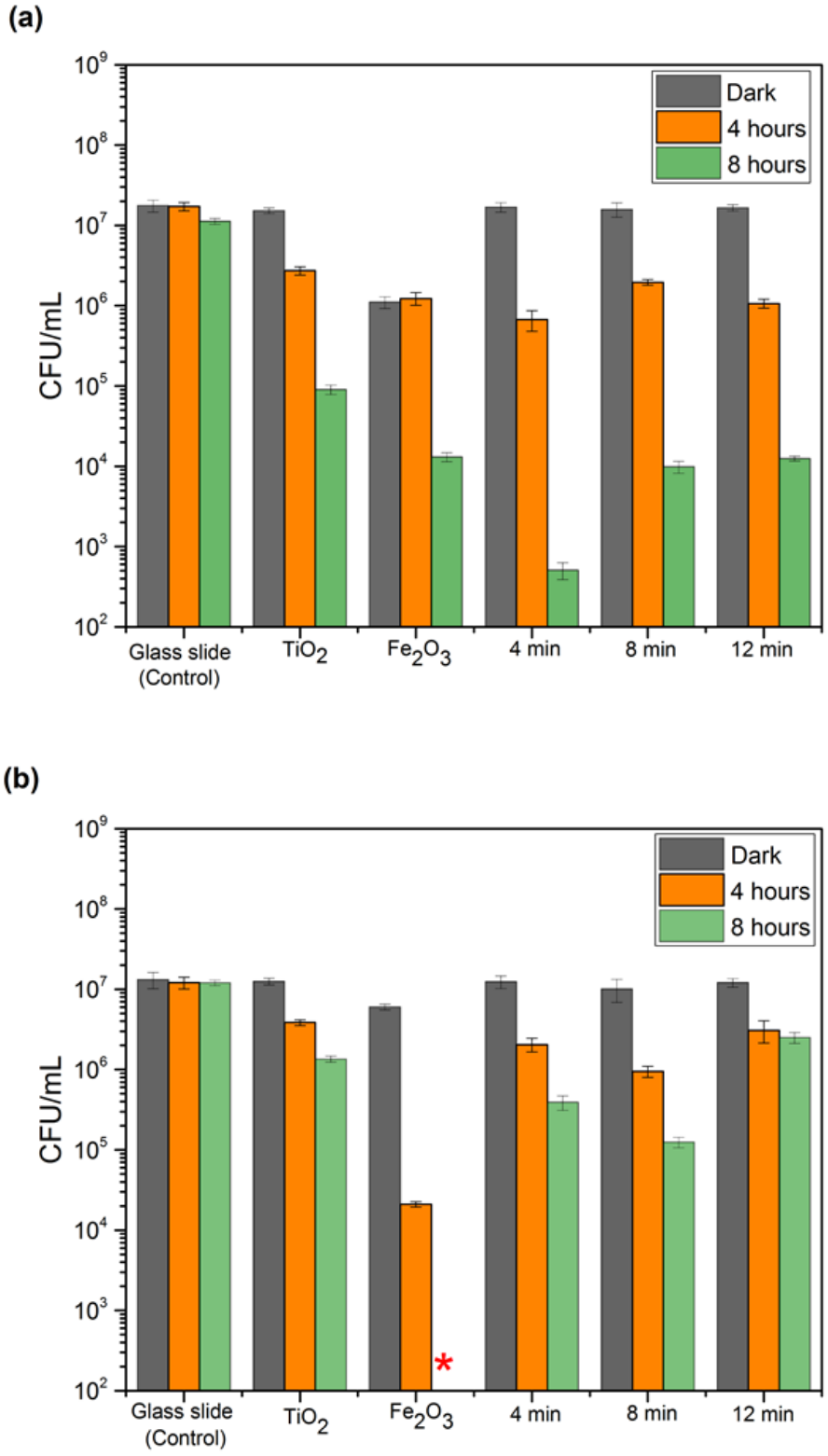

Figure 6.13 Viable bacteria counts after incubation of TiO_2, α-Fe_2O_3 and TiO_2/α-Fe_2O_3 films under white light (4 and 8 hours) and under darkness. The TiO_2/α-Fe_2O_3 films were made by AACVD and APCVD with different deposition times (4, 8 and 12 min). Fig.(a) is against E.coli, Fig. (b) is against S.aureus

6.7 Conclusion

TiO_2 films were deposited on α-Fe_2O_3 films to produce white light-activated photocatalytic properties and antimicrobial samples. TiO_2/α-Fe_2O_3 layers with different deposition times were shown to degrade stearic acid more strongly than pure TiO_2 and α-Fe_2O_3 films. This could result from enhanced morphology, red shifting of the bandgap and a reduction in electron-hole recombination, as confirmed by Time-resolved photoluminescence results. All samples showed bactericidal activity against *E. coli* and *S. aureus.* A reduction in viable bacteria was observed on the samples after 4 and 8 hours under white light, while a small reduction was also observed on α-Fe_2O_3 films after 8 hours in the dark. Against *E.coli.* The highest reduction in viable bacteria was seen with TiO_2/α-Fe_2O_3 (4 min) after 8 hours. Against *S. aureus*, with α-Fe_2O_3, the level of viable bacteria after 8 hours under white light fell to a level below the detection limit (100 CFU/mL). TiO_2/α-Fe_2O_3 and α-Fe_2O_3 films are promising materials with the potential to reduce hospital acquired infection (HAI) when used in health care facilities.

Stable and highly efficient photoelectrochemical water splitting using TiO_2/α-Fe_2O_3 heterojunction films produced by chemical vapour deposition.

6.8 Introduction

Photoelectrochemical water splitting using solar energy holds promise as a sustainable energy generation technology[341-346]. The production of electric power from hydrogen is desirable, as it is an environmentally-friendly energy carrier and it decreases the dependence on fossil fuels. However, traditional methods for producing hydrogen from oil, coal and methane have a negative impact on the environment, particularly in the context of climate change, as they result in the production of large amounts of carbon dioxide (CO_2).[347-349] The use of photoanodes in water splitting has attracted considerable attention after Fujishima and Honda (1972)[19] reported water splitting TiO_2. Since then, there have been many studies in this field to improve PEC efficiency and catalyst stability.

TiO_2 exists in three natural structures (anatase, rutile and brookite), and has a wide band gap (>3.0 eV) that restricts photo-absorption in the UV region[114, 139, 350]. However, hematite (α-Fe_2O_3) not only has a lower bandgap (2.0 - 2.2 eV) that encourages absorption in the visible region, but it is relatively non-toxic, shows good stability, has a suitable valence band edge position and is low cost[351-356]. Together, these factors make hematite one of the most promising metal oxides for water splitting.

Despite of this, hematite has some significant drawbacks. One of these is that its conduction band edge is located at an energy level below the reversible hydrogen potential[357]. Furthermore, photogenerated holes that are created on Fe_2O_3 have low ability to participate in water oxidation[357], due to the small hole diffusion length of Fe_2O_3 [358] compared with high penetration depth[359]. A number of studies have used hematite as an oxygen evolution photoanode for water-splitting, these kinds of materials need an external electrical bias to produce hydrogen at the cathode.

It should also be noted that, despite of its promise in principle, the efficiency of water splitting of hematite obtained in practice is, so far, negligible compared to theoretical calculations (16.8%) [357, 360], due to high charge recombination, short hole diffusion length and poor electrical conductivity. In order to improve the efficiency of Fe_2O_3 in water splitting, efforts have been made to enhance its efficiency as a photoanode, by doping it with various elements or coupling hematite (α-Fe_2O_3) with other metal oxide semiconductors, such as TiO_2, Ta_2O_5 and WO_3[357, 361-365]. In fact, research into the use of Fe_2O_3 goes back a considerable time. It was in 1976 that the first paper on Fe_2O_3 for water splitting was published by Hardee and Bard[366]. They found that with Fe_2O_3 on a Ti and Pt substrate, the photocurrent under 500 nm illumination in KCl was 0.8 V vs. the saturated calomel electrode (V_{SCE}). Another paper was published in the same year by Quinn et al[367]. On Fe_2O_3 single crystals under 475 nm illumination, and in 0.5M NaOH, the photocurrent was 1.57 V vs. the reversible hydrogen electrode (V_{RHE}).

However, as said, improved PEC performance of hematite can be achieved by surface treatment and/or metal ion doping, which reduces electron-hole recombination[368] and increases donor density[369]. Surface treatment also leads to accelerated solar water oxidation[370-372].

In this chapter, we describe, for the first time, hematite deposited by AACVD on FTO substrate at 450°C, and followed by anatase TiO_2 deposited as a second layer by APCVD, then annealed at 500° C to remove carbon contamination. This approach (TiO_2/α-Fe_2O_3 layers) improved the water splitting efficiency and stability compared to α-Fe_2O_3 films. Furthermore, TiO_2 films deposited by this method showed excellent water splitting performance under sunlight. A pure Fe_2O_3 film, deposited by AACVD, proved effective in water splitting (0.8 mA cm^{-2} at 1.23 *vis* RHE) and was stable for approximately 3.7 hours. A significant improvement in photocurrent density of the heterojunction was observed after coupling TiO_2 (1.75 mA cm^{-2} at 1.23 *vis* RHE), which improved the stability to 16 hours. Charge carrier recombination dynamics and carrier lifetimes of TiO_2/Fe_2O_3

films were investigated by transient absorption spectroscopy (TAS). A correlation between PEC eff efficiency and carrier lifetimes measured by TAS was observed.

6.9 Experimental section

Pure Fe_2O_3, pure TiO_2 and series TiO_2/Fe_2O_3 films were deposited on FTO instead of glass substrate following the procedure presented in (6.2 section).

6.9.1 Photoelectrochemical performance (PEC)

PEC measurements were obtained using 1 M NaOH electrolyte (Fluka, in ID water, pH 13.6) in a three-electrode electrochemical cell **(Figure 6.14)** under simulated sunlight (100 mW cm $^{-2}$, AM 1.5G). Platinum wire was used as a counter electrode, and Ag/AgCl in saturated KCl used as a reference. A potentiostat (Ivium technology) controlled the photoelectrode, and the reversible hydrogen electrode (RHE) is given by:

$E_{RHE} = E_{AgCl} + 0.059pH + E°_{AgCl}$, where $E°_{AgCl} = 0.1976V$ at 25 °C

The potential range was measured from -1.0 to 1.23 V and scanned at 50 mV/s, and an Ivium CompactStat (IVIUM Technologies) Lamp was used to simulate sunlight at the intensity given above (100 mW cm $^{-2}$, AM 1.5G). Illumination intensity was calibrated using a silicon reference cell with an optical meter (Newport, Model 1918-R). Incident-photon-to-current efficiency (IPCE) measurements were obtained using 1 M NaOH electrolyte and a 200 W Xe lamp at 1.23 V vs RHE. IPCE values can be calculated from:

$$IPCE\% = \frac{12400 \times I_{SC}(Acm^{-2})}{\lambda(nm) \times P_{in}(Wcm^{-2})} \times 100$$

Where I_{SC} is the current density at 1.23 V vs *RHE*, λ is the wavelength of the incident monochromatic light, and P_{in} is the intensity of the light at a specific wavelength. Mott–

Schottky measurements were made in the dark at 1kHz frequency, using the same electrolyte as for IPCE.

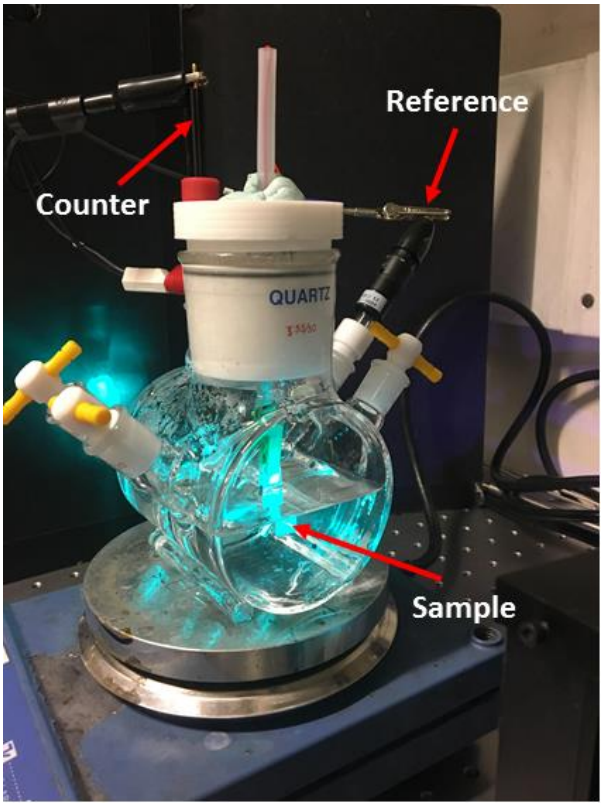

Figure 6.14 The photoelectrochemical cell used in experiments

6.9.2 Transient Absorption Spectroscopy (TAS)

Transient absorption measurements were performed on a home-built pump-probe setup. The monochromatic pump pulse was provided by a Q-switched laser system (InnoLAS, picolo AOT MOPA, picosecond Nd:YVO4 Laser System) where the fundamental frequency was tripled to produce a 355-nm output, and the pulse energy was modulated to be 300 uJ/cm^2 with a reflective neutral medium filter. The broad-band probe pulse, spectrally ranging from 420 nm to 1100 nm, was generated through the supercontinuum approach by focusing a seed pulse of

1300 nm on a 3-mm c-cut Sapphire crystal. The seed pulse was outputted from an optical parametric amplifier (Light Conversion, TOPAS prime) after pumped by a commercial Ti:Sapphire amplifier (Coherent Legend Elite Duo, 4.5 mJ, 3 kHz, 100 fs). The delay time between the pump and probe pulses were controlled by an electronic delay generator (Stanford Research System DG535) with a jitter of roughly 100 ps. The spot sizes of the laser pulses were determined from the transmissivity through a 75-nm laser precision pinhole, 20% for the pump and 50 % for the probe, so the pump pulse was more than three times larger than the probe pulse. In the measurements, the pump and probe pulses were overlapped in the front surface of samples. All measurements were performed under the room temperature, and samples were protected in a nitrogen-filled chamber.

6.10 Results and discussion

6.10.1 Scanning electron microscopy (SEM)

The morphology of Fe_2O_3, TiO_2 and TiO_2/α-Fe_2O_3 films was analysed using SEM **(Figure 6.15).** The morphology of α-Fe_2O_3 consisted of approximately spherical particles with an average diameter of 100 - 200 nm **(Figure 6.15a)**, while pure TiO_2 films consisted of densely packed particles ranging from 200 to 400 nm in diameter **(Figure 6.15b)**.

The morphology of the TiO_2/ α-Fe_2O_3 series of films was different to pure α-Fe_2O_3 and TiO_2 films. The TiO_2/α-Fe_2O_3 film with a deposition time of 4 mins consisted of particles ranging between 50 to100 nm in diameter **(Figure 6.15c),** while the film with a deposition time of 8 mins had a similar morphology to pure TiO_2, consisting of densely packed particles around 500 nm wide **(Figure 6.15d)**. The TiO_2/ α-Fe_2O_3 (12 min) film consisted of densely-packed, needle-shaped particles, which were typically 200 - 400 nm long **(Figure 6.15e).**

The side on micrographs showed that the pure α-Fe_2O_3 on substrate and its thickness are between 368 and 422 nm **(Figure 6.15a)** and TiO_2 film was *ca.* 470 nm thick **(Figure 6.15b)**. In addition, the thickness of TiO_2 films in the TiO_2/α-Fe_2O_3 films with deposition times of 4, 8 and 12 mins were about 438, 500 and 633 nm respectively (Figure 6.15c,d and e).

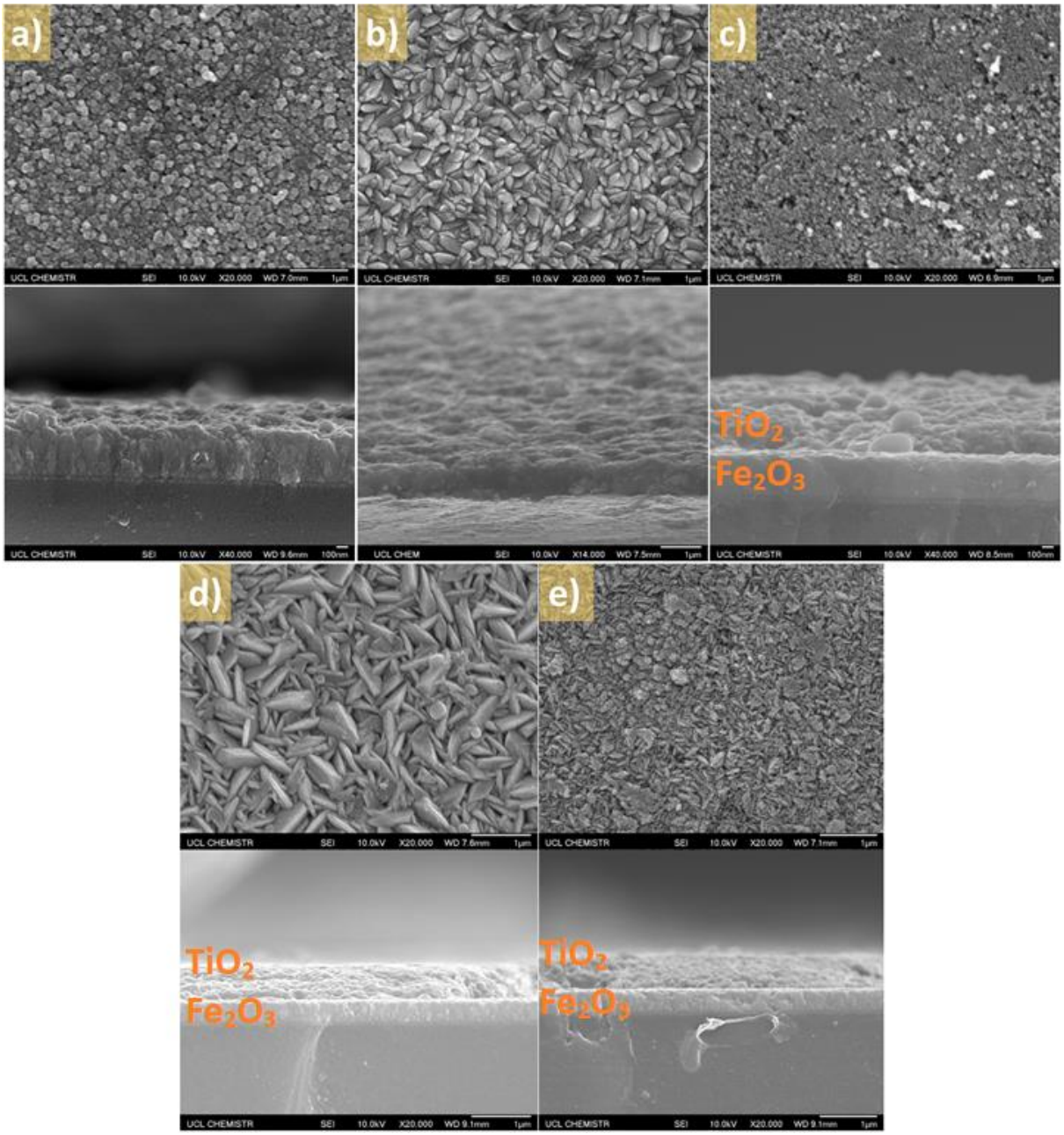

Figure 6.15 SEM images of a) α-Fe_2O_3, b) pure TiO_2, c) TiO_2/α-Fe_2O_3 (4 min), d) TiO_2/ α-Fe_2O_3 (8min) , (e) TiO_2/ α-Fe_2O_3 (12 min) films grown by AACVD and APCVD on FTO at 450 °C then annealed at 500 °C. The thickness was presented by side-on SEM images.

6.10.2 Atomic force microscopy (AFM)

To further study film morphology, AFM was used to investigate the surface topography of all samples used in this study (**Figure 6.16)**. AFM measurements were taken at a scale of 10 × 10 µm. From the resulting images, it is clear that the particles are similar, closely packed, pseudo-spherical grains, though (as can be seen in Figure 6a) Fe_2O_3 appears to consist of smaller grains, and have a flatter surface, than other samples. AFM images of TiO_2 and the TiO_2/Fe_2O_3 series showed an aggregate of particles. However, the roughness of the surfaces varied. We know this because the RMS (root means square) roughness of all samples was measured by AFM at a scale of 10 × 10 µm. The roughness of TiO_2 was 20.3 nm, almost double that of α-Fe_2O_3 (10.2 nm), while the roughness of the TiO_2/Fe_2O_3 (4 min) and TiO_2/Fe_2O_3 (12 min) samples were reasonably similar, at 36.7 nm and 31.7 nm respectively. The TiO_2/Fe_2O_3 (8 min) sample, however, had a significantly lower surface value of about 19.8 nm. On the other hand, all samples had a similar surface area - 101 μm^2 for α-Fe_2O_3 , and 103, 104, 102 and 105 μm^2 for TiO_2, TiO_2/Fe_2O_3 (4 min, 8 min and 12 min) respectively.

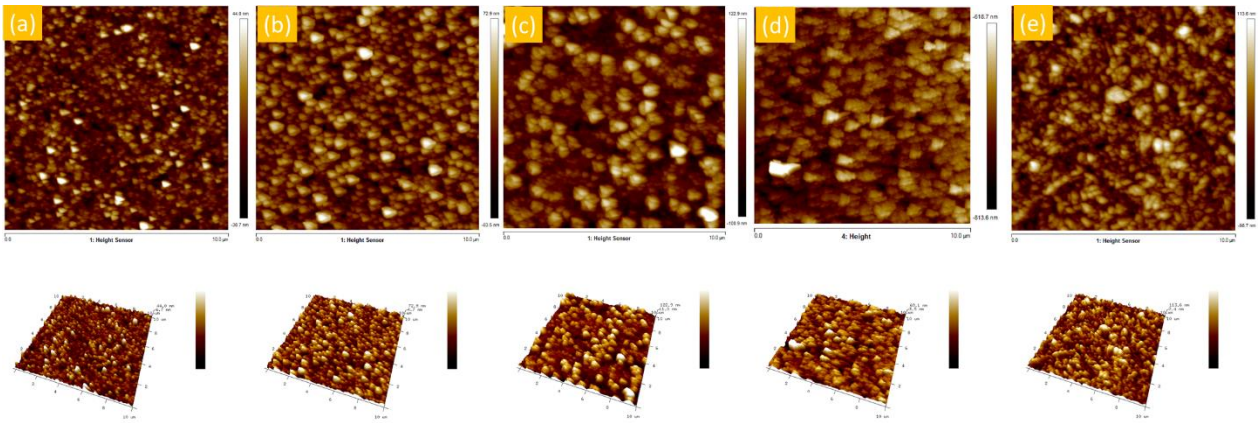

Figure 6.16 2D (top) and 3D (bottom) images of the surface of (a) α-Fe_2O_3; (b) TiO_2; (c, d, e) TiO_2/α-Fe_2O_3 (4, 8, 12 min) respectively, at a scale of 10 × 10 µm.

6.10.3 Photoelectrochemical (PEC) performances

Figure 6.17 shows the current-voltage (I-V) curves for (a) TiO_2/α-Fe_2O_3 layers and pure α-Fe_2O_3 and (b) TiO_2 films in conditions of darkness and simulated sunlight (AM 1.5 G, 100 mW cm^{-2}). As can be seen from Figure 6.17a, the photocurrent of hematite in conditions of darkness sharply increases at a voltage of approximately 1.70 V_{RHE}. However, the same samples under simulated sunlight conditions show an onset potential around 0.4 V_{RHE}, with photocurrent rising until about 1.4 V_{RHE}. The Fe_2O_3 photocurrent peak of about 0.7 mA cm^{-2}, reached at 1.23 V_{RHE}, where the RHE corresponds to the potential of the reversible oxygen electrode.

Also shown in **Figure 6.17(a)** are the photocurrent graphs of TiO_2/α-Fe_2O_3, with different TiO_2 thicknesses, under sunlight conditions. We can see that the layer of TiO_2, deposited by APCVD, caused not only an increase in α-Fe_2O_3 photocurrent, but also an improvement onset potential. Specifically, the photocurrents of TiO_2/α-Fe_2O_3 (4 and 8 min) showed an onset potential at 0.1 and 0.5 V_{RHE} respectively, with current increasing to approximately 1.2 and 1.75 mA cm^{-2} at 1.23 V_{RHE} respectively. The sample with a deposition time of 8 min reached a photocurrent of around 2.3 mA cm^{-2} at 1.45 V_{RHE}. However, when the TiO_2 layer is thicker (12 min deposition time) the photocurrent decreased compared with pure hematite, reaching around 0.3 mA cm^{-2} at 1.2 V_{RHE}. For all samples, the J-V curves in dark conditions were increased by up to 1.67 $V_{RHE.}$

The highest photocurrent so far achieved for Fe_2O_3 was by Michael Gratzel et al[353], in 2011. This photocurrent was around 2.3 mA cm^{-2} at 1.23 $_{RHE}$. Guo et al[373] improved the performance of the hematite photoanode by doping (hematite) nanorod films with Ru. This resulted in the best performance so far, achieving approximately 5.7 mA cm^{-2} at 1.23 $_{RHE}$.

The pure TiO_2 (deposition time 8 min) was fabricated onto PEC photoanodes, and its performance assessed in 1M NaOH in both dark and simulated sunlight (AM 1.5 G, 100 mW cm^{-2}) conditions. As can be seen in **Figure 6.17(b)**, the photocurrent density, in sunlit conditions, of this

TiO_2 sample was approximately 1.0 mA cm^{-2} at 1.23 V_{RHE}, which is higher, as it has been previously reported for (undoped) TiO_2. The photocurrent of the same sample under dark conditions increased rapdly at a voltage of about 1.9 V_{RHE}. However, appropriate thickness of TiO_2 on α-Fe_2O_3 can increase hole injection through surface contact with the solution, thus reducing electron-hole recombination – an effect confirmed by transient absorption spectroscopy TAS (See the TAS section of this chapter).

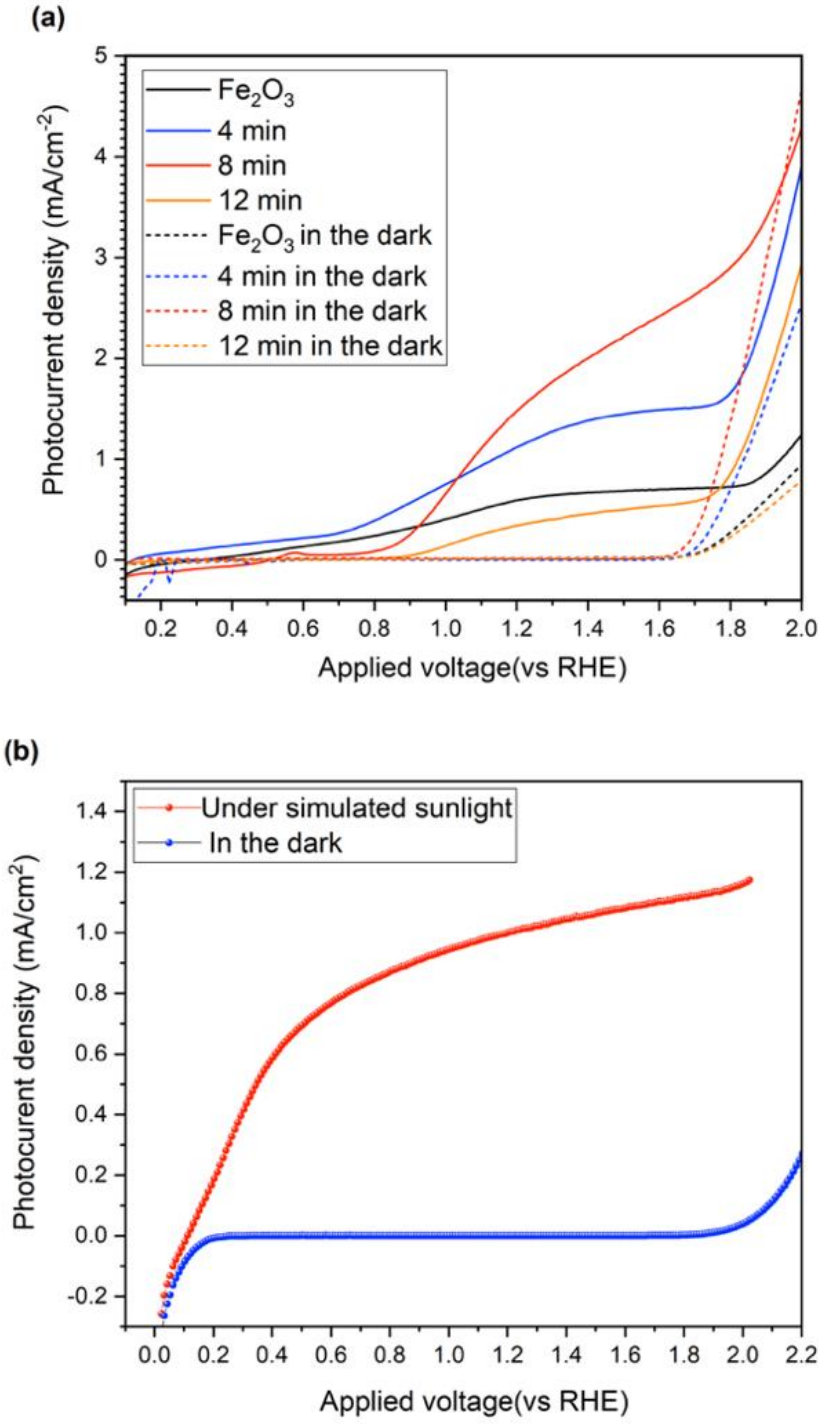

Figure 6.17 PEC performance of (a) hematite and TiO_2/hematite films at different deposition times (4, 8 and 12 min); (b) TiO_2 films. All films were deposited on FTO glass, and hematite was deposited using AACVD at 450 °C using Fe(II) acetylacentonate in ethylacetate. TiO_2 films were deposited by APCVD using titanium isoporopxide at 450°C, then annealed under N_2 for 1h to remove carbon contamination. Water oxidation was measured in 1M NaOH (pH 13.7) in conditions of darkness and AM 1.5 G illumination (100 mW/cm^2).

The valence and conduction band edge position of TiO_2 and Fe_2O_3 films in contact with an electrolyte at pH = 13.7 with respect to the reversible hydrogen electrode (RHE) potential are obtained from the flat band (**Figure 6.20**); the band gap of TiO_2 and Fe_2O_3 are 3.2 and 1.95 eV respectively. The conduction band of TiO_2 lies at 0.16 eV, while hematite showed a conduction band at 0.46 eV. These conduction band edges lie below the H_2O/H_2 electrochemical level of water reduction. They are unable to reduce H_2O without the use of an external bias **(Figure 6.18)**. In addition, the conduction band of the Fe_2O_3 film is more positive than the conduction band of anatase TiO_2 films, which agrees with the photocurrent onset potential (**Figure 6.17**). The valence band of TiO_2 film lies very deep in comparison to the valence band of Fe_2O_3 film and it is even below the water oxidation potential at 1.23 V vs NHE, which is able to oxidise H_2O to O_2 **(Figure 6.18)**.

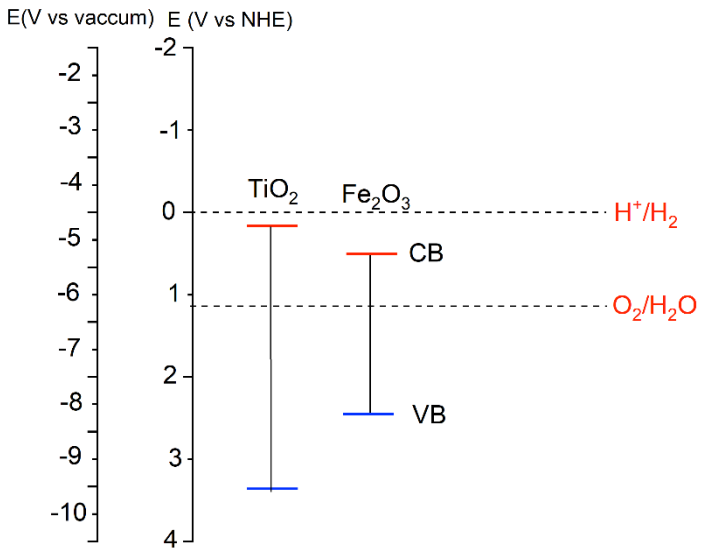

Figure 6.18 Valence and conduction band position of TiO_2 and Fe_2O_3 thin films at pH = 13.7

For all samples, incident-photon-to-current efficiency (IPCE) at 1.23 V vs RHE was recorded as a function of different incident light wavelengths, in order to compare the behaviour of TiO_2 films with Fe_2O_3 and TiO_2/Fe_2O_3 films. The results are shown in **Figure 6.19**. Improvements in IPCE values of TiO_2/Fe_2O_3 samples were seen, compared with pure Fe_2O_3, over the range of wavelengths used in this study (300 – 550 nm). This was particularly true in the visible region. For example, the IPCE value of TiO_2/Fe_2O_3 (8 min) at 420 nm increased to 7.47%, up from 3.9% (Fe_2O_3 alone). A similar improvement occurred with the TiO_2/Fe_2O_3 (4 min) sample, which increased to 6.5%. In the UV region, IPCE values of TiO_2/Fe_2O_3 (4 min) were similar to pure Fe_2O_3, while, for TiO_2/Fe_2O_3 (12 min), they decreased. It is worth noting that, at 500 nm, the IPCE value of Fe_2O_3 drops to zero, but the IPCE value of TiO_2/Fe_2O_3 (8 min) is 1.95% at this wavelength. However, these results are consistent with previous studies, which report increasing IPCE values in the visible region more than in the UV region[374]. This contrasts with studies on Zr, Sn and Ti, which show that, with these elements, doping has only a small effect on the IPCE values of hematite in the visible region, and a large effect in the UV region[363, 368, 375].

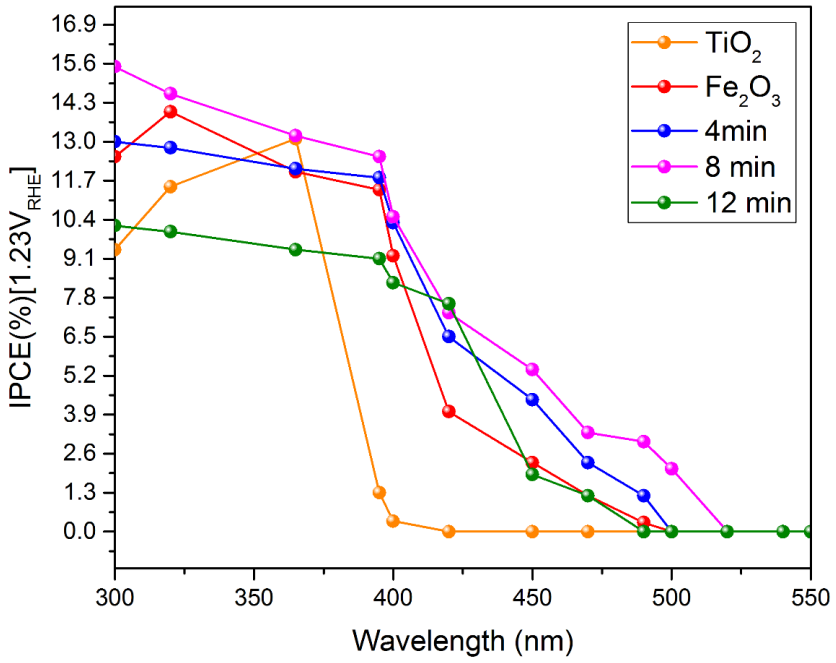

Figure 6.19. The incident-photon-to-current efficiency (IPCE) of TiO_2, Fe_2O_3 and TiO_2/Fe_2O_3 samples.

Mott –Schottky (M-S) calculations were used to investigate flat band potential (V_{fb}) and donor density (N_d) of Fe_2O_3, TiO_2 and TiO_2/Fe_2O_3 samples. Measurements were obtained in conditions of darkness at a frequency of 1kHz, and the following equation was used:

$$\frac{1}{C^2} = \frac{2}{\varepsilon\varepsilon_o e N_D A^2}\left(E - V_{fb} - \frac{k_B T}{e}\right) \qquad (1)$$

Where A is the active area, e is electron charge, ε_o is the permittivity of a vacuum, ε is the dielectric constant, T is the absolute temperature, k is the Boltzmann constant and E is the applied potential.[376] The results are shown in **Figure 6.20**.

All samples showed a positive gradient, as Fe_2O_3, TiO_2 and TiO_2/Fe_2O_3 are n-type semiconductors. From **Figure 6.20(a)**, it can be seen that Fe_2O_3 films show a flat band potential at approximately 0.48 V_{RHE} and a donor density of about 3.27×10^{19} cm^{-3}. TiO_2 thin films show a V_{fb} of about 0.16 V vs RHE and donor density of 1.68×10^{18} cm^{-3} **Figure 6.20b**. From **Figure 6.20(a)**, we see that TiO_2/Fe_2O_3 (4, 8 and 12 min) showed a $V_{fb} \approx 0.06$, 0.52 and 0.74 V_{RHE} and donor density $N_D \approx 2.24\times10^{19}$, 4.66×10^{19} and 1.75×10^{19} respectively. This shift in the value of V_{fb} for TiO_2/Fe_2O_3 could be due to efficient hole transport from hematite to TiO_2, resulting in a greater water oxidation reaction on the surface[374]. However, as the V_{fb} of hematite is usually between 0.4 – 0.8 V_{RHE}[377], our results for hematite broadly agree with those of Hen Dotan and et al[378].

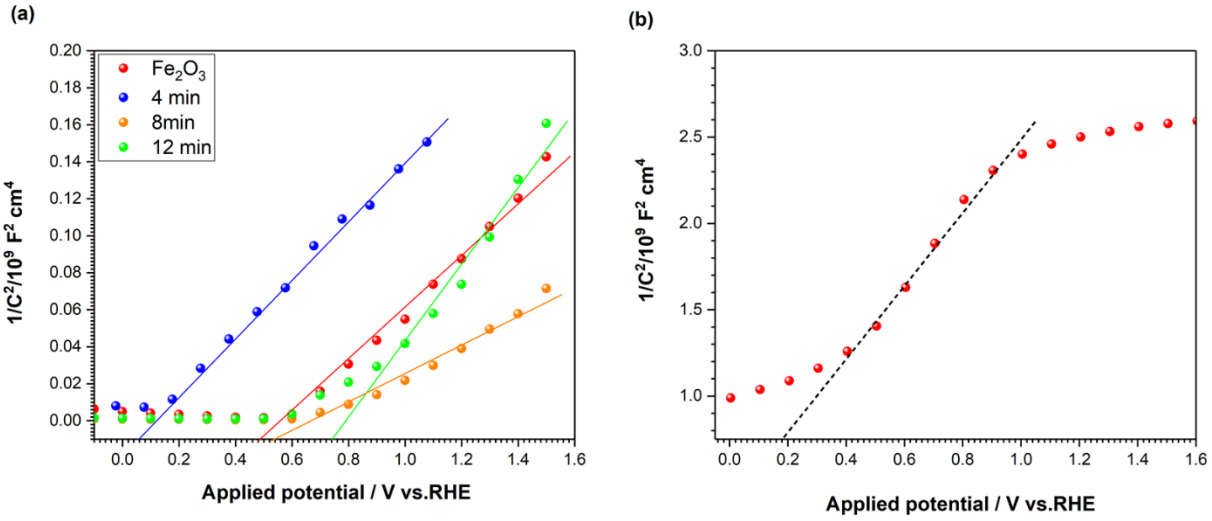

Figure 6.20 Mott –Schottky plots for three electrodes, using (a) Fe_2O_3 and TiO_2/α-Fe_2O_3 films, and (b) anatase TiO_2 as photoanode. Flat band potential and donor density of the samples were calculated for this analysis.

6.10.4 Long-term stability

The stability of photoelectrodes plays an important role in the generation and commercial viability of PEC hydrogen production devices. Therefore, ways to increase the stability of semiconductors have received much attention in recent studies. **Figure 6.21** shows the stability of hematite and TiO_2/α-Fe_2O_3 (8 min) films under simulated sunlight of intensity 100 mW/cm^2. The hematite film was deposited by AACVD, and was stable for over 6.5 hours with an average photocurrent density of approximately 1.0 mAcm^{-2}. Surprisingly, the addition of a TiO_2 layer increased the stability of hematite to over 16 hours.

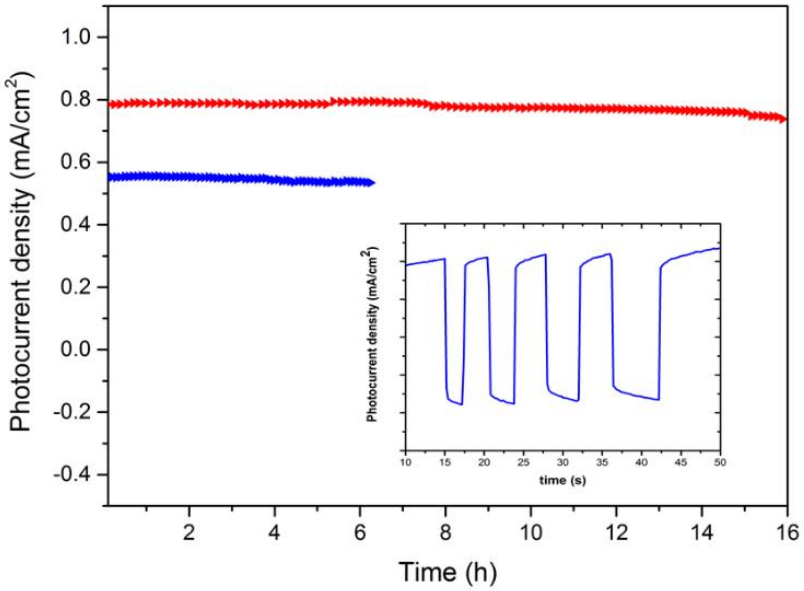

Figure 6.21 Polarization curve of the Fe_2O_3 sample (blue) and TiO_2/α-Fe_2O_3 sample (red) under simulated solar illumination (100 mW cm^2) and a constant bias of 1 mAcm^{-2}. Measurements were obtained with the samples in 1 M NaOH electrolyte under sunlight.

The morphology of TiO_2/α-Fe_2O_3 (8 min) film was examined using SEM, both before and after PEC and stability tests. Before these tests, as noted in **(Figure 6.22)** of this chapter, the morphology of this sample consisted of densely packed particles, approximately 500 nm wide **(Fig. 6.22a)**, but this changed to irregular forms with signs of pin holes, voids and cracks after the tests **(Fig.**

6.22b). This change in sample morphology after a long (over 16 hours) test phase, indicates that stability of the sample is dependent on the TiO_2 surface, as TiO_2 is more stable than Fe_2O_3.

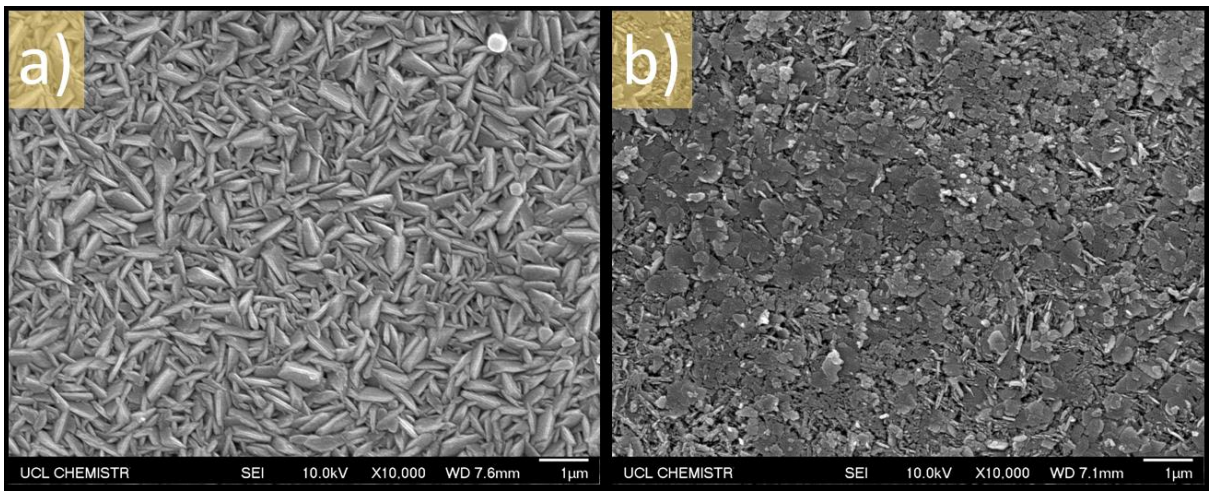

Figure 6.22. SEM images of the TiO_2/α-Fe_2O_3 (8 min) anode, before and after PEC and stability tests. Photocurrent stability testing took over 16 hours under simulated solar illumination (100 mW cm^2) and under a constant bias of 1 mA/cm^{-2}.

Figure 6.23 shows XPS results for TiO_2/α-Fe_2O_3 (8 min), before and after PEC and stability measurements. These results show that there is a decrease in XPS intensity for Ti 2p and Fe 2p after the test. This indicates that decomposition occurred on both TiO_2 and α-Fe_2O_3 samples.

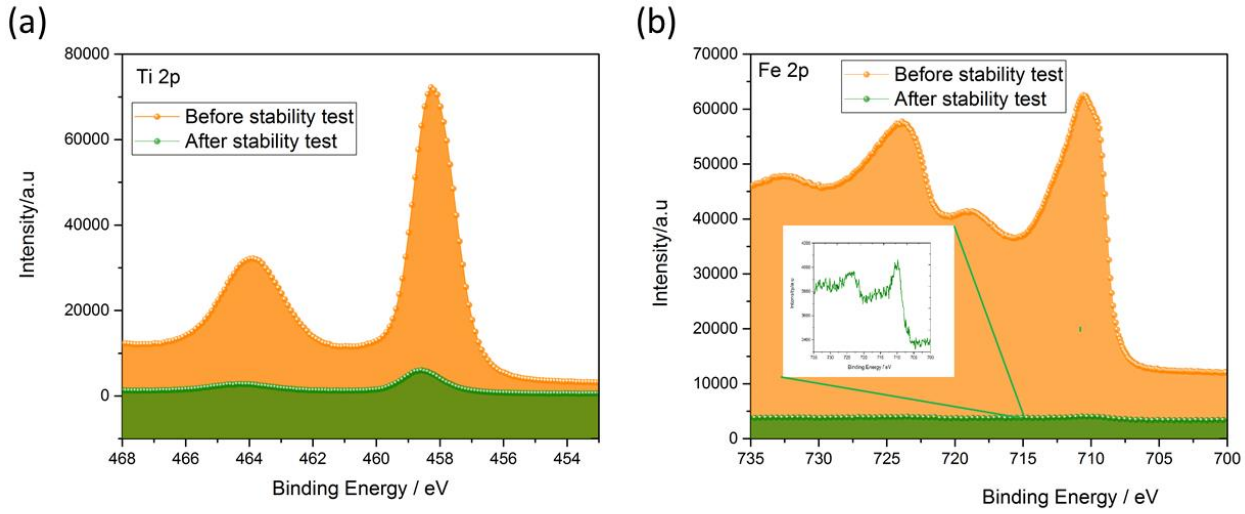

Figure 6.23. Surface X-ray photoelectron spectra (XPS) for (a) Ti 2p, and (b) Fe 2p, before and after the stability test.

6.10.5 Transient absorption spectroscopy (TAS)

Transient absorption spectroscopy was used to investigate the charge carrier dynamics in TiO_2, α-Fe_2O_3 and TiO_2/Fe_2O_3 films on a nanosecond - microsecond timescale at room temperature (25°C). Different thicknesses of TiO_2 on α-Fe_2O_3 have been shown to increase the photocurrent in water splitting reactions. Here, TAS was used to investigate the effect of coupling hematite with TiO_2 on photo-generated charge carrier dynamics and lifetime. **Figure 6.24** shows transient absorption spectra of TiO_2, Fe_2O_3, and TiO_2/ α-Fe_2O_3 samples. Pristine TiO_2 films show a broad and structured photo-induced absorption (PIA) band with peaks at 630 and 770 nm, consistent with results reported previously [379]. According to Akihiro Furube *et.al* [379], this broad PIA band consists of several components: the PIA band at 630 nm is mainly related to trapped holes, while the PIA at 770-nm is from trapped electrons. Our experiments confirm that the absorption of photogenerated holes is around 630 nm, while other studies suggested a spectral range from 450-570 nm with a lifetime of μs-ms. However, this point is still a subject of ongoing debate[379]. From the transient absorption, we also observe that the 770 nm PIA band vanishes after 100 ns, while the 630 nm PIA band persist beyond 1 us. This suggests that the electrons are relatively short-lived compared to the holes.

The TA spectra of Fe_2O_3 thin films showed an absorption peak at 560 nm with a small tail at 680 nm, which can be attributed to trapped photo-generated holes and electrons respectively, or could be caused by reactive oxygen species on the surface[380-382] . In addition, the signal intensity of pure hematite here is twice as high as that of pure TiO_2 **(Figure 6.24)**. The dynamics of photo-generated holes in TiO_2 and Fe_2O_3 has previously been examined by using various hole scavengers such as methanol (for TiO_2), and thiocyanate, isopropanol and iodide (for Fe_2O_3)[212, 382]. While the decay dynamics of photo-generated holes in Fe_2O_3 did not show any sensitivity to the chemical environment, when measured with TAS at 580 nm on a

time scale of μs- ms, the decay dynamics of photo-generated holes in TiO_2 showed a strong sensitivity to methanol at 460 nm[212].

In our experiments, the TiO_2/Fe_2O_3 samples show absorption at 560 and 700 nm, which we assign to trapped photogenerated holes in Fe_2O_3, since the holes in Fe_2O_3 have a significantly stronger absorption than those in TiO_2. This could leads to a spectral overlap of trapped holes in Fe_2O_3 with those in TiO_2. However, when the TiO_2 thickness is increased (as in the 12-min sample), we find absorption bands at 560 and 650 nm for Fe_2O_3 and TiO_2, respectively, as well as a band at 770 nm for electrons.

The TA spectra of the series of TiO_2/Fe_2O_3 films demonstrate how the spectra evolve with increasing thickness of the TiO_2 layer (that is, increasing reaction time). In the case of the thinnest TiO_2 layer, the TA spectra feature larger contributions from the Fe_2O_3 with a significant PIA band peaking around 560 nm. As the thickness of the TiO_2 layer increases, the TiO_2 contribution gradually increases and the 650 nm PIA band finally is more pronounced than the 560-nm PIA band.

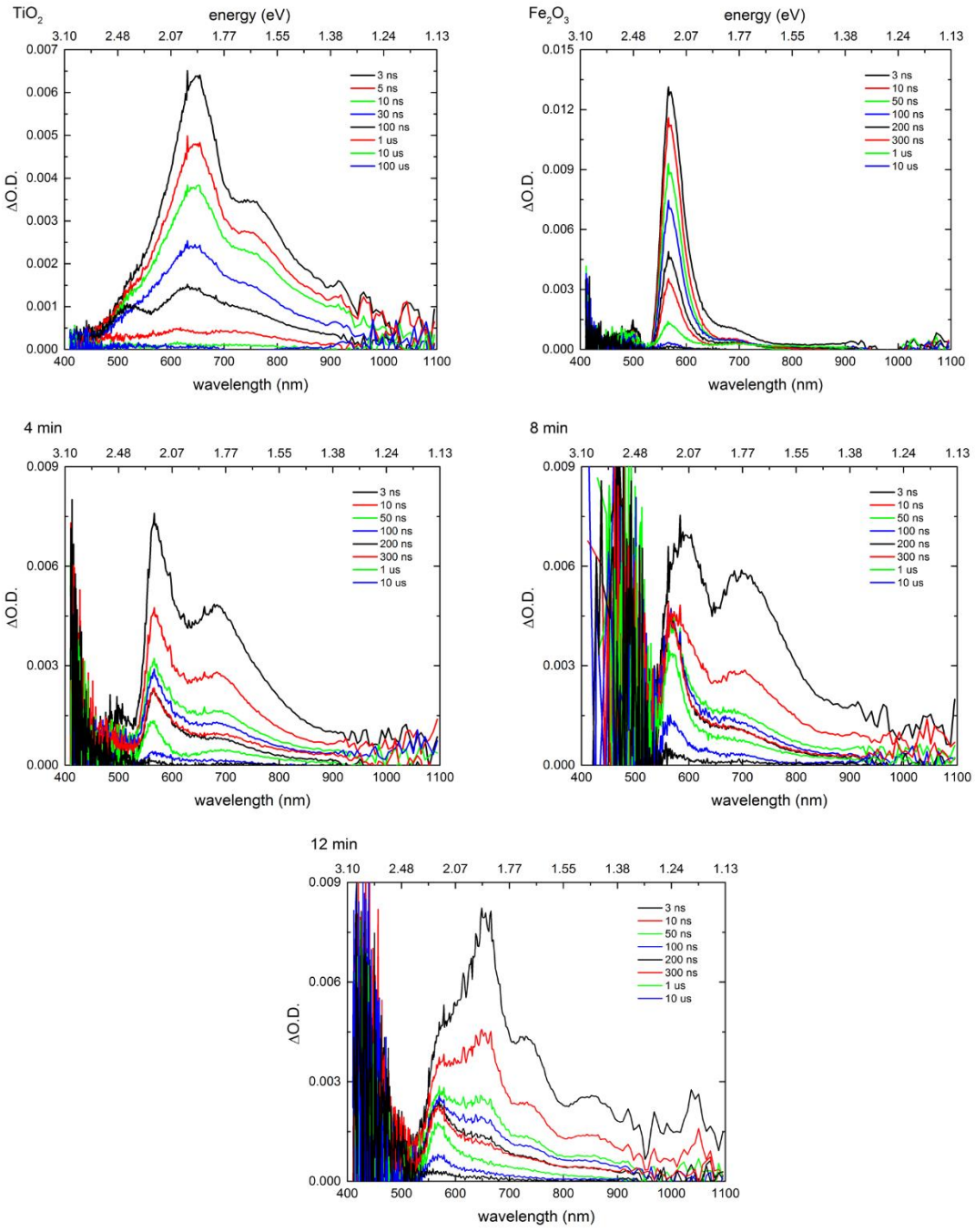

Figure 6.24. Transient absorption spectra at different delay times for pure TiO_2, pure Fe_2O_3, and TiO_2/Fe_2O_3 films. The pump has a wavelength of 355 nm, and a fluence density of 300 uJ/cm^2.

The temporal evolution of the transient absorption decay was recorded at 560 nm for TiO_2 excited at 355 nm with pulse energy densities of 300 uJ/cm^2 in the sub-nanosecond range. In

case of TiO_2, the fastest TA decay occurred at 560 nm with a lifetime of $t_{50\%}$ = 85 ns, in which $t_{50\ \%}$ is the time it takes for the signal to decay to 50% of the initial amplitude. For hematite, the TA decay was monitored at 560 nm, and the initial signal intensity (at this wavelength) was found to be around 0.013 ΔO.D. with a lifetime of $t_{50\%}$ = 112 ns. The TiO_2/α-Fe_2O_3 (4, 8, 12 min) samples displayed initial signal intensities of 0.075, 0.006 and 0.0045 ΔO.D. at 560 nm respectively with lifetimes of $t_{50\%}$ = 66 ns, 1200 ns, and 880 ns. Comparably slow decays and noticeable signal increase was observed at 560 nm in the TiO_2/α-Fe_2O_3 (8 min) sample, compared to pure Fe_2O_3 and TiO_2. These results are in line with the photocurrent results obtained during water oxidation **(Figure 6.25)**, suggesting that the low efficiency of pure Fe_2O_3 is due to fast electron-hole recombination. However, at 560 nm, single-layer TiO_2 exhibits a lower signal intensity than Fe_2O_3, because the valence-band of Fe_2O_3 is higher than that of TiO_2. On the other hand, TiO_2/Fe_2O_3 films, and particularly TiO_2/α-Fe_2O_3 (8 min) show noticeably slower recombination. This may be a consequence of the transfer of photogenerated holes from Fe_2O_3 to TiO_2. In addition, photogenerated electrons in TiO_2 can be transferred to Fe_2O_3, increasing the photo hole lifetime in TiO_2 films.

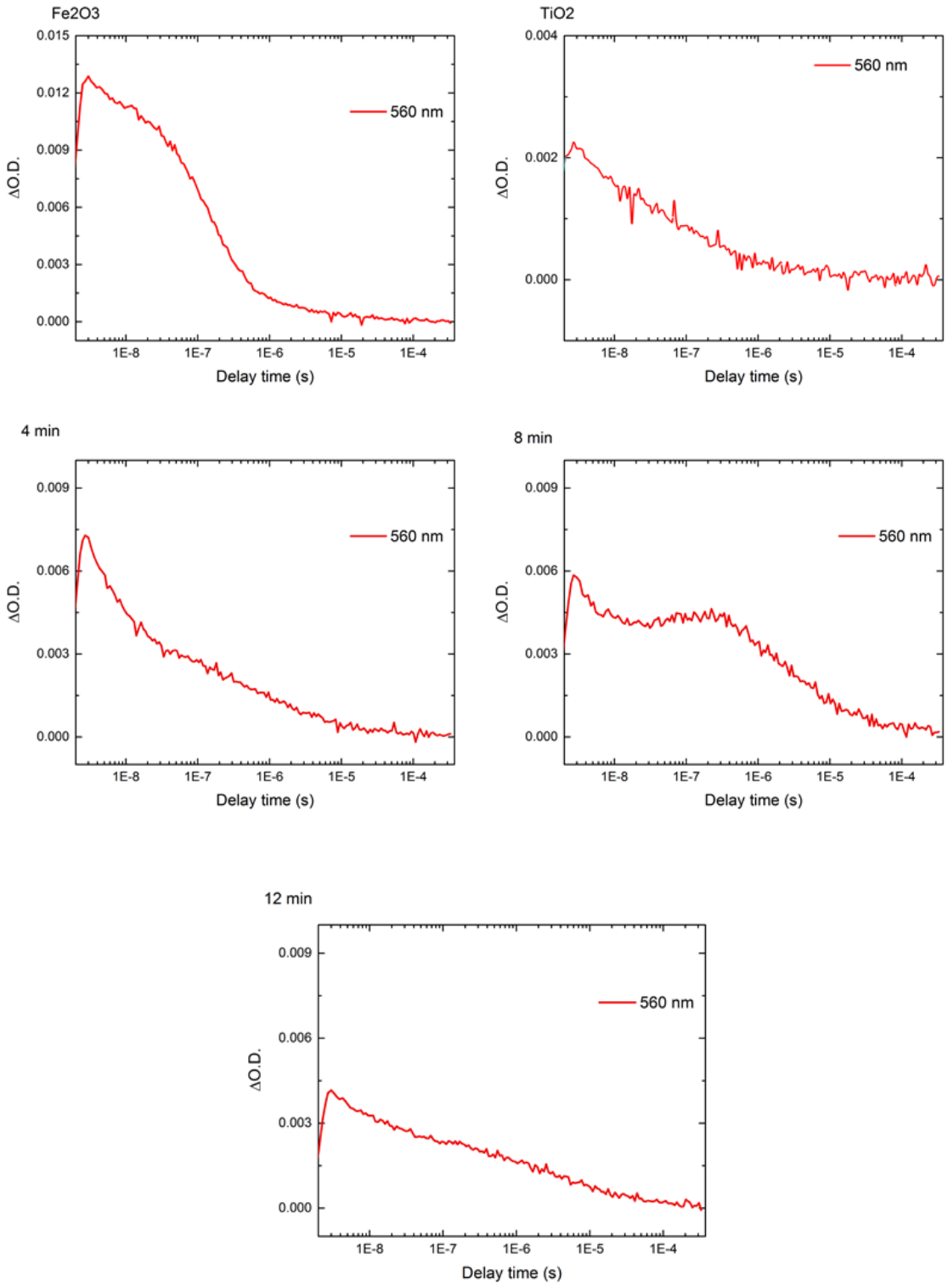

Figure 6.25. Transient absorption decay curves at 560 nm for pure TiO_2, pure Fe_2O_3, and TiO_2/Fe_2O_3 thin films.

6.11 Conclusion

The process of aerosol assisted chemical vapour deposition (AACVD) used to deposit iron oxide on FTO glass, at 450ºC using [Iron(II) acetylacetonate [$Fe(CH_3COCH=C(O)CH_3)_2$] precursors. This is the first time AACVD Fe_2O_3 thin films have been made by AACVD. The process of APCVD was then used to deposit TiO_2 on the Fe_2O_3 films, with deposition times of 4, 8 and 12 minutes, using titanium isopropoxide [$Ti(OCH(CH3)_2)_4$. XRD and Raman spectra were used as the confirmation of phase's formation of the resulting samples, with Fe_2O_3 and TiO_2 in the hematite and anatase phase only, and, from XPS studies, Fe and Ti were found to be in the Fe^{3+} and Ti^{4+} form. The bandgap of TiO_2/Fe_2O_3 thin films was seen to decrease, compared with Fe_2O_3 thin films, and a very significant increase in photocurrent was seen in TiO_2/Fe_2O_3, compared with pure Fe_2O_3 or TiO_2 films. PEC measurements of TiO_2/Fe_2O_3 deposited on FTO revealed a photocurrent 1.7 mA cm^{-2} at 1.23 V vs NHE, in 1M NaOH tested under AM1.5 1 sunlight conditions. When transient absorption spectroscopy (TAS) was used to investigated lifetime and electron-hole recombination, TiO_2/Fe_2O_3 showed an increase in the lifetime compared with pure hematite. This could be a result of the improvement in the photocurrent (due to decreased electron-hole recombination).

This study has clearly demonstrated the promise of TiO_2/Fe_2O_3 films as a water-splitting and high-stability material. However, further study of photocurrents of TiO_2/Fe_2O_3 films is required, using different synthetic techniques, as well as further study of electron-hole behaviour by using chemical scavengers.

Chapter 7

CONCLUSIONS AND FUTURE WORK

"In the next chapter, a brief summary of the results described in this thesis is presented. In this chapter also, a future work that we think it can improve photocatalytic properties is introduced."

7.1 Conclusions

Improving the photocatalytic properties of TiO_2 has been given more attention during the last five decades, and this has been reflected in a dramatic increase in the number of publications on this topic. For example, 1000 papers were published between 1970 and 2000, but 28 000 were published in 2000–2015. Multiple approaches have been used in this thesis, such as solid solutions, heterojunctions and nanostructuring.

In this work, in the first experimental chapter, Chapter 2, different copper concentrations were doped into anatase–TiO_2 lattice for the first time using AACVD. In this chapter, we used XPS to determine that Cu was present in TiO_2. As the Cu concentration of the precursor solution increased to 20%, the Cu peaks were Cu(0)/Cu(I) and Cu (II) on the surface. The photocatalytic activity of Cu-doped TiO_2 films under UVA irradiation was tested against the degradation of stearic acid. It was found that the photocatalytic properties were enhanced compared with pure TiO_2 films. Transient absorption spectroscopy (TAS) was carried out on Cu-doped TiO_2 films and pure TiO_2 films, with Cu-doped films showing extended exciton lifetimes relative to pure TiO_2 that correlated with the photocatalytic activity. The enhancement in exciton lifetimes could be due to interactions between substitutional and interstitial Cu in the anatase lattice. These results were confirmed by photoluminescence measurements. The antimicrobial activity of Cu-doped TiO_2 and TiO_2 films was tested against a Gram-negative bacterium, *E. coli*, and Gram-positive bacterium, *S. aureus*, under dark and UVA-irradiated conditions. The activity was higher in the Cu-doped TiO_2 film compared with the undoped film under UVA at 365 nm.

Chapter 3 was a continuation of the previous chapter on Cu-doped TiO_2 films. For the first time, rutile–TiO_2 films were successfully fabricated on a thin layer of ZrO_2 at a low temperature, 500ºC, using AACVD; then, different copper concentrations were doped rutile–

TiO_2 films on ZrO_2 films. We found that the presence of copper improved the photocatalytic activity of the rutile–TiO_2 films under white light and UVA irradiation for the degradation of stearic acid. Interestingly, as the Cu concentration increased in the rutile–TiO_2 structure, the films showed surface plasmon resonance (SPR) bands at ~613 and 629.5 because the SPR of Cu-doped TiO_2 films showed excellent photocatalytic activity under white light. In addition, the photoinduced wettability of these films was measured before and after UV-365 nm irradiation. A significant increase in the water contact angle was observed after Cu doping. After UVA irradiation, there was a decrease in the water contact angle; the lowest copper concentration in the rutile–TiO_2 films was observed as a significant decrease in the water contact angle compared with other films.

As previously mentioned, TiO_2 exists in three different crystalline phases (the anatase, rutile and brookite forms). A wide range of studies have focussed on anatase and rutile or mixed anatase/rutile and their applications, including photocatalysis activities, such as in water splitting, air purification, self-cleaning materials and degradation of organic pollutants. The brookite phase has little been studied as the photocatalyst, due to difficulties in its preparation and obtaining high purity in this phase. For the bandgap energy, there is general agreement that the bandgaps of rutile and anatase TiO_2 are 3.0 and 3.2 eV, respectively. In contrast, the bandgap energy of the brookite form is not precisely known. In chapter 4, brookite TiO_2 thin films were grown by AACVD from single-source titanium butoxide. The bandgap of the brookite form and its valence band were compared with those in theoretical studies. Our films showed a direct bandgap of 3.4 eV, and this result is in excellent agreement with the calculated band structure.

Photocatalytic activity was investigated under UVA (365 nm) for the degradation of organic pollutants (stearic acid). Surprisingly, the brookite thin film exhibited higher photocatalytic activity compared with pure anatase grown under similar conditions. The hole–

electron dynamics in the brookite and anatase forms were investigated using TAS. Both films demonstrated similar behaviours in the hole–electron dynamics. In addition, TAS measurements in brookite and anatase were investigated using the hole scavenger methanol and in argon. There was a substantial effect in methanol for the brookite sample. Therefore, the difference in the photocatalytic activities may be due to the different surface areas, where the brookite form showed a higher surface area than the anatase form did.

Chapter 5 explored doping zinc and nitrogen with TiO_2 lattice using the AACVD method. In this chapter, three precursors sources were used to grow (Zn, N)-doped TiO_2 thin films, and a range of zinc concentrations was employed. In these experiments, the precursors of nitrogen and zinc were mixed together in one bubbler before aerosol was generated. Thus, changes in the relative concentrations of zinc with the remaining nitrogen concentration were constant. In addition, the change in functional properties could be correlated with the change in the zinc concentrations in (Zn, N)-doped TiO_2 films. From the XPS results for nitrogen, two environments were achieved – sitting interstitially within the TiO_2 lattice and substitution of O^{2-} by N^{3-} species. Previous studies have mentioned that substitution of O^{2-} by N^{3-} species leads to a narrowing bandgap energy of TiO_2. This results in an improvement in the photocatalytic activity of TiO_2 under visible light. In addition, visible light activities have been achieved by creating oxygen vacancies upon combination with nitrogen anions. In contrast, N-doped TiO_2 leads to creating other N species, such as NO_X and NH_X groups and chemisorbed nitrogen γ-N_2; these species have similar binding energy to interstitial nitrogen, and thus, it is difficult to determine the role of nitrogen in this case as N-doped TiO_2 photocatalysis. In this chapter, the antimicrobial activities of (Zn,N)-doped TiO_2 films with different Zn concentrations and TiO_2 were investigated against the Gram-negative bacterium *E. coli* under UVA and white light. Zn,N-doped TiO_2 showed an improvement in antimicrobial activity compared with pure TiO_2 and N:TiO_2 films. As previously mentioned, the killing of bacteria by metal oxides is likely to

be due to the oxidative stress caused by the generation of reactive oxygen species (ROS). From this, the generation of superoxide ($O_2^{\bullet -}$) radical from the surfaces of the samples was studied by using XTT sodium salt under UVA irradiation. Further, the increase in the superoxide ($O_2^{\bullet -}$) concentrations generated from (Z,N)-doped TiO_2 were observed compared with pure TiO_2 films. The TAS measurements showed that (Zn, N) doping enhanced the charge carrier generation rates.

In the final chapter of this thesis, chapter 6, AACVD and APCVD were used for depositing TiO_2/Fe_2O_3 heterojunction films on glass and FTO substrates. Heterojunction systems can be employed for enhancing photocatalytic properties. The band structure in the heterojunction system can align favourably and increase photogenerated electrons and holes between two semiconductors. In addition, the electron–hole recombination can inhibit by charge separation; thus, the photocatalytic efficiency is increased. In this system, using TiO_2/Fe_2O_3 heterojunction films, the photocatalytic activities for the degradation of stearic acid and antimicrobial activity were investigated, and a significant enhancement in these activities was observed. In contrast, the PEC of TiO_2/Fe_2O_3 was studied, and we found that the photocurrent density of TiO_2/Fe_2O_3 was enhanced compared with that of pure TiO_2 and Fe_2O_3. TAS was employed to study the lifetime of the photogenerated hole–electron in these samples in the nanosecond to microsecond timescale. The TAS results provided evidence of a long lifetime for the photogenerated hole–electron, which is necessary for enhancing water splitting.

7.2 Future work

Although good results were achieved in this thesis, we think that further studies on CVD systems are necessary for improving the deposition methods, and such work will enhance the photocatalytic properties of semiconductors. While AACVD is a well-known method, we consider that we have not scratched the surface of its potential applications in depth. Therefore, the continuation of these applications and further investigation of this method may lead to the discovery of new materials, especially for producing solid solutions or heterojunction systems. In the literature, there are some non-TiO_2 based photocatalysts, such as $BiVO_4$, Bi_2O_3 and NiO, *etc* that have been suggested to have photocatalytic activity under visible light. It was observed that hydrogenation of TiO_2 typically occurs when TiO_2 nanoparticles are treated under hydrogen at a high temperature and pressure, and it was found that hydrogenation of TiO_2 leads to decreasing the bandgap and enhancing the photocatalytic performance. We would like to use AACVD to grow H:TiO_2 films. In doing this, we hope to investigate the films' photocatalytic activity, including water purification, antimicrobial activity and water splitting; furthermore, we would like to investigate the photogenerated hole–electron lifetime. Moreover, we want to further develop our TiO_2/Fe_2O_3 heterojunction films as photocatalysts by using TiO_2 nanowires/Fe_2O_3 films, as it was found that the presence of TiO_2 nanowires can enhance photocatalytic performance, especially with water splitting. We plan to investigate the antimicrobial mechanism of metal oxide films in depth by using liquid phase electron microscopy (LPEM). This work has explored growing brookite TiO_2 thin films using AACVD. This technique is considered a simple and reliable method for coating thin films because it depends on the solubility rather than the volatility of precursors. This work could open the door for further research on the brookite TiO_2 thin films in different applications such as solar cells, water splitting and hydrogen production.

Regarding further work on brookite TiO_2 thin films, we observed that the photocatalytic activity of Cu-doped rutile and anatase TiO_2 films was improved compared to that of un-doped TiO_2. Hence, we will try to deposit Cu-doped brookite TiO_2 thin films using AACVD and then we will carry out a comprehensive study of its photocatalytic properties, including the degradation of stearic acid, water splitting and charge carrier recombination. In addition, N-doped anatase TiO_2 showed photocatalytic activity under visible light and led to a shift in the band gap toward the visible region. Thus, the formation of such an N-doped brookite TiO_2 thin film would allow for the production of photocatalytic materials under visible light.

8. References

1. P. R. Hunter, M. Waite, E. Ronchi and Organisation for Economic Co-operation and Development., *Drinking water and infectious disease : establishing the links*, CRC Press, Boca Raton, Fla., 2003.
2. M. A. Ashraf, *Environ Sci Pollut R*, 2017, **24**, 4223-4227.
3. *E Mediterr Health J*, 2017, **23**, 788-789.
4. E. Awuah, K. B. Nyarko, P. A. Owusu and K. Osei-Bonsu, *Desalination*, 2009, **248**, 453-459.
5. S. Y. Lee and S. J. Park, *J Ind Eng Chem*, 2013, **19**, 1761-1769.
6. J. Schneider, M. Matsuoka, M. Takeuchi, J. L. Zhang, Y. Horiuchi, M. Anpo and D. W. Bahnemann, *Chem Rev*, 2014, **114**, 9919-9986.
7. I. T. Peternel, N. Koprivanac, A. M. L. Bozic and H. M. Kugic, *J Hazard Mater*, 2007, **148**, 477-484.
8. C. H. Wu and C. L. Chang, *J Hazard Mater*, 2006, **128**, 265-272.
9. J. M. Herrmann, *Catal Today*, 1999, **53**, 115-129.
10. J. C. Sin, S. M. Lam, A. R. Mohamed and K. T. Lee, *Int J Photoenergy*, 2012, DOI: Artn 18515910.1155/2012/185159.
11. D. S. Bhatkhande, V. G. Pangarkar and A. A. C. M. Beenackers, *J Chem Technol Biot*, 2002, **77**, 102-116.
12. H. Choi, S. R. Al-Abed, D. D. Dionysiou, E. Stathatos and P. Lianos, *Sustain Sci Eng*, 2010, **2**, 229-254.
13. U. I. Gaya and A. H. Abdullah, *J Photoch Photobio C*, 2008, **9**, 1-12.
14. J. A. Byrne, P. A. Fernandez-Ibanez, P. S. M. Dunlop, D. M. A. Alrousan and J. W. J. Hamilton, *Int J Photoenergy*, 2011, DOI: Artn 79805110.1155/2011/798051.
15. K. Y. Foo and B. H. Hameed, *Adv Colloid Interfac*, 2010, **159**, 130-143.
16. M. N. Chong, B. Jin, C. W. K. Chow and C. Saint, *Water Res*, 2010, **44**, 2997-3027.
17. M. Pelaez, N. T. Nolan, S. C. Pillai, M. K. Seery, P. Falaras, A. G. Kontos, P. S. M. Dunlop, J. W. J. Hamilton, J. A. Byrne, K. O'Shea, M. H. Entezari and D. D. Dionysiou, *Appl Catal B-Environ*, 2012, **125**, 331-349.
18. J. J. Fan, Z. Z. Li, W. Y. Zhou, Y. C. Miao, Y. J. Zhang, J. H. Hu and G. S. Shao, *Appl Surf Sci*, 2014, **319**, 75-82.
19. A. Fujishima and K. Honda, *Nature*, 1972, **238**, 37-+.
20. S. Banerjee, D. D. Dionysiou and S. C. Pillai, *Appl Catal B-Environ*, 2015, **176**, 396-428.
21. H. Tang, K. Prasad, R. Sanjines and F. Levy, *Sensor Actuat B-Chem*, 1995, **26**, 71-75.
22. Q. H. Yi, H. Wang, S. Cong, Y. J. Cao, Y. Wang, Y. H. Sun, Y. H. Lou, J. Zhao, J. Wu and G. F. Zou, *Nanoscale Res Lett*, 2016, **11**.
23. J. H. Braun, A. Baidins and R. E. Marganski, *Prog Org Coat*, 1992, **20**, 105-138.
24. K. M. Tyner, A. M. Wokovich, D. E. Godar, W. H. Doub and N. Sadrieh, *Int J Cosmetic Sci*, 2011, **33**, 234-244.
25. C. C. Chen, W. H. Ma and J. C. Zhao, *Curr Org Chem*, 2010, **14**, 630-644.
26. A. Kubacka, M. S. Diez, D. Rojo, R. Bargiela, S. Ciordia, I. Zapico, J. P. Albar, C. Barbas, V. A. P. M. dos Santos, M. Fernandez-Garcia and M. Ferrer, *Sci Rep-Uk*, 2014, **4**.
27. P. Evans and D. W. Sheel, *Surf Coat Tech*, 2007, **201**, 9319-9324.
28. D. O. Scanlon, C. W. Dunnill, J. Buckeridge, S. A. Shevlin, A. J. Logsdail, S. M. Woodley, C. R. A. Catlow, M. J. Powell, R. G. Palgrave, I. P. Parkin, G. W. Watson, T. W. Keal, P. Sherwood, A. Walsh and A. A. Sokol, *Nat Mater*, 2013, **12**, 798-801.

29. X. Q. Gong, A. Selloni, M. Batzill and U. Diebold, *Nat Mater*, 2006, **5**, 665-670.
30. X. Y. Xin, T. Xu, L. Wang and C. Y. Wang, *Sci Rep-Uk*, 2016, **6**.
31. H. F. Xu, G. Vanamu, Z. M. Nie, H. Konishi, R. Yeredla, J. Phillips and Y. F. Wang, *J Nanomater*, 2006, DOI: Artn 7890210.1155/Jnm/2006/78902.
32. C. F. Goodeve and J. A. Kitchener, *T Faraday Soc*, 1938, **34**, 0570-0579.
33. R. H. Austin and S. F. Lim, *P Natl Acad Sci USA*, 2008, **105**, 17217-17221.
34. S. M. Woodley and C. R. A. Catlow, *Comp Mater Sci*, 2009, **45**, 84-95.
35. D. Dambournet, I. Belharouak and K. Amine, *Chem Mater*, 2010, **22**, 1173-1179.
36. J. Augustynski, *Electrochim Acta*, 1993, **38**, 43-46.
37. M. Sachs, E. Pastor, A. Kafizas and J. R. Durrant, *J Phys Chem Lett*, 2016, **7**, 3742-3746.
38. R. Quesada-Cabrera, C. Sotelo-Vazquez, J. A. Darr and I. P. Parkin, *Appl Catal B-Environ*, 2014, **160**, 582-588.
39. M. Takeuchi, K. Sakamoto, G. Martra, S. Coluccia and M. Anpo, *J Phys Chem B*, 2005, **109**, 15422-15428.
40. J. C. Yu, J. G. Yu, H. Y. Tang and L. Z. Zhang, *J Mater Chem*, 2002, **12**, 81-85.
41. A. Borras, C. Lopez, V. Rico, F. Gracia, A. R. Gonzalez-Elipe, E. Richter, G. Battiston, R. Gerbasi, N. McSporran, G. Sauthier, E. Gyorgy and A. Figueras, *J Phys Chem C*, 2007, **111**, 1801-1808.
42. R. Asahi, T. Morikawa, T. Ohwaki, K. Aoki and Y. Taga, *Science*, 2001, **293**, 269-271.
43. R. Asahi, T. Morikawa, H. Irie and T. Ohwaki, *Chem Rev*, 2014, **114**, 9824-9852.
44. S. Z. Chen, P. Y. Zhang, D. M. Zhuang and W. P. Zhu, *Catal Commun*, 2004, **5**, 677-680.
45. C. Di Valentin, E. Finazzi, G. Pacchioni, A. Selloni, S. Livraghi, M. C. Paganini and E. Giamello, *Chem Phys*, 2007, **339**, 44-56.
46. R. Quesada-Cabrera, C. Sotelo-Vazqueza, M. Quesada-Gonzalez, E. P. Melian, N. Chadwick and I. P. Parkin, *J Photoch Photobio A*, 2017, **333**, 49-55.
47. Z. P. Xing, Z. Z. Li, X. Y. Wu, G. F. Wang and W. Zhou, *Int J Hydrogen Energ*, 2016, **41**, 1535-1541.
48. M. S. Zhu, C. Y. Zhai, L. Q. Qiu, C. Lu, A. S. Paton, Y. K. Du and M. C. Goh, *Acs Sustain Chem Eng*, 2015, **3**, 3123-3129.
49. T. Umebayashi, T. Yamaki, H. Itoh and K. Asai, *Appl Phys Lett*, 2002, **81**, 454-456.
50. T. Ohno, M. Akiyoshi, T. Umebayashi, K. Asai, T. Mitsui and M. Matsumura, *Appl Catal a-Gen*, 2004, **265**, 115-121.
51. C. W. Dunnill, Z. A. Aiken, A. Kafizas, J. Pratten, M. Wilson, D. J. Morgan and I. P. Parkin, *J Mater Chem*, 2009, **19**, 8747-8754.
52. L. Lin, W. Lin, Y. X. Zhu, B. Y. Zhao and Y. C. Xie, *Chem Lett*, 2005, **34**, 284-285.
53. J. C. Yu, L. Z. Zhang, Z. Zheng and J. C. Zhao, *Chem Mater*, 2003, **15**, 2280-2286.
54. N. O. Gopal, H. H. Lo, T. F. Ke, C. H. Lee, C. C. Chou, J. D. Wu, S. C. Sheu and S. C. Ke, *J Phys Chem C*, 2012, **116**, 16191-16197.
55. C. Sotelo-Vazquez, N. Noor, A. Kafizas, R. Quesada-Cabrera, D. O. Scanlon, A. Taylor, J. R. Durrant and I. P. Parkin, *Chem Mater*, 2015, **27**, 3234-3242.
56. J. J. Xu, Y. H. Ao, D. G. Fu and C. W. Yuan, *Appl Surf Sci*, 2008, **254**, 3033-3038.
57. W. Ho, J. C. Yu and S. Lee, *Chem Commun*, 2006, DOI: 10.1039/b515513d, 1115-1117.
58. Q. J. Xiang, J. G. Yu and M. Jaroniec, *Phys Chem Chem Phys*, 2011, **13**, 4853-4861.
59. Q. Xiao, L. L. Ouyang, L. Gao and C. Yao, *Appl Surf Sci*, 2011, **257**, 3652-3656.
60. J. F. Ju, X. Chen, Y. J. Shi, J. W. Miao and D. H. Wu, *Powder Technol*, 2013, **237**, 616-622.

61. X. B. Chen, L. Liu and F. Q. Huang, *Chem Soc Rev*, 2015, **44**, 1861-1885.
62. X. B. Chen, L. Liu, P. Y. Yu and S. S. Mao, *Science*, 2011, **331**, 746-750.
63. X. J. Yang, S. Wang, H. M. Sun, X. B. Wang and J. S. Lian, *T Nonferr Metal Soc*, 2015, **25**, 504-509.
64. G. Marci, V. Augugliaro, M. J. Lopez-Munoz, C. Martin, L. Palmisano, V. Rives, M. Schiavello, R. J. D. Tilley and A. M. Venezia, *J Phys Chem B*, 2001, **105**, 1033-1040.
65. Y. Zhao, C. Z. Li, X. H. Liu, F. Go, H. L. Du and L. Y. Shi, *Appl Catal B-Environ*, 2008, **79**, 208-215.
66. T. B. Nguyen, M. J. Hwang and K. S. Ryu, *B Korean Chem Soc*, 2012, **33**, 243-247.
67. P. Singla, M. Sharma, O. P. Pandey and K. Singh, *Appl Phys a-Mater*, 2014, **116**, 371-378.
68. Z. J. Li, W. Z. Shen, W. S. He and X. T. Zu, *J Hazard Mater*, 2008, **155**, 590-594.
69. J. F. Zhu, W. Zheng, H. E. Bin, J. L. Zhang and M. Anpo, *J Mol Catal a-Chem*, 2004, **216**, 35-43.
70. S. Y. Zhu, T. F. Shi, W. H. Liu, S. L. Wei, Y. I. Xie, C. Z. Fan and Y. Lie, *Physica B*, 2007, **396**, 177-180.
71. R. D. Santos, G. A. Faria, C. Giles, C. A. P. Leite, H. D. Barbosa, M. A. Z. Arruda and C. Longo, *Acs Appl Mater Inter*, 2012, **4**, 5555-5561.
72. P. V. Kamat and D. Meisel, *Curr Opin Colloid In*, 2002, **7**, 282-287.
73. P. V. Kamat, *J Phys Chem B*, 2002, **106**, 7729-7744.
74. E. Kowalska, H. Remita, C. Colbeau-Justin, J. Hupka and J. Belloni, *J Phys Chem C*, 2008, **112**, 1124-1131.
75. A. Furube, L. Du, K. Hara, R. Katoh and M. Tachiya, *J Am Chem Soc*, 2007, **129**, 14852-+.
76. M. Alvaro, B. Cojocaru, A. A. Ismail, N. Petrea, B. Ferrer, F. A. Harraz, V. I. Parvulescu and H. Garcia, *Appl Catal B-Environ*, 2010, **99**, 191-197.
77. M. A. Debeila, M. C. Raphulu, E. Mokoena, M. Avalos, V. Petranovskii, N. J. Coville and M. S. Scurrell, *Mat Sci Eng a-Struct*, 2005, **396**, 70-76.
78. Y. Nakato, M. Shioji and H. Tsubomura, *Chem Phys Lett*, 1982, **90**, 453-456.
79. M. V. Dozzi, A. Saccomanni and E. Selli, *J Hazard Mater*, 2012, **211**, 188-195.
80. J. T. Carneiro, C. C. Yang, J. A. Moma, J. A. Moulijn and G. Mul, *Catal Lett*, 2009, **129**, 12-19.
81. I. M. Arabatzis, T. Stergiopoulos, D. Andreeva, S. Kitova, S. G. Neophytides and P. Falaras, *J Catal*, 2003, **220**, 127-135.
82. P. Sathishkumar, R. Sivakumar, S. Anandan, J. Madhavan, P. Maruthamuthu and M. Ashokkumar, *Water Res*, 2008, **42**, 4878-4884.
83. Y. M. Liu, W. Liang, W. G. Zhang, J. J. Zhang and P. D. Han, *Solid State Commun*, 2013, **164**, 27-31.
84. N. P. Chadwick, E. N. K. Glover, S. Sathasivam, S. N. Basahel, S. A. Althabaiti, A. O. Alyoubi, I. P. Parkin and C. J. Carmalt, *J Mater Chem A*, 2016, **4**, 407-415.
85. C. S. Kim, J. W. Shin, Y. H. Cho, H. D. Jang, H. S. Byun and T. O. Kim, *Appl Catal a-Gen*, 2013, **455**, 211-218.
86. H. R. Zhang, Y. Liang, X. D. Wu and H. W. Zheng, *Mater Res Bull*, 2012, **47**, 2188-2192.
87. Y. Cong, J. L. Zhang, F. Chen, M. Anpo and D. N. He, *J Phys Chem C*, 2007, **111**, 10618-10623.
88. J. A. Al-Tawfiq and P. A. Tambyah, *J Infect Public Heal*, 2014, **7**, 339-344.
89. K. Page, M. Wilson and I. P. Parkin, *J Mater Chem*, 2009, **19**, 3819-3831.
90. W. R. Sanborn, *Am J Public Health Nations Health*, 1963, **53**, 1278-1283.

91. T. Matsunaga, R. Tomoda, T. Nakajima and H. Wake, *Fems Microbiol Lett*, 1985, **29**, 211-214.
92. H. M. Yadav, S. V. Otari, V. B. Koli, S. S. Mali, C. K. Hong, S. H. Pawar and S. D. Delekar, *J Photoch Photobio A*, 2014, **280**, 32-38.
93. M. Umadevi, M. Sangari, R. Parimaladevi, A. Sivanantham and J. Mayandi, *J Fluorine Chem*, 2013, **156**, 209-213.
94. C. W. Dunnill and I. P. Parkin, *Dalton T*, 2011, **40**, 1635-1640.
95. X. T. Hong, Z. P. Wang, W. M. Cai, F. Lu, J. Zhang, Y. Z. Yang, N. Ma and Y. J. Liu, *Chem Mater*, 2005, **17**, 1548-1552.
96. S. Ramandi, M. H. Entezari and N. Ghows, *Ultrason Sonochem*, 2017, **38**, 234-245.
97. B. Appavu and S. Thiripuranthagan, *J Photoch Photobio A*, 2017, **340**, 146-156.
98. J. Bahadur, S. Agrawal, V. Panwar, A. Parveen and K. Pal, *Macromol Res*, 2016, **24**, 488-493.
99. Y. Yao, Y. Ohko, Y. Sekiguchi, A. Fujishima and Y. Kubota, *J Biomed Mater Res B*, 2008, **85b**, 453-460.
100. M. Cho, H. Chung, W. Choi and J. Yoon, *Water Res*, 2004, **38**, 1069-1077.
101. D. Wang, L. X. Zhao, H. Y. Ma, H. Zhang and L. H. Guo, *Environ Sci Technol*, 2017, **51**, 10137-10145.
102. Y. Li, W. Zhang, J. F. Niu and Y. S. Chen, *Acs Nano*, 2012, **6**, 5164-5173.
103. A. Azam, A. S. Ahmed, M. Oves, M. S. Khan, S. S. Habib and A. Memic, *Int J Nanomed*, 2012, **7**, 6003-6009.
104. S. M. Dizaj, F. Lotfipour, M. Barzegar-Jalali, M. H. Zarrintan and K. Adibkia, *Mat Sci Eng C-Mater*, 2014, **44**, 278-284.
105. G. Grass, C. Rensing and M. Solioz, *Appl Environ Microb*, 2011, **77**, 1541-1547.
106. A. R. West, *Basic solid state chemistry*, John Wiley & Sons, New York, 2nd edn., 1999.
107. P. W. Atkins, *The elements of physical chemistry : with applications in biology*, W.H. Freeman, New York, 3rd edn., 2001.
108. K. S. Yeung and Y. W. Lam, *Thin Solid Films*, 1983, **109**, 169-178.
109. W. Sugimura, T. Yamazaki, H. Shigetani, J. Tanaka and T. Mitsuhashi, *Jpn J Appl Phys 1*, 1997, **36**, 7358-7359.
110. Q. Xie, Y. L. Jiang, C. Detavernier, D. Deduytsche, R. L. Van Meirhaeghe, G. P. Ru, B. Z. Li and X. P. Qu, *J Appl Phys*, 2007, **102**.
111. R. Mechiakh, F. Meriche, R. Kremer, R. Bensaha, B. Boudine and A. Boudrioua, *Opt Mater*, 2007, **30**, 645-651.
112. K. R. Patil, S. D. Sathaye, Y. B. Khollam, S. B. Deshpande, N. R. Pawaskar and A. B. Mandale, *Mater Lett*, 2003, **57**, 1775-1780.
113. A. C. Jones and M. L. Hitchman, *Chemical vapour deposition : precursors, processes and applications*, Royal Society of Chemistry, Cambridge, UK, 2009.
114. A. M. Alotaibi, S. Sathasivam and I. P. Parkin, *Rsc Adv*, 2015, **5**, 67944-67950.
115. W. L. Yang and C. A. Wolden, *Thin Solid Films*, 2006, **515**, 1708-1713.
116. H. Lee, Y. K. Park, S. J. Kim, J. H. Park, S. J. Ki and S. C. Jung, *Surf Eng*, 2015, **31**, 134-139.
117. S. K. Pradhan, P. J. Reucroft, F. Q. Yang and A. Dozier, *J Cryst Growth*, 2003, **256**, 83-88.
118. D. Y. Guo, A. Ito, T. Goto, R. Tu, C. B. Wang, Q. Shen and L. M. Zhang, *J Adv Ceram*, 2013, **2**, 162-166.
119. N. Rausch and E. P. Burte, *J Electrochem Soc*, 1993, **140**, 145-149.
120. P. Marchand, I. A. Hassan, I. P. Parkin and C. J. Carmalt, *Dalton T*, 2013, **42**, 9406-9422.

121. C. Chew, P. Bishop, C. Salcianu, C. J. Carmalt and I. P. Parkin, *Rsc Adv*, 2014, **4**, 13182-13190.
122. X. H. Hou and K. L. Choy, *Chem Vapor Depos*, 2006, **12**, 583-596.
123. I. A. Hassan, I. P. Parkin, S. P. Nair and C. J. Carmalt, *J Mater Chem B*, 2014, **2**, 2855-2860.
124. N. Noor and I. P. Parkin, *Thin Solid Films*, 2013, **532**, 26-30.
125. V. Diesen, C. W. Dunnill, J. C. Bear, S. Firth, M. Jonsson and I. P. Parkin, *Chem Vapor Depos*, 2014, **20**, 91-97.
126. B. J. Blackburn, C. Drosos, D. B. Brett, M. A. Parkes, C. J. Carmalt and I. P. Parkin, *Rsc Adv*, 2016, **6**, 111797-111805.
127. I. A. Hassan, A. Ratnasothy, D. S. Bhachu, S. Sathasivam and C. J. Carmalt, *Aust J Chem*, 2013, **66**, 1274-1280.
128. M. A. Ehsan, T. A. N. Peiris, K. G. U. Wijayantha, H. Khaledi, H. N. Ming, M. Misran, Z. Arifin and M. Mazhar, *Thin Solid Films*, 2013, **540**, 1-9.
129. C. Sotelo-Vazquez, R. Quesada-Cabrera, J. A. Darr and I. P. Parkin, *J Mater Chem A*, 2014, **2**, 7082-7087.
130. M. Ohring, *The materials science of thin films*, Academic Press, Boston, 1992.
131. B. A. Thrush, *Photoch Photobio Sci*, 2003, **2**, 453-454.
132. G. Porter, *Proc R Soc Lon Ser-A*, 1950, **200**, 284-&.
133. G. Porter and M. R. Topp, *Nature*, 1968, **220**, 1228-&.
134. S. R. Pendlebury, X. L. Wang, F. Le Formal, M. Cornuz, A. Kafizas, S. D. Tilley, M. Gratzel and J. R. Durrant, *J Am Chem Soc*, 2014, **136**, 9854-9857.
135. R. Godin, A. Kafizas and J. R. Durrant, *Curr Opin Electroche*, 2017, **2**, 136-143.
136. A. Kafizas, X. L. Wang, S. R. Pendlebury, P. Barnes, M. Ling, C. Sotelo-Vazquez, R. Quesada-Cabrera, C. Li, I. P. Parkin and J. R. Durrantt, *J Phys Chem A*, 2016, **120**, 715-723.
137. R. Berera, R. van Grondelle and J. T. M. Kennis, *Photosynth Res*, 2009, **101**, 105-118.
138. F. E. Lytle, R. M. Parrish and W. T. Barnes, *Appl Spectrosc*, 1985, **39**, 444-451.
139. A. M. Alotaibi, S. Sathasivam, B. A. D. Williamson, A. Kafizas, C. Sotelo-Vazquez, A. Taylor, D. O. Scanlon and I. P. Parkin, *Chem Mater*, 2018, **30**, 1353-1361.
140. X. L. Wang, A. Kafizas, X. O. Li, S. J. A. Moniz, P. J. T. Reardon, J. W. Tang, I. P. Parkin and J. R. Durrant, *J Phys Chem C*, 2015, **119**, 10439-10447.
141. A. L. Linsebigler, G. Q. Lu and J. T. Yates, *Chem Rev*, 1995, **95**, 735-758.
142. C. McCullagh, J. M. C. Robertson, D. W. Bahnemann and P. K. J. Robertson, *Res Chem Intermediat*, 2007, **33**, 359-375.
143. K. Hashimoto, H. Irie and A. Fujishima, *Jpn J Appl Phys 1*, 2005, **44**, 8269-8285.
144. I. P. Parkin and R. G. Palgrave, *J Mater Chem*, 2005, **15**, 1689-1695.
145. M. C. Blount, D. H. Kim and J. L. Falconer, *Environ Sci Technol*, 2001, **35**, 2988-2994.
146. E. I. Cedillo-Gonzalez, R. Ricco, M. Montorsi, M. Montorsi, P. Falcaro and C. Siligardi, *Build Environ*, 2014, **71**, 7-14.
147. T. Adachi, S. S. Latthe, S. W. Gosavi, N. Roy, N. Suzuki, H. Ikari, K. Kato, K. Katsumata, K. Nakata, M. Furudate, T. Inoue, T. Kondo, M. Yuasa, A. Fujishima and C. Terashima, *Appl Surf Sci*, 2018, **458**, 917-923.
148. K. H. Guan, *Surf Coat Tech*, 2005, **191**, 155-160.
149. M. Sahu and P. Biswas, *Nanoscale Res Lett*, 2011, **6**, 1-14.
150. Y. Q. Wang, R. R. Zhang, J. B. Li, L. L. Li and S. W. Lin, *Nanoscale Res Lett*, 2014, **9**.
151. H. Yan, X. D. Wang, M. Yao and X. J. Yao, *Prog Nat Sci-Mater*, 2013, **23**, 402-407.
152. O. Ola and M. M. Maroto-Valer, *Appl Catal a-Gen*, 2015, **502**, 114-121.

153. X. H. Wang, J. G. Li, H. Kamiyama, M. Katada, N. Ohashi, Y. Moriyoshi and T. Ishigaki, *J Am Chem Soc*, 2005, **127**, 10982-10990.
154. J. F. Zhu, F. Chen, J. L. Zhang, H. J. Chen and M. Anpo, *J Photoch Photobio A*, 2006, **180**, 196-204.
155. T. V. Nguyen and J. C. S. Wu, *Appl Catal a-Gen*, 2008, **335**, 112-120.
156. D. Tahir and S. Tougaard, *J Phys-Condens Mat*, 2012, **24**.
157. M. L. Kremer, *Int J Chem Kinet*, 2006, **38**, 725-736.
158. B. Wu, R. Huang, M. Sahu, X. Y. Feng, P. Biswas and Y. J. Tang, *Sci Total Environ*, 2010, **408**, 1755-1758.
159. K. B. Jaimy, V. P. Safeena, S. Ghosh, N. Y. Hebalkar and K. G. K. Warrier, *Dalton T*, 2012, **41**, 4824-4832.
160. W. Y. Choi, A. Termin and M. R. Hoffmann, *J Phys Chem-Us*, 1994, **98**, 13669-13679.
161. J. P. Ruparelia, A. K. Chatteriee, S. P. Duttagupta and S. Mukherji, *Acta Biomater*, 2008, **4**, 707-716.
162. M. You, T. G. Kim and Y. M. Sung, *Cryst Growth Des*, 2010, **10**, 983-987.
163. G. Colon, M. Maicu, M. C. Hidalgo and J. A. Navio, *Appl Catal B-Environ*, 2006, **67**, 41-51.
164. C. Karunakaran, G. Abiramasundari, P. Gomathisankar, G. Manikandan and V. Anandi, *J Colloid Interf Sci*, 2010, **352**, 68-74.
165. H. S. Park, D. H. Kim, S. J. Kim and K. S. Lee, *J Alloy Compd*, 2006, **415**, 51-55.
166. E. Celik, Z. Gokcen, N. F. A. Azem, M. Tanoglu and O. F. Emrullahoglu, *Mat Sci Eng B-Solid*, 2006, **132**, 258-265.
167. W. J. Zhang, Y. Li, S. L. Zhu and F. H. Wang, *Catal Today*, 2004, **93-5**, 589-594.
168. S. Sathasivam, R. R. Arnepalli, B. Kumar, K. K. Singh, R. J. Visser, C. S. Blackman and C. J. Carmalt, *Chem Mater*, 2014, **26**, 4419-4424.
169. S. Sathasivam, R. R. Arnepalli, K. K. Singh, R. J. Visser, C. S. Blackman and C. J. Carmalt, *Rsc Adv*, 2015, **5**, 11812-11817.
170. A. M. Alotaibi, S. Sathasivam, S. P. Nair and I. P. Parkin, *J Mater Chem B*, 2016, **4**, 666-671.
171. D. S. Bhachu, S. J. A. Moniz, S. Sathasivam, D. O. Scanlon, A. Walsh, S. M. Bawaked, M. Mokhtar, A. Y. Obaid, I. P. Parkin, J. W. Tang and C. J. Carmalt, *Chem Sci*, 2016, **7**, 4832-4841.
172. N. Chadwick, S. Sathasivam, A. Kafizas, S. M. Bawaked, A. Y. Obaid, S. Al-Thabaiti, S. N. Basahel, I. P. Parkin and C. J. Carmalt, *J Mater Chem A*, 2014, **2**, 5108-5116.
173. S. Sathasivam, D. S. Bhachu, Y. Lu, S. M. Bawaked, A. Y. Obaid, S. Al-Thabaiti, S. N. Basahel, C. J. Carmalt and I. P. Parkin, *Chem Vapor Depos*, 2015, **21**, 21-25.
174. S. D. Ponja, S. Sathasivam, I. P. Parkin and C. J. Carmalt, *Rsc Adv*, 2014, **4**, 49723-49728.
175. C. E. Knapp and C. J. Carmalt, *Chem Soc Rev*, 2016, **45**, 1036-1064.
176. A. Mills and J. S. Wang, *J Photoch Photobio A*, 2006, **182**, 181-186.
177. G. Kresse, *J Non-Cryst Solids*, 1995, **193**, 222-229.
178. G. Kresse and J. Hafner, *Phys Rev B*, 1994, **49**, 14251-14269.
179. G. Kresse and J. Furthmuller, *Comp Mater Sci*, 1996, **6**, 15-50.
180. G. Kresse and J. Furthmuller, *Phys Rev B*, 1996, **54**, 11169-11186.
181. J. Paier, M. Marsman, K. Hummer, G. Kresse, I. C. Gerber and J. G. Angyan, *J Chem Phys*, 2006, **125**.
182. J. Heyd, G. E. Scuseria and M. Ernzerhof, *J Chem Phys*, 2003, **118**, 8207-8215.
183. Y. K. Frodason, K. M. Johansen, T. S. Bjorheim, B. G. Svensson and A. Alkauskas, *Phys Rev B*, 2017, **95**.

184. J. L. Lyons, A. Alkauskas, A. Janotti and C. G. Van de Walle, *Phys Status Solidi B*, 2015, **252**, 900-908.
185. C. G. Van de Walle and J. Neugebauer, *J Appl Phys*, 2004, **95**, 3851-3879.
186. A. Alkauskas, M. D. McCluskey and C. G. Van de Walle, *J Appl Phys*, 2016, **119**.
187. J. B. Varley, A. Janotti and C. G. Van de Walle, *Adv Mater*, 2011, **23**, 2343-+.
188. J. Franck, *Naturwissenschaften*, 1924, **12**, 1063-1068.
189. E. Condon, *Phys Rev*, 1926, **28**, 1182-1201.
190. K. L. Mittal, *Electrocomp Sci Tech*, 1976, **3**, 21-42.
191. W. F. Zhang, Y. L. He, M. S. Zhang, Z. Yin and Q. Chen, *J Phys D Appl Phys*, 2000, **33**, 912-916.
192. F. Tian, Y. P. Zhang, J. Zhang and C. X. Pan, *J Phys Chem C*, 2012, **116**, 7515-7519.
193. M. C. Biesinger, L. W. M. Lau, A. R. Gerson and R. S. C. Smart, *Appl Surf Sci*, 2010, **257**, 887-898.
194. G. Deroubaix and P. Marcus, *Surf Interface Anal*, 1992, **18**, 39-46.
195. H. Tang, K. Prasad, R. Sanjines, P. E. Schmid and F. Levy, *J Appl Phys*, 1994, **75**, 2042-2047.
196. I. Takahashi, D. J. Payne, R. G. Palgrave and R. G. Egdell, *Chem Phys Lett*, 2008, **454**, 314-317.
197. G. Liu, C. H. Sun, H. G. Yang, S. C. Smith, L. Z. Wang, G. Q. Lu and H. M. Cheng, *Chem Commun*, 2010, **46**, 755-757.
198. D. S. Bhachu, S. Sathasivam, G. Sankar, D. O. Scanlon, G. Cibin, C. J. Carmalt, I. P. Parkin, G. W. Watson, S. M. Bawaked, A. Y. Obaid, S. Al-Thabaiti and S. N. Basahel, *Adv Funct Mater*, 2014, **24**, 5075-5085.
199. S. P. Lim, A. Pandikumar, H. N. Lim, R. Ramaraj and N. M. Huang, *Sci Rep-Uk*, 2015, **5**.
200. S. K. S. Patel and N. S. Gajbhiye, *Mater Chem Phys*, 2012, **132**, 175-179.
201. M. R. Hasan, S. B. A. Hamid, W. J. Basirun, S. H. M. Suhaimy and A. N. C. Mat, *Rsc Adv*, 2015, **5**, 77803-77813.
202. L. Q. Jing, X. J. Sun, B. F. Xin, B. Q. Wang, W. M. Cai and H. G. Fu, *J Solid State Chem*, 2004, **177**, 3375-3382.
203. F. M. Pesci, A. J. Cowan, B. D. Alexander, J. R. Durrant and D. R. Klug, *J Phys Chem Lett*, 2011, **2**, 1900-1903.
204. F. Le Formal, S. R. Pendlebury, M. Cornuz, S. D. Tilley, M. Gratzel and J. R. Durrant, *J Am Chem Soc*, 2014, **136**, 2564-2574.
205. A. Fujishima, X. T. Zhang and D. A. Tryk, *Surf Sci Rep*, 2008, **63**, 515-582.
206. L. L. Wang, C. McCleese, A. Kovalsky, Y. X. Zhao and C. Burda, *J Am Chem Soc*, 2014, **136**, 12205-12208.
207. T. M. Clarke, A. M. Ballantyne, J. Nelson, D. D. C. Bradley and J. R. Durrant, *Adv Funct Mater*, 2008, **18**, 4029-4035.
208. L. J. E. Anderson, K. M. Mayer, R. D. Fraleigh, Y. Yang, S. Lee and J. H. Hafner, *J Phys Chem C*, 2010, **114**, 11127-11132.
209. L. Wang, H. Y. Wang, B. R. Gao, L. Y. Pan, Y. Jiang, Q. D. Chen, W. Han and H. B. Sun, *Ieee J Quantum Elect*, 2011, **47**, 1177-1184.
210. A. M. Peiro, C. Colombo, G. Doyle, J. Nelson, A. Mills and J. R. Durrant, *J Phys Chem B*, 2006, **110**, 23255-23263.
211. S. Devahasdin, C. Fan, K. Y. Li and D. H. Chen, *J Photoch Photobio A*, 2003, **156**, 161-170.
212. J. Tang, J. R. Durrant and D. R. Klug, *J Am Chem Soc*, 2008, **130**, 13885-13891.
213. S. Kundu, A. Kafizas, G. Hyett, A. Mills, J. A. Darr and I. P. Parkin, *J Mater Chem*, 2011, **21**, 6854-6863.

214. A. J. Cowan, J. W. Tang, W. H. Leng, J. R. Durrant and D. R. Klug, *J Phys Chem C*, 2010, **114**, 4208-4214.
215. R. Quesada-Cabrera, C. Sotelo-Vazquez, J. C. Bear, J. A. Darr and I. P. Parkin, *Adv Mater Interfaces*, 2014, **1**.
216. F. Sayilkan, M. Asilturk, P. Tatar, N. Kiraz, S. Sener, E. Arpac and H. Sayilkan, *Mater Res Bull*, 2008, **43**, 127-134.
217. B. F. Gao, T. M. Lim, D. P. Subagio and T. T. Lim, *Appl Catal a-Gen*, 2010, **375**, 107-115.
218. T. Luttrell, S. Halpegamage, J. G. Tao, A. Kramer, E. Sutter and M. Batzill, *Sci Rep-Uk*, 2014, **4**.
219. B. Tryba, J. Orlikowski, R. J. Wrobel, J. Przepiorski and A. W. Morawski, *J Mater Eng Perform*, 2015, **24**, 1243-1252.
220. G. D. Yang, Z. Jiang, H. H. Shi, T. C. Xiao and Z. F. Yan, *J Mater Chem*, 2010, **20**, 5301-5309.
221. M. V. Dozzi, C. D'Andrea, B. Ohtani, G. Valentini and E. Selli, *J Phys Chem C*, 2013, **117**, 25586-25595.
222. S. W. Yang and L. Gao, *Mater Res Bull*, 2008, **43**, 1872-1876.
223. H. Y. Liu and L. Gao, *J Am Ceram Soc*, 2004, **87**, 1582-1584.
224. D. L. Shieh, Y. S. Lin, J. H. Yeh, S. C. Chen, B. C. Lin and J. L. Lin, *Chem Commun*, 2012, **48**, 2528-2530.
225. X. H. Xia, Y. Gao, Z. Wang and Z. J. Jia, *J Phys Chem Solids*, 2008, **69**, 2888-2893.
226. S. Ponja, S. Sathasivam, N. Chadwick, A. Kafizas, S. M. Bawaked, A. Y. Obaid, S. Al-Thabaiti, S. N. Basahel, I. P. Parkin and C. J. Carmalt, *J Mater Chem A*, 2013, **1**, 6271-6278.
227. S. Sathasivam, D. S. Bhachu, Y. Lu, N. Chadwick, S. A. Althabaiti, A. O. Alyoubi, S. N. Basahel, C. J. Carmalt and I. P. Parkin, *Sci Rep-Uk*, 2015, **5**.
228. S. N. Basahel, T. T. Ali, M. Mokhtar and K. Narasimharao, *Nanoscale Res Lett*, 2015, **10**.
229. Y. F. Wang, L. P. Li, X. S. Huang, Q. Li and G. S. Li, *Rsc Adv*, 2015, **5**, 34302-34313.
230. S. M. Chang and R. A. Doong, *J Phys Chem B*, 2006, **110**, 20808-20814.
231. T. Mazza, E. Barborini, P. Piseri, P. Milani, D. Cattaneo, A. Li Bassi, C. E. Bottani and C. Ducati, *Phys Rev B*, 2007, **75**.
232. M. S. Kim, Y. D. Ko, J. H. Hong, M. C. Jeong, J. M. Myoung and I. Yun, *Appl Surf Sci*, 2004, **227**, 387-398.
233. F. A. Akgul, G. Akgul, N. Yildirim, H. E. Unalan and R. Turan, *Mater Chem Phys*, 2014, **147**, 987-995.
234. M. C. Biesinger, *Surf Interface Anal*, 2017, **49**, 1325-1334.
235. B. Erdem, R. A. Hunsicker, G. W. Simmons, E. D. Sudol, V. L. Dimonie and M. S. El-Aasser, *Langmuir*, 2001, **17**, 2664-2669.
236. J. Tauc, *Mater Res Bull*, 1968, **3**, 37-&.
237. J. M. Kum, Y. J. Park, H. J. Kim and S. O. Cho, *Nanotechnology*, 2015, **26**.
238. A. A. Salam, R. Singaravelan, P. Vasanthi and S. B. Alwar, *J Nanostructure Chem*, 2015, **5**, 383-392.
239. O. A. Yeshchenko, I. S. Bondarchuk, V. S. Gurin, I. M. Dmitruk and A. V. Kotko, *Surf Sci*, 2013, **608**, 275-281.
240. S. D. Mo and W. Y. Ching, *Phys Rev B Condens Matter*, 1995, **51**, 13023-13032.
241. T. Shibata, H. Irie, M. Ohmori, A. Nakajima, T. Watanabe and K. Hashimoto, *Phys Chem Chem Phys*, 2004, **6**, 1359-1362.
242. M. Landmann, E. Rauls and W. G. Schmidt, *J Phys-Condens Mat*, 2012, **24**.

243. J. F. Zhang, P. Zhou, J. J. Liu and J. G. Yu, *Phys Chem Chem Phys*, 2014, **16**, 20382-20386.
244. G. H. Li and K. A. Gray, *Chem Mater*, 2007, **19**, 1143-1146.
245. J. G. Li, T. Ishigaki and X. D. Sun, *J Phys Chem C*, 2007, **111**, 4969-4976.
246. H. F. Lin, L. P. Li, M. L. Zhao, X. S. Huang, X. M. Chen, G. S. Li and R. C. Yu, *J Am Chem Soc*, 2012, **134**, 8328-8331.
247. B. Zhao, F. Chen, Q. W. Huang and J. L. Zhang, *Chem Commun*, 2009, DOI: 10.1039/b909883f, 5115-5117.
248. I. N. Kuznetsova, V. Blaskov, I. Stambolova, L. Znaidi and A. Kanaev, *Mater Lett*, 2005, **59**, 3820-3823.
249. M. Monai, T. Montini and P. Fornasiero, *Catalysts*, 2017, **7**.
250. A. Di Paola, M. Bellardita and L. Palmisano, *Catalysts*, 2013, **3**, 36-73.
251. O. Glemser and E. Schwarzmann, *Angew Chem Int Edit*, 1956, **68**, 791-791.
252. D. H. Kim, W. S. Kim, S. Kim and S. H. Hong, *Acs Appl Mater Inter*, 2014, **6**, 11817-11822.
253. J. E. S. Haggerty, L. T. Schelhas, D. A. Kitchaev, J. S. Mangum, L. M. Garten, W. H. Sun, K. H. Stone, J. D. Perkins, M. F. Toney, G. Ceder, D. S. Ginley, B. P. Gorman and J. Tate, *Sci Rep-Uk*, 2017, **7**.
254. M. Burbano, D. O. Scanlon and G. W. Watson, *J Am Chem Soc*, 2011, **133**, 15065-15072.
255. A. M. Ganose, C. N. Savory and D. O. Scanlon, *J Phys Chem Lett*, 2015, **6**, 4594-4598.
256. A. B. Kehoe, D. J. Temple, G. W. Watson and D. O. Scanlon, *Phys Chem Chem Phys*, 2013, **15**, 15477-15484.
257. P. Marchand, S. Sathasivam, B. A. D. Williamson, D. Pugh, S. M. Bawaked, S. N. Basahel, A. Y. Obaid, D. O. Scanlon, I. P. Parkin and C. J. Carmalt, *J Mater Chem C*, 2016, **4**, 6761-6768.
258. M. K. Rajpalke, W. M. Linhart, M. Birkett, K. M. Yu, D. O. Scanlon, J. Buckeridge, T. S. Jones, M. J. Ashwin and T. D. Veal, *Appl Phys Lett*, 2013, **103**.
259. A. Walsh, S. Y. Chen, S. H. Wei and X. G. Gong, *Adv Energy Mater*, 2012, **2**, 400-409.
260. S. B. Zhang and J. E. Northrup, *Phys Rev Lett*, 1991, **67**, 2339-2342.
261. J. Paier, M. Marsman, K. Hummer, G. Kresse, I. C. Gerber and J. G. Angyan, *J Chem Phys*, 2006, **124**.
262. J. Buckeridge, K. T. Butler, C. R. A. Catlow, A. J. Logsdail, D. O. Scanlon, S. A. Shevlin, S. M. Woodley, A. A. Sokol and A. Walsh, *Chem Mater*, 2015, **27**, 3844-3851.
263. V. Celik and E. Mete, *Phys Rev B*, 2012, **86**.
264. H. A. Huy, B. Aradi, T. Frauenheim and P. Deak, *Phys Rev B*, 2011, **83**.
265. A. Janotti, J. B. Varley, P. Rinke, N. Umezawa, G. Kresse and C. G. Van de Walle, *Phys Rev B*, 2010, **81**.
266. J. P. Perdew, K. Burke and M. Ernzerhof, *Phys Rev Lett*, 1996, **77**, 3865-3868.
267. S. Sathasivam, R. R. Arnepalli, D. S. Bhachu, Y. Lu, J. Buckeridge, D. O. Scanlon, B. Kurnar, K. K. Singh, R. J. Visser, C. S. Blackman and C. J. Carmalt, *J Phys Chem C*, 2016, **120**, 7013-7019.
268. C. N. Savory, A. M. Ganose, W. Travis, R. S. Atri, R. G. Palgrave and D. O. Scanlon, *J Mater Chem A*, 2016, **4**, 12648-12657.
269. B. A. D. Williamson, J. Buckeridge, J. Brown, S. Ansbro, R. G. Palgrave and D. O. Scanlon, *Chem Mater*, 2017, **29**, 2402-2413.
270. C. R. Crick and I. P. Parkin, *J Mater Chem*, 2011, **21**, 14712-14716.
271. W. B. Hu, L. P. Li, G. S. Li, C. L. Tang and L. Sun, *Cryst Growth Des*, 2009, **9**, 3676-3682.

272. J. G. Li, C. C. Tang, D. Li, H. Haneda and T. Ishigaki, *J Am Ceram Soc*, 2004, **87**, 1358-1361.
273. A. Pottier, C. Chaneac, E. Tronc, L. Mazerolles and J. P. Jolivet, *J Mater Chem*, 2001, **11**, 1116-1121.
274. G. A. Tompsett, G. A. Bowmaker, R. P. Cooney, J. B. Metson, K. A. Rodgers and J. M. Seakins, *J Raman Spectrosc*, 1995, **26**, 57-62.
275. M. N. Iliev, V. G. Hadjiev and A. P. Litvinchuk, *Vib Spectrosc*, 2013, **64**, 148-152.
276. T. Ohsaka, F. Izumi and Y. Fujiki, *J Raman Spectrosc*, 1978, **7**, 321-324.
277. M. Koelsch, S. Cassaignon, J. F. Guillemoles and J. R. Jolivet, *Thin Solid Films*, 2002, **403**, 312-319.
278. T. A. Kandiel, A. Feldhoff, L. Robben, R. Dillert and D. W. Bahnemann, *Chem Mater*, 2010, **22**, 2050-2060.
279. M. Gratzel and F. P. Rotzinger, *Chem Phys Lett*, 1985, **118**, 474-477.
280. T. Zhu and S. P. Gao, *J Phys Chem C*, 2014, **118**, 11385-11396.
281. J. J. Yeh and I. Lindau, *Atom Data Nucl Data*, 1985, **32**, 1-155.
282. R. Wang, K. Hashimoto, A. Fujishima, M. Chikuni, E. Kojima, A. Kitamura, M. Shimohigoshi and T. Watanabe, *Nature*, 1997, **388**, 431-432.
283. B. Moss, K. K. Lim, A. Beltram, S. Moniz, J. W. Tang, P. Fornasiero, P. Barnes, J. Durrant and A. Kafizas, *Sci Rep-Uk*, 2017, **7**.
284. J. J. M. Vequizo, H. Matsunaga, T. Ishiku, S. Karnimura, T. Ohno and A. Yamakata, *Acs Catal*, 2017, **7**, 2644-2651.
285. M. Dorraj, B. T. Goh, N. A. Sairi, P. M. Woi and W. J. Basirun, *Appl Surf Sci*, 2018, **439**, 999-1009.
286. N. R. Khalid, E. Ahmed, Z. L. Hong, L. Sana and M. Ahmed, *Curr Appl Phys*, 2013, **13**, 659-663.
287. M. A. Malati and W. K. Wong, *Surf Technol*, 1984, **22**, 305-322.
288. X. Z. Li, F. B. Li, C. L. Yang and W. K. Ge, *J Photoch Photobio A*, 2001, **141**, 209-217.
289. V. Etacheri, C. Di Valentin, J. Schneider, D. Bahnemann and S. C. Pillai, *J Photoch Photobio C*, 2015, **25**, 1-29.
290. F. Dong, S. Guo, H. Wang, X. F. Li and Z. B. Wu, *J Phys Chem C*, 2011, **115**, 13285-13292.
291. G. S. Wu and A. Chen, *J Photoch Photobio A*, 2008, **195**, 47-53.
292. B. Naik, S. M. Kim, C. H. Jung, S. Y. Moon, S. H. Kim and J. Y. Park, *Adv Mater Interfaces*, 2014, **1**.
293. J. Cadet, T. Delatour, T. Douki, D. Gasparutto, J. P. Pouget, J. L. Ravanat and S. Sauvaigo, *Mutat Res-Fund Mol M*, 1999, **424**, 9-21.
294. J. F. Zhao, B. W. Zhang, J. Y. Li, Y. C. Liu and W. F. Wang, *Chem Commun*, 2016, **52**, 11595-11598.
295. Y. C. Zhao and C. T. Jafvert, *Environ Sci-Nano*, 2015, **2**, 136-142.
296. A. Mills and M. McFarlane, *Catal Today*, 2007, **129**, 22-28.
297. L. Q. Jing, B. F. Xin, F. L. Yuan, L. P. Xue, B. Q. Wang and H. G. Fu, *J Phys Chem B*, 2006, **110**, 17860-17865.
298. J. J. Li, S. C. Cai, Z. Xu, X. Chen, J. Chen, H. P. Jia and J. Chen, *J Hazard Mater*, 2017, **325**, 261-270.
299. L. Y. Hu, J. Y. Wang, J. X. Zhang, Q. Y. Zhang and Z. H. Liu, *Rsc Adv*, 2014, **4**, 420-427.
300. C. Di Valentin, G. Pacchioni, A. Selloni, S. Livraghi and E. Giamello, *J Phys Chem B*, 2005, **109**, 11414-11419.

301. M. Sanchez-Dominguez, G. Morales-Mendoza, M. J. Rodriguez-Vargas, C. C. Ibarra-Malo, A. A. Rodriguez-Rodriguez, A. V. Vela-Gonzalez, S. A. Perez-Garcia and R. Gomez, *J Environ Chem Eng*, 2015, **3**, 3037-3047.
302. Y. L. Yu, J. S. Wang, W. Li, W. J. Zheng and Y. Cao, *Crystengcomm*, 2015, **17**, 5074-5080.
303. A. J. Able, D. I. Guest and M. W. Sutherland, *Plant Physiol*, 1998, **117**, 491-499.
304. R. Q. Cabrera, E. R. Latimer, A. Kafizas, C. S. Blackman, C. J. Carmalt and I. P. Parkin, *J Photoch Photobio A*, 2012, **239**, 60-64.
305. D. S. Bhachu, S. Sathasivam, C. J. Carmalt and I. P. Parkin, *Langmuir*, 2014, **30**, 624-630.
306. V. Augugliaro, M. Litter, L. Palmisano and J. Soria, *J Photoch Photobio C*, 2006, **7**, 127-144.
307. A. Kafizas, Y. M. Ma, E. Pastor, S. R. Pendlebury, C. Mesa, L. Francas, F. Le Formal, N. Noor, M. Ling, C. Sotelo-Vazquez, C. J. Carmalt, I. P. Parkin and J. R. Durrant, *Acs Catal*, 2017, **7**, 4896-4903.
308. A. Fujishima, T. N. Rao and D. A. Tryk, *Electrochim Acta*, 2000, **45**, 4683-4690.
309. A. Kudo and Y. Miseki, *Chem Soc Rev*, 2009, **38**, 253-278.
310. A. Mills and S. LeHunte, *J Photoch Photobio A*, 1997, **108**, 1-35.
311. K. Nakata and A. Fujishima, *J Photoch Photobio C*, 2012, **13**, 169-189.
312. S. Gupta and M. Tripathi, *Chinese Sci Bull*, 2011, **56**, 1639-1657.
313. S. Nahar, M. F. M. Zain, A. A. H. Kadhum, H. A. Hasan and M. R. Hasan, *Materials*, 2017, **10**.
314. K. Koci, L. Obalova, L. Matejova, D. Placha, Z. Lacny, J. Jirkovsky and O. Solcova, *Appl Catal B-Environ*, 2009, **89**, 494-502.
315. H. Han, F. Riboni, F. Karlicky, S. Kment, A. Goswami, P. Sudhagar, J. Yoo, L. Wang, O. Tomanec, M. Petr, O. Haderka, C. Terashima, A. Fujishima, P. Schmuki and R. Zboril, *Nanoscale*, 2017, **9**, 134-142.
316. Y. Xia and L. Yin, *Phys Chem Chem Phys*, 2013, **15**, 18627-18634.
317. Q. Sun, W. Leng, Z. Li and Y. Xu, *J Hazard Mater*, 2012, **229-230**, 224-232.
318. K. H. Hwang, B. C. Kang, D. Y. Jung, Y. J. Kim and J. H. Boo, *Sci Rep-Uk*, 2015, **5**.
319. G. Hyett, M. Green and I. P. Parkin, *J Am Chem Soc*, 2006, **128**, 12147-12155.
320. S. P. Lim, N. M. Huang, H. N. Lim and M. Mazhar, *Ceram Int*, 2014, **40**, 8045-8052.
321. S. Cerneaux, X. Y. Xiong, G. P. Simon, Y. B. Cheng and L. Spiccia, *Nanotechnology*, 2007, **18**.
322. C. B. D. Marien, C. Marchal, A. Koch, D. Robert and P. Drogui, *Environ Sci Pollut R*, 2017, **24**, 12582-12588.
323. H. M. Yadav and J. S. Kim, *Sci Adv Mater*, 2017, **9**, 1114-1119.
324. H. M. Yang, K. Zhang, R. R. Shi, X. W. Li, X. D. Dong and Y. M. Yu, *J Alloy Compd*, 2006, **413**, 302-306.
325. L. C. Jiang and W. D. Zhang, *Electroanal*, 2009, **21**, 988-993.
326. Y. You, L. Wan, S. Y. Zhang and D. F. Xu, *J Cent South Univ T*, 2007, **14**, 154-157.
327. M. O. Abou-Helal and W. T. Seeber, *Appl Surf Sci*, 2002, **195**, 53-62.
328. R. Han, W. Li, W. W. Pan, M. G. Zhu, D. Zhou and F. S. Li, *Sci Rep-Uk*, 2014, **4**.
329. Q. Wei, Z. J. Zhang, Z. C. Li, Q. Zhou and Y. Zhu, *J Phys D Appl Phys*, 2008, **41**.
330. A. Furlani, M. V. Russo, G. Polzonetti, K. Martin, H. H. Wang and J. R. Ferraro, *Appl Spectrosc*, 1990, **44**, 331-334.
331. R. P. Gupta and S. K. Sen, *Phys Rev B*, 1974, **10**, 71-77.
332. R. P. Gupta and S. K. Sen, *Phys Rev B*, 1975, **12**, 15-19.
333. A. P. Grosvenor, B. A. Kobe, M. C. Biesinger and N. S. McIntyre, *Surf Interface Anal*, 2004, **36**, 1564-1574.

334. N. S. Mcintyre and D. G. Zetaruk, *Anal Chem*, 1977, **49**, 1521-1529.
335. K. Gajda-Schrantz, S. Tymen, F. Boudoire, R. Toth, D. K. Bora, W. Calvet, M. Gratzel, E. C. Constable and A. Braun, *Physical Chemistry Chemical Physics*, 2013, **15**, 1443-1451.
336. A. P. Singh, N. Kodan, B. R. Mehta, A. Dey and S. Krishnamurthy, *Mater Res Bull*, 2016, **76**, 284-291.
337. P. Thomas, P. Sreekanth and K. E. Abraham, *J Appl Phys*, 2015, **117**.
338. D. L. Shi, M. E. Sadat, A. W. Dunn and D. B. Mast, *Nanoscale*, 2015, **7**, 8209-8232.
339. K. R. Raghupathi, R. T. Koodali and A. C. Manna, *Langmuir*, 2011, **27**, 4020-4028.
340. M. Long, Y. Zhang, Z. Shu, A. D. Tang, J. Ouyang and H. M. Yang, *Chem Commun*, 2017, **53**, 6255-6258.
341. C. Bailleux, *Int J Hydrogen Energ*, 1981, **6**, 461-471.
342. A. Landman, H. Dotan, G. E. Shter, M. Wullenkord, A. Houaijia, A. Maljusch, G. S. Grader and A. Rothschild, *Nat Mater*, 2017, **16**, 646-+.
343. C. H. Liao, C. W. Huang and J. C. S. Wu, *Catalysts*, 2012, **2**, 490-516.
344. K. Mazloomi and C. Gomes, *Renew Sust Energ Rev*, 2012, **16**, 3024-3033.
345. S. J. A. Moniz, S. A. Shevlin, D. J. Martin, Z. X. Guo and J. W. Tang, *Energ Environ Sci*, 2015, **8**, 731-759.
346. United States. Department of Energy. Basic Energy Sciences Advisory Committee. and Oak Ridge National Laboratory., *Basic research needs to assure a secure energy future : a report*, Oak Ridge National Laboratory, Oak Ridge, TN, 2003.
347. R. di Primio, B. Horsfield and M. A. Guzman-Vega, *Nature*, 2000, **406**, 173-176.
348. N. S. Lewis and D. G. Nocera, *P Natl Acad Sci USA*, 2007, **104**, 20142-20142.
349. S. Solomon, G. K. Plattner, R. Knutti and P. Friedlingstein, *P Natl Acad Sci USA*, 2009, **106**, 1704-1709.
350. M. Andersson, L. Osterlund, S. Ljungstrom and A. Palmqvist, *J Phys Chem B*, 2002, **106**, 10674-10679.
351. M. P. Dareedwards, J. B. Goodenough, A. Hamnett and P. R. Trevellick, *J Chem Soc Farad T 1*, 1983, **79**, 2027-2041.
352. J. W. Jang, C. Du, Y. F. Ye, Y. J. Lin, X. H. Yao, J. Thorne, E. Liu, G. McMahon, J. F. Zhu, A. Javey, J. H. Guo and D. W. Wang, *Nat Commun*, 2015, **6**.
353. A. Kay, I. Cesar and M. Gratzel, *J Am Chem Soc*, 2006, **128**, 15714-15721.
354. K. G. Mcgregor, M. Calvin and J. W. Otvos, *J Appl Phys*, 1979, **50**, 369-373.
355. C. Sanchez, K. D. Sieber and G. A. Somorjai, *J Electroanal Chem*, 1988, **252**, 269-290.
356. R. Shinar and J. H. Kennedy, *Sol Energ Mater*, 1982, **6**, 323-335.
357. K. Sivula, F. Le Formal and M. Gratzel, *Chem Mater*, 2009, **21**, 2862-2867.
358. J. H. Kennedy and K. W. Frese, *J Electrochem Soc*, 1978, **125**, 709-714.
359. I. Balberg and H. L. Pinch, *J Magn Magn Mater*, 1978, **7**, 12-15.
360. A. B. Murphy, P. R. F. Barnes, L. K. Randeniya, I. C. Plumb, I. E. Grey, M. D. Horne and J. A. Glasscock, *Int J Hydrogen Energ*, 2006, **31**, 1999-2017.
361. J. J. Deng, J. Zhong, A. W. Pu, D. Zhang, M. Li, X. H. Sun and S. T. Lee, *J Appl Phys*, 2012, **112**.
362. M. Forster, R. J. Potter, Y. Yang, Y. Li and A. J. Cowan, *Chemphotochem*, 2018, **2**, 183-189.
363. Y. C. Ling, G. M. Wang, D. A. Wheeler, J. Z. Zhang and Y. Li, *Nano Lett*, 2011, **11**, 2119-2125.
364. A. W. Pu, J. J. Deng, M. Li, J. Gao, H. Zhang, Y. Y. Hao, J. Zhong and X. H. Sun, *J Mater Chem A*, 2014, **2**, 2491-2497.
365. T. Wang, W. J. Luo, X. Wen, Z. G. Zou and W. Huang, *Chemnanomat*, 2016, **2**, 652-655.

366. K. L. Hardee and A. J. Bard, *J Electrochem Soc*, 1976, **123**, 1024-1026.
367. R. K. Quinn, R. D. Nasby and R. J. Baughman, *Mater Res Bull*, 1976, **11**, 1011-1017.
368. S. H. Shen, P. H. Guo, D. A. Wheeler, J. G. Jiang, S. A. Lindley, C. X. Kronawitter, J. Z. Zhang, L. J. Guo and S. S. Mao, *Nanoscale*, 2013, **5**, 9867-9874.
369. G. M. Wang, Y. C. Ling, D. A. Wheeler, K. E. N. George, K. Horsley, C. Heske, J. Z. Zhang and Y. Li, *Nano Lett*, 2011, **11**, 3503-3509.
370. M. Barroso, C. A. Mesa, S. R. Pendlebury, A. J. Cowan, T. Hisatomi, K. Sivula, M. Gratzel, D. R. Klug and J. R. Durrant, *P Natl Acad Sci USA*, 2012, **109**, 15640-15645.
371. F. Le Formal, N. Tetreault, M. Cornuz, T. Moehl, M. Gratzel and K. Sivula, *Chem Sci*, 2011, **2**, 737-743.
372. L. F. Xi, P. S. Bassi, S. Y. Chiam, W. F. Mak, P. D. Tran, J. Barber, J. S. C. Loo and L. H. Wong, *Nanoscale*, 2012, **4**, 4430-4433.
373. X. L. Guo, L. L. Wang and Y. W. Tan, *Nano Energy*, 2015, **16**, 320-328.
374. S. H. Shen, J. G. Zhou, C. L. Dong, Y. F. Hu, E. N. Tseng, P. H. Guo, L. J. Guo and S. S. Mao, *Sci Rep-Uk*, 2014, **4**.
375. S. H. Shen, C. X. Kronawitter, D. A. Wheeler, P. H. Guo, S. A. Lindley, J. G. Jiang, J. Z. Zhang, L. J. Guo and S. S. Mao, *J Mater Chem A*, 2013, **1**, 14498-14506.
376. C. H. Bak, K. Kim, K. Jung, J. B. Kim and J. H. Jang, *J Mater Chem A*, 2014, **2**, 17249-17252.
377. B. Iandolo, H. X. Zhang, B. Wickman, I. Zoric, G. Conibeer and A. Hellman, *Rsc Adv*, 2015, **5**, 61021-61030.
378. H. Dotan, K. Sivula, M. Gratzel, A. Rothschild and S. C. Warren, *Energ Environ Sci*, 2011, **4**, 958-964.
379. R. Katoh, M. Murai and A. Furube, *Chem Phys Lett*, 2010, **500**, 309-312.
380. Z. Q. Huang, Y. J. Lin, X. Xiang, W. Rodriguez-Cordoba, K. J. McDonald, K. S. Hagen, K. S. Choi, B. S. Brunschwig, D. G. Musaev, C. L. Hill, D. W. Wang and T. Q. Lian, *Energ Environ Sci*, 2012, **5**, 8923-8926.
381. G. X. Pei, J. H. J. Wijten and B. M. Weckhuysen, *Phys Chem Chem Phys*, 2018, **20**, 9806-9811.
382. S. R. Pendlebury, M. Barroso, A. J. Cowan, K. Sivula, J. W. Tang, M. Gratzel, D. Klug and J. R. Durrant, *Chem Commun*, 2011, **47**, 716-718.